
MATTER-WAVE DYNAMICS IN
TIME-AVERAGED OPTICAL POTENTIALS
WITH TUNABLE INTERACTIONS

Von der QUEST-Leibniz-Forschungsschule der
Gottfried Wilhelm Leibniz Universität Hannover

zur Erlangung des Grades
Doktor der Naturwissenschaften
- Dr. rer. nat. -
genehmigte Dissertation von

M.Sc. Alexander Herbst
geboren am 16.06.1992,
in Hannover

Referent:

Prof. Dr. Ernst M. Rasel

Institut für Quantenoptik

Gottfried Wilhelm Leibniz Universität Hannover

Korreferent:

Dr. Dennis Schlippert

Institut für Quantenoptik

Gottfried Wilhelm Leibniz Universität Hannover

Korreferent:

Prof. Dr. Éric Charron

Institut des Sciences Moléculaires d'Orsay

Université Paris-Saclay, CNRS

Tag der Disputation:

17.06.2024

ABSTRACT

MATTER-WAVE DYNAMICS IN TIME-AVERAGED OPTICAL POTENTIALS WITH TUNABLE INTERACTIONS

Atom interferometers have emerged as a pivotal tool for accurate measurements of inertial effects and are used as a versatile instrument in both fundamental physics investigations and various applications. In particular, they have excelled in quantum tests of the Universality of Free Fall and are expected to be instrumental in the development of future gravitational wave detectors and in the search for dark matter. However, these experiments impose stringent requirements for a large atomic flux in combination with ultra-low expansion rates to enhance their sensitivity and to restrict systematic effects.

In this thesis, time-averaged optical potentials in conjunction with tunable interactions are used to rapidly create collimated ^{39}K BOSE-EINSTEIN condensates. Combining these two methods for the first time allows to reach an unprecedented evaporation duration of only 170 ms with an atom number of $(6.14 \pm 0.35) \times 10^4$, well-suited for interferometry applications. By individually tailoring trap frequencies and interaction strength it is also demonstrated how the resulting flux of more than 3×10^5 particles/s can be maintained when transitioning to large condensates of up to $(5.73 \pm 0.24) \times 10^5$ atoms within less than 2 s of evaporative cooling. These advancements enable the preparation of suitable interferometry input states well within the actual interferometer time, thereby enabling dead-time free measurements with superior sensitivity.

Moreover, the same techniques are used to implement a matter-wave lens, directly applicable in the optical-dipole trap without necessitating extended free-fall times. By incorporating tunable interactions, a collimation scheme previously developed with ^{87}Rb is enhanced, yielding measured energies as low as (340 ± 12) pK in one direction. Dedicated theory simulations are used to arrive at an intricate understanding of the related dynamics, allowing to extrapolate a 2D ballistic expansion energy of (438 ± 77) pK for the performed experiment. Based on these results an extended multi-stage collimation scheme is proposed which will reduce the expansion energy to below 20 pK in three dimensions, far surpassing the requirements of current 10 m baseline devices such as the Hannover VLBAI facility. These results pave the way to realize state-of-the-art matter-wave collimation in compact or lab-based apparatuses, independent of the unique features of long-baseline devices or micro-gravity environments. Ultimately, the various implemented methods will allow to perform interferometry experiments in trapped configurations and enable squeezing-enhanced interferometry schemes for measurements below the standard quantum limit.

Keywords: time-averaged optical potentials, tunable interactions, Bose-Einstein condensate, high flux source system, matter-wave lensing, delta-kick collimation

CONTENTS

1	Introduction	1
1.1	Light-pulse atom interferometry	1
1.2	Bose-Einstein condensation of ^{39}K	4
1.2.1	Bose-Einstein condensates	4
1.2.2	Evaporative cooling	5
1.2.3	Feshbach resonances	6
1.3	Atomic source systems for atom interferometry	7
1.4	Delta-Kick collimation	9
1.5	Scope of this thesis	11
2	Publications	15
2.1	Quantum test of the Universality of Free Fall using rubidium and potassium	15
2.2	Rapid generation of all-optical ^{39}K Bose-Einstein condensates using a low-field Feshbach resonance	25
2.3	High-flux source system for matter-wave interferometry exploiting tunable interactions	37
2.4	All-optical matter-wave lens using time-averaged potentials	47
2.5	Matter-wave collimation to picokelvin energies with scattering length and potential shape control	55
3	Conclusion and outlook	65
3.1	Summary	65
3.2	Further enhancement of atomic flux	65
3.3	Improved matter-wave collimation for multiple atomic species	67
3.3.1	Limitations and improvements	67
3.3.2	Application to other atomic species	67
3.4	Towards BEC interferometry in ATLAS	68
3.4.1	State preparation of $ F = 1, m_F = 0\rangle$	68
3.4.2	Interferometry laser system	70
3.4.3	Dual-species considerations for testing the UFF	71
3.5	Guided atom interferometry	72
3.6	Squeezing-enhanced interferometry	76
3.7	Conclusion	79
	Bibliography	81
	Acknowledgments	101

LIST OF FIGURES

Figure 1.1	Comparison of a Mach-Zehnder interferometer based on light and atoms.	2
Figure 1.2	False color images of the phase transition from a thermal ensemble to a Bose-Einstein condensate	4
Figure 1.3	Measured Feshbach resonances for a mixture of $ F = 1, m_F = 0\rangle$ and $ F = 1, m_F = -1\rangle$	7
Figure 1.4	Comparison of pulsed and continuous Delta-Kick collimation sequences.	10
Figure 3.1	Comparison of different atomic source systems for Bose-Einstein condensates	66
Figure 3.2	Potential state preparation schemes for $ F = 1, m_F = 0\rangle$. .	69
Figure 3.3	Combined Bragg and Raman laser system	71
Figure 3.4	Different realizations of beam splitters in a guided geometry	73
Figure 3.5	Simplified sequence to perform an acceleration measurement along the z -direction with a fully guided interferometer.	75
Figure 3.6	Simplified measurement sequence for rotations around the z -direction with a fully guided configuration.	75
Figure 3.7	A Delta-Kick squeezing-enhanced atom interferometry scheme.	77
Figure 3.8	A squeezing-enhance trapped interferometer scheme . .	78

ACRONYMS

AI	atom interferometer
AOD	acousto-optic deflector
AOM	acousto-optic modulator
ARP	adiabatic rapid passage
ATLAS	ATom LASer
BEC	Bose-EINSTEIN condensate
BS	beam splitter
COM	center-of-mass
CPM	center-position modulation
DKC	Delta-Kick collimation
EOM	electro-optic modulator
IMU	inertial measurement unit
ISS	International Space Station
MOT	magneto-optical trap
ODT	optical dipole trap
PSD	phase space density
QPORT	Quantum TransPORT
RF	radio frequency
SLM	spatial light modulator
SQL	standard quantum limit
TAP	time-averaged potential
UFF	Universality of Free Fall
VLBAI	Very Long Baseline Atom Interferometer

INTRODUCTION

The first interferometry experiments with light date back to the 19th century [1]. Today, laser interferometry [2] has become a fundamental tool for society with cutting-edge applications ranging from laser gyroscopes [3], indispensable for modern air travel, to the detection of gravitational waves [4], pioneering a new field of astronomy and enhancing our understanding of the universe. While laser-based devices excel at detecting relative changes in distance, accelerometers such as the FG5 [5] face challenges due to their lack of bias stability [6] and laser gyroscopes require frequent re-calibration [7]. An alternative approach exploits the wave-like properties of massive particles [8] which allow to observe interference effects at low energy scales, ultimately opening up the field of matter-wave interferometry [9]. Initial experiments with electrons confirmed the existence of interference patterns consistent with BRAGG's law [10], leading to the proposal and subsequent realization of a first interferometer utilizing thin crystal lamellae as beam splitters [11, 12]. Similarly, three-grating geometries enabled neutron interferometers, measuring the induced phase shift due to gravity [13] and later facilitated the diffraction and interference of atoms [14, 15]. With the advent of sophisticated cooling schemes, mostly made possible by advancements in laser technology, macroscopic and many-particle systems such as BOSE-EINSTEIN condensates (BECs) [16] and most recently molecules followed [17].

Compared to classical sensors, systems based on the manipulations of large ensembles of neutral atoms offer several advantages. Although their technical development is still ongoing, they are ultimately expected to outperform their classical counterparts [6]. The ability to prepare well-defined atomic quantum states allows superior control over the initial conditions and improves the reproducibility of measurements compared to any classical setup. Furthermore, the inherent properties of atoms are directly linked to the definitions of the international system of units, hence allowing for drift-free and absolute measurements. While their inertial mass facilitates direct coupling to accelerations and particularly gravity, their electric polarizability and magnetic moment also render them sensitive to electric and magnetic fields, thereby providing a flexible platform for sensing a variety of quantities. However, this versatility also requires tailoring the external and internal atomic states with respect to the specific needs of the measurement to be conducted and necessitates excellent control of the environment in order to mitigate any unwanted systematic effects.

1.1 LIGHT-PULSE ATOM INTERFEROMETRY

In contrast to the early attempts, light-pulse atom interferometers (AIs) [19–21] realize their beam splitting processes through the coherent manipulation with light, and have emerged as a versatile tool for a multitude of measurements ranging from fundamental physics to technical applications [9]. The first demonstration

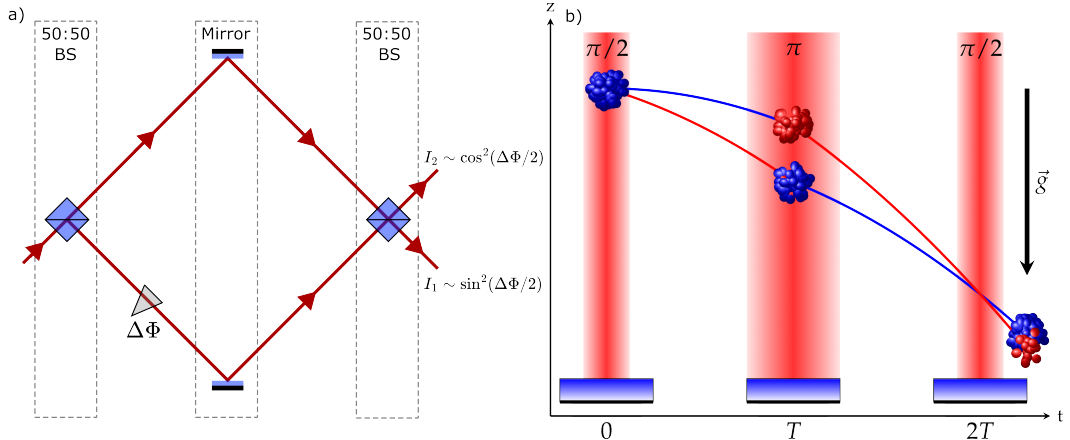


Figure 1.1: Comparison of a Mach-Zehnder interferometer based on light and atoms.

(a) In the light interferometer, a coherent source is split along two different paths using a 50:50 beam splitter (BS) and subsequently recombined. Interference patterns emerge in the output ports due to the accumulated phase differences $\Delta\Phi$ between both trajectories, e.g. caused by a difference in path length or when the refractive index along one trajectory changes. (b) Similarly, the wave-nature of atoms allows to create superposition states with separate trajectories and light-pulses acting as splitters, mirrors, and re-combiners. Here, the phase difference originates from the laser-phase imprinted on the atoms during the atom-light interactions at different positions in the interferometer beam and thereby allows to determine the experienced acceleration \vec{g} along the beam axis. Figure (b) was taken from Ref. [18] without modifications and is licensed under CC BY 3.0.

measured the gravitational acceleration of sodium atoms [19] and the sensitivity of AIs to inertial effects has steadily improved since then [22–26]. In fundamental physics, atom interferometry has contributed to the quest for a unified theory by probing the limits of both general relativity [27–30] and quantum mechanics [31–33]. Furthermore, advances in metrology have been achieved, including measurements of the gravitational constant [34] and the fine-structure constant [35, 36]. Today, applications in navigation and earth observation are explored based on compact platforms [37–39] and first prototypes have already been implemented on ships [40], planes [41], sounding rockets [42] and even the International Space Station (ISS) [43].

The most common configuration, which is used for gravimetry is the MACH-ZEHNDER type AI. Its working principle can be understood as the matter-wave analog of a laser interferometer of the same type. A comparison between both concepts is presented in Figure 1.1. In the laser interferometer (Fig. 1.1a) the light beam is split using a partially reflective mirror, typically with 50 % reflectivity. The separated beams travel along two distinct trajectories, which exposes them to different external effects, inducing a relative phase shift between both paths. Eventually, they are recombined at a second beam splitter and interfere. The accumulated phase difference can be determined by analyzing the spatial intensity distribution in one output port or by comparing the total intensities of both ports to each other.

For matter-waves (Fig. 1.1b), the splitting, mirroring and recombination processes are realized through atom-light interactions [9]. Most commonly, RABI oscillations of the atomic ensemble based on one of the following two processes are used:

Stimulated RAMAN transitions [19] change both, the internal and external state offering the advantage of state-selective imaging, even when the spatial resolution of the interferometer output ports is limited and the ensembles overlap. This method is particularly suitable for thermal sources of laser-cooled atoms where the ensemble's kinetic energy exceeds the photon recoil energy. On the other hand, BRAGG diffraction [44] only alters the external momentum state, making it advantageous for ultracold ensembles with reduced expansion rate. Moreover, when using identical internal states, the interferometer is inherently less susceptible e.g. to the differential AC STARK shift, thereby reducing systematic errors. Alternative schemes include using KAPITZA-DIRAC gratings [45], BLOCH oscillations [46] or ultranarrow single-photon clock transitions [47].

Analogous to the 50:50 beam splitter of the laser interferometer a RABI $\pi/2$ -pulse creates an equal superposition between two different momentum modes $|p_1\rangle$ and $|p_2 = p_1 + \Delta p\rangle$. In the simple presented configuration, two counter-propagating laser beam with wave vectors \vec{k}_i transfer the total momentum $\Delta p = \hbar k_{\text{eff}} = \hbar |\vec{k}_1 - \vec{k}_2|$, leading to two separate trajectories. During the pulse separation time T the atoms propagate freely, before a π -pulse inverts the momentum states, acting as a mirror. After another evolution time T the two paths coincide and a final $\pi/2$ -pulse superimposes the states, thereby closing the interferometer. In the example, shown in Figure 1.1b, the differential phase shift is induced by the gravitational acceleration and given by

$$\Delta\phi = \vec{k}_{\text{eff}} \cdot \vec{g} \cdot T^2 \quad (1.1)$$

to the lowest order. It scales with the enclosed space time area $k_{\text{eff}} \cdot T^2$ and the acceleration that the ensemble experienced in the direction of beam splitting. When performing the described sequence one can show that the sensitivity for measuring g is given by:

$$\Delta g = \frac{1}{\sqrt{N} C k_{\text{eff}} T^2} \quad (1.2)$$

for a single measurement with a total number of atoms N , participating in an interferometer with fringe contrast C . For multiple subsequent measurements with experimental cycle time t_{cycle} averaging with respect to integration time τ allows to reach a sensitivity of $\sigma_g(\tau) = \Delta g \cdot \sqrt{t_{\text{cycle}}/\tau}$.

To enhance the sensitivity, several methods are feasible: Enlarging the enclosed space-time area can be achieved by large momentum transfer beam splitters, increasing the transferred momentum to multiples of $\hbar k_{\text{eff}}$. Suitable methods include multi-photon BRAGG diffraction [48] or dedicated lattice geometries [49]. By implementing quantum optimal control protocols in an optical lattice, the current record of $600 \hbar k_{\text{eff}}$ in an interferometer has been realized with FLOQUET states [50]. Alternatively, the pulse separation time can be extended, which offers quadratic scaling but also requires long-baseline devices for terrestrial applications [24, 51–53]. When considering classical states, the atom number contributes with $1/\sqrt{N}$ at the standard quantum limit (SQL), due to quantum projection noise limiting the phase read-out. Using entangled states allows to gain sensitivity and approach the Heisenberg limit with superior $1/N$ -scaling, but comes with significantly more demanding hardware requirements and complicated preparation schemes [54]. In both cases the AI benefits from high initial atom numbers, which, in conjunction

with the cycle time-scaling, justifies the development of high flux atomic source systems with large N/t_{cycle} . Finally, a major limitation for the contrast arises from the expansion of the ensemble in the interferometer beam, causing inhomogeneous RABI oscillations due to the usually Gaussian intensity distribution [55]. This issue can be mitigated by employing a velocity selection scheme on the expense of the total atom number [19]. Alternatively, various cooling processes enable the generation of atomic ensembles with reduced momentum spread. In this context, the **BEC** is of particular interest and will be discussed in the next section.

1.2 BOSE-EINSTEIN CONDENSATION OF ^{39}K

1.2.1 *Bose-Einstein condensates*

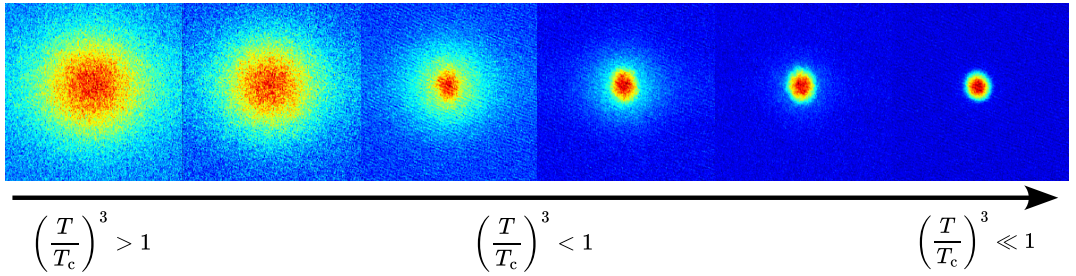


Figure 1.2: **False color images of the phase transition from a thermal ensemble to a Bose-Einstein condensate.** By reducing the laser intensity of the confining trap, an ensemble of ^{39}K atoms is cooled down to underneath the critical temperature. The images are taken after 20 ms time-of-flight, hence indicating the momentum spread of the ensemble. While initially featuring a gaussian envelope with wide momentum distribution (left), crossing the critical temperature (middle) allows to observe bimodal distribution with a fraction of already condensed atoms in the center. A further temperature reduction then leads to a quasi-pure **BEC** (right) with significantly reduced expansion energy and much narrower momentum spread.

A **BOSE-EINSTEIN** condensate is a coherent state-of-matter in which an ensemble of bosons collectively occupies the motional energy ground state and can be described through the same wave-function, thus rendering the particles indistinguishable from each other [56]. It is therefore a direct manifestation of the wave nature of particles, and hence offers exciting opportunities to investigate quantum phenomena at the macroscopic level. Starting from a dilute atomic gas a **BEC** forms when the thermal **DE BROGLIE** wavelength [8]

$$\lambda_{\text{dB}} = \sqrt{\frac{2\pi\hbar^2}{mk_B T}}, \quad (1.3)$$

which defines a length scale for the wave-like behavior of the individual atoms, approaches the distance between them. This process can be described in terms of the phase space density (**PSD**) $\Lambda = n\lambda_{\text{dB}}^3$ with peak atomic density

$$n = N \left(\frac{m\bar{\omega}^2}{2\pi k_B T} \right)^{3/2}, \quad (1.4)$$

within a trap with geometric mean of trap frequencies $\bar{\omega} = (\omega_x \omega_y \omega_z)^{1/3}$. When $\Lambda \approx 2.612$, equal to the value of the RIEMANN zeta function $\zeta(3/2)$, the individual wave-functions start to overlap and the phase transition occurs. For given atom number and trap frequencies one can therefore define a critical temperature T_c that must be reached to observe condensation experimentally:

$$T_c = \frac{\hbar \bar{\omega}}{k_B} \left(\frac{N}{\zeta(3/2)} \right)^{1/3}. \quad (1.5)$$

The phase transition around T_c is shown exemplarily in Figure 1.2. Once the temperature has been reduced below the critical temperature, the proportion of condensed atoms N_c to total atom number N can be determined as $N_c/N = 1 - (T/T_c)^3$ [57].

The existence of such a macroscopic ground-state occupation was already predicted in 1924 by ALBERT EINSTEIN [58] based on calculations carried out by SATYENDRANATH BOSE [59] earlier in the same year. Yet, it took more than 70 years until it was realized experimentally with ensembles of ^{87}Rb [60] and ^{23}Na [61], since the critical temperature is typically at the order of a few tens to a few hundred billionths of kelvin above absolute zero. Achieving these temperatures required a sophisticated combinations of laser and evaporative cooling techniques within optical and magnetic traps in an ultra-high vacuum environment. The implementation of these methods is discussed in the next section.

1.2.2 Evaporative cooling

Laser cooling atoms in magneto-optical traps (MOTs) and especially with optical molasses allows to reach temperatures of a few microkelvin, hence it is not sufficient to cross the critical temperature and achieve quantum degeneracy. Few exceptions exist when considering more sophisticated schemes, e.g. when cooling strontium on a narrow linewidth transition [62] or by employing Raman side-band cooling [63]. Yet, these techniques are limited to particular atomic species or certain use cases, e.g. when a low atom number is sufficient, or the expansion rate of the ensemble in free fall is irrelevant. For a more generally applicable scheme, evaporative cooling in magnetic or optical dipole traps (ODTs) is used as a final step to bridge the lacking orders of magnitude in PSD.

The basic principle of evaporative cooling relies on the scattering properties of the ensemble and its energy distribution. In thermal equilibrium (at a given temperature T), the atoms obey the MAXWELL-BOLTZMANN distribution, which features a high-energy tail with only minimal occupancy. By applying an energy dependent removal mechanism the tail can be truncated, lowering the average energy of the ensemble. In an ODT this is done by lowering the trap depth [64], while a radio frequency (RF)-knife is used in magnetic traps, causing an energy dependent transfer into an untrapped state [65]. In parallel, elastic collisions between the atoms cause the system to rethermalize, restoring the original energy distribution, but at a lower overall temperature. By continuously repeating this process, the atom number is reduced, but the PSD can be increased since $\Lambda \propto N/T^3$, eventually reaching the phase transition. To ultimately realize large ensembles at ultracold temperatures one hence has to keep the process maximally efficient and remove as much energy

per particle as possible, by allowing the atoms to always reach thermal equilibrium. Here the relevant time-scale τ_{el} is given by the elastic collision rate Γ_{el}

$$\tau_{\text{el}} \propto \frac{1}{\Gamma_{\text{el}}} \quad \text{with} \quad \Gamma_{\text{el}} = 4\pi a^2 n \bar{v} \quad (1.6)$$

and depends on the absolute values of the scattering length a , the atomic peak density and the average relative velocity \bar{v} of the atoms.

1.2.3 Feshbach resonances

In the specific case of ${}^{39}\text{K}$ a straightforward implementation of these methods is not feasible, as it features a negative background scattering length [66]. While this characteristic does not hinder evaporative cooling, it leads to an attractive mean-field potential, causing the system to collapse when the number of condensed particles exceeds a critical value and thus prevents effective BEC formation [67]. Similar issues exist for ${}^{133}\text{Cs}$ [68] or ${}^{85}\text{Rb}$ [69]. In such scenarios, exploiting FESHBACH resonances [70] has become an indispensable tool to achieve condensation, as they allow shifting the scattering length to positive values and hence stabilize the BEC through repulsive interactions. An extensive review of FESHBACH resonances and their applications can be found in Ref. [71]. Today, they are a widespread tool for studies of interaction dynamics [72], the formation of ultracold molecules from bosons [73–75] and fermions [76, 77] and are used to enable and improve evaporative cooling [68, 69, 78].

A FESHBACH resonance occurs in collision processes between two atoms, when the energy of a bound molecular state approaches the energy of the unbound state. In this situation even weak coupling between both states results in strong mixing, thereby altering the scattering length. When the magnetic moments of unbound and bound state differ, the energy difference between both, and consequently coupling strength and scattering length, can be tuned by applying homogeneous magnetic fields, leading to so-called magnetic FESHBACH resonances. Since their formation relies solely on the magnetic properties of the involved atoms and their general capability to form bound molecular states, a wide variety of atomic species and their isotopes possess them [66, 79–84]. Alternatively, laser excitation can also induce resonant coupling of two colliding ground state atoms to an excited molecular state, thereby altering the scattering length [85]. Compared to their magnetic counterpart, such optical FESHBACH resonances feature a finite scattering length maximum and often exhibit large losses, due to the short lifetime of the excited molecular state and the associated spontaneous decay [86]. Nevertheless, they are considered useful when magnetic tuning is not feasible, e.g. for atoms such as strontium and ytterbium. By coupling to forbidden inter-combination transitions the lifetime of the excited state can be significantly enhanced, allowing practical changes of the scattering length across large intervals [87–89].

For ${}^{39}\text{K}$ several broad magnetic FESHBACH resonances exist and are addressable with comparably low field strengths ranging from a few 10 G to a few 100 G. These favorable features allow precise tuning of the scattering length without the need for extended coil setups, making ${}^{39}\text{K}$ an ideal platform to explore interaction dynamics and their utilization for matter-wave optics. A recent overview of the resonances for

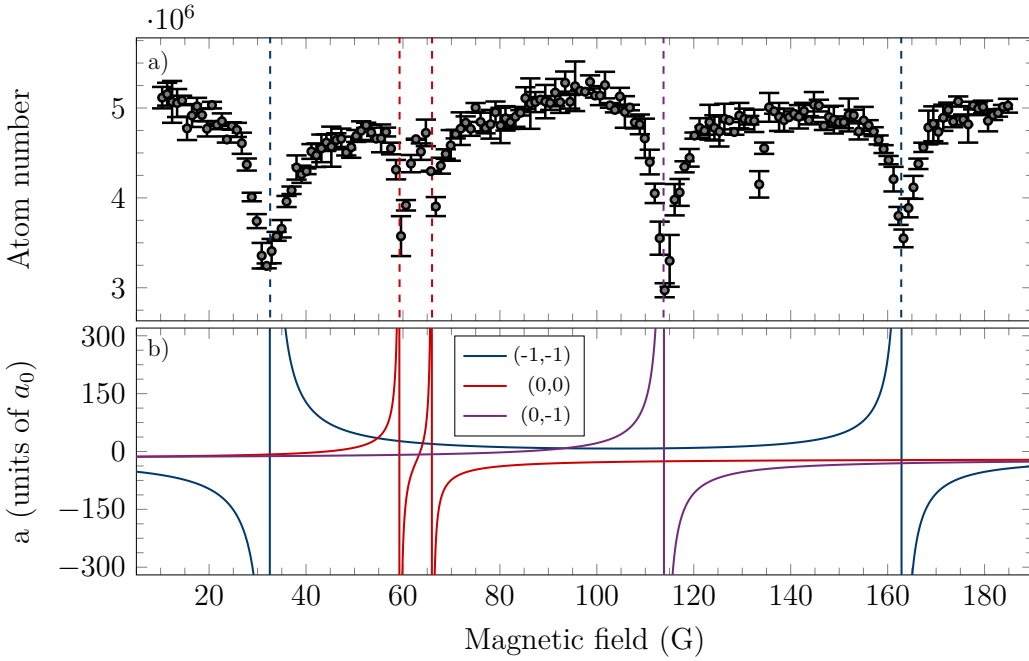


Figure 1.3: **Measured Feshbach resonances for a mixture of $|F = 1, m_F = 0\rangle$ and $|F = 1, m_F = -1\rangle$.** (a) Measured atom numbers in the ODT after applying a homogeneous magnetic field for 1.5 s. FESHBACK resonances can be identified by the sharp dips in atom number since three-body losses are greatly enhanced in their direct vicinity. (b) Expected FESHBACK resonances for $|F = 1, m_F = 0\rangle$ and $|F = 1, m_F = -1\rangle$. The legend indicates the corresponding m_F -pair. The nonassignable atom number loss can be explained by atoms remaining in $|F = 2, m_F = -2\rangle$ after state preparation, for which a possible resonance was recently determined theoretically [90].

all potassium isotopes can be found in Ref. [90]. The ones relevant for this thesis were identified by measuring the atom number loss for a given magnetic field and are shown in Figure 1.3.

Early attempts to achieve Bose-Einstein condensation with the aid of magnetic FESHBACK resonances were performed in combination with initial sympathetic cooling with ^{87}Rb [78, 91]. These experiments relied on the positive scattering length between ^{87}Rb and ^{39}K to facilitate energy exchange and lower the temperature of the ^{39}K atoms while evaporatively cooling ^{87}Rb . The FESHBACK resonances were only employed in a final step, when their application became unavoidable to stabilize the BEC. Purely direct evaporative cooling has been demonstrated shortly afterwards [92] and has become the standard procedure as it eliminates the need for a second species. Recently, all-optical preparation sequences prior to evaporative cooling have gained interest due to their capability to shorten the experimental cycle time and further simplify the setups [93].

1.3 ATOMIC SOURCE SYSTEMS FOR ATOM INTERFEROMETRY

As discussed, BECs are of particular interest for atom interferometry, since their low expansion rates allow for high fidelity beam splitter using RAMAN [94] or

BRAGG pulses [95, 96]. Furthermore, they exhibit reduced systematic errors related to their initial kinematics and enable long pulse separation times without loss of contrast from diluting the ensemble [97] or inhomogeneous RABI oscillations [55]. However, atom interferometers commonly operate with ensembles at temperatures of a few microkelvins [98–100]. While this restricts the accessible free fall time, cooling atomic ensembles to sub-Doppler temperatures can typically be performed within a few ten milliseconds with various methods. In comparison preparing a BEC often takes several seconds, thereby increasing the experimental cycle time and significantly lowering the atomic flux.

Different approaches exist to circumvent this issue, with the most successful one thus far being undoubtedly the use of multi-layer atom chips for ^{87}Rb [101, 102]. Allowing for a compact design with high trap frequencies in close proximity to the current conducting chip structure, such setups enable rapid evaporation schemes, with a demonstrated evaporation duration below 500 ms and 1 Hz experimental repetition rate. Their advantages make them especially successful in the scope of dedicated micro-gravity experiments [42, 96, 103, 104], and they have been prominently featured on board of a sounding rocket [103] and the ISS [43, 105].

In an alternative approach BECs of various species have been created in ODTs [68, 106–110]. Compared to magnetic confinement, utilizing induced dipole forces allows to trap atoms regardless of magnetic substate or lack thereof. Notably, this feature allowed to create BECs of ytterbium [107] and strontium [109]. Additionally, the absence of in-vacuum components allows for unrestricted optical access. This is particularly important for multi-axis interferometry [111, 112] and the large interferometer beams, required for long-baseline devices [52]. While ODTs offer a great level of flexibility, they also suffer from significant drawbacks: Since the focused Gaussian beams of an ODT only feature a minimal overlap with a laser-cooled cloud in the trapping region, it is challenging to create large volume traps suitable for evaporative cooling. Although this issue can be partially alleviated by employing larger beam waists, this has detrimental effects on the evaporation duration as it results in lower trap frequencies, reducing the elastic collision rate. Furthermore, trap frequencies are naturally reduced during evaporation, due to their direct coupling to the trap depth. Consequently, ODTs require an evaporation duration at least an order of magnitude longer than what can be achieved with high-performance chip traps.

Considerable efforts have been made to overcome the corresponding scaling laws [113]. While certain species allow for direct laser cooling schemes [62, 63], a more general approach involves adding a tight dimple beam to an otherwise large volume trap to locally increase trap frequencies and PSD. However, this approach typically results in low final atom numbers [114]. Recent advances also make use of machine learning techniques in order to find rapid evaporation trajectories specifically tailored towards the individual setup used [115]. The most successful and by now widely employed approach relies on lifting the coupling of trap depth and frequencies by dynamically altering the potential shape, tailoring it towards the optimal configuration for every step in the experimental sequence. An early realization of such an approach was based on a movable lens system, allowing for trap compression during evaporation to maintain high trap frequencies [116]. While this method reduced the evaporation duration to 2 s the necessary hardware

integration considerably restricted the setup's flexibility. Alternatively, spatial light modulators (**SLMs**) can be used to create more flexible beam patterns, only limited by the waist of the trapping beam and the pixel size of the **SLM** [117]. However, their low diffraction efficiency made these devices unfavorable for large volume traps based on lasers with multiple watts of optical power. Hence their use is mainly restricted to optical tweezer configurations for single atoms and ions or the manipulation of **BECs**, provided by different means.

As of today, time-averaged potentials (**TAPs**) [118, 119] are commonly used to alter the potential shape, since they can be created with minimal power loss and do not require any mechanical moving parts. Instead, they rely on a center-position modulation (**CPM**) of the trapping beams, implemented with acousto-optic elements by modulating the driving **RF**-signal. As long as the **RF** modulation frequency is much larger, typically by a factor of several hundred [120], than the trap frequencies, the atoms do not experience the moving laser beam, but instead the time-average of its motion, resulting in a static optical potential. By choosing appropriate frequency ramps these systems can realize nearly arbitrary potential shapes, only limited by the natural waist of the used laser beam and the maximum bandwidth and diffraction angle of the acousto-optic element [18, 119, 121, 122]. They allow to initially load high atom numbers by improving the mode match through a larger effective beam waist, realizing favorable initial conditions while effectively tailoring trap frequency through compression during evaporation. In Ref. [122], combining **TAPs** with a dimple-like beam geometry allowed to realize ensembles of more than 5×10^4 condensed particles after 250 ms of evaporative cooling with an experimental cycle time of only 500 ms, showcasing a performance more than competitive to the magnetic chip traps.

1.4 DELTA-KICK COLLIMATION

In addition to the ability to rapidly create **BECs** with a large atom number, modern precision experiments impose stringent limits on the expansion energy, as they target several seconds of pulse separation time to reach the desired sensitivity. For example, probing the Universality of Free Fall (**UFF**) below the 10^{-15} -level, requires achieving expansion energies smaller than 50 pK for an STE quest-like space mission [124–126]. Likewise, proposed long-baseline devices for the detection of gravitational waves or dark matter impose requirements below 100 pK [53, 127]. These examples highlight the need for dedicated collimation techniques that go far below the few tens of nanokelvin, typical for a **BEC** released from an **ODT** [68, 128, 129].

With further evaporative cooling expansion energies below 500 pK were demonstrated, albeit only for a **BEC** of 2500 atoms [130]. With spin-gradient cooling this value was improved to below 400 pK [131]. Alternatively, different Delta-Kick collimation (**DKC**) techniques [132] allow reaching the desired energy regime without loss of atoms and have successfully been implemented in magnetic [96, 133–135], electrostatic [136] and also optical traps [18]. In contrast to traditional cooling mechanisms, **DKC** preserves the **PSD**, justifying the term **collimation** instead of cooling. One generally distinguishes between two cases, the pulsed and the continuous **DKC**. A comparison of both mechanisms is presented in Figure 1.4.

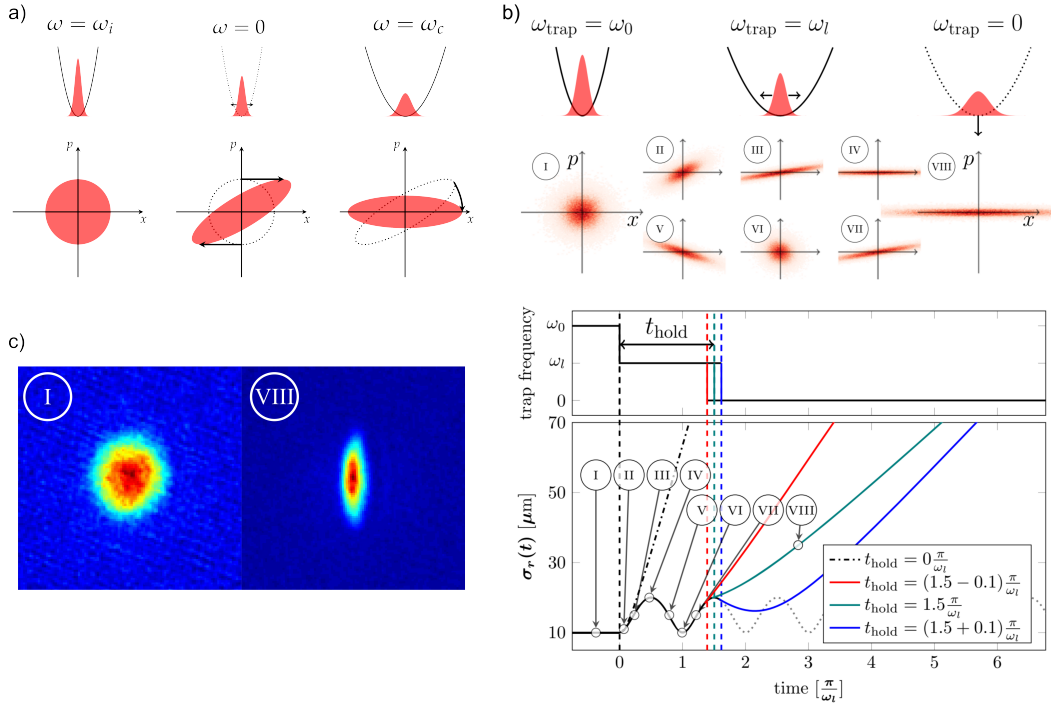


Figure 1.4: Comparison of pulsed and continuous Delta-Kick collimation sequences. (a) Working principle of the pulsed **DKC**. Starting from an initial trap ($\omega = \omega_i$), the ensemble is released and allowed to freely expand ($\omega = \omega_0$), thereby sheering the phase-space distribution. Afterwards the trap is turned back on for a brief time ($\omega = \omega_c$) to convert kinetic into potential energy, rotating the phase-space distribution, until the momentum spread becomes minimal. The panel was taken from Ref. [18] and is licensed under [CC BY 3.0](#). For this figure the sub-panel designations were removed and single elements were re-scaled. **(b)** Working principle of the continuous **DKC**. Starting from a similar trap ($\omega_{\text{trap}} = \omega_0$), a rapid relaxation of the trap frequencies ($\omega_{\text{trap}} = \omega_l < \omega_0$) excite size oscillations of the ensemble. Subsequently, a release at their turning point ($\omega_{\text{trap}} = 0$) is used to realize a minimal momentum spread in free-fall. Underneath, the size oscillations in the trap together with the corresponding phase-space diagrams at different points of the sequence are shown. The panel was taken from Ref. [123] and is licensed under [CC BY 4.0](#). For this figure the sub-panel designations were removed. **(c)** Comparison of two ^{39}K **BECs** after 25 ms time-of-flight, released at point I without a lens (left) and after applying the lens with a release close to the optimal point VIII (right). While the vertical axis remains unaffected by the employed 2D continuous lens, the momentum spread in horizontal direction is significantly reduced.

A pulsed **DKC** relies on the brief application of an optical or magnetic potential, to reduce the kinetic energy of an ensemble already in free-fall (Fig. 1.4a). Upon released from an initial trap, the atomic cloud starts to expand due to its finite momentum distribution. Additionally, the mean-field energy, which dominates the **BEC** at high densities and non-vanishing scattering length in the trap, acts as repulsive force, thereby accelerating the expansion [56]. If the cloud expands over a longer period of time in free-fall, its density decreases to such an extent that it enters the non-interacting ballistic regime. At that point re-applying a potential lowers the kinetic energy of the atoms, as they have to perform work against it. Furthermore,

they are not accelerated again afterwards, as the mean-field energy has already been converted. Fundamentally, the kinetic energies that can be obtained using this method are only limited by the size of the cloud due to HEISENBERG's uncertainty principle. Because the necessary potentials need to be applied at the position of the atomic ensemble, the pulsed [DKC](#) scheme is particularly suitable for micro-gravity environments, where the experimental device remains stationary relative to the atoms.

However, under the influence of gravity the atoms quickly leave the trapping zone of stationary devices. While additional coils or optical systems in a dedicated interaction zone have been demonstrated as a feasible approach, realizing 50 pK in two dimensions [[137](#)], their implementation is often challenging. Alternatively, continuous [DKC](#) circumvents this issue entirely as it allows to perform the collimation directly in the initial trapping potential (Fig. [1.4b](#)). Here, rapidly changing the trap frequencies by altering the magnetic [[24](#)] or optical confinement [[18](#)] induces common-mode oscillations of the ensemble size. By releasing the ensemble at the turning point of the width oscillation the momentum spread is reduced, due to the increase in cloud size with the additional benefit of also lowering the density and thereby reducing interactions and related acceleration of the expansion. Yet, for most experimental configurations the final size of the atom cloud that can be achieved using such methods is not sufficient to fully remove the mean-field energy from the ensemble, limiting the achievable expansion energy. Additionally, such schemes are often restricted to one or two dimensions, as the available degrees of freedom do not allow to freely control the trap frequencies in all directions. Consequently, the current record of 38 pK in three dimensions has been achieved by combining continuous and pulsed collimation sequences in micro-gravity [[104](#)].

1.5 SCOPE OF THIS THESIS

This thesis is based on several publications in peer-reviewed journals with the aim of establishing a testbed for atom interferometry with ultracold ^{39}K in trapped and free-falling geometries. All experiments were conducted at an already existing dual-species atom interferometer apparatus for molasses cooled ensembles of ^{87}Rb and ^{39}K , namely the ATom LASer ([ATLAS](#)) experiment at the Institute of Quantum Optics in Hannover. Historically, [ATLAS](#) has been used to test the [UFF](#) comparing the gravitational acceleration of both species in a differential measurement [[27](#)]. Since then, it has additionally become a versatile demonstrator for numerous technologies, to be integrated in the Hannover Very Long Baseline Atom Interferometer ([VLBAI](#)) facility [[52](#)], which is currently in commissioning [[120](#), [138](#)].

Analyzing the latest [UFF](#) test campaign revealed the limitations of the apparatus, directly linked to the overall performance of the potassium source and the momentum spread of the thermal clouds during free fall. Publication 1 [[139](#)] provides a comprehensive overview of the conducted measurement campaign, ultimately leading to an exclusion of violations at the 10^{-7} -level :

Publication 1

Henning Albers, **Alexander Herbst**, Logan L. Richardson, Hendrik Heine, Dipankar Nath, Jonas Hartwig, Christian Schubert, Christian Vogt, Marian Woltmann, Claus Lämmerzahl, Sven Herrmann, Wolfgang Ertmer, Ernst M. Rasel, and Dennis Schlippert, "Quantum test of the universality of free fall using rubidium and potassium", *The European Physical Journal D* **74** (2020), doi: [10.1140/epjd/e2020-10132-6](https://doi.org/10.1140/epjd/e2020-10132-6).

To address the identified challenges an **ODT** with **TAPs** had already been implemented to create **BECs**, initially demonstrated for ^{87}Rb [18]. Within the scope of this thesis the setup was further retrofitted to enable the rapid generation of ^{39}K **BECs** and their subsequent collimation to energies below the nanokelvin range in two dimensions. The modifications allowed loading the **ODT** with a large atom number and high initial **PSD** by enhancing the sub-DOPPLER cooling of ^{39}K , switching from a D_2 -molasses to a grey molasses scheme on the D_1 -line [140]. For this purpose, an entire new laser system was integrated. Furthermore, a three-axis magnetic field stabilization was implemented to enable a multi-loop state preparation scheme [141] based on microwave adiabatic rapid passages (**ARPs**) in combination with optical pumping on the D_1 -line. Finally, to tune the atomic scattering length with magnetic FESHBACH resonances an H-bridge was added to the **MOT** coils, allowing to switch them between anti-HELMHOLTZ and HELMHOLTZ-configuration, thereby providing the capability to generate homogeneous magnetic fields of up to 400 G. While these techniques are well-established individually, the specific design choices and scope of the experimental apparatus required their adaption and combination in unique ways, leading to a detailed description of the new components together with the first creation of a ^{39}K **BEC** in publication 2 [142]:

Publication 2

Alexander Herbst, Henning Albers, Knut Stolzenberg, Sebastian Bode, and Dennis Schlippert, "Rapid generation of all-optical ^{39}K Bose-Einstein condensates using a low-field Feshbach resonance", *Physical Review A* **106**, 043320 (2022), doi: [10.1103/PhysRevA.106.043320](https://doi.org/10.1103/PhysRevA.106.043320).

These results already feature a decent experimental performance, especially regarding the evaporation process, allowing the creation of **BECs** with 5.8×10^4 condensed particles after 850 ms of evaporative cooling. However, to compete with state-of-the-art solutions based on other trapping mechanisms in the framework of matter-wave interferometry a further enhancement of atomic flux was necessary but hindered by the limited capabilities of the 1960 nm laser system generating the **ODT**. To overcome its shortcomings, a new 1064 nm laser system was integrated. Compared to the previous system, the **TAPs** were no longer generated by a 1-axis acousto-optic modulator (**AOM**) but rather by a 2-axis acousto-optic deflector (**AOD**), which in principle allows to extend shaping the potentials along the second beam axis. At the same time, the usable **CPM** stroke was increased by more than a factor of five,

allowing for effective beam waists of over 1.5 mm. Furthermore, as the new laser system was no longer power-limited, the use of a recycled beam configuration was avoided and independent control of the two individual beams was implemented instead. Together, this opened up a wider range of accessible trap configurations and, in particular, trap frequencies. In combination with dynamically tuning the scattering length during the evaporation stage, as opposed to the static configurations used before, these enhanced capabilities allowed the realization of BEC after only 170 ms of evaporative cooling. The developed sequence enables interferometers entirely limited by the pulse separation time with the potential to reach a theoretical short-term stability better than $1 \times 10^{-9} \text{ m/s}^2$ after 1 s of integration time. The experimental sequence together with the expected interferometry performance has been published in publication 3 [143]:

Publication 3

Alexander Herbst, Timothé Estrampes, Henning Albers, Vera Vollenkemper, Knut Stolzenberg, Sebastian Bode, Eric Charron, Ernst M. Rasel, Naceur Gaaloul, and Dennis Schlippert, “**High-flux source system for matter-wave interferometry exploiting tunable interactions**”, *Physical Review Research* **6**, 013139 (2024), doi: [10.1103/PhysRevResearch.6.013139](https://doi.org/10.1103/PhysRevResearch.6.013139).

For sufficiently low momentum spread of the atomic ensemble, the short-term stability of an atom interferometer is mainly governed by the atomic flux. However, for the long-term stability the ensembles' expansion is always the limiting factor restricting the achievable pulse separation time, due to loss of contrast. To reduce the expansion energy below a few tens of nanokelvin, an all-optical continuous DKC scheme based on TAPs utilizing size oscillations of the atom cloud was ultimately investigated. As before, initial measurements were performed with ^{87}Rb and allowed reaching expansion energies as low as 3.2 nK in one dimension, a gain by more than order of magnitude compared to the immediate release from the ODT. By applying the same technique to thermal ensembles, it was further demonstrated how the evaporation sequence could be shortened in cases when only certain temperature limits have to be met. These findings were published in publication 4 [123]:

Publication 4

Henning Albers, Robin Corgier, **Alexander Herbst**, Ashwin Rajagopalan, Christian Schubert, Christian Vogt, Marian Woltmann, Claus Lämmerzahl, Sven Herrmann, Eric Charron, Wolfgang Ertmer, Ernst M. Rasel, Naceur Gaaloul, and Dennis Schlippert “**All-optical matter-wave lens using time-averaged potentials**”, *Communications Physics* **5**, 60 (2022), doi: [10.1038/s42005-022-00825-2](https://doi.org/10.1038/s42005-022-00825-2).

To apply the same method to ^{39}K tunable interactions were additionally taken into account. Measurements were limited to the case of a BEC, as the rapid evaporation scheme made further short-cutting obsolete. The collimation sequence was

implemented in both weak and strong interaction regimes, to quantify the resulting effects and the lowest expansion energy in two dimensions was determined to be (438 ± 77) pK for a scattering length of $10 a_0$. In particular, the interplay of atomic interactions and trap frequencies was thoroughly analyzed using a scaling approach [144, 145] in the strong and a variational approach [146, 147] in the weak interaction regime. Arriving at an accurate description of the system allowed interpolating achievable three-dimensional expansion energies to below 20 pK in the revised setup as already featured in publication 3 [143], leading to the concluding publication 5 [148]:

Publication 5

Alexander Herbst, Timothé Estrampes, Henning Albers, Robin Corgier, Knut Stolzenberg, Sebastian Bode, Eric Charron, Ernst M. Rasel, Naceur Gaaloul, and Dennis Schlippert, “Matter-wave collimation to picokelvin energies with scattering length and potential shape control”, Communications Physics 7, 132 (2024), doi: [10.1038/s42005-024-01621-w](https://doi.org/10.1038/s42005-024-01621-w).

PUBLICATIONS

2.1 QUANTUM TEST OF THE UNIVERSALITY OF FREE FALL USING RUBIDIUM AND POTASSIUM

Authors: Henning Albers, Alexander Herbst, Logan L. Richardson, Hendrik Heine, Dipankar Nath, Jonas Hartwig, Christian Schubert, Christian Vogt, Marian Woltmann, Claus Lämmerzahl, Sven Herrmann, Wolfgang Ertmer, Ernst M. Rasel, and Dennis Schlippert,

Journal: The European Physical Journal D

Article Number: 74, 145 (2020)

DOI: [10.1140/epjd/e2020-10132-6](https://doi.org/10.1140/epjd/e2020-10132-6)

Contribution: W.E., E.M.R., C.S., J.H., and D.S. designed the atom interferometer and its laser system. L.L.R., H.A., D.N., J.H., and D.S. contributed to the design of the atom interferometer and its laser system and realised the overall setup. H.A., L.L.R., H.H., and D.N. operated the final experimental setup. H.A., A.H., D.S., J.H., C.S., and H.H. performed the analysis of the data presented in this manuscript. D.S., H.A., L.L.R., C.S., and A.H. drafted the initial manuscript. C.V., M.W., C.L., and S.H. provided major input to the manuscript and all authors critically reviewed and approved of the final version.

This article is licenced under a Creative Commons Attribution 4.0 International License [CC BY 4.0](https://creativecommons.org/licenses/by/4.0/) which permits reproduction. No changes to the original content were made.

Quantum test of the Universality of Free Fall using rubidium and potassium*

Henning Albers¹, Alexander Herbst¹, Logan L. Richardson^{1,2}, Hendrik Heine¹, Dipankar Nath¹, Jonas Hartwig¹, Christian Schubert¹, Christian Vogt³, Marian Woltmann³, Claus Lämmerzahl³, Sven Herrmann³, Wolfgang Ertmer¹, Ernst M. Rasel¹, and Dennis Schlippert^{1,a}

¹ Leibniz Universität Hannover, Institut für Quantenoptik, Welfengarten 1, 30167 Hannover, Germany

² College of Optical Sciences, University of Arizona, Tucson, AZ 85721, USA

³ ZARM Zentrum für angewandte Raumfahrttechnologie und Mikrogravitation, Universität Bremen, Am Fallturm 2, 28359 Bremen, Germany

Received 2 March 2020 / Received in final form 22 May 2020

Published online 7 July 2020

© The Author(s) 2020. This article is published with open access at Springerlink.com

Abstract. We report on an improved test of the Universality of Free Fall using a rubidium-potassium dual-species matter wave interferometer. We describe our apparatus and detail challenges and solutions relevant when operating a potassium interferometer, as well as systematic effects affecting our measurement. Our determination of the Eötvös ratio yields $\eta_{\text{Rb},\text{K}} = -1.9 \times 10^{-7}$ with a combined standard uncertainty of $\sigma_\eta = 3.2 \times 10^{-7}$.

1 Introduction

Matter wave interferometry is an effective toolbox to probe our understanding of nature. Based on coherent manipulation of atomic ensembles, sensors capable of performing accurate inertial measurements have been demonstrated [1–10]. These new atomic sensors allow accessing novel methods to understand fundamental physics [11–15].

The Einstein equivalence principle (EEP) is a cornerstone for the theory of general relativity [16]. It is composed of three components: Local Lorentz Invariance, Local Position Invariance, and the Universality of Free Fall. A violation of any of the components would imply a violation of the EEP and could therefore yield modifications of general relativity with the possibility to reconcile it with quantum field theory and therefore form of a theory of quantum gravity.

The Universality of Free Fall (UFF) states the equality of inertial and gravitational mass $m_{\text{in}} = m_{\text{gr}}$ and implies that all objects freely falling in the same gravitational field experience the same acceleration. As a figure of merit for UFF tests in the Newtonian framework we can express differential acceleration measurements in the so-called Eötvös ratio

$$\eta_{\text{A},\text{B}} \equiv 2 \frac{g_{\text{A}} - g_{\text{B}}}{g_{\text{A}} + g_{\text{B}}} = 2 \frac{\left(\frac{m_{\text{gr}}}{m_{\text{in}}}\right)_{\text{A}} - \left(\frac{m_{\text{gr}}}{m_{\text{in}}}\right)_{\text{B}}}{\left(\frac{m_{\text{gr}}}{m_{\text{in}}}\right)_{\text{A}} + \left(\frac{m_{\text{gr}}}{m_{\text{in}}}\right)_{\text{B}}}, \quad (1)$$

* Contribution to the Topical Issue “Quantum Technologies for Gravitational Physics”, edited by Tanja Mehlstäubler, Yanbei Chen, Guglielmo M. Tino and Hsien-Chi Yeh.

^a e-mail: schlippert@iqo.uni-hannover.de

where A and B are the test masses, and $g_{\text{A},\text{B}}$ is their respective local gravitational acceleration.

Tests of the UFF can be grouped in three categories depending on the nature of the test masses: (i) classical, (ii) semi-classical, and (iii) quantum tests as reported in Table 1. The UFF has been tested extensively by classical means, yielding the best uncertainty at parts in 10^{14} . In addition, since the first observation of a gravitationally induced phase in a matter-wave interferometer [17], a variety of quantum tests based on atom interferometry have emerged. Due to their well-defined characteristics, isotopic purity, and by granting access to a novel range of species, they promise high sensitivity to possible violations of the EEP, e.g. when parametrizing observable physics in the minimal Standard Model extension [18–20] or in dilaton coupling scenarios [21].

In this article we report on an improved dual-species test of the Universality of Free Fall using laser-cooled ^{87}Rb and ^{39}K [22]. Improvements are mainly achieved by a better input state preparation for potassium yielding in an increased signal-to-noise ratio and longer integration time. After a description of the experimental apparatus in Section 2, we discuss our measurement scheme (Sect. 3) and close with a discussion of systematic effects (Sect. 4) affecting the measurement. In Section 5, we present possible mitigation strategies and paths towards improved quantum tests of the UFF on ground [23–26] and in space [27–29].

2 Experimental apparatus

The experimental apparatus includes a vacuum system in which the atoms are interrogated, a laser system

Table 1. Overview of UFF tests. We refer to experiments comparing the free fall acceleration of two isotopes of the same (different) chemical species as “dual-isotope” (“dual-species”). Experiments comparing the free fall of different internal states of the same isotope are labelled “dual-state”. FCC – Falling corner cube; AI – Atom interferometer.

Experiment	Test Masses	Type	Eötvös ratio $\eta_{A,B}$	Ref.
Capacitive accelerometers	Ti–Pt	Classical	$-0.1(1.3) \times 10^{-14}$	[30]
Lunar laser ranging	Earth–Moon	Classical	$-3(5) \times 10^{-14}$	[31]
Torsion balance	^9Be –Ti	Classical	$0.3(1.8) \times 10^{-13}$	[32]
Dual-FCC	Cu–U	Classical	$1.3(5.0) \times 10^{-10}$	[33]
FCC vs AI	SiO_2 – ^{133}Cs	Semi-classical	$7(7) \times 10^{-9}$	[34]
FCC vs AI	SiO_2 – ^{87}Rb	Semi-classical	$4.4(6.5) \times 10^{-9}$	[35]
Dual-state AI	^{87}Rb	Quantum	$0.9(2.7) \times 10^{-10}$	[36]
Dual-state AI	^{87}Rb	Quantum	$1.4(2.8) \times 10^{-9}$	[37]
Dual-state AI	^{87}Rb	Quantum	$0.2(1.2) \times 10^{-7}$	[38]
Dual-isotope AI	^{85}Rb – ^{87}Rb	Quantum	$2.8(3.0) \times 10^{-8}$	[39]
Dual-isotope AI	^{85}Rb – ^{87}Rb	Quantum	$1.2(3.2) \times 10^{-7}$	[40]
Dual-isotope AI	^{87}Sr – ^{88}Sr	Quantum	$0.2(1.6) \times 10^{-7}$	[41]
Dual-species AI	^{87}Rb – ^{39}K	Quantum	$-0.3(5.4) \times 10^{-7}$	[22]
Dual-species AI	^{87}Rb – ^{39}K	Quantum	$0.9(3.0) \times 10^{-4}$	[42]
Dual-species AI	^{87}Rb – ^{39}K	Quantum	$-1.9(3.2) \times 10^{-7}$	This work

generating the light fields for manipulating the atoms, and optics for beam shaping and collecting fluorescence for detection at the vacuum chamber. Below, these elements are described in more detail.

2.1 Vacuum system

The vacuum system consists of three main parts as depicted in Figure 1 and is enclosed in a single-layer permalloy magnetic shield [43,44]. Cooling and trapping of ^{87}Rb and ^{39}K takes place in a double magneto-optical trap (MOT) setup comprising two custom-made aluminum chambers with indium-sealed viewports separated by a differential pumping tube. Atoms are loaded into the 2D MOT from background vapor generated by ovens heated to $30\text{ }^\circ\text{C}$ ($75\text{ }^\circ\text{C}$), yielding a partial pressure of 1×10^{-7} mbar (6×10^{-6} mbar) for rubidium (potassium). A tube connects the 3D MOT chamber with a high aperture detection zone, allowing for 200 ms of free fall (19 cm center to center).

2.2 Laser system

For trapping and cooling of both atomic species we use the same laser system as in our previous work [22] and described in detail in [44,45].

In the following we refer to the $|F=2\rangle \rightarrow |F'=3\rangle$ as the cooling and the $|F=1\rangle \rightarrow |F'=2\rangle$ as the repumping transition. Frequency references for the system are generated by two external cavity diode lasers (ECDL) [46,47] which are stabilized to the D_2 line of rubidium (potassium) at 780 nm (767 nm) by means of frequency modulation spectroscopy.

The light fields for cooling and repumping of rubidium are generated by two ECDLs in a master-slave configuration. The repumping laser is stabilized to the reference

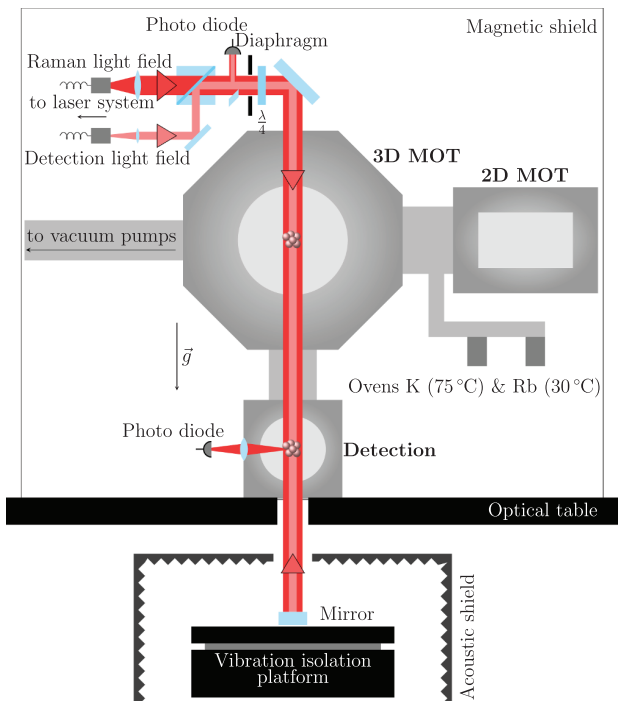


Fig. 1. Schematic of the vacuum system and peripherals comprising the sensor head of the experimental setup. The collimated light for the Raman pulses (dark red) and for detection (light red) are superimposed on a polarizing beam splitter which also cleans the Raman light polarization and allows for correcting detection intensity noise. Downstream, the light is shaped by a diaphragm to suppress reflections and unwanted diffraction from the viewport edge when passing the chamber and is circularly polarized afterwards. A retro-reflection mirror is situated on a vibration isolation platform in an acoustic isolation housing. Fluorescence readout is performed while the atoms fall through the large numerical aperture detection zone.

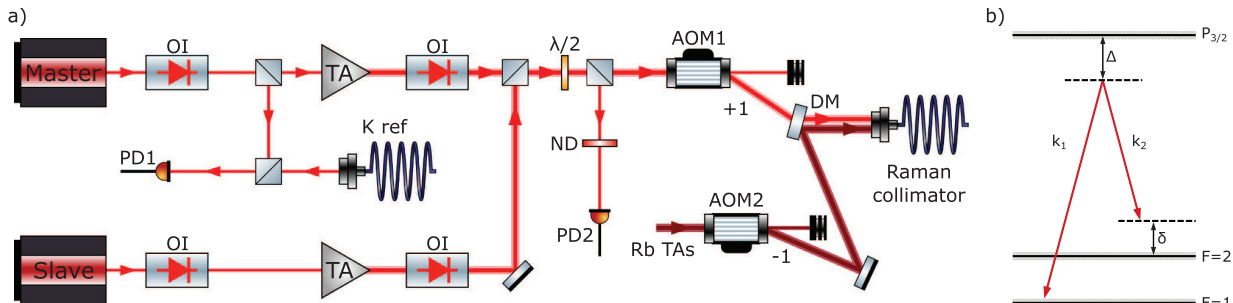


Fig. 2. (a) Schematic of the potassium Raman laser system (light red) and the superposition with the rubidium Raman laser (dark red). Two ECDLs in a master-slave configuration are used for each species. The master laser is offset locked (PD1) to the reference laser, while the slave laser is locked against the master (PD2). Both beams are amplified using tapered amplifiers and can be switched with an AOM. (b) Level scheme of the Raman transition. A global detuning Δ is used for both lasers with an additional, variable detuning δ for the slave laser. Abbreviations: OI – optical isolator, TA – tapered amplifier, AOM – acousto-optical modulator, PD – photo diode, DM – dichroic mirror, ND – neutral density filter.

laser and phase locked to be on resonance to the repumping transition. The cooling laser is phase-locked with respect to the repumper with an offset of -3.1Γ from the cooling transition, where $\Gamma \approx 2\pi 6\text{ MHz}$ is the natural linewidth of rubidium and potassium.

The potassium cooling system consists of three independent ECDLs. For the 2D MOT, one ECDL is phase locked to the reference and detuned by -1.3Γ from the cooling transition. Repumping light is generated by passing this light through a double-pass acousto-optical modulator (AOM) operated at half the hyperfine transition frequency ($f_{\text{HFS}} \approx 461\text{ MHz}$). The radio frequency power is set to generate a 50:50 intensity ratio for cooling and repumping light. The repumping light generated with this setup has a detuning of -4Γ from resonance. For the 3D MOT, two independent cooling and repumping lasers are phase locked to the reference laser with a variable detuning to provide the flexibility needed for the potassium sub-Doppler cooling scheme [48].

All generated light fields except the rubidium repumper are amplified using tapered amplifiers (TA), while the intensity is controlled with AOMs. Our setup yields cooling (C) and repumping (RP) intensities at the position of the atoms of $I_C \approx 8I_{\text{sat}}$, $I_{\text{RP}} \approx 0.1I_{\text{sat}}$ ($I_C = I_{\text{RP}} \approx 12I_{\text{sat}}$) for rubidium (potassium), where I_{sat} is each species's saturation intensity [49,50].

To generate Raman beam splitter light, we utilize two additional ECDLs in master-oscillator power amplification (MOPA) configuration operated as a master-slave pair for each species. A schematic of the utilized system for potassium and the layout for superimposing the light with the rubidium Raman system is depicted in Figure 2a. For the rubidium system a similar setup is used. The master lasers are phase locked (PD1) to the reference lasers on the $|F=1\rangle \rightarrow |F'=2\rangle$ transition with a global detuning Δ of 3.3 GHz for potassium, and 1.6 GHz for rubidium (cf. Fig. 2b). To compensate for the Doppler shift, the slave lasers are phase locked (PD2) with a dynamic detuning δ to the master lasers on the $|F=2\rangle \rightarrow |F'=2\rangle$ transition. The beam splitting light fields for both species can be switched independently using AOMs (AOM1 and

AOM2 in Fig. 2). A dichroic mirror (DM) is used to superimpose the beam splitting light for both species. Due to the small difference in wavelengths of the D_2 lines of ^{87}Rb and ^{39}K , we use common broadband optics at the experiment apparatus. Therefore we are able to generate a spatially and temporally overlapped cold atom cloud as well as superimposed Raman beams.

2.3 Interferometry and detection optics

The Raman beams are set up in a retro-reflected $\sigma^+ - \sigma^+$ polarization configuration. They are collimated to a $1/e^2$ -radius of $\sim 1.2\text{ cm}$ using an achromatic lens ($f = 100\text{ mm}$) and pass a cleanup polarization beam splitter, where they are superimposed with the detection light (Fig. 1). We obtain powers in the Raman master (slave) beam of 110 mW (110 mW) for potassium and 45 mW (90 mW) for rubidium. Both the detection and the Raman beams pass a diaphragm limiting the beam diameter such that no unwanted diffraction appears at the viewports. A $\lambda/4$ retardation plate generates the circular polarization. The beams are aligned parallel to gravity with two silver-coated mirrors. Below the chamber the beams are retro-reflected by a mirror [Optique Fichou] with a $\lambda/20$ peak-to-valley flatness. This mirror serves as the reference plane of the inertial measurements. To suppress seismic noise, it is mounted on top of a benchtop vibration isolation platform [Minus-K BM-1], and the entire assembly is housed within a foam insulated acoustic isolation box. For state-selective fluorescence detection, we utilize an optical system collecting fluorescence light with a large aperture lens ($f = 50\text{ mm}$) and imaging it onto a photo diode [OSI Optoelectronics PIN-10D] in a $2f - 2f$ configuration.

3 Measurements

3.1 Input state preparation

Initially, the atoms are loaded within 1.3 s into the 3D-MOT. Subsequently, the magnetic fields are switched

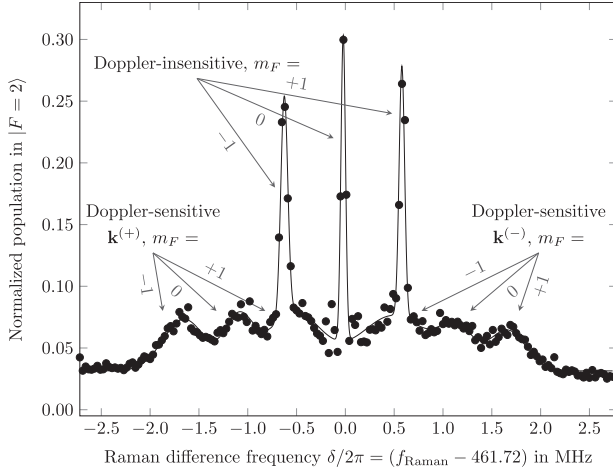


Fig. 3. Typical potassium Raman resonance spectrum obtained by scanning δ and applying single Raman pulses. The spectrum is acquired at the following parameters: pulse width $\tau = 15 \mu\text{s}$, offset field $B_0 = 430 \text{ mG}$, time of flight $t_{\text{TOF}} = 43.25 \text{ ms}$, temperature $T_{\text{at}} = 32.6 \mu\text{K}$. The solid black line is a guide to the eye. In the retro-reflected setup using σ/σ -polarization, a total of nine resonances are visible, three of which form one subset of Doppler-insensitive transitions. The remaining two subsets of three Doppler-sensitive transitions each are labeled $k^{(+)}$ for upward and $k^{(-)}$ for downward momentum transfer. Figure modified from reference [45].

off for the optical molasses to enable sub-Doppler cooling. Following the gray molasses method outlined in reference [48] for ^{39}K and standard sub-Doppler cooling techniques for ^{87}Rb we typically obtain 5×10^8 (6×10^7) atoms at a temperature of $21 \mu\text{K}$ ($28 \mu\text{K}$) for rubidium (potassium) within 15 ms. Due to the trade-off in molasses temperature in favor of ^{39}K , the temperature of ^{87}Rb is higher than the typical value of $8 \mu\text{K}$ when optimizing for ^{87}Rb only.

The procedure described in the following combines a state preparation with a vertical velocity selection for an increased signal-to-noise ratio [51,52]. Subsequent to the sub-Doppler cooling the atoms are optically pumped into the $|F = 1, m_F\rangle$ manifold. Afterwards they are released into free fall. A quantization field of $B_0 = 500 \text{ mG}$ is applied to lift the degeneracy of the magnetic sub-levels as depicted in a Raman resonance spectrum in Figure 3. A microwave pulse transfers the atoms from the $|F = 1, m_F = 0\rangle$ into the $|F = 2, m_F = 0\rangle$ state. The microwave transitions are realized using a Yagi-Uda type antenna for potassium and a loop antenna for rubidium. Then, the $|F = 1\rangle$ state is depopulated by optically pumping the remaining atoms into the $|F = 2\rangle$ manifold with an equal distribution. This results in a population of the $|F = 2, m_F = 0\rangle$ state with up to 45% of the atoms [52]. After a time of flight of 44 ms accommodating these steps, a velocity-selective Raman pulse selects a narrow vertical velocity class [53] of atoms from the $|F = 2, m_F = 0\rangle$ state by transferring them into the $|F = 1, m_F = 0\rangle$ state. The remaining atoms from the $|F = 2\rangle$ manifold are removed

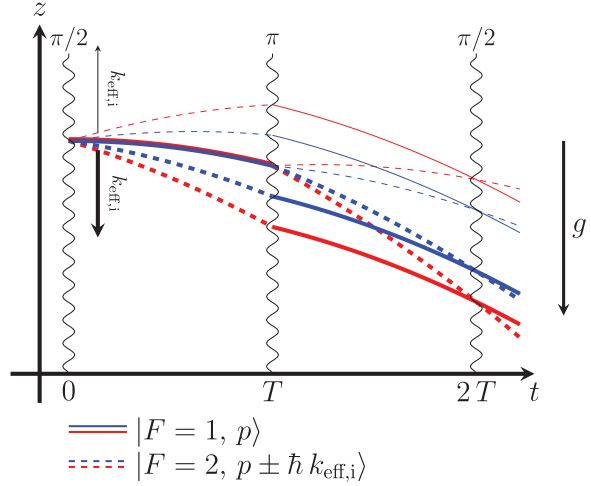


Fig. 4. Space-time diagram of a dual-species Mach-Zehnder matter-wave interferometer in a constant gravitational field for the downward (thick lines) and upward (thin lines) direction of momentum transfer. Stimulated Raman transitions at times 0, T , and $2T$ couple the states $|F_i = 1, p\rangle$ (solid lines) and $|F_i = 2, p \pm \hbar k_{\text{eff},i}\rangle$ (dashed lines), where i stands for Rb (blue lines) or K (red lines). The velocity change induced by the Raman pulses is not to scale with respect to the gravitational acceleration.

by a light pulse addressing the cooling transition, concluding the preparation sequence.

3.2 Mach-Zehnder atom interferometry

Atom interferometry is performed simultaneously with both species using the atomic sources described in Section 3.1. We employ two-photon Raman transitions [54] driven by counter-propagating beams with wave vectors $k_i = 2\pi/\lambda_i$, where λ_i refers to the D_2 transition wavelength. The index i indicates the species ^{87}Rb and ^{39}K . We form a Mach-Zehnder-type atom interferometer with a $\pi/2 - \pi - \pi/2$ pulse sequence separated by free evolution times T to coherently split, reflect, and recombine the wavepackets. The atomic recoil $\Delta p \approx 2\hbar k_i = \hbar k_{\text{eff},i}$ induced by atom-light interaction leads to a finite space-time area enclosed by the AI (Fig. 4).

For our scale factors, the presence of our commercial vibration isolation platform allows us to scan fringes as opposed to using an ellipse fitting algorithm commonly used in differential atom interferometers [55–57].

The population of the output ports of the interferometer depends on the accumulated phase difference $\Delta\phi$ between the two paths of the interferometer [34,58,59] and is given by:

$$P_{|F=2\rangle} = A \cdot \cos(\Delta\phi) + P_0, \quad (2)$$

where $P_{|F=2\rangle}$ is the fraction of atoms in the excited $|F = 2\rangle$ state, $C = A/P_0$ is the contrast, and P_0 the offset. The population is measured by a normalized state selective fluorescence detection, within which the pulses

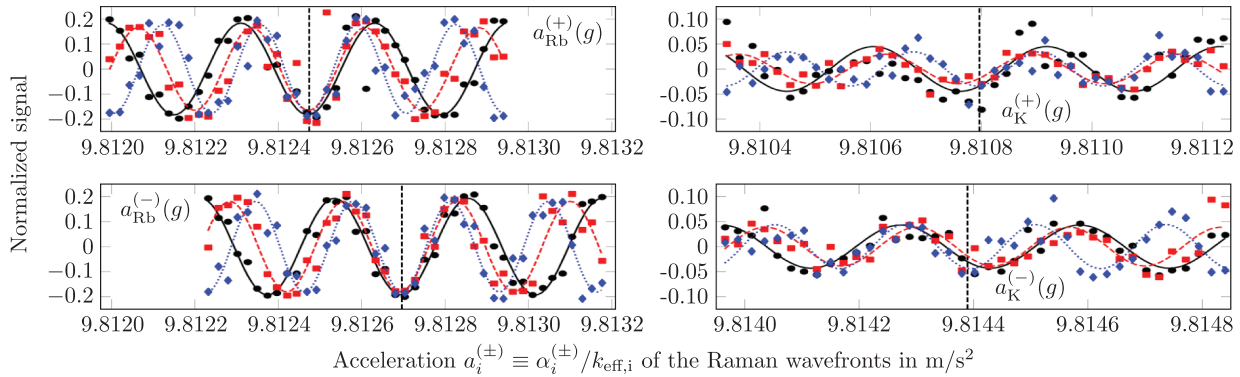


Fig. 5. Determination of the differential gravitational acceleration of rubidium (left) and potassium (right). Typical fringe signals and sinusoidal fit functions are plotted in dependence of the effective Raman wave front acceleration for pulse separation times $T = 35$ ms (black circles and solid black line), $T = 38$ ms (red squares and dashed blue line), and $T = 41$ ms (blue diamonds and dotted red line) for upward (+) and downward (-) direction of momentum transfer. The central fringe positions $a_i^{(\pm)}(g)$, $i = \text{Rb}, \text{K}$ for $T = 41$ ms are marked with dashed vertical lines. The data sets are corrected for slow linear drifts caused by varying offsets in the detection and global signal offsets.

reading out potassium are nested within the rubidium detection sequence.

The leading order phase shift of such an interferometer due to an acceleration¹ a_i in the direction of beam splitting reads [34,58,59]

$$\Delta\phi = k_{\text{eff},i} a_i T^2. \quad (3)$$

Applying a phase-continuous frequency ramp α_i not only maintains the Raman resonance condition under the influence of a gravitational Doppler shift, but also mimics an effective acceleration of the Raman wave fronts

$$a_i = \frac{\alpha_i}{k_{\text{eff},i}} \quad (4)$$

and accordingly enters the phase shift as follows:

$$\Delta\phi_i = (g_i - \frac{\alpha_i}{k_{\text{eff},i}}) \cdot k_{\text{eff},i} \cdot T^2. \quad (5)$$

For $\alpha_i = k_{\text{eff},i} \cdot g_i$ the accumulated phase shift $\Delta\phi_i = 0$ for all pulse separation times T .

We apply the momentum reversal technique [51,60] to suppress systematic errors independent of the direction of momentum transfer. We distinguish two types of undesired phase perturbations, k -dependent ($\delta\phi_{\text{dep}}$) and k -independent ($\delta\phi_{\text{ind}}$) shifts. In our setup, the two possible counter-propagating Raman beam configurations have opposite effective wave vectors and allow for selecting the direction of momentum transfer. We label these particular transitions as $\mathbf{k}^{(+)}$ and $\mathbf{k}^{(-)}$ (Fig. 3).

The phase shifts in $\mathbf{k}^{(+)}$ and $\mathbf{k}^{(-)}$ configuration can be written as:

$$\Delta\phi_+ = k_{\text{eff}} a T^2 + \delta\phi_{\text{ind}} + \delta\phi_{\text{dep}} \quad (6)$$

$$\Delta\phi_- = -k_{\text{eff}} a T^2 + \delta\phi_{\text{ind}} - \delta\phi_{\text{dep}}. \quad (7)$$

¹ If derived from the Schrödinger equation with masses m_{in} in the kinetic term and m_{gr} in the Newtonian potential, a prefactor resembling those in equation (1), $a_i \rightarrow \frac{m_{\text{gr}}}{m_{\text{in}}} a_i$ becomes apparent.

Consequently, their phase difference is given by:

$$\Delta\phi_{\text{tot}} = \frac{\Delta\phi_+ - \Delta\phi_-}{2} = k_{\text{eff}} a T^2 + \delta\phi_{\text{dep}}. \quad (8)$$

Hence, by alternating the direction of momentum transfer we can largely suppress momentum independent ($\delta\phi_{\text{ind}}$) systematic effects, e.g. the AC-Stark shift, with dynamics slower than a typical momentum reversal sequence as described in the following subsection.

3.3 Obtaining the Eötvös ratio

The gravitational accelerations g_i (Eq. (5)) are determined through the central fringe positions $a_i^{(\pm)}(g)$. For determining the latter, we operate both interferometers at three pulse separation times $T = 35, 38, 41$ ms. Figure 5 displays scans around the respective $a_i^{(\pm)}(g)$. Here, for the downward direction of momentum transfer the sign of the phase shift is inverted in order to yield a positive value $g_i > 0$.

We then operate both interferometers simultaneously around their central fringe positions with $T = 41$ ms. To this end we scan across the central fringe positions in 10 steps and alternate the direction of momentum transfer afterwards. This procedure constitutes a single measurement cycle with a duration of 32 s (2×10 shots). Each measurement cycle yields g_{Rb} and g_{K} , allowing us to compute an Eötvös ratio (Eq. (1)).

4 Data analysis and results

4.1 Statistical analysis

We acquire 30 000 shots over consecutive 13 h. This is limited by technical circumstances related to the stability of the laser locks. Figure 6 shows the normalized Allan

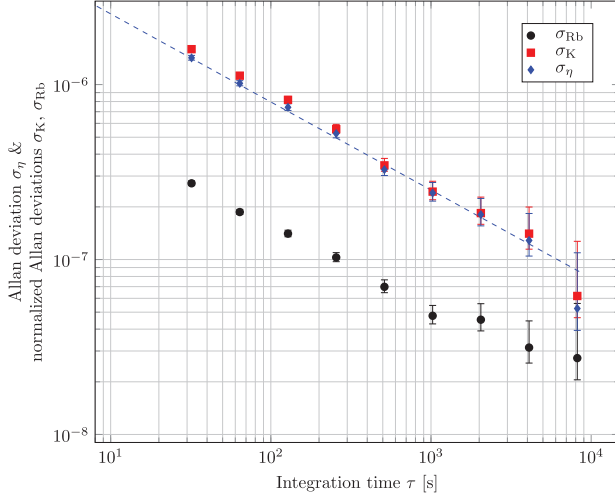


Fig. 6. Normalized Allan deviations σ_{Rb} , σ_K , and the Allan deviation σ_η of the signals providing us with the accelerations g_{Rb} and g_K of rubidium (black circles) potassium (red squares), and of the Eötvös ratio $\eta_{Rb,K}$ (blue diamonds) in their dependence of the integration time τ . Using a fit $\propto 1/\sqrt{\tau}$ (blue dashed line) we extract a statistical uncertainty of the Eötvös ratio of $\sigma_\eta = 9 \times 10^{-8}$ after 8192 s integration. The measurement is solely limited by the stability of the potassium signal.

deviation of our measurement which yields an instability $\sigma_\eta = 9 \times 10^{-8}$ after 8192 s integration time. This instability is fully dominated by the potassium interferometer due to its larger technical noise influence stemming mainly from the detection at a significantly lower contrast (Fig. 5). The latter can be explained by the underlying large transverse expansion rate of potassium and related homogeneous excitation when the ensemble diameter becomes comparable to the Raman beam diameter.

4.2 Systematic effects

Table 2 lists the systematic effects that are not suppressed by the momentum reversal method. Here, the analysis follows references [60–65] with the following assumptions for Rb (K): temperature – 21 μ K (28 μ K) with a 10% uncertainty; initial size – 1 mm (1 mm); π -pulse width – 15 μ s (15 μ s); free evolution time – 41 ms (41 ms); time-of-flight prior to the 1st interferometry pulse – 54.5 ms; differential center-of-mass (COM) position uncertainty in z – 1 mm; differential COM velocity uncertainty in z – 1 mm/s.

Below we discuss the treatment of the dominant systematic contributions originating from stray magnetic fields and wave front aberration.

4.2.1 Zeeman effect

Magnetic fields along the interferometric trajectories change each respective species's hyperfine transition frequency. Due to state preparation into the $|F = 1, m_F = 0\rangle$

Table 2. Estimated bias contributions for the $\eta_{Rb,K}$ ratio and their uncertainties σ . We estimate the uncertainties to be uncorrelated at the discussed level of accuracy.

Contribution	Correction $\Delta\eta$	Uncertainty $\delta\eta$
Zeeman effect	-1.3×10^{-6}	6.0×10^{-8}
Wave front aberration	0	3×10^{-7}
Coriolis force	0	9×10^{-9}
2-photon light shift	3.08×10^{-8}	6×10^{-10}
Effective wave vector	0	1.3×10^{-9}
1st order gravity gradient	0	1×10^{-10}
Total bias	-1.28×10^{-6}	3.1×10^{-7}

magnetically insensitive state the Zeeman effect cancels to first order. However spatial and temporal variations of the magnetic field along the axis of interferometry contribute a non-zero bias phase resulting from the remaining clock shift affecting atoms in $m_F = 0$.

Magnetic fields shift the hyperfine transition frequency by $\Delta\omega_{\text{clock},i}^i = 2\pi\kappa^i \cdot B^2$, where $\kappa^{Rb} = 575.15 \text{ Hz/G}^2$ for ^{87}Rb , and $\kappa^K = 8.5 \text{ kHz/G}^2$ for ^{39}K . Based on a characterization using Raman spectroscopy at different positions along the vertical axis we can model the magnetic field as

$$B(z(t), t) = B_0(t) + \frac{\partial B}{\partial z} \cdot z_{\text{COM}}(t) \quad (9)$$

where $B_0(t)$ describes the temporal behaviour of the bias field due to the switching behaviour of the respective power supply², and $z_{\text{COM}}(t)$ is the free fall center of mass motion of the atoms defined as: $z_{\text{COM}}(t) = z_0 + (v_0 \pm v_{\text{rec}}/2) \cdot t + 1/2at^2$ with z_0 being the initial position of the atoms, v_0 the velocity, and v_{rec} the recoil velocity defined as $v_{\text{rec}} = \hbar k_{\text{eff}}/m$. Only the recoil velocity is dependent on the direction of momentum transfer, and therefore all other components are suppressed by k -reversal. Using the sensitivity function formalism [66] we can calculate the frequency shifts

$$\Delta\omega_{Z^{(\pm)},i}(t) \equiv \pm 2\pi\kappa^i \cdot \frac{\partial B}{\partial z} \cdot B(t) \cdot v_{\text{rec},i} t, \quad (10)$$

with the clock shift $\Delta\omega_{\text{clock},i}$. Computing the integral of the clock shift weighted with the sensitivity function $g_s(t)$

$$\Delta\Phi_i^Z \equiv \int_{-\infty}^{\infty} g_s(t) \Delta\omega_{Z^{(\pm)},i}(t) dt \quad (11)$$

allows deriving the bias due to the Zeeman effect. With a gradient $\frac{\partial B}{\partial z} = 3 \text{ mG/cm}$ and using the sensitivity formalism for rubidium and potassium the inferred bias affecting the Eötvös ratio amounts to $-1.30(0.06) \times 10^{-6}$. We note that the resulting bias was also confirmed using a perturbation theory formalism [67].

² We have characterized the switch-on to be saturating at 500 mG with a time constant of 90 ms.

4.2.2 Wave front aberration

Our estimation of systematic uncertainty owing to wave front aberration is based on numerical simulation. To this end, we take into account the Raman light fields' propagation including curvatures of view ports and the retro-reflection mirror, uncertainty in the positioning of the collimation lens, and differential ensemble expansion. In 10^4 trials, we randomly vary these parameters as follows and calculate the resulting phase contribution [63]: for the top and bottom view port curvatures ($\lambda/10$) and the retro-reflection mirror ($\lambda/20$) we assume uncertainties of 10 %, for the positioning of the collimation lens we assume an uncertainty of 0.1 % and the ensemble temperatures are varied with an uncertainty of 10 %. Statistical analysis then yields an uncertainty in the Eötvös ratio of 3×10^{-7} due to wave front aberration.

4.3 Summary & discussion

We determine an Eötvös ratio of $\eta_{\text{Rb},\text{K}} = -1.9 \times 10^{-7}$ with a combined (statistical and systematic) standard uncertainty of 3.2×10^{-7} , constituting about a factor of two improvement over our previous result [22]. We estimate a contribution of the statistical uncertainty of 9×10^{-8} and the systematic uncertainty of 3.1×10^{-7} .

Increased free fall times in comparison to our previous result [22] lead to larger systematic error contributions, e.g., due to the distance traveled through the magnetic field gradient which yields an increased correction, and more challenging characterization of it resulting in a larger uncertainty. The increase in the contribution from wave front aberration is caused by a more defensive modeling of all relevant optical components.

5 Conclusion & outlook

We reported on a test of the UFF with our dual atom interferometer operating simultaneously with ^{87}Rb and ^{39}K . The result of our measurement of the Eötvös parameter is $-1.9(3.2) \times 10^{-7}$ with the lowest uncertainty in an atom interferometer with two different chemical elements reported so far. It corresponds to an improvement of a factor of two with respect to our previous result which we attribute to an improved state preparation of the ^{39}K ensemble.

Our analysis shows that the intrinsic noise of the ^{39}K interferometer limits the statistical uncertainty. The reasons are the residual transverse expansion rate implying imperfections in the coherent excitation leading to a reduction in contrast. Among the systematic effects, we identify the inhomogeneity in the magnetic bias field and wave front aberration as the main contributors.

Advanced cooling techniques such as evaporation in an optical dipole trap [68] are expected to enhance the contrast [69,70] and will allow us to reduce wave front-related errors by achieving colder temperatures and by tuning the differential expansion of the two species. The homogeneity of the magnetic field can be improved by an upgrade

of the magnetic shield [71], a more in-depth characterization, and advanced center-of-mass control over the ensembles. By relying on the differential suppression of vibration noise between the two elements [57] we envisage the perspective for a test on the level of 10^{-9} .

To date, the universality of free fall has proven to be successful with no precision test uncovering a significant deviation. Atom interferometers add a complementary approach to the toolbox for these tests. Compared to the best classical tests (Tab. 1), this still represents a modest result, but further enhancements are possible and realistic. Using evaporated atoms and matter-wave collimation techniques [72–74] opens the pathway to upgrade the beam splitters to hundreds of coherent photon momentum kicks [75–82] and extended free evolution times on the order of seconds. Very long baseline atom interferometers relying on these techniques promise to venture beyond 10^{-13} [23–26]. In parallel, microgravity research investigates the benefits and the adaption of atom interferometers to operation in drop tower experiments [74,83,84], on a sounding rocket [85], the international space station [28,86], and dedicated satellite missions [27,29] with the target of 10^{-15} and beyond.

Open access funding provided by Projekt DEAL. We are grateful to É. Wodey, H. Ahlers, and B. Barrett for discussions and critical proof reading of the manuscript, and T. Hensel for careful cross checks concerning the systematic error originating from magnetic fields. This project is supported by the German Space Agency (DLR) with funds provided by the Federal Ministry for Economic Affairs and Energy (BMWi) due to an enactment of the German Bundestag under grant No. DLR 50WM1641 (PRIMUS-III). The authors furthermore acknowledge financial support by the German Science Foundation (DFG) through the Collaborative Research Centers 1128 “geo-Q” (projects A02 and F01), 1227 “DQ-mat” (project B07), the Deutsche Forschungsgemeinschaft (DFG, German Research Foundation) under Germany’s Excellence Strategy “EXC-2123 QuantumFrontiers” 390837967 (research unit B02), “Niedersächsisches Vorab” through the “Quantum- and NanoMetrology” (QUANOMET) initiative within the project QT3, and “Wege in die Forschung (II)” of Leibniz Universität Hannover. A.H. and D.S. gratefully acknowledge funding by the Federal Ministry of Education and Research (BMBF) through the funding program Photonics Research Germany under contract number 13N14875.

Author contribution statement

W.E., E.M.R., C.S., J.H., and D.S. designed the atom interferometer and its laser system. L.L.R., H.A., D.N., J.H., and D.S. contributed to the design of the atom interferometer and its laser system and realised the overall setup. H.A., L.L.R., H.H., and D.N. operated the final experimental setup. H.A., A.H., D.S., J.H., C.S., and H.H. performed the analysis of the data presented in this manuscript. D.S., H.A., L.L.R., C.S., and A.H. drafted the initial manuscript. C.V., M.W., C.L., and S.H. provided major input to the manuscript and all authors critically reviewed and approved of the final version.

Publisher's Note The EPJ Publishers remain neutral with regard to jurisdictional claims in published maps and institutional affiliations.

Open Access This is an open access article distributed under the terms of the Creative Commons Attribution License (<https://creativecommons.org/licenses/by/4.0/>), which permits unrestricted use, distribution, and reproduction in any medium, provided the original work is properly cited.

References

1. J.K. Stockton, K. Takase, M.A. Kasevich, Phys. Rev. Lett. **107**, 133001 (2011)
2. V. Ménoret, P. Vermeulen, N. Le Moigne, S. Bonvalot, P. Bouyer, A. Landragin, B. Desruelle, Sci. Rep. **8**, 12300 (2018)
3. Z.-K. Hu, B.-L. Sun, X.-C. Duan, M.-K. Zhou, L.-L. Chen, S. Zhan, Q.-Z. Zhang, J. Luo, Phys. Rev. A **88**, 043610 (2013)
4. D. Savoie, M. Altorio, B. Fang, L.A. Sidorenkov, R. Geiger, A. Landragin, Sci. Adv. **4**, eaau7948 (2018)
5. C. Freier, M. Hauth, V. Schkolnik, B. Leykauf, M. Schilling, H. Wziontek, H.-G. Scherneck, J. Müller, A. Peters, J. Phys.: Conf. Ser. **723**, 012050 (2016)
6. P. Berg, S. Abend, G. Tackmann, C. Schubert, E. Giese, W.P. Schleich, F.A. Narducci, W. Ertmer, E.M. Rasel, Phys. Rev. Lett. **114**, 063002 (2015)
7. F. Sorrentino, A. Bertoldi, Q. Bodart, L. Cacciapuoti, M. de Angelis, Y.-H. Lien, M. Prevedelli, G. Rosi, G.M. Tino, Appl. Phys. Lett. **101**, 114106 (2012)
8. Y. Bidel, N. Zahzam, C. Blanchard, A. Bonnin, M. Cadoret, A. Bresson, D. Rouxel, M.F. Lequentrec-Lalancette, Nat. Commun. **9**, 627 (2018)
9. R. Geiger, V. Ménoret, G. Stern, N. Zahzam, P. Cheinet, B. Battelier, A. Villing, F. Moron, M. Lours, Y. Bidel, A. Bresson, A. Landragin, P. Bouyer, Nat. Commun. **2**, 474 (2011)
10. Y. Bidel, N. Zahzam, A. Bresson, C. Blanchard, M. Cadoret, A.V. Olesen, R. Forsberg, J. Geod. **94**, 20 (2020)
11. G. Rosi, F. Sorrentino, L. Cacciapuoti, M. Prevedelli, G.M. Tino, Nature **510**, 518 (2014)
12. M. Jaffe, P. Haslinger, V. Xu, P. Hamilton, A. Upadhye, B. Elder, J. Khoury, H. Müller, Nat. Phys. **13**, 938 (2017)
13. P. Haslinger, M. Jaffe, V. Xu, O. Schwartz, M. Sonnleitner, M. Ritsch-Marte, H. Ritsch, H. Müller, Nat. Phys. **14**, 257 (2017)
14. R. Bouchendira, P. Cladé, S. Guellati-Khélifa, F. Nez, F. Biraben, Phys. Rev. Lett. **106**, 080801 (2011)
15. R.H. Parker, C. Yu, W. Zhong, B. Estey, H. Müller, Science **360**, 191 (2018)
16. C.M. Will, Liv. Rev. Relativ. **9**, 3 (2006)
17. R. Colella, A.W. Overhauser, S.A. Werner, Phys. Rev. Lett. **34**, 1472 (1975)
18. V. Alan Kostelecký, J.D. Tasson, Phys. Rev. D **83**, 016013 (2011)
19. M.A. Hohensee, H. Müller, R.B. Wiringa, Phys. Rev. Lett. **111**, 151102 (2013)
20. H. Mueller. Quantum mechanics, matter waves, and moving clocks, [arXiv:1312.6449](https://arxiv.org/abs/1312.6449) (2013)
21. T. Damour, Classical Quantum Gravity **29**, 184001 (2012)
22. D. Schlippert, J. Hartwig, H. Albers, L.L. Richardson, C. Schubert, A. Roura, W.P. Schleich, W. Ertmer, E.M. Rasel, Phys. Rev. Lett. **112**, 203002 (2014)
23. S. Dimopoulos, P.W. Graham, J.M. Hogan, M.A. Kasevich, Phys. Rev. Lett. **98**, 111102 (2007)
24. C. Overstreet, P. Asenbaum, T. Kovachy, R. Notermans, J.M. Hogan, M.A. Kasevich, Phys. Rev. Lett. **120**, 183604 (2018)
25. L. Zhou et al., Gen. Relativ. Gravitation **43**, 1931 (2011)
26. J. Hartwig, S. Abend, C. Schubert, D. Schlippert, H. Ahlers, K. Posso-Trujillo, N. Gaaloul, W. Ertmer, E.M. Rasel, New J. Phys. **17**, 035011 (2015)
27. D.N. Aguilera, H. Ahlers, B. Battelier, A. Bawamia, A. Bertoldi, R. Bondarescu, K. Bongs, P. Bouyer, C. Braxmaier, L. Cacciapuoti, C. Chaloner, M. Chwalla, W. Ertmer, M. Franz, N. Gaaloul, M. Gehler, D. Gerardi, L. Gesa, N. Gürlebeck, J. Hartwig, M. Hauth, O. Hellmig, W. Herr, S. Herrmann, A. Heske, A. Hinton, P. Ireland, P. Jetzer, U. Johann, M. Krutzik, A. Kubelka, C. Lämmerzahl, A. Landragin, I. Lloro, D. Massonnet, I. Mateos, A. Milke, M. Nofrarias, M. Oswald, A. Peters, K. Posso-Trujillo, E. Rasel, E. Rocco, A. Roura, J. Rudolph, W. Schleich, C. Schubert, T. Schultdt, S. Seidel, K. Sengstock, C.F. Sopuerta, F. Sorrentino, D. Summers, G.M. Tino, C. Trenkel, N. Uzunoglu, W. von Klitzing, R. Walser, T. Wendrich, A. Wenzlawski, P. Weels, A. Wicht, E. Wille, M. Williams, P. Windpassinger, N. Zahzam, Classical Quantum Gravity **31**, 115010 (2014)
28. J. Williams, S.-w. Chiow, N. Yu, H. Müller, New J. Phys. **18**, 025018 (2016)
29. J. Bergé et al., Exploring the foundations of the universe with space tests of the equivalence principle, [arXiv:1908.11785](https://arxiv.org/abs/1908.11785) (2019)
30. P. Touboul, G. Métris, M. Rodrigues, Y. André, Q. Baghi, J. Bergé, D. Boulanger, S. Bremer, P. Carle, R. Chhun, B. Christophe, V. Cipolla, T. Damour, P. Danto, H. Dittus, P. Fayet, B. Foulon, C. Gageant, P.-Y. Guidotti, D. Hagedorn, E. Hardy, P.-A. Huynh, H. Inchauspe, P. Kayser, S. Lala, C. Lämmerzahl, V. Lebat, P. Leseur, F. Liorzou, M. List, F. Löffler, I. Panet, B. Pouilloux, P. Prieur, A. Rebray, S. Reynaud, B. Rievers, A. Robert, H. Selig, L. Serron, T. Sumner, N. Tanguy, P. Visser, Phys. Rev. Lett. **119**, 231101 (2017)
31. F. Hofmann, J. Müller, Classical Quantum Gravity **35**, 035015 (2018)
32. S. Schlamminger, K.-Y. Choi, T.A. Wagner, J.H. Gundlach, E.G. Adelberger, Phys. Rev. Lett. **100**, 041101 (2008)
33. T.M. Niebauer, M.P. McHugh, J.E. Faller, Phys. Rev. Lett. **59**, 609 (1987)
34. A. Peters, K.Y. Chung, S. Chu, Nature **400**, 849 (1999)
35. S. Merlet, Q. Bodart, N. Malossi, A. Landragin, F. Pereira Dos Santos, O. Gitlein, L. Timmen, Metrologia **47**, L9 (2010)
36. K. Zhang, M.-K. Zhou, Y. Cheng, L.-L. Chen, Q. Luo, W.-J. Xu, L.-S. Cao, X.-C. Duan, Z.-K. Hu, Testing the universality of free fall at 10^{-10} level by comparing the atoms in different hyperfine states with bragg diffraction, [arXiv:1805.07758](https://arxiv.org/abs/1805.07758) (2018)
37. G. Rosi, G. D'Amico, L. Cacciapuoti, F. Sorrentino, M. Prevedelli, M. Zych, Č. Brukner, G.M. Tino, Nat. Commun. **8**, 15529 (2017)

38. X.-C. Duan, X.-B. Deng, M.-K. Zhou, K. Zhang, W.-J. Xu, F. Xiong, Y.-Y. Xu, C.-G. Shao, J. Luo, Z.-K. Hu, Phys. Rev. Lett. **117**, 023001 (2016)

39. L. Zhou, S. Long, B. Tang, X. Chen, F. Gao, W. Peng, W. Duan, J. Zhong, Z. Xiong, J. Wang, Y. Zhang, M. Zhan, Phys. Rev. Lett. **115**, 013004 (2015)

40. A. Bonnin, N. Zahzam, Y. Bidel, A. Bresson, Phys. Rev. A **88**, 043615 (2013)

41. M.G. Tarallo, T. Mazzoni, N. Poli, D.V. Sutyrin, X. Zhang, G.M. Tino, Phys. Rev. Lett. **113**, 023005 (2014)

42. B. Barrett, L. Antoni-Micollier, L. Chichet, B. Battelier, T. Lévèque, A. Landragin, P. Bouyer, Nat. Commun. **7**, 13786 (2016)

43. M. Zaiser, Eine Quelle quantenentarteter Gase für die Atominterferometrie, Ph.D. thesis, Leibniz Universität Hannover, 2010

44. J.M. Hartwig, Analyse eines atomaren Gravimeters hinsichtlich eines Quantentests des Äquivalenzprinzips, Ph.D. thesis, Leibniz Universität Hannover, 2013

45. D. Schlippert, Quantum test of the Universality of Free Fall, Ph.D. thesis, Leibniz Universität Hannover, 2014

46. X. Baillard, A. Gauguet, S. Bize, P. Lemonde, Ph. Laurent, A. Clairon, P. Rosenbusch, Opt. Commun. **266**, 609 (2006)

47. M. Gilowski, Ch. Schubert, M. Zaiser, W. Herr, T. Wübbena, T. Wendrich, T. Müller, E.M. Rasel, W. Ertmer, Opt. Commun. **280**, 443 (2007)

48. M. Landini, S. Roy, L. Carcagní, D. Trypogeorgos, M. Fattori, M. Inguscio, G. Modugno, Phys. Rev. A **84**, 043432 (2011)

49. D.A. Steck, Rubidium 87 D Line Data, <http://steck.us/alkalidata> (2015)

50. T.G. Tiecke, Properties of Potassium (2019)

51. J.M. McGuirk, G.T. Foster, J.B. Fixler, M.J. Snadden, M.A. Kasevich, Phys. Rev. A **65**, 033608 (2002)

52. L. Antoni-Micollier, B. Barrett, L. Chichet, G. Condon, B. Battelier, A. Landragin, P. Bouyer, Phys. Rev. A **96**, 023608 (2017)

53. M. Kasevich, D.S. Weiss, E. Riis, K. Moler, S. Kasapi, S. Chu, Phys. Rev. Lett. **66**, 2297 (1991)

54. M. Kasevich, S. Chu, Phys. Rev. Lett. **67**, 181 (1991)

55. G. Varoquaux, R.A. Nyman, R. Geiger, P. Cheinet, A. Landragin, P. Bouyer, New J. Phys. **11**, 113010 (2009)

56. X. Chen, J. Zhong, H. Song, L. Zhu, J. Wang, M. Zhan, Phys. Rev. A **90**, 023609 (2014)

57. B. Barrett, L. Antoni-Micollier, L. Chichet, B. Battelier, P.-A. Gominet, A. Bertoldi, P. Bouyer, A. Landragin, New J. Phys. **17**, 085010 (2015)

58. M. Kasevich, S. Chu, Appl. Phys. B **54**, 321 (1992)

59. P.R. Berman, V. Kharchenko, *Atom Interferometry* (1997)

60. A. Louchet-Chauvet, T. Farah, Q. Bodart, A. Clairon, A. Landragin, S. Merlet, F. Pereira Dos Santos, New J. Phys. **13**, 065025 (2011)

61. S. Dimopoulos, P.W. Graham, J.M. Hogan, M.A. Kasevich, Phys. Rev. D **78**, 042003 (2008)

62. A. Gauguet, T.E. Mehlstäubler, T. Lévèque, J. Le Gouët, W. Chaibi, B. Canuel, A. Clairon, F. Pereira Dos Santos, A. Landragin, Phys. Rev. A **78**, 043615 (2008)

63. C. Schubert, J. Hartwig, H. Ahlers, K. Posso-Trujillo, N. Gaaloul, U. Velte, A. Landragin, A. Bertoldi, B. Battelier, P. Bouyer, F. Sorrentino, G.M. Tino, M. Krutzik, A. Peters, S. Herrmann, C. Lämmerzahl, L. Cacciapouti, E. Rocco, K. Bongs, W. Ertmer, E.M. Rasel, Differential atom interferometry with ^{87}Rb and ^{85}Rb for testing the UFF in STE-QUEST, [arXiv:1312.5963](https://arxiv.org/abs/1312.5963) (2013)

64. A. Peters, K.Y. Chung, S. Chu, Metrologia **38**, 25 (2001)

65. B. Dubetsky, Appl. Phys. B **125**, 187 (2019)

66. P. Cheinet, B. Canuel, F. Pereira Dos Santos, A. Gauguet, F. Yver-Leduc, A. Landragin, IEEE Trans. Instrum. Meas. **57**, 1141 (2008)

67. C. Ufrecht, Theoretical approach to high-precision atom interferometry, Ph.D. thesis, Universität Ulm, 2019

68. G. Salomon, L. Fouché, S. Lepoutre, A. Aspect, T. Bourdel, Phys. Rev. A **90**, 033405 (2014)

69. S. Abend, et al., Phys. Rev. Lett. **117**, 203003 (2016)

70. S.S. Szigeti, J.E. Debs, J.J. Hope, N.P. Robins, J.D. Close, New J. Phys. **14**, 023009 (2012)

71. É. Wodey, D. Tell, E.M. Rasel, D. Schlippert, R. Baur, U. Kissling, B. Kölliker, M. Lorenz, M. Marrer, U. Schläpfer, M. Widmer, C. Ufrecht, S. Stuiber, P. Fierlinger, Rev. Sci. Instrum. **91**, 035117 (2020)

72. J. Rudolph, Matter-wave optics with Bose-Einstein condensates in microgravity, Ph.D. thesis, Leibniz Universität Hannover, 2016

73. T. Kovachy, J.M. Hogan, A. Sugarbaker, S.M. Dickerson, C.A. Donnelly, C. Overstreet, M.A. Kasevich, Phys. Rev. Lett. **114**, 143004 (2015)

74. H. Müntinga, H. Ahlers, M. Krutzik, A. Wenzlawski, S. Arnold, D. Becker, K. Bongs, H. Dittus, H. Duncker, N. Gaaloul, C. Gherasim, Phys. Rev. Lett. **110**, 093602 (2013)

75. M. Gebbe et al., Twin-lattice atom interferometry, [arXiv:1907.08416](https://arxiv.org/abs/1907.08416) (2019)

76. B. Plotkin-Swing, D. Gochnauer, K.E. McAlpine, E.S. Cooper, A.O. Jamison, S. Gupta, Phys. Rev. Lett. **121**, 133201 (2018)

77. M. Jaffe, V. Xu, P. Haslinger, H. Müller, P. Hamilton, Phys. Rev. Lett. **121**, 040402 (2018)

78. K. Kotru, D.L. Butts, J.M. Kinast, R.E. Stoner, Phys. Rev. Lett. **115**, 103001 (2015)

79. G.D. McDonald, C.C.N. Kuhn, S. Bennetts, J.E. Debs, K.S. Hardman, J.D. Close, N.P. Robins, Eur. Phys. Lett. **105**, 63001 (2014)

80. S.-W. Chiow, T. Kovachy, H.-C. Chien, M.A. Kasevich, Phys. Rev. Lett. **107**, 130403 (2011)

81. S.-W. Chiow, S. Herrmann, S. Chu, H. Müller, Phys. Rev. Lett. **103**, 050402 (2009)

82. P. Cladé, S. Guellati-Khélifa, F. Nez, F. Biraben, Phys. Rev. Lett. **102**, 240402 (2009)

83. S. Kulas, C. Vogt, A. Resch, J. Hartwig, S. Ganske, J. Matthias, D. Schlippert, T. Wendrich, W. Ertmer, E. Maria Rasel, M. Damjanic, P. Weßels, A. Kohfeldt, E. Luvsandamdin, M. Schiemangk, C. Grzeschik, M. Krutzik, A. Wicht, A. Peters, S. Herrmann, C. Lämmerzahl, Microgravity Sci. Technol. **29**, 37 (2017)

84. C. Vogt, M. Woltmann, S. Herrmann, C. Lämmerzahl, H. Albers, D. Schlippert, E.M. Rasel, Phys. Rev. A **101**, 13634 (2020)

85. D. Becker et al., Nature **562**, 391 (2018)

86. G.M. Tino et al., Nucl. Phys. B (Proc. Suppl.) **243–244**, 203 (2013)

2.2 RAPID GENERATION OF ALL-OPTICAL ^{39}K BOSE-EINSTEIN CONDENSATES USING A LOW-FIELD FESHBACH RESONANCE

Authors: Alexander Herbst, Henning Albers, Knut Stolzenberg, Sebastian Bode, and Dennis Schlippert

Journal: Physical Review A

Article Number: 106, 043320 (2022)

DOI: [10.1103/PhysRevA.106.043320](https://doi.org/10.1103/PhysRevA.106.043320)

Author contribution: A.H., H.A., S.B., K.S., and D.S. contributed to the design, operation, and maintenance of the overall setup and especially the dipole trap laser system. A.H. and H.A. set up the D₁ laser system. A.H. with support of S.B. integrated the active magnetic field stabilization and the Feshbach field system. A.H. designed the experimental sequence and performed the measurements. A.H. with support of H.A. performed the numerical evaporation simulations and evaluated the data. A.H., H.A., S.B. and D.S. drafted the initial manuscript. All authors discussed the results and contributed to, reviewed, and approved of the manuscript.

Rapid generation of all-optical ^{39}K Bose-Einstein condensates using a low-field Feshbach resonance

A. Herbst¹, H. Albers¹, K. Stolzenberg, S. Bode, and D. Schlippe¹^{*}

Leibniz Universität Hannover, Institut für Quantenoptik, Welfengarten 1, 30167 Hannover, Germany



(Received 23 February 2022; accepted 23 September 2022; published 21 October 2022)

Ultracold potassium is an interesting candidate for quantum technology applications and fundamental research as it allows controlling intra-atomic interactions via low-field magnetic Feshbach resonances. However, the realization of high-flux sources of Bose-Einstein condensates remains challenging due to the necessity of optical trapping to use magnetic fields as free parameters. We investigate the production of all-optical ^{39}K Bose-Einstein condensates with different scattering lengths using a Feshbach resonance near 33 G. By tuning the scattering length in a range between $75a_0$ and $300a_0$ we demonstrate a tradeoff between evaporation speed and final atom number and decrease our evaporation time by a factor of 5 while approximately doubling the evaporation flux. To this end, we are able to produce fully condensed ensembles with 5.8×10^4 atoms within 850-ms evaporation time at a scattering length of $232a_0$ and 1.6×10^5 atoms within 3.9 s at $158a_0$, respectively. We deploy a numerical model to analyze the flux and atom number scaling with respect to scattering length, identify current limitations, and simulate the optimal performance of our setup. Based on our findings we describe routes towards high-flux sources of ultracold potassium for inertial sensing.

DOI: [10.1103/PhysRevA.106.043320](https://doi.org/10.1103/PhysRevA.106.043320)

I. INTRODUCTION

Decades after their first experimental realization [1,2], Bose-Einstein condensates (BECs) have become a central tool in research ranging from many-body physics [3] to quantum technology applications such as computation [4], simulation [5], and sensing and metrology [6]. High-flux sources of Bose-Einstein condensates have always been of particular interest, especially with respect to signal-to-noise ratios and quantum projection noise.

To this end, the state of the art has been established by sources based on atom chips [7,8] as demonstrated in the scope of compact apparatuses for microgravity experiments [9–12] and as chosen for current and planned experiments in orbit on the International Space Station [13,14]. Here, forming traps near the current-conducting structures allows generating strongly confining traps and hence rapid and efficient evaporation. However, the nearby surface of the atom chip may sometimes be considered unfavorable, e.g., with respect to clipping of atom optics light fields or, in presence of notable temperature gradients, due to blackbody radiation [15]. In an alternative approach, Bose-Einstein condensation has been demonstrated in all-optical setups [16–19] capable of trapping any magnetic substate. With the ability to focus optical dipole trap beams into the center of the experimental apparatus,

generally this leaves a larger clear aperture for optical access as compared to atom chip solutions [20,21]. Contrary to their magnetic counterparts, the trap depth in optical traps formed by static focused Gaussian beams is inherently linked to the trap's confinement. Accordingly, lowering the trap depth, as demanded for evaporative cooling, leads to a loss of peak atomic density and elastic-scattering rate, thus inhibiting efficient cooling. Recent studies have shown a variety of tools to counteract these scaling laws [22], e.g., by movable lens systems [23] enabling a tunable increase in confinement by tighter optical waists or dynamically shaped time-averaged potentials [24–26]. Finally, while trapping any substate irrespective of high or low magnetic-field seeking, with the external magnetic field as a free parameter optical traps offer ideal conditions for studying and utilizing Feshbach resonances [27,28]. As a versatile means of tailoring interactions, Feshbach resonances have for instance enabled the production of cold molecules from a Fermi gas [29,30], molecular BECs [31–33], sympathetic cooling [34,35], ground-state molecules [36], and studies of interaction dynamics [37,38]. Finally, for cooling fermionic species, Feshbach-induced collisions have been proposed and demonstrated as an evaporation knife [39,40].

In this paper, we demonstrate rapid evaporation of ^{39}K gases to quantum degeneracy from a time-averaged optical trap. By using low-field Feshbach resonances [18,41,42] we are able to directly tune the rethermalization rate and show a dependence between evaporation flux in the BEC and the scattering length when sufficiently distant from the resonance. Accordingly, compared to the largest prepared BEC we are able to decrease our evaporation time by a factor of 5 while approximately doubling the evaporation flux when tuning the scattering length. By generating Feshbach magnetic fields via

^{*}schlippe@iqo.uni-hannover.de

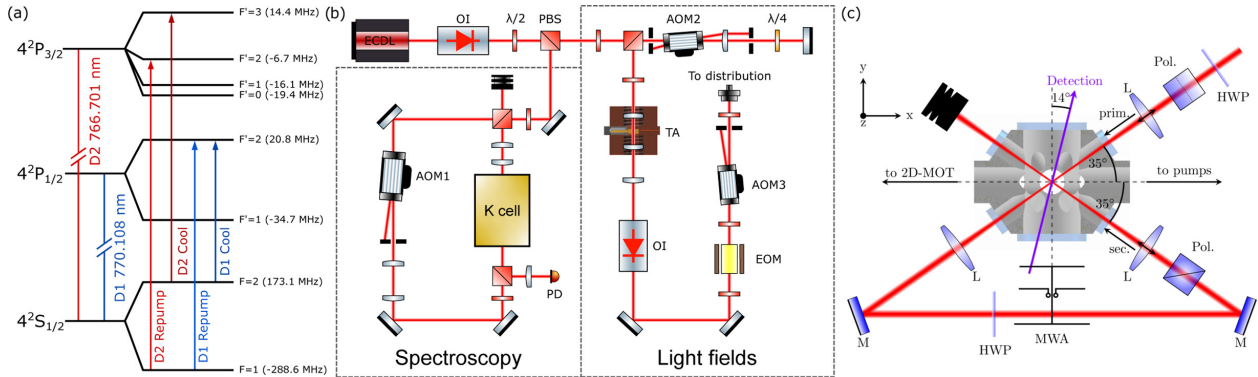


FIG. 1. (a) Level structure of ^{39}K : For trapping and cooling of potassium, transitions on both the D_1 line and the D_2 line are used. (b) Layout of the laser system for D_1 cooling: The external cavity laser (EDL) is stabilized via modulation transfer spectroscopy to the $|F = 1/2\rangle \rightarrow |F' = 1/2\rangle$ crossover transition. The double-pass AOM (AOM2) shifts the laser's frequency to match the D_1 cooling transition before passing the amplifier (TA). Optical isolators (OI) are used to prevent potential back-reflections into TA and ECDL. The free-space electro-optical modulator creates the repump light. The subsequent AOM (AOM3) allows for fast amplitude switching. (c) Optical dipole trap layout: The primary laser beam (prim.) is focused, recollimated, redirected, and focused a second time (sec.) through the vacuum chamber by three lenses (L) with a focal length of 150 mm. To suppress heating effects the linear polarization of the laser is 90° rotated by $\lambda/2$ retardation plates (HWP) and cleaned up by two laser polarizers (Pol.), which are oriented orthogonal to each other. A Yagi-Uda microwave antenna (MWA) is used for coherent manipulation of the atoms. Quantization coil pairs are aligned with the depicted coordinate system, while the Feshbach fields are generated by another Helmholtz pair along the y axis. The detection (purple arrow) is performed under an angle of 14° with respect to the y axis.

readily existing coils employed for our magneto-optical trap (MOT), our approach might be implemented more easily in other existing setups compared to previously demonstrated hybrid trap techniques [18]. We describe our apparatus and the detailed experimental sequence including direct loading of the optical trap and a multistage magnetic state preparation. We finally discuss the prospects of using our result in compact quantum inertial sensors using tunable interactions.

II. EXPERIMENTAL SETUP

A. Laser system

Trapping and cooling of potassium is performed using transitions on both the D_1 line at 770.108 nm and the D_2 line at 766.701 nm [Fig. 1(a)]. The D_2 -laser system and its performance have been described previously [43,44]. In this paper we additionally operate a laser system on the D_1 line [Fig. 1(b)]. To this end, 5 mW of an external cavity diode laser's [45,46] output are used for frequency stabilization to the potassium D_1 -crossover line $|F = 1/2\rangle \rightarrow |F' = 1/2\rangle$ in a vapor cell by means of modulation transfer spectroscopy [47]. The remaining 30 mW are frequency shifted by a double-pass acousto-optical modulator (AOM) to match the D_1 cooling transition $|F = 2\rangle \rightarrow |F' = 2\rangle$ which has an offset of 152.3 MHz with respect to the crossover transition. Subsequently, the light is amplified by a tapered amplifier [Eagleyard EYP-TPA-0765-01500-3006-CMT03-0000] yielding a total output power of 1.5 W. The repump transition $|F = 1\rangle \rightarrow |F' = 1\rangle$ is addressed using a sideband generated by a resonant free-space electro-optical modulator [Qubig PM – K39 + 41] driven with a maximum input power of 31.7 dBm, allowing one to freely tune the power ratio between carrier and sideband in a range from 0 to 1. The cooling and repumping fields are then transported

via a polarization-maintaining fiber [S&K PMC-E-630-4.1-NA012-3-APC.EC-1000-P] with 60% coupling efficiency yielding 500 mW in total at the fiber output. Finally, the fiber output is superimposed with the D_2 light using a narrow-line interference filter and distributed between MOT and detection fibers.

B. Optical dipole trap

Our optical dipole trap (ODT) is based on a 1960-nm fiber laser [IPG, TLR-50-1960-LP] operated at 38-W output power. The laser's intensity is stabilized by a field programmable gate array feedback loop controlling and linearizing a Pockels cell and analyzer setup, which reduces the power by approximately 40%. Subsequent the light passes an AOM [Polytec ATM-1002FA53.24, custom made] with 60% diffraction efficiency.

We then focus the elliptical beam in the vacuum chamber with a beam waist of $30(45) \mu\text{m}$ in horizontal (vertical) direction and realize a recycled cross under an angle of 70° [Fig. 1(c)] with a maximum power of 8 W in the primary and 6 W in the secondary beam. The high power losses are mainly caused by imperfect optical elements available for the wavelength of 1960 nm.

The previously mentioned AOM is used to modulate the center position of the laser beam. The modulation reaches amplitudes of up to $200 \mu\text{m}$ in the primary and $300 \mu\text{m}$ in the secondary recycled beam. By this we generate time-averaged potentials [24,26,48] in the horizontal plane. The shape of the resulting potential depends on the modulation of the AOM driving radio frequency, which is generated using a voltage-controlled oscillator [Mini-Circuits, ZOS – 150+] controlled by the output of an arbitrary waveform generator [Rigol, DG1022Z]. The waveform of the control voltage is chosen

TABLE I. Identified Feshbach resonances, used to calibrate the magnetic fields. The magnetic-field values are taken from Ref. [52].

Atom pair (F, m_F)			Literature magnetic field (G)
(1, -1)	+	(1, -1)	32.6 ± 1.5
(1, 0)	+	(1, 0)	59.3 ± 0.6
(1, 0)	+	(1, 0)	66.0 ± 0.9
(1, 0)	+	(1, -1)	113.76 ± 0.1
(1, -1)	+	(1, -1)	162.8 ± 0.9

to generate preferably parabolic potentials with a modulation frequency of 20 kHz. The amplitude of the waveform defines the spatial width of the center-position modulation (CPM) of the laser beam and is controlled using a modulation input on the arbitrary waveform generator.

With this we can reach trap depths from $U_0 = 130 \text{ nK}$ to $530 \mu\text{K}$, corresponding to trapping frequencies of $\omega/2\pi = \{4; 6; 50\} \text{ Hz}$ to $\{1.3; 1.9; 2.2\} \text{ kHz}$ in $\{x; y; z\}$ direction.

C. Magnetic-field control

The coil setup creating the magnetic fields consists of three Helmholtz pairs oriented along the coordinate system in Fig. 1(b) and the main coil pair along the y axis. The former are used to define the quantization axes during state preparation and imaging as well as for compensating stray magnetic fields ($|B_{x,y,z}| \leq 1 \text{ G}$) during cooling and trapping. The stabilization electronics allow for two different operation modes. In presence of the MOT and Feshbach magnetic fields the system is stabilizing the current, utilizing current transducers [LEM CASR 15-NP]. During the state preparation the magnetic fields are directly stabilized using a three-axis flux-gate sensor [Bartington MAG-03IE1000] with a measurement range of $\pm 10 \text{ G}$ mounted close to the vacuum chamber giving us a short-term stability of $\sigma_{[x,y,z]}(\tau) = \{3.9; 2.2; 1.4\} \times 10^{-5} \text{ G}$ at $\tau = 1 \text{ s}$ and $B_{x,y,z} = 1 \text{ G}$.

The main coils can be operated in Helmholtz and anti-Helmholtz configuration providing the homogeneous magnetic field for tuning the interaction strength during evaporation and the gradient magnetic fields [49] in the laser cooling stages. To switch between these configurations a home-built H bridge, based on metal-oxide-semiconductor field-effect transistors [IXYS 747-IXFN170N65X2] with a low drain-source on-resistance of $13 \text{ m}\Omega$, is used. The coils are driven in series by one power supply [EA-PSI 9200-25] with a maximum voltage of 200 V limiting the current to 11.1 A due to the coils' internal resistance (18Ω). For current stabilization the power supply's internal stabilization loop is used stating a current stability of $<0.15\%$.

For characterizing the applied magnetic field at the position of the atoms we perform an initial estimation using a Biot-Savart model of our setup. Subsequently, we determine the coil current needed for several Feshbach resonances by observing the related enhancement of atom losses [50,51]. By comparing the corresponding field estimates to the literature values of the resonances we identified the six resonances expected [41,52] (Table I) in our setup for a mixture of $|F = 1, m_F = -1\rangle$ and $|F = 1, m_F = 0\rangle$ at $15 \mu\text{K}$ be-

low 200 G. Ultimately, the coil currents and magnetic-field literature values are used for the final calibration yielding 41.2 G/A with a maximum magnetic-field strength of 450 G and an accuracy of 0.2 G/A.

III. QUANTUM GAS PRODUCTION

A. Loading sequence

Our dipole trap loading scheme [Fig. 2(a)] comprises three steps. Initially, we load 1×10^9 atoms in a three-dimensional MOT within 4 s from a beam formed by a two-dimensional (2D) MOT. Afterwards we switch off the D_2 cooling light and simultaneously turn on the D_1 cooling light field, thus enabling a D_1 gray molasses dipole trap loading scheme, which is particularly robust against ac Stark shifts, as induced by the ODT [53]: By ramping up the magnetic-field gradient from 4 to 15 G/cm and the D_2 repumping light down to $0.25I_{\text{sat}}$ we perform a hybrid $D_1 - D_2$ compressed MOT, to increase the density and simultaneously cool the ensemble to below $200 \mu\text{K}$ within 16 ms. We then switch off the remaining D_2 repumping light and the magnetic-field gradient to perform gray molasses cooling with a D_1 cooling to repumping ratio of 3:1, ramping the cooling (repumping) intensity per beam from $4I_{\text{sat}}$ ($1.3I_{\text{sat}}$) to $0.28I_{\text{sat}}$ ($0.09I_{\text{sat}}$). The ramp length is optimized experimentally to take the decay time of the magnetic gradient field into account. The coldest ensembles are realized for a total ramp length of 40 ms. In free space, i.e., in absence of the ODT, our cooling sequence yields a final temperature of $7 \mu\text{K}$.

For loading the ODT we maximize the number of atoms trapped by adjusting the beam balancing and magnetic offset fields, thus optimizing the overlap at the expense of the final temperature which then yields $12 \mu\text{K}$. We find the optimal loading parameters of the ODT by trading off trap depth U_0 and trap volume. Assuming an initial cloud of N_0 atoms with Gaussian density distribution $D_G(x)$ of width σ and energy distribution

$$W(E) = \frac{1}{\pi E k_B T} e^{-\frac{E}{k_B T}}, \quad (1)$$

the ratio of atoms loaded can be estimated for the one-dimensional case by [54]

$$p_N = \frac{1}{N_0} \int_0^{U_0} \int_{-s_0}^{s_0} D_G(x) W(E) dx dE, \quad (2)$$

with the spatial limits $s_0 = \sqrt{\frac{\omega^2}{2} \ln(\frac{U_0}{E})}$. Primarily, p_N depends on the ratio of trap depth to temperature $U_0/k_B T$ and the width of the trap compared to the atomic ensemble ω/σ . Thus, at constant optical power increasing the CPM amplitude and accordingly the width ω increases the number of atoms trapped, until the trap becomes too shallow and the number of atoms decreases. With the optical dipole trap already turned on at the maximum available power during the MOT loading and cooling sequence we load a maximum of 12×10^6 atoms into the trap at a CPM amplitude of $160 \mu\text{m}$. This corresponds to a transfer efficiency of 2%, with 3×10^6 atoms positioned in the beams' crossing region. At this stage we are limited by the trap's depth of $54 \mu\text{K}$ resulting in a final temperature of

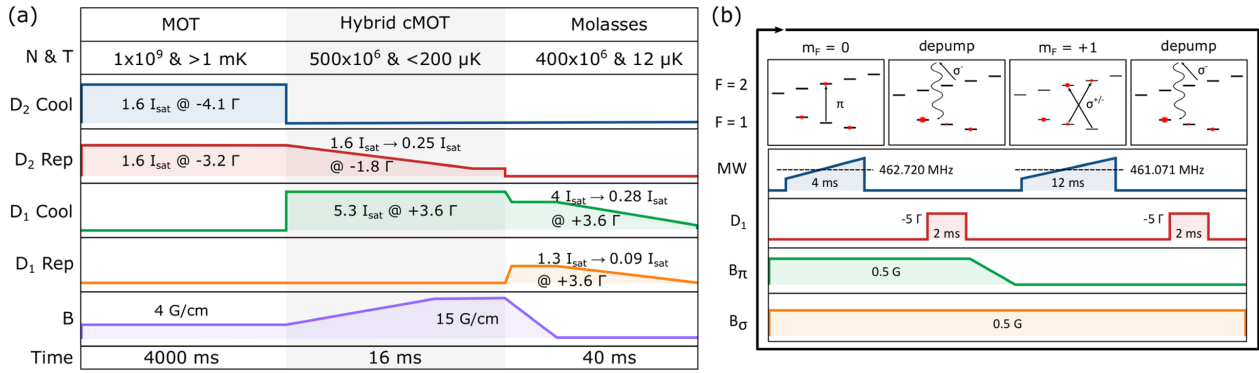


FIG. 2. (a) Loading scheme of the optical dipole trap: We initially load a MOT on the D_2 line from a two-dimensional MOT. Afterwards we use a hybrid $D_1 - D_2$ compressed MOT to increase the peak density while cooling the ensemble simultaneously. Subsequently sub-Doppler temperatures of $12 \mu\text{K}$ are achieved by D_1 gray molasses cooling. All stated intensities refer to one beam, respectively. This scheme allows us to directly load the ODT, without the need for magnetic trapping as an intermediate step. (b) State preparation loop within the optical dipole trap: A combination of microwave adiabatic rapid passages and optical pumping is used to shift the population towards $m_F = -1$, starting from an equally populated mixture in $F = 1$. A blow-away sequence is added at the end to increase the purity of the ensemble. After four loops, each 70 ms long, we reach an almost pure ensemble ($> 98\%$) with a temperature increase of $0.3 \mu\text{K}$ per loop, as determined via time-of-flight measurements.

the trapped atoms of $8.5 \mu\text{K}$, determined via a time-of-flight measurement after 100 ms of rethermalization time.

B. State preparation

Upon loading the dipole trap we depump the atomic ensemble into $|F = 1\rangle$ by shining in 1 mW of D_1 cooling light with a detuning of -1Γ via the detection optics, thus creating an equidistributed m_F mixture. To generate a spin-polarized ensemble in $|F = 1, m_F = -1\rangle$, we adapt a multiloop state preparation scheme [55] combining optical pumping on the D_1 line with coherent transfers [Fig. 2(b)]. While the original publication makes use of optical Raman pulses, we utilize microwave adiabatic rapid passages driven by a Yagi-Uda-type directed antenna. In order to use a minimal number of loops in the final sequence we experimentally optimize each step towards the highest transfer efficiency.

We initially apply a quantization field of 0.7 G at an angle of 45° to the antenna's Poynting vector oriented in the horizontal plane. This allows us to transfer the population of $|F = 1, m_F = 0\rangle$ to $|F = 2, m_F = 0\rangle$ by driving a π transition sweeping the microwave from 461.710 to 461.730 MHz within 4 ms. We subsequently apply σ^- -polarized D_1 cooling light via the detection optics with a detuning of -5Γ for 2 ms in order to depump the atoms into $|F = 1\rangle$ via spontaneous emission, hence populating $|F = 1, m_F = 0\rangle$ and $|F = 1, m_F = -1\rangle$. Due to the mismatch of quantization field axis and detection beam orientation by 14° we also drive the $|F = 2, m_F = -2\rangle \rightarrow |F' = 2, m_F = -2\rangle$ transition, thus preventing accumulation in $|F = 2, m_F = -2\rangle$. We then rotate the magnetic-field axis to be parallel to the antenna's Poynting vector by tuning the vertical field component to zero, effectively resulting in a quantization field in the horizontal plane of 0.5 G. In this configuration we are able to drive a σ -polarized microwave adiabatic rapid passage. Sweeping from 462.062 to 462.080 MHz in 12 ms we transfer

atoms from $|F = 1, m_F = +1\rangle$ to $|F = 2, m_F = 0\rangle$. Due to the symmetry of the level structure the same microwave pulse also drives the unwanted transition from $|F = 1, m_F = 0\rangle$ to $|F = 2, m_F = -1\rangle$. However, since $|F = 1, m_F = 0\rangle$ has already been addressed with the first pulse fewer atoms are available for undesired transitions. We afterwards apply the same optical depumping pulse as before, thus transferring the atoms back into $|F = 1\rangle$. While this sequence does not yield a pure magnetic substate, it shifts the m_F distribution towards $m_F = -1$. Repeating the sequence multiple times allows us to accumulate atoms in $|F = 1, m_F = -1\rangle$. As a final step, we purify the ensemble by a blow-away sequence: We apply the same microwave pulses as before but tune the D_1 cooling laser closer to resonance (-1Γ) to purposely heat atoms out of the trap during optical pumping.

We find the necessary number of loops by optimizing towards the highest atom number in the BEC for a given evaporation ramp, observing no beneficial effects for more than four loops as described. In this configuration we reach an almost pure ensemble ($> 98\%$ in $|F = 1, m_F = -1\rangle$) with 70% of the initial atoms remaining in the trap. To determine the heating from optical pumping we perform a time-of-flight measurement out of the ODT before the state preparation sequence and after each loop. Since the D_1 line does not feature closed transitions, with $0.3 \mu\text{K}$ per loop the observed heating is minimal and yields a final temperature of $9.6 \mu\text{K}$.

C. Feshbach resonances and evaporation

To address Feshbach resonances we generate homogeneous magnetic fields by switching the MOT magnetic-field coils from anti-Helmholtz to Helmholtz configuration. We then ramp up the magnetic field to the desired value in 100 ms. The corresponding scattering length close to the resonances can be calculated using the background scattering length a_{BG} ,

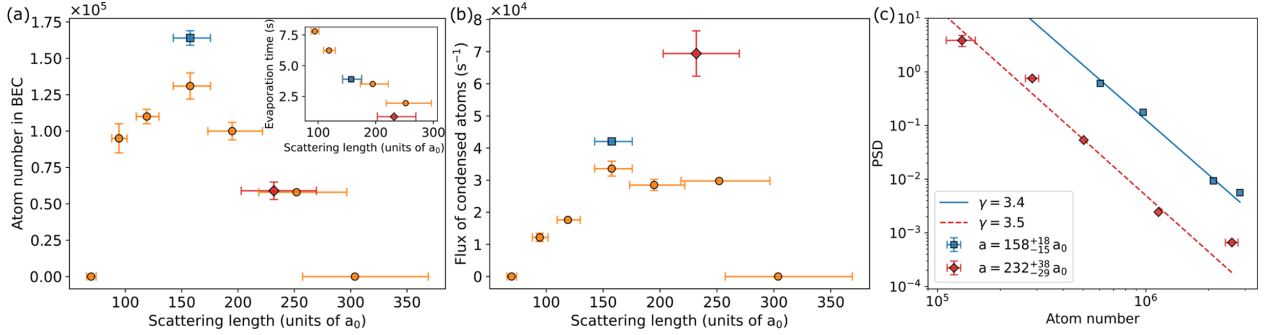


FIG. 3. (a) BEC size and time dependency with respect to scattering length: The orange circles show the results, when a given evaporation ramp is rescaled towards the highest atom number in the BEC at a given scattering length. For a free optimization, including all variables described in the Sec. III C, the largest fully condensed BEC is realized at a scattering length of $158a_0$ (blue square). For lower and higher scattering lengths the final atom number is reduced. The inlay shows the time needed for evaporating. For higher scattering lengths the higher elastic collision rates allow for faster evaporation resulting in a smaller time constant. The fastest BEC is realized at a scattering length of $232a_0$ (red diamond) with a total evaporation time of 850 ms. The error bars for the scattering length are determined via error propagation using Eq. (3) and the magnetic-field accuracy stated in Sec. II C. (b) Flux of the evaporative cooling against scattering length: The highest flux is achieved for the fastest evaporation ramp at a scattering length of $232a_0$. The error bars for the flux are derived via error propagation using the uncertainty in atom number, resulting in larger values for shorter evaporation times. (c) Phase-space density trajectory for largest BEC and highest flux: For the evaporation efficiency γ only the data points on the ramp and not the starting point are taken into account. We find equal efficiency for both cases but deteriorated initial conditions at $232a_0$, due to the magnetic field spending an extended time at the resonance resulting in additional heating.

the resonance widths Δ_i , and its center B_{0i} [41,56]:

$$a(B) = a_{\text{BG}} \left(1 - \sum_i \frac{\Delta_i}{B - B_{0i}} \right). \quad (3)$$

Once a stable final magnetic field and thus atomic scattering length is established we use the dipole trap's intensity stabilization in combination with the AOM to piecewise decrease the trap power in five linear ramps. In parallel, the center-position modulation is ramped down and reaches zero with the final ramp at the end of the evaporation sequence. The initial center-position modulation amplitude is determined by the optimal mode match for trap loading. We optimize each step with respect to the final atom number in the BEC by tuning the intensity reduction, the CPM amplitude reduction, and the ramp lengths as free parameters.

IV. EXPERIMENTAL RESULTS

We systematically optimize BEC production for different scattering lengths [Fig. 3(a)]. Initially, we optimize the ramp itself. In accordance with Ref. [24] we find our evaporation sequence to be most efficient using an exponential reduction for the trap power jointly with a linear reduction slope for the center-position modulation amplitude, as this allows us to counteract the reduction in trap frequency from the power reduction.

We achieve a fully condensed BEC of 1.3×10^5 atoms at a scattering length of $158a_0$ after evaporating over the course of 3.9 s. Contrary to findings in Ref. [18], where dynamical tuning, i.e., starting at a lower scattering length and subsequently increasing it, counteracted light-assisted collisions caused by a multimode fiber laser at 1070 nm, we do not observe similar beneficial effects with respect to the final atom number in the BEC. This behavior qualitatively agrees with experiments

demonstrating the absence of light-induced collisions at larger trap wavelengths, e.g., 1550 nm in Ref. [42]. To analyze the scaling behavior with respect to scattering length, we additionally optimize the BEC size at lower and higher scattering length, by rescaling the overall length of evaporation ramp while maintaining its shape (Fig. 3, orange circles). At a lower scattering length the time needed for evaporation is increased, since the evaporation rate Γ_{ev} scales with the scattering length squared [57]

$$\Gamma_{\text{ev}} = 4\pi a^2 n_0 \bar{v} \eta e^{-\eta}, \quad (4)$$

thus stretching the length of the overall sequence. Additionally, the final atom number is reduced due to the trapped atoms' lifetime of 15 s. At scattering lengths $\leq 75a_0$ this effect becomes dominant and we are unable to reach condensation. For scattering lengths $> 158a_0$ we also find a reduced final atom number, which we explain by the enhancement of the three-body loss rate $\Gamma_{3\text{B}}$, scaling with the scattering length to the power of 4 [50]:

$$\Gamma_{3\text{B}} = \frac{K_3}{N} \int n^3 d^3 r \quad \text{with} \quad K_3 = n_l C(a) \frac{\hbar}{m} a^4. \quad (5)$$

However, the higher evaporation rate now allows one to significantly reduce the time needed for evaporation. We experimentally find a limit for this tradeoff at $> 300a_0$ where the three-body losses become dominant and inhibit Bose-Einstein condensation. Based on the initial findings we individually alter the relative length of the five linear ramps towards the globally largest BEC size (Fig. 3, blue square) and the largest BEC size at the shortest evaporation time possible (Fig. 3, red diamond). Realizing the best ratio of desired to undesired losses, we find a maximum atom number of 1.6×10^5 in the BEC at $158a_0$, close to the initial configuration and with the same total ramp length. Our fastest evaporation is performed within 850 ms at a scattering length of $232a_0$ yielding a fully

condensed BEC of 5.8×10^4 atoms. Compared to the trajectory at $158a_0$ this corresponds to a reduction in evaporation time by a factor of 5 while approximately doubling the evaporation flux, which we define as final atom number in the condensate over evaporation time [Fig. 3(b)].

For the phase-space density ρ , measured after each linear ramp, we find the evaporation efficiency $\gamma = -\frac{d \ln(\rho)}{d \ln(N)}$ to be the same for both cases due to the individual optimization [Fig. 3(c)], but with worse initial conditions at $232a_0$.

V. DISCUSSION

A. Current limitations

Currently, our experiment is limited by three effects: Thermal lensing in the ODT, the stability of the Feshbach fields, and worse initial conditions for higher scattering lengths. Thermal lensing is a common problem for setups operating laser beams at higher power. The effects of all-optical elements involved have been discussed, concluding that the dominant contribution originates from the TeO_2 crystal used in AOMs [58]. Operating a laser at 1960-nm wavelength, the problem is further amplified, as most of our optics need to be custom made and typically are subject to higher absorption compared to components for standard wavelengths, e.g., at 1560 or 1064 nm (see Sec. II B). To quantify the effect, we displace the secondary dipole trap beam, realizing two parallel, tilt-free single beam traps. Measuring the center position of the trapped atoms at different points of the evaporation sequence, we observe a focus drift of up to $200 \mu\text{m}$ ($450 \mu\text{m}$) for the primary (secondary) beam. From the experimental optimization we find the ramps at higher scattering length and shorter time scales to be more sensitive regarding deviations from the optimal evaporation trajectory. Thus, the reduction in control of the trap parameters from thermal lensing, together with the magnetic-field instability, as outlined in Sec. II C, imposes an upper limit on the scattering length that can be used effectively in our setup.

Additionally, we observe deteriorating initial conditions when operating closer to the resonance, thus limiting the final atom number in the BEC. When ramping to the desired magnetic-field value after loading the ODT, we sweep across the resonance and hence induce a loss of atoms and heating. For higher scattering lengths the required magnetic-field values are positioned closer to the resonance and the resulting slower sweeps in its direct vicinity amplify the deteriorating effects described above. In the explicit case of the trajectory at $232a_0$ for the $1-\sigma$ band of our magnetic-field estimate there is a five times longer overlap with the resonance compared to the trajectory at $158a_0$. As a result, the initial phase-space density is reduced by an order of magnitude.

B. Performance comparison

State-of-the-art atomic sources generate an evaporation flux of $\geq 2 \times 10^5 \text{ s}^{-1}$ with total experimental cycle times at the order of $\approx 1 \text{ s}$ for atom interferometry applications utilizing ^{87}Rb [7]. Using ^{39}K a comparable evaporation flux of $2.4 \times 10^5 \text{ s}^{-1}$ has been demonstrated in a hybrid setup with a magnetic trap as intermediate step, requiring a magnetic-field gradient of 270 G/cm and an experimental cycle time of 15 s

due to magnetic transport [18]. All-optical cooling allows for shorter cycle times and a simplified apparatus with respect to the generation of magnetic fields. In our setup, the current density necessary for generating 1-G/cm gradient in anti-Helmholtz configuration generates $\approx 20 \text{ G}$ when switched to Helmholtz configuration, thus putting the low-field Feshbach resonances in ^{39}K readily in reach with standard quadrupole field coils as used for laser cooling. For a similar all-optical setup an experimental cycle time of 7 s has previously been reported and yielded an evaporation flux of $\approx 1 \times 10^4 \text{ s}^{-1}$ with a final atom number of 2×10^4 in the pure condensate [42]. At $232a_0$ ($158a_0$) we realize an evaporation flux of $6.8 \times 10^4 \text{ s}^{-1}$ ($4.1 \times 10^4 \text{ s}^{-1}$) improving on this result by a factor of ≈ 7 (≈ 4). Accordingly, our final atom number of 5.8×10^4 (1.6×10^5) corresponds to an improvement by a factor of ≈ 3 (≈ 8). To this end our repetition rate is limited by the MOT loading and the data transfer after detection, resulting in a comparable cycle time of 6 s (9 s).

VI. OUTLOOK

A. Further enhancement of atomic flux

To achieve results comparable to ^{87}Rb chip traps, the experimental cycle time and the evaporative flux need further enhancement. By using more sophisticated loading techniques such as a high-flux 2D^+ -MOT design [18,59] or even cryogenic buffer-gas beam sources [60], we expect to reduce the MOT loading time to below 1 s, theoretically enabling cycle times of $\approx 2 \text{ s}$. Similarly, an upgraded ODT setup would allow us to trap more atoms by using a higher beam power together with a larger center-position modulation amplitude, extending the crossing region over the whole molasses without further reducing the trap depth. Additionally, by altering the trapping beam's path such that the gray molasses can be used in free-space configuration the temperature during loading could be improved by a factor of 2. Regarding the deteriorated phase-space density caused by the sweep time of the magnetic fields, possible mitigation strategies include the use of dedicated fast control loops or initially sweeping to a higher field value, allowing us to cross the Feshbach resonance with the same sweep rate irrespective of the final scattering length.

To explore the theoretical limits of our existing setup we perform additional simulations without the current limitations as identified in Sec. V A. We follow the model described in Ref. [24], incorporating Eqs. (4) and (5). The optical potential is generated by two identical beams with 8-W initial power, a vertical waist of $50 \mu\text{m}$, a horizontal waist of $28 \mu\text{m}$, and ideally overlapping foci. We assume 3×10^6 atoms to be trapped in the crossing region initially with a temperature of $10 \mu\text{K}$. Evaporation trajectories are defined by an exponential power and linear CPM amplitude reduction and simulated for a given scattering length on a two-dimensional grid given by evaporation time and final beam power. The simulation is aborted once a BEC fraction $> 90\%$ is estimated using

$$\frac{N_c}{N} = 1 - \left(\frac{T}{T_c} \right)^3 \quad (6)$$

and final atom number and evaporation time are adjusted accordingly. Similar to the experiment we analyze the results

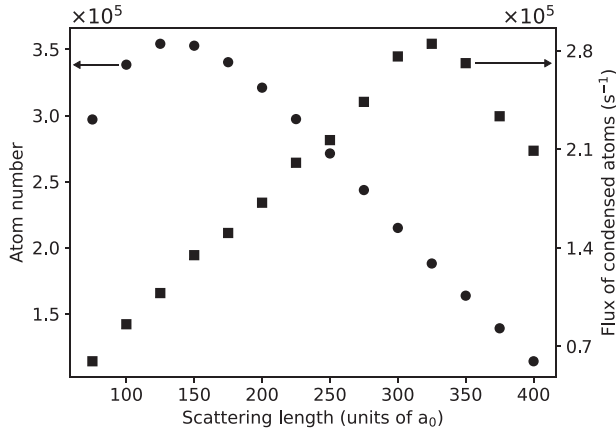


FIG. 4. Extrapolated performance, simulated for ideal experimental conditions: For each data point 2000 evaporation trajectories are evaluated. Similar to the experimental optimization, the results for the trajectory yielding the highest final atom number are depicted. Qualitatively, we find the same behavior as observed in the experiment with improved numbers.

with the highest evaporation efficiency (Fig. 4). The simulation results in a peak atom number of 3.5×10^5 at $125a_0$ after 3.5 s of evaporative cooling. Towards higher scattering lengths the final atom number declines due to the reduced ratio of desired to undesired losses, necessitating additional evaporative cooling. A peak flux of $2.3 \times 10^5 \text{ s}^{-1}$ is simulated at $325a_0$, allowing for a final atom number of 1.5×10^5 after 640 ms. Under optimal conditions we thus expect the extrapolated flux to be competitive with results achieved in hybrid traps [18]. While resolving each of the identified limitations comes with its own technological challenges, our findings indicate the potential of the discussed techniques to realize a ^{39}K optical dipole trap on par with the current performance of ^{87}Rb chip traps.

Since the increase of evaporation flux in the BEC only depends on the accessibility of sufficiently broad Feshbach resonances this scheme could also be utilized for different elements. Potentially useful Feshbach resonances are found for ^{87}Rb (at $\approx 1007 \text{ G}$ with $\Delta = 0.17 \text{ G}$) [61], ^{85}Rb (at $\approx 155 \text{ G}$ with $\Delta = 11.6 \text{ G}$) [62], and ^{23}Na (at $\approx 90 \text{ G}$ with $\Delta = 1 \text{ G}$) [63], but are subject to individual challenges regarding their width and absolute field magnitude.

B. Application to atom interferometry

To apply our methods to atom interferometry a magnetically insensitive population in $m_F = 0$ is desired, requiring a state transfer either before or after evaporation. If the atoms are already prepared in $m_F = 0$, evaporation can be performed in the vicinity of the low-field resonance at 59.3 G (Fig. 5). A suitable multiloop preparation scheme has been demonstrated in Ref. [55] and yields comparable results regarding the final purity of the ensemble and the number of required loops. So far, direct evaporative cooling in $m_F = 0$ has been shown on the broad resonance at 471 G, with a final atom number in the BEC comparable to the results achieved in $m_F = -1$ [18]. However, due to the narrower shape of the resonance at 59.3

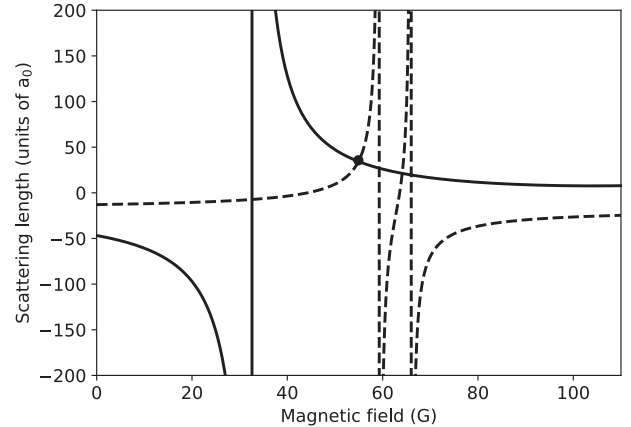


FIG. 5. Modeling of the scattering length with respect to magnetic field: Low-field Feshbach resonances with parameters from Ref. [52] for $|1, -1\rangle + |1, -1\rangle$ (solid line) and $|1, 0\rangle + |1, 0\rangle$ (dashed line), according to Eq. (3). At 54.9 G both resonances share the same scattering length (dot), allowing us to easily transfer a BEC via radio-frequency adiabatic rapid passages between both states.

G a magnetic field of 58.56 G with an instability below 20 mG is needed in order to achieve the same scattering length stability as in our present experiment. This corresponds to an improvement by a factor of 5, potentially requiring substantial changes to the coil and control setup. Moreover, the associated three-body loss coefficient has experimentally been found to be an order of magnitude larger than the one belonging to $m_F = -1$ at 32.6 G, thus rendering efficient evaporation unlikely [64,65].

Alternatively, the atoms can be transferred to $m_F = 0$ via a radio-frequency adiabatic rapid passage after producing the BEC in $m_F = -1$, a technique, which is commonly used for producing quantum droplets [64,65]. Starting from the magnetic-field values used in our experiment, a direct transfer would result in an atomic interaction quench to a lower value (Fig. 5), leading to unwanted density fluctuations [66]. Instead, for upcoming experiments we plan to sweep the magnetic field to 54.9 G where both m_F states share the same scattering length, allowing us to transfer the atoms with a radio-frequency sweep at $\approx 40 \text{ MHz}$.

We envisage applications of our source in atom interferometry for inertial sensing. On one hand, supporting high-fidelity beam splitting and exquisite control of systematic effects high-flux BEC sources are of direct interest in free falling light-pulse atom interferometry [67,68]. In addition, BECs offer routes to create entanglement via one-axis twisting dynamics [69] or delta-kick squeezing techniques [70] and routes to transfer spin squeezing to momentum states have been demonstrated [71]. For the specific case of ^{39}K , one approach to circumvent the BEC's inherent instability in absence of Feshbach magnetic fields during the interferometer is to exploit ballistic expansion with subsequent matter-wave lensing [11,26,72] to operate at low densities. On the other hand, applications in trapped interferometry using optical guiding potentials will benefit from tunable interactions [73,74], e.g., to mitigate phase diffusion due to collisions. Compared to free

falling interferometry, here an additional challenge is imposed by the necessity to operate at a constant Feshbach field. To this end, even with the low-field resonances present in ^{39}K , special care needs to be taken to avoid magnetic-field gradients and curvature, e.g., by careful design and the use of trimming coils. Likewise, the use of magnetic shields may pose challenges regarding their compatibility with regular switching of large magnetic fields in their proximity but could be mitigated by active magnetic-field control over the comparably small volume of interest of a few cubic millimeters. Recently a guided ^{39}K multiloop atom interferometer has been demonstrated near the resonance at 562 G [74]. Despite the presence of an additional axial magnetic potential with trapping frequencies of 2.8 Hz originating from the Helmholtz coils, an interrogation time on the order of milliseconds was achieved. These results pose a promising step towards using resonances at lower field values where the field curvature can be reduced and an enhanced interrogation time can be expected.

VII. CONCLUSION

We have demonstrated an all-optical high flux source of ^{39}K BECs. By altering the scattering length via a low-field Feshbach resonance, the evaporation sequence can be individually optimized towards either atom number in the condensate or evaporation flux. In combination with using time-averaged optical potentials our technique allows us to improve on results previously achieved with all-optical setups in either atom number by a factor of 8 or evaporation flux by a factor of 7.

Therefore, our source's performance is comparable to other high-flux sources using ^{87}Rb [23] or ^{174}Yb [24]. We envisage applications in the field of atom interferometry, where measurements are ultimately bound by quantum projection noise. Here, its Feshbach resonances position ^{39}K in an interesting spot regarding the possibilities to mitigate systematic effects and dephasing due to collisional shifts at comparably low fields.

ACKNOWLEDGMENTS

We are indebted to Ernst Rasel for inspiring discussions on the general scope of the project and Torben Schulze for fruitful input on the use of potassium Feshbach resonances in our experiment. We thank Carsten Klempert for discussions on the application of our method to other species and Torben Schulze, Ludwig Mathey, Christian Schubert, and Naceur Gaaloul for constructive comments on our paper. This work is funded by the Federal Ministry of Education and Research through the funding program Photonics Research Germany under Contract No. 13N14875. The authors further acknowledge support by the German Space Agency (DLR) with funds provided by the Federal Ministry for Economic Affairs and Climate Action due to an enactment of the German Bundestag under Grant No. DLR 50WM2041 (PRIMUS-IV) and by the Deutsche Forschungsgemeinschaft (DFG, German Research Foundation) under Project-ID 274200144-SFB 1227 (Project No. B07) and under Germany's Excellence Strategy - EXC-2123 QuantumFrontiers - 390837967.

- [1] M. Anderson, J. Ensher, M. Matthews, C. Wieman, and E. Cornell, *Science* **269**, 198 (1995).
- [2] K. B. Davis, M.-O. Mewes, M. A. Joffe, M. R. Andrews, and W. Ketterle, *Phys. Rev. Lett.* **74**, 5202 (1995).
- [3] I. Bloch, J. Dalibard, and W. Zwerger, *Rev. Mod. Phys.* **80**, 885 (2008).
- [4] T. D. Ladd, F. Jelezko, R. Laflamme, Y. Nakamura, C. Monroe, and J. L. O'Brien, *Nature (London)* **464**, 45 (2010).
- [5] I. Bloch, J. Dalibard, and S. Nascimbène, *Nat. Phys.* **8**, 267 (2012).
- [6] M. Gebbe, J.-N. Siemß, M. Gersemann, H. Müntinga, S. Herrmann, C. Lämmerzahl, H. Ahlers, N. Gaaloul, C. Schubert, K. Hammerer, S. Abend, and E. M. Rasel, *Nat. Commun.* **12**, 2544 (2021).
- [7] J. Rudolph, W. Herr, C. Grzeschik, T. Sternke, A. Grote, M. Popp, D. Becker, H. Müntinga, H. Ahlers, A. Peters, C. Lämmerzahl, K. Sengstock, N. Gaaloul, W. Ertmer, and E. M. Rasel, *New J. Phys.* **17**, 065001 (2015).
- [8] D. M. Farkas, K. M. Hudek, E. A. Salim, S. R. Segal, M. B. Squires, and D. Z. Anderson, *Appl. Phys. Lett.* **96**, 093102 (2010).
- [9] H. Müntinga, H. Ahlers, M. Krutzik, A. Wenzlawski, S. Arnold, D. Becker, K. Bongs, H. Dittus, H. Duncker, N. Gaaloul, C. Gherasim, E. Giese, C. Grzeschik, T. W. Hänsch, O. Hellmig, W. Herr, S. Herrmann, E. Kajari, S. Kleinert, C. Lämmerzahl *et al.*, *Phys. Rev. Lett.* **110**, 093602 (2013).
- [10] M. D. Lachmann, H. Ahlers, D. Becker, A. N. Dinkelaker, J. Grosse, O. Hellmig, H. Müntinga, V. Schkolnik, S. T. Seidel, T. Wendrich, A. Wenzlawski, B. Carrick, N. Gaaloul, D. Lüdtke, C. Braxmaier, W. Ertmer, M. Krutzik, C. Lämmerzahl, A. Peters, W. P. Schleich *et al.*, *Nat. Commun.* **12**, 1317 (2021).
- [11] C. Deppner, W. Herr, M. Cornelius, P. Stromberger, T. Sternke, C. Grzeschik, A. Grote, J. Rudolph, S. Herrmann, M. Krutzik, A. Wenzlawski, R. Corgier, E. Charron, D. Guéry-Odelin, N. Gaaloul, C. Lämmerzahl, A. Peters, P. Windpassinger, and E. M. Rasel, *Phys. Rev. Lett.* **127**, 100401 (2021).
- [12] D. Becker, M. D. Lachmann, S. T. Seidel, H. Ahlers, A. N. Dinkelaker, J. Grosse, O. Hellmig, H. Müntinga, V. Schkolnik, T. Wendrich, A. Wenzlawski, B. Weps, R. Corgier, T. Franz, N. Gaaloul, W. Herr, D. Lüdtke, M. Popp, S. Amri, H. Duncker *et al.*, *Nature (London)* **562**, 391 (2018).
- [13] D. C. Aveline, J. R. Williams, E. R. Elliott, C. Dutenhoffer, J. R. Kellogg, J. M. Kohel, N. E. Lay, K. Oudrhiri, R. F. Shotwell, N. Yu, and R. J. Thompson, *Nature (London)* **582**, 193 (2020).
- [14] K. Frye, S. Abend, W. Bartosch, A. Bawamia, D. Becker, H. Blume, C. Braxmaier, S.-W. Chiow, M. A. Efremov, W. Ertmer, P. Fierlinger, T. Franz, N. Gaaloul, J. Grosse, C. Grzeschik, O. Hellmig, V. A. Henderson, W. Herr, U. Israelsson, J. Kohel *et al.*, *EPJ Quantum Technol.* **8**, 1 (2021).
- [15] P. Haslinger, M. Jaffe, V. Xu, O. Schwartz, M. Sonnleitner, M. Ritsch-Marte, H. Ritsch, and H. Müller, *Nat. Phys.* **14**, 257 (2018).

[16] M. D. Barrett, J. A. Sauer, and M. S. Chapman, *Phys. Rev. Lett.* **87**, 010404 (2001).

[17] J.-F. Clément, J.-P. Brantut, M. Robert-de Saint-Vincent, R. A. Nyman, A. Aspect, T. Bourdel, and P. Bouyer, *Phys. Rev. A* **79**, 061406(R) (2009).

[18] M. Landini, S. Roy, G. Roati, A. Simoni, M. Inguscio, G. Modugno, and M. Fattori, *Phys. Rev. A* **86**, 033421 (2012).

[19] S. Stellmer, R. Grimm, and F. Schreck, *Phys. Rev. A* **87**, 013611 (2013).

[20] S. Kulas, C. Vogt, A. Resch, J. Hartwig, S. Ganske, J. Matthias, D. Schlippert, T. Wendrich, W. Ertmer, E. M. Rasel, M. Damjanic, P. Weßels, A. Kohfeldt, E. Luvsandamdin, M. Schiemangk, C. Grzeschik, M. Krutzik, A. Wicht, A. Peters, S. Herrmann *et al.*, *Microgravity Science and Technology* **29**, 37 (2016).

[21] C. Vogt, M. Woltmann, S. Herrmann, C. Lämmerzahl, H. Albers, D. Schlippert, and E. M. Rasel, *Phys. Rev. A* **101**, 013634 (2020).

[22] K. M. O'Hara, M. E. Gehm, S. R. Granade, and J. E. Thomas, *Phys. Rev. A* **64**, 051403(R) (2001).

[23] T. Kinoshita, T. Wenger, and D. S. Weiss, *Phys. Rev. A* **71**, 011602(R) (2005).

[24] R. Roy, A. Green, R. Bowler, and S. Gupta, *Phys. Rev. A* **93**, 043403 (2016).

[25] G. Condon, M. Rabault, B. Barrett, L. Chichet, R. Arguel, H. Eneriz-Imaz, D. Naik, A. Bertoldi, B. Battelier, P. Bouyer, and A. Landragin, *Phys. Rev. Lett.* **123**, 240402 (2019).

[26] H. Albers, R. Corgier, A. Herbst, A. Rajagopalan, C. Schubert, C. Vogt, M. Woltmann, C. Lämmerzahl, S. Herrmann, E. Charron, W. Ertmer, E. M. Rasel, N. Gaaloul, and D. Schlippert, *Commun. Phys.* **5**, 60 (2022).

[27] S. Inouye, M. R. Andrews, J. Stenger, H.-J. Miesner, D. M. Stamper-Kurn, and W. Ketterle, *Nature (London)* **392**, 151 (1998).

[28] C. Chin, R. Grimm, P. Julienne, and E. Tiesinga, *Rev. Mod. Phys.* **82**, 1225 (2010).

[29] C. A. Regal, C. Ticknor, J. L. Bohn, and D. S. Jin, *Nature (London)* **424**, 47 (2003).

[30] J. Cubizolles, T. Bourdel, S. J. J. M. F. Kokkelmans, G. V. Shlyapnikov, and C. Salomon, *Phys. Rev. Lett.* **91**, 240401 (2003).

[31] S. Jochim, M. Bartenstein, A. Altmeyer, G. Hendl, S. Riedl, C. Chin, J. H. Denschlag, and R. Grimm, *Science* **302**, 2101 (2003).

[32] M. W. Zwierlein, C. A. Stan, C. H. Schunck, S. M. F. Raupach, S. Gupta, Z. Hadzibabic, and W. Ketterle, *Phys. Rev. Lett.* **91**, 250401 (2003).

[33] M. Greiner, C. A. Regal, and D. S. Jin, *Nature (London)* **426**, 537 (2003).

[34] G. Roati, M. Zaccanti, C. D'Errico, J. Catani, M. Modugno, A. Simoni, M. Inguscio, and G. Modugno, *Phys. Rev. Lett.* **99**, 010403 (2007).

[35] R. L. D. Campbell, R. P. Smith, N. Tammuz, S. Beattie, S. Moulder, and Z. Hadzibabic, *Phys. Rev. A* **82**, 063611 (2010).

[36] K. K. Voges, P. Gersema, M. Meyer zum Alten Borglooh, T. A. Schulze, T. Hartmann, A. Zenesini, and S. Ospelkaus, *Phys. Rev. Lett.* **125**, 083401 (2020).

[37] Z. Zhang, L. Chen, K.-X. Yao, and C. Chin, *Nature (London)* **592**, 708 (2021).

[38] C. Eigen, J. A. P. Glidden, R. Lopes, E. A. Cornell, R. P. Smith, and Z. Hadzibabic, *Nature (London)* **563**, 221 (2018).

[39] L. Mathey, E. Tiesinga, P. S. Julienne, and C. W. Clark, *Phys. Rev. A* **80**, 030702(R) (2009).

[40] S. Peng, H. Liu, J. Li, and L. Luo, Cooling a Fermi gas with three-body recombination near a narrow Feshbach resonance, *arXiv:2107.07078* (2021).

[41] C. D'Errico, M. Zaccanti, M. Fattori, G. Roati, M. Inguscio, G. Modugno, and A. Simoni, *New J. Phys.* **9**, 223 (2007).

[42] G. Salomon, L. Fouché, S. Lepoutre, A. Aspect, and T. Bourdel, *Phys. Rev. A* **90**, 033405 (2014).

[43] D. Schlippert, J. Hartwig, H. Albers, L. Richardson, C. Schubert, A. Roura, W. P. Schleich, W. Ertmer, and E. M. Rasel, *Phys. Rev. Lett.* **112**, 203002 (2014).

[44] H. Albers, A. Herbst, L. L. Richardson, H. Heine, D. Nath, J. Hartwig, C. Schubert, C. Vogt, M. Woltmann, C. Lämmerzahl, S. Herrmann, W. Ertmer, E. M. Rasel, and D. Schlippert, *Eur. Phys. J. D* **74**, 145 (2020).

[45] X. Baillard, A. Gauguet, S. Bize, P. Lemonde, P. Laurent, A. Clairon, and P. Rosenbusch, *Opt. Commun.* **266**, 609 (2006).

[46] M. Gilowski, C. Schubert, M. Zaiser, W. Herr, T. Wübbena, T. Wendrich, T. Müller, E. Rasel, and W. Ertmer, *Opt. Commun.* **280**, 443 (2007).

[47] D. J. McCarron, S. A. King, and S. L. Cornish, *Meas. Sci. Technol.* **19**, 105601 (2008).

[48] H. Albers, Time-averaged optical potentials for creating and shaping Bose-Einstein condensates, Ph.D. thesis, Leibniz Universität Hannover, 2020.

[49] M. Zaiser, Eine Quelle quantenentarteter Gase für die Atominterferometrie, Ph.D. thesis, Leibniz Universität Hannover, 2010.

[50] T. Weber, J. Herbig, M. Mark, H.-C. Nägerl, and R. Grimm, *Phys. Rev. Lett.* **91**, 123201 (2003).

[51] P. O. Fedichev, M. W. Reynolds, and G. V. Shlyapnikov, *Phys. Rev. Lett.* **77**, 2921 (1996).

[52] E. Tiemann, P. Gersema, K. K. Voges, T. Hartmann, A. Zenesini, and S. Ospelkaus, *Phys. Rev. Res.* **2**, 013366 (2020).

[53] G. Salomon, L. Fouché, P. Wang, A. Aspect, P. Bouyer, and T. Bourdel, *Europhys. Lett.* **104**, 63002 (2013).

[54] N. Gaaloul, A. Suzor-Weiner, L. Pruvost, M. Telmini, and E. Charron, *Phys. Rev. A* **74**, 023620 (2006).

[55] L. Antoni-Micollier, B. Barrett, L. Chichet, G. Condon, B. Battelier, A. Landragin, and P. Bouyer, *Phys. Rev. A* **96**, 023608 (2017).

[56] E. Tiesinga, B. J. Verhaar, and H. T. C. Stoof, *Phys. Rev. A* **47**, 4114 (1993).

[57] W. Ketterle and N. V. Druten, in *Advances In Atomic, Molecular, and Optical Physics* (Elsevier, Amsterdam, 1996), pp. 181–236.

[58] C. Simonelli, E. Neri, A. Ciamei, I. Goti, M. Inguscio, A. Trenkwalder, and M. Zaccanti, *Opt. Express* **27**, 27215 (2019).

[59] J. Catani, P. Maioli, L. De Sarlo, F. Minardi, and M. Inguscio, *Phys. Rev. A* **73**, 033415 (2006).

[60] Z. Lasner, D. Mitra, M. Hiradfar, B. Augenbraun, L. Cheuk, E. Lee, S. Prabhu, and J. Doyle, *Phys. Rev. A* **104**, 063305 (2021).

[61] A. Marte, T. Volz, J. Schuster, S. Dürr, G. Rempe, E. G. M. van Kempen, and B. J. Verhaar, *Phys. Rev. Lett.* **89**, 283202 (2002).

[62] J. L. Roberts, N. R. Claussen, J. P. Burke, C. H. Greene, E. A. Cornell, and C. E. Wieman, *Phys. Rev. Lett.* **81**, 5109 (1998).

[63] S. Knoop, T. Schuster, R. Scelle, A. Trautmann, J. Appmeier, M. K. Oberthaler, E. Tiesinga, and E. Tiemann, *Phys. Rev. A* **83**, 042704 (2011).

[64] G. Semeghini, G. Ferioli, L. Masi, C. Mazzinghi, L. Wolswijk, F. Minardi, M. Modugno, G. Modugno, M. Inguscio, and M. Fattori, *Phys. Rev. Lett.* **120**, 235301 (2018).

[65] C. R. Cabrera, L. Tanzi, J. Sanz, B. Naylor, P. Thomas, P. Cheiney, and L. Tarruell, *Science* **359**, 301 (2018).

[66] C.-L. Hung, V. Gurarie, and C. Chin, *Science* **341**, 1213 (2013).

[67] T. Hensel, S. Loriani, C. Schubert, F. Fitzek, S. Abend, H. Ahlers, J. N. Siemß, K. Hammerer, E. M. Rasel, and N. Gaaloul, *Eur. Phys. J. D* **75**, 108 (2021).

[68] D. Schlippert, C. Meiners, R. Rengelink, C. Schubert, D. Tell, É. Wodey, K. Zipfel, W. Ertmer, and E. Rasel, in *CPT and Lorentz Symmetry* (World Scientific, Singapore, 2021).

[69] R. Corgier, L. Pezzè, and A. Smerzi, *Phys. Rev. A* **103**, L061301 (2021).

[70] R. Corgier, N. Gaaloul, A. Smerzi, and L. Pezzè, *Phys. Rev. Lett.* **127**, 183401 (2021).

[71] F. Anders, A. Idel, P. Feldmann, D. Bondarenko, S. Loriani, K. Lange, J. Peise, M. Gersemann, B. Meyer-Hoppe, S. Abend, N. Gaaloul, C. Schubert, D. Schlippert, L. Santos, E. Rasel, and C. Klemp, *Phys. Rev. Lett.* **127**, 140402 (2021).

[72] T. Kovachy, J. M. Hogan, A. Sugarbaker, S. M. Dickerson, C. A. Donnelly, C. Overstreet, and M. A. Kasevich, *Phys. Rev. Lett.* **114**, 143004 (2015).

[73] M. Fattori, C. D'Errico, G. Roati, M. Zaccanti, M. Jona-Lasinio, M. Modugno, M. Inguscio, and G. Modugno, *Phys. Rev. Lett.* **100**, 080405 (2008).

[74] H. Kim, K. Krzyzanowska, K. C. Henderson, C. Ryu, E. Timmermans, and M. Boshier, One second interrogation time in a 200 round-trip waveguide atom interferometer, [arXiv:2201.11888](https://arxiv.org/abs/2201.11888) (2022).

2.3 HIGH-FLUX SOURCE SYSTEM FOR MATTER-WAVE INTERFEROMETRY EXPLOITING TUNABLE INTERACTIONS

Authors: Alexander Herbst, Timothé Estrampes, Henning Albers, Vera Vollenkemper, Knut Stolzenberg, Sebastian Bode, Eric Charron, Ernst M. Rasel, Naceur Gaaloul, and Dennis Schlippert

Journal: Physical Review Research

Article Number: 6, 013139 (2024)

DOI: [10.1103/PhysRevResearch.6.013139](https://doi.org/10.1103/PhysRevResearch.6.013139)

Author contribution: A.H., H.A., V.V., S.B., K.S., E.M.R., and D.S. contributed to the design, operation, and maintenance of the overall setup. A.H. designed the optical dipole trap and implemented it together with V.V. and support of K.S. and S.B.. T.E. under the lead of N.G. and E.C. set the theoretical framework for the data analysis. A.H. performed the measurements. T.E. performed the numerical simulations of the expansion energy. A.H., T.E. and H.A. evaluated the presented data. A.H., T.E. with support of E.C. and D.S. drafted the initial manuscript. All authors critically discussed the results and contributed to, reviewed, and approved of the manuscript.

High-flux source system for matter-wave interferometry exploiting tunable interactions

A. Herbst¹, T. Estrampes^{1,2}, H. Albers¹, V. Vollenkemper¹, K. Stolzenberg¹,
S. Bode¹, E. Charron², E. M. Rasel¹, N. Gaaloul¹, and D. Schlippert^{1,*}

¹Leibniz Universität Hannover, Institut für Quantenoptik, Welfengarten 1, 30167 Hannover, Germany

²Université Paris-Saclay, Centre National de la Recherche Scientifique, Institut des Sciences Moléculaires d'Orsay, 91405 Orsay, France



(Received 26 July 2023; accepted 9 January 2024; published 2 February 2024)

Atom interferometers allow determining inertial effects to high accuracy. Quantum-projection noise as well as systematic effects impose demands on large atomic flux as well as ultralow expansion rates. Here we report on a high-flux source of ultracold atoms with free expansion rates near the Heisenberg limit directly upon release from the trap. Our results are achieved in a time-averaged optical dipole trap and enabled through dynamic tuning of the atomic scattering length across two orders of magnitude interaction strength via magnetic Feshbach resonances. We demonstrate Bose-Einstein condensates with more than 6×10^4 particles after evaporative cooling for 170 ms and their subsequent release with a minimal expansion energy of 4.5 nK in one direction. Based on our results we estimate the performance of an atom interferometer and compare our source system to a high performance chip trap, as readily available for ultraprecise measurements in microgravity environments.

DOI: [10.1103/PhysRevResearch.6.013139](https://doi.org/10.1103/PhysRevResearch.6.013139)

I. INTRODUCTION

Quantum sensors based on atom interferometry [1–4] allow for the absolute determination of inertial effects to great accuracy [5–9]. As such, they hold enormous potential across a broad spectrum of research areas, encompassing earth observation, environmental monitoring, navigation, and resource exploration. In fundamental physics they have been successfully used to test the weak equivalence principle [10–13], challenge the fundamental assumptions of quantum mechanics [14–17], and determine fundamental constants [18–20]. Recent proposals now aim for the search for dark matter [21–23] and the detection of gravitational waves in frequency bands complementary to those accessible using laser interferometers [24–29].

In order to reach the required sensitivity levels, a high atomic flux in combination with an extended pulse separation time is necessary. To enhance the latter the use of Bose-Einstein condensates (BECs) [30,31] presents a viable approach. In comparison to thermal ensembles, BECs allow for a superior control of systematic errors, yield higher signal-to-noise ratios, and notably exhibit smaller expansion rates [32,33]. While they readily attain expansion energies in the nanokelvin regime, delta-kick collimation techniques [34] can be employed for further reduction and values as low as 38 pK have been demonstrated in a microgravity environment [35]. However, the initial preparation of a BEC can significantly

increase the experimental cycle time and neutralize a potential sensitivity gain. Considerable efforts have been invested in overcoming this limitation by exploring rapid cooling schemes. Source systems based on multilayer atom chips have been demonstrated as a convincing solution for magnetically trappable atoms and ^{87}Rb in particular [36,37]. Their strong confinement and high trap frequencies allow to realize BECs with more than 1×10^5 atoms and repetition rates on the order of 1 Hz, including less than 500 ms of evaporative cooling. In a complementary approach, optical dipole traps (ODTs) are used when dealing with atoms insensitive to magnetic fields such as strontium or ytterbium or when experimental constraints do not allow for the implementation of chips. In these cases the issue is more severe as the inherent coupling of trap depth and trap frequencies intrinsically counteracts runaway evaporation at low intensity, resulting in evaporation sequences taking up to tens of seconds. Previous attempts to circumvent the corresponding scaling laws [38] include the use of movable lens systems [39], time-averaged optical potentials [40], or hybrid approaches incorporating laser cooling on broad and narrow transitions [41] and direct laser cooling in the ODT [42]. Most recently, machine learning techniques have also been implemented, resulting in evaporation ramps with durations below 200 ms [43]. Yet, most of these methods come with their own challenges regarding final atom number, expansion energy, or condensate fraction. Notably, optical setups which exhibit the same performance as chip traps are still lacking.

In this paper we present a scheme to enhance evaporative cooling of ^{39}K in an ODT. Contrary to ^{87}Rb , ^{39}K offers the advantage of broad Feshbach resonances [44] at low magnetic fields, which can be used to tailor interactions [45]. By combining an initial trap compression with a dynamic tuning of the scattering length over two orders of magnitude and trapping frequencies along the evaporation ramp, we realize

*schlippert@iqo.uni-hannover.de

Published by the American Physical Society under the terms of the Creative Commons Attribution 4.0 International license. Further distribution of this work must maintain attribution to the author(s) and the published article's title, journal citation, and DOI.

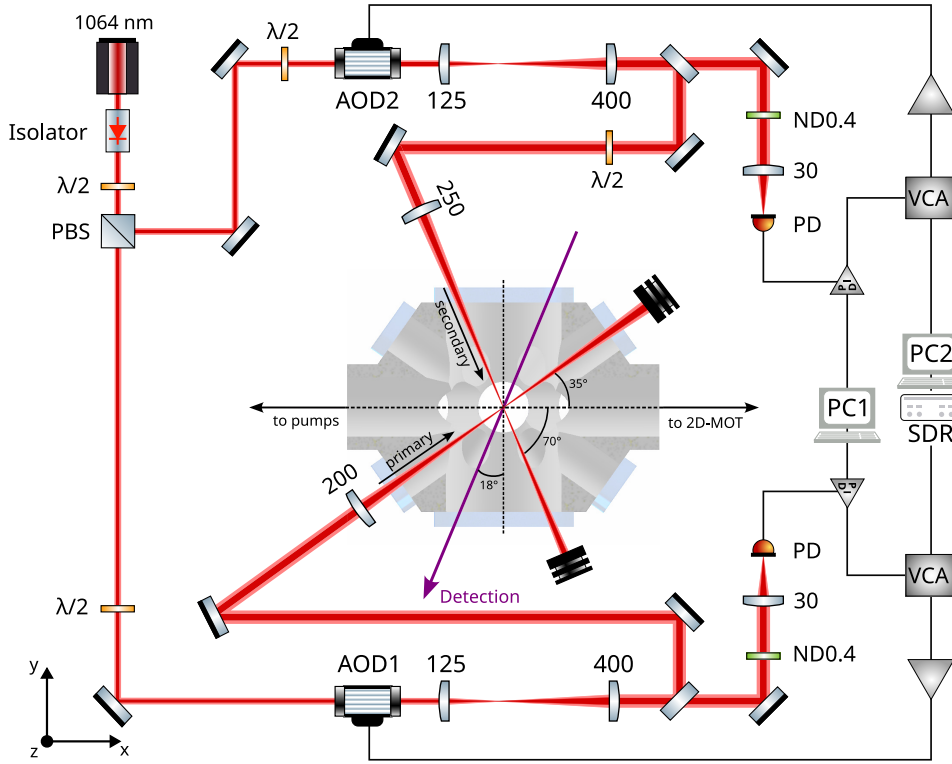


FIG. 1. Schematic representation of the crossed ODT setup. A single-frequency laser source (Coherent Mephisto MOPA) is split into two independent beams, allowing for up to 16 W per path. Beam waists were determined with a beamcam (DataRay TaperCamD-LCM), while the crossing angle of the beams within the chamber was measured with vertical imaging. Time-averaged potentials are implemented with AODs (AA Opto-Electronic DTSXY-400-1064), allowing us to independently modulate each beam's center position in the horizontal and vertical directions with a maximum modulation amplitude of 1.5 mm (resp. 1.8 mm for the secondary beam). In this paper, only the horizontal axes of the AODs are modulated using a software defined radio (Ettus USRP X310) to provide the waveform, while the vertical axes are driven with a constant frequency. For intensity stabilization, less than 0.1% of the optical power is detected by an amplified photodetector (Femto OE-200) and used to control the diffraction efficiency of the AOD via a homebuild PID controller together with a voltage controlled attenuate (MiniCircuits ZX73-2500-S+).

a nearly constant evaporation flux of 3×10^5 atoms/s for an evaporation time ranging from 170 ms to 2 s. Furthermore, tuning the scattering length to near zero thereafter offers a straightforward way to obtain a momentum spread close to the theoretical minimum, directly after release from the trapping potential. Our source system improves the flux performance of an ODT setup to that of a state-of-the-art device, enabling future sensor setups with superior sensitivity for a wider range of applications.

II. SOURCE SYSTEM

A. Ensemble preparation

Our ODT is created from two focused laser beams at a wavelength of 1064 nm, crossing under an angle of 74° with natural beam waists of $(24.5 \pm 1.6) \mu\text{m}$ [resp. $(30.3 \pm 3.2) \mu\text{m}$] for the primary [secondary] beam at the position of the atoms. A simplified overview of our setup is presented in Fig. 1.

For loading we use an all-optical scheme without the need for a magnetic trap as intermediate step. We first prepare 5×10^8 atoms at a temperature of $(5.93 \pm 0.07) \mu\text{K}$ using gray

molasses cooling on the D_1 line [46] with the magneto-optical trapping (MOT) setup and sequence as described in Ref. [47]. During the molasses step, we switch on the ODT and let the atoms fall freely through it afterwards, loading the trap within 50 ms. Implementing time-averaged optical potentials by means of acousto-optic deflectors (AODs) we are not restricted to the natural beam waists, but rather realize a trap of harmonic shape and variable spatial size in the horizontal plane [40]. Due to the Ramsauer minimum of ^{39}K [48], direct loading of traps deeper than $400 \mu\text{K}$ is unfavorable and we always find the maximum loading efficiency at trap depths between 60 and $80 \mu\text{K}$. Instead of increasing the trap depth, we therefore use 15.8 W of optical power per beam to increase the center-position modulation amplitude via the AODs, creating larger effective beam waists in the horizontal plane. Extending the spatial overlap with the resulting pancake-shaped trap, we improve mode matching of ODT and molasses. The maximum atom number loaded into the ODT is achieved with equal horizontal modulation strokes of 1.4 mm in the crossing region and a trap depth of $(65 \pm 7) \mu\text{K}$. In this configuration we load more than 2×10^7 atoms into the ODT. Compared to the configuration without any spatial modulation, we hereby

improve the loading performance by more than an order of magnitude. Subsequently, we perform a multiloop state preparation sequence as described previously in Ref. [47] and ultimately prepare a total of $(14.8 \pm 0.5) \times 10^6$ atoms in $|F = 1, m_F = -1\rangle$ with $(10.7 \pm 0.4) \times 10^6$ atoms in the immediate crossing region at a temperature of $(7.14 \pm 0.05) \mu\text{K}$. The high optical beam power together with the pancake shape also offers the advantage of achieving a high vertical trap frequency, resulting in a favorable initial phase space density (PSD) of $(1.18 \pm 0.59) \times 10^{-3}$ in the crossing region prior to evaporative cooling.

B. Evaporative cooling

The optimization of our evaporative cooling sequence is based on the model provided in Ref. [40]. The time needed for rethermalization is inversely proportional to the elastic collision rate $\Gamma_{\text{el}} \propto N\bar{\omega}^3 a^2/T$ for atom number N , temperature T , geometric mean of the trapping frequencies $\bar{\omega}$, and scattering length a , which therefore limits the speed of evaporative cooling [50,51]. However, the efficiency of the process, and consequently the number of condensed particles realizable for given initial conditions, depends on the ratio β of the evaporation rate to the remaining loss rates. In the case of an ODT and evaporative cooling on time scales significantly faster than the trap lifetime, the three-body recombination rate $\Gamma_{3b} \propto N^2\bar{\omega}^6 a^4/T^3$ poses the dominant loss channel [52]. Hence $\beta \approx \Gamma_{\text{el}}/\Gamma_{3b} \propto (N/\bar{\omega}^3)(T/a)^2$, allowing us to optimize evaporation trajectories for either large atom numbers or high evaporation speed by choosing trapping frequencies and scattering length, accordingly.

We optimize our evaporation sequence for a given total evaporation time towards the largest number of condensed particles, thus maximizing β , for a given value of Γ_{el} . Extending beyond previous work [47], we do so by not operating at a constant scattering length, but rather dynamically tuning the interactions within six linear ramps in coordination with the powers and spatial modulation of the optical beams. Our optimized ramps in terms of trap depth, trap frequency, and scattering length together with the resulting phase space density are presented in Fig. 2. For all ramps the initial configurations are identical and highlighted with a black pentagon. Each individual ramp duration is depicted in a different color. Markers indicate the start and end points of the linear ramp sections, at which we also measure atom number and temperature to obtain the PSD. The optical power and modulation stroke are always chosen such that the trap depth decreases approximately exponentially with time constant τ as shown in Fig. 2(a). For the ramps with a total duration below 1 s, depicted in blue and red, we additionally perform a rapid compression as a first step prior to reducing the trap depth to increase the density of the ensemble. This allows us to achieve the high trap frequencies required to ensure the necessary evaporation rate for the short ramps early on, as shown in Fig. 2(b). For the longer ramps, depicted in orange and purple, lower evaporation rates are sufficient and hence we choose frequencies comparable to the initial configuration. Especially for the short ramps a high initial scattering length of $1977^{+641}_{-387} a_0$ assists the compression, by maximizing the rethermalization rate in the otherwise dilute sample. By this

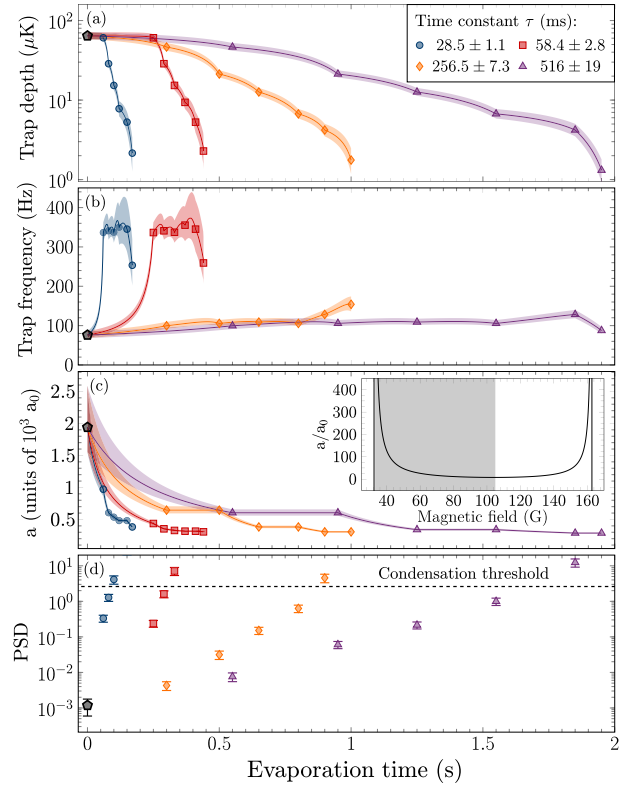


FIG. 2. Ramps optimized for evaporative cooling on different time scales with constant evaporative flux, together with the resulting phase space densities. Along each of the four ramps, markers indicate start and end points of the six sections, which are individually optimized. Trap depths (a) and frequency curves (b) are obtained from a simulation of the confining potential. Here, the error bands are estimated as the 2σ -uncertainty interval via error propagation, taking measurements of the beam waist, intensity, and geometry within the chamber into account. For modeling the scattering length (c) we follow Ref. [44], together with the properties of the individual resonances as reported in Ref. [49]. Our experimentally determined magnetic field uncertainty is used to assign the error bands. The inset shows the overall behavior of the scattering length in between the resonances at 32.6 and 162.8 G for atoms in $|F = 1, m_F = -1\rangle$. Magnetic field values used in this paper are highlighted by the shaded area. To determine the PSD (d), we perform atom number measurements at each marker position, averaging over 100 experimental cycles. Temperatures are obtained from fitting the expansion velocity to time-of-flight measurements of the ensemble size with data taken between 1 and 30 ms of free fall with 1-ms spacing and at least four measurements at each point in time.

we keep atom number loss associated with the related heating process from the compression $dT/dt = (\dot{\omega}/\omega)T$ to a minimum. In any case, we proceed by exponentially reducing the scattering length as shown in Fig. 2(c). By doing so, we counteract the relative increase in losses from the temperature reduction by reducing the scattering length, since temperature and scattering length obey the same power law in β . Here, evaporating in the vicinity of the broad Feshbach resonance at 32.6 G allows us to precisely tune the interactions as needed. The behavior of the scattering length for a wider range of

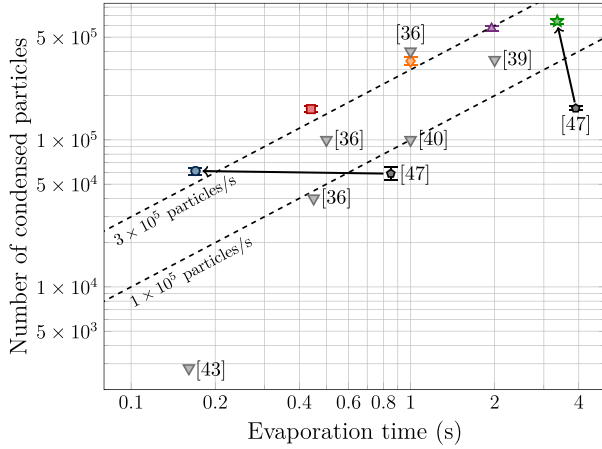


FIG. 3. Final particle numbers in the condensate, against total evaporation time. Our previously achieved results with constant scattering length in a 1960-nm trap are depicted with black pentagons, while our current results with variable scattering length in the 1064-nm trap are highlighted, following the color and shape coding of Fig. 2. The error bars are given by the standard deviation of 100 measurements of the particle number for each point. For comparison, the performance of other fast BEC sources is depicted with gray upside-down triangles.

magnetic fields is depicted in the inset of Fig. 2(c), where the magnetic field range used in this paper is highlighted as a shaded gray area. For our shortest ramp we cross the phase transition after a total evaporation time of 100 ms, as indicated by the blue data point above the condensation threshold at $\zeta(3/2) \approx 2.612$ in Fig. 2(d), while requiring a total ramp length of 170 ms to achieve a quasipure condensate of $(6.14 \pm 0.35) \times 10^4$ particles.

The evaporation performance for all ramps in terms of particle number is depicted in Fig. 3 and compared to previously obtained results. Note that the color and shape coding resembles the one that was already used in Fig. 2. The method presented here allows us to achieve evaporation durations comparable to the machine learning enhanced case [43], but with a 20-fold increase in atom number. Furthermore, unlike the high-flux chip source in Ref. [36], we realize a nearly constant evaporation flux of 3×10^5 atoms/s for evaporation times between 170 ms and 2 s. For longer evaporation durations we find a significant reduction in flux as losses associated with the lifetime become non-negligible. Nevertheless, we realize our largest BEC (green star) with $(6.41 \pm 0.28) \times 10^5$ atoms after an evaporation time of 3.35 s (ramp not shown in Fig. 2). Compared to our previous results with static scattering length in a 1960-nm trap, depicted as black pentagons [47], we increased the speed of our fastest sequence by a factor of 5 while maintaining the particle number and improved the largest particle number by a factor of 4, as marked by the black arrows.

C. Limited momentum spread

We further exploit the tunability of the atomic interactions to minimize the expansion energy of the ensemble upon

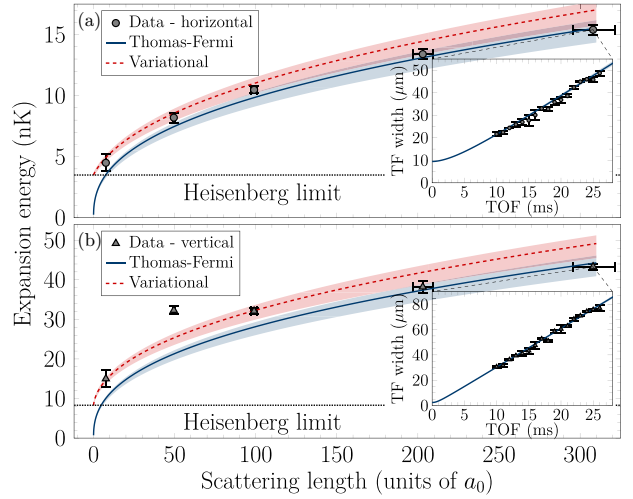


FIG. 4. Expansion energy of the BEC at different scattering lengths in horizontal (a) and vertical (b) direction. For each data point we perform a TOF series, determining the ensemble size between 10 and 26 ms of free fall with 1-ms spacing and at least four measurements per point. Contrary to the measurements performed in Sec. II B we do not measure below 10 ms to avoid the resolution limitation of our detection system. The insets show the TOF series for the data taken at $308 a_0$, which are used together with the measurements at $203 a_0$ to determine the trap frequencies, by fitting a scaling approach, shown as solid lines, with the error band corresponding to the stated trap frequency error. The error bars of the energy measurements originate as one-sigma deviation from the fit error of the expansion velocity and from the magnetic field uncertainty for the scattering length. Error bands of the simulations are obtained via a Monte Carlo method within the trap frequency interval.

release from the trap. Without interactions, the fundamental limit for the one-dimensional momentum spread of a BEC released from a harmonic potential is determined by the oscillator length $a_{ho} = [\hbar/m\omega]^{1/2}$ with the corresponding energy $E = \hbar\omega/2k_B$, when expressed in units of Kelvin. In experiments, larger energies are commonly observed as the nonvanishing mean field energy acts as a repulsive force upon release. Using a Feshbach resonance has already been demonstrated as a viable approach to reach the fundamental limit with BECs of cesium [53,54] and potassium [55]. We here confirm these results and measure the expansion energy for different scattering lengths by performing a least-square fit of the ensemble expansion based on time-of-flight (TOF) series (Fig. 4), which are useful for discussing the performance of an atom interferometer in the next section.

After creating the BEC using the 1-s-long evaporation ramp, we adiabatically sweep the magnetic field and perform measurements at different scattering lengths between the $|F = 1, m_F = -1\rangle$ resonances at 32.6 and 162.8 G, as shown by the gray shaded area in the inset of Fig. 2(c). Notably, the broad minimum of $7.59 a_0$ at 104.1 G allows us to approach an interaction free ensemble without the need for additional state transfers, but explicitly does not allow for zero or negative scattering lengths [45]. We then release the BEC from a trap with initial frequencies $\{\omega_x, \omega_y, \omega_z\} = 2\pi \times \{145.5 \pm 7.3, 11.5 \pm 0.6, 342 \pm 17\}$ Hz. Here, trap frequencies are

extracted from subsequent TOF measurements using a global fit on both datasets at $a = (203 \pm 6) a_0$ and $308^{+14}_{-13} a_0$, allowing for a 5 % error (Fig. 4 insets). In this regime, we model the ensemble's dynamics during the TOF by solving a scaling approach, assuming a parabolic spatial distribution of the atomic density, consistent with the Thomas-Fermi (TF) approximation [56,57]. The rms widths of the condensate density are given by $\rho_i(t) = \rho_i(0) \lambda_i(t)$ with scaling factor $\lambda_i(t)$ and $\rho_i(0) = R_i(0)/\sqrt{7}$, for $R_i(0)$ being the initial TF radius of the i direction [58]. As the interactions decrease the TF approximation becomes less accurate, since the kinetic term becomes more relevant. Hence the initial width can no longer be described by the previous $\rho_i(0)$, which would shrink to zero, and it becomes preferable to describe the BEC dynamics by a variational approach based on a Gaussian wave function with rms width $\rho_i(t)$ for lower scattering length [59,60].

In Fig. 4 we observe a good agreement between the TF approximation (solid blue line) and the experimental data (black points and triangles), for scattering lengths above $150 a_0$, while the variational approach (dashed red lines) offers a better agreement below. At $(7.59 \pm 0.01) a_0$ we find expansion energies of $(4.5 \pm 0.7) \text{ nK}$ [resp. $(15.0 \pm 2.2) \text{ nK}$] in the horizontal [vertical] direction. For a vanishing scattering length, e.g., realizable at 43.7 G for atoms in $|F = 1, m_F = 0\rangle$, the variational approach predicts a minimum expansion energy of 3.5 nK (8.3 nK).

III. EXPECTED INTERFEROMETER PERFORMANCE

We estimate the instability of an atom interferometer in Mach-Zehnder geometry for a setup utilizing our source configuration. We follow the calculations performed in Ref. [61] for a Raman beamsplitter with 1.2-cm beam radius and a pulse duration of $t_\pi = 15 \mu\text{s}$. At the standard quantum limit the instability of the interferometer after integration time τ is given by

$$\sigma(\tau) = \frac{1}{C\sqrt{N}k_{\text{eff}}T_I^2} \times \sqrt{\frac{t_{\text{cycle}}}{\tau}},$$

when neglecting the finite pulse duration. Its scaling with $[t_{\text{cycle}}/N]^{1/2}$ results in the formerly stated requirement for a high atomic flux. For our analysis we further divide the cycle time into the time in between interferometry pulses T_I , the evaporation time t_{evap} , and the remaining time t_{prep} used for loading the ODT, state preparation, and detection: $t_{\text{cycle}} = t_{\text{prep}} + t_{\text{evap}} + 2T_I$. Following Ref. [62], we determine the contrast C as the product of the excitation probabilities from the atom-light interactions. Here, the final expansion energy causes inhomogeneous Rabi frequencies, due to the velocity acceptance and intensity profile of the Raman beams. We calculate the resulting instability for different preparation times in combination with the evaporation times and the lowest expansion energy we experimentally demonstrated in the previous section. Additionally, we compare the obtained results to the ones achievable with the chip trap.

Our experimental preparation time is limited to $t_{\text{prep}} = 7 \text{ s}$ by MOT loading and the time required for the final data transfer of the taken images. For our setup the total atomic flux $N/(t_{\text{prep}} + t_{\text{evap}})$ scales beneficially with the longer

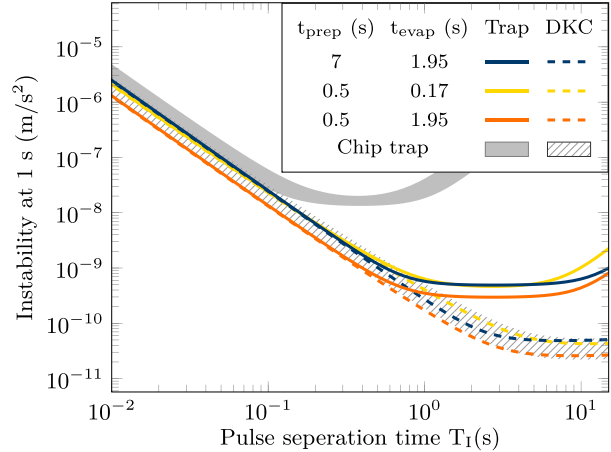


FIG. 5. Calculated instability of a Mach-Zehnder atom interferometer at the standard quantum limit using different source configurations with our evaporation sequence. We show the expected instability for different pulse separation times for an immediate release from the trap (solid lines) and compare them to an interferometer after performing an additional matter-wave collimation to 50 pK (dashed lines). The shaded areas show the respective performance of a chip-based source system with values taken from Ref. [36] for the case of an immediate release from the trap and from Ref. [35] for the DKC case.

evaporation ramps since we keep N/t_{evap} constant. We hence choose $t_{\text{evap}} = 1.95 \text{ s}$ for benchmarking. Here the calculation yields a minimum instability of $5 \times 10^{-10} \text{ m/s}^2$ at 1-s integration time, as indicated by the solid blue line in Fig. 5. When comparing to the accessible values by the chip trap directly after evaporative cooling, shown as the filled gray band, this corresponds to an improvement by over an order of magnitude, due to the smaller expansion energy of our setup which offsets our longer preparation time. Naturally, the results can be improved by a rapid MOT-loading scheme. Preparation times below 1 s are readily achievable with an intense atomic source as provided by a 2D⁺ MOT, combining a MOT in two dimensions with a pusher-retarder beam configuration [63,64]. Even further reduction is possible when considering cryogenic sources [65]. A reasonable preparation time of $t_{\text{prep}} = 500 \text{ ms}$ already yields an instability of $3 \times 10^{-10} \text{ m/s}^2$ as depicted by the solid orange line in Fig. 5. Additionally, such a setup allows us to access the regime below $1 \times 10^{-9} \text{ m/s}^2$ even with our shortest evaporation ramp of $t_{\text{evap}} = 170 \text{ ms}$ and enables sensors whose cycle time is entirely limited by the pulse separation time (yellow line).

Importantly, these results do not require additional matter-wave collimation when minimizing interactions. However, delta-kick collimation techniques can be implemented to additionally reduce the expansion energy [34]. To estimate the expected performance in this regime, we consider the method that has already been demonstrated with an ODT on a long baseline, realizing expansion energies of 50 pK [66]. For the chip based source system we consider the current record of 38 pK which has been achieved in microgravity [35]. Since both setups now feature similar expansion energies and our evaporation sequences allow for similar cycle times we find

the same instability regime below $5 \times 10^{-11} \text{ m/s}^2$ for both apparatuses, as shown by the overlap of the dashed lines with the area filled with a gray diagonal line pattern.

IV. OUTLOOK

We have demonstrated a rapid, all-optical source system for large ensembles of quantum-degenerated ${}^{39}\text{K}$, reduced its expansion energy by tuning atomic interactions, and calculated the resulting instability of a Mach-Zehnder atom interferometer at the standard quantum limit. Our analysis yields a superior performance for short cycle times and especially enables sensors which can prepare atomic ensembles well within the actual interferometry sequence. Hence the presented sequence allows us to effectively reduce the dead time in between measurements to zero, which has immediate applications in the field of hybrid inertial sensing, where a high data rate is required [8].

Moreover, for a delta-kick collimated ensemble we expect a performance similar to the best chip traps, which is of interest for experiments dedicated to high-accuracy measurements in fundamental physics. Especially ground-based long baseline experiments benefit from the demonstrated method, e.g., the Very Long Baseline Atom Interferometer, which does not allow for the use of chip traps, due to the choice of atoms, scale of the device, and optical access requirements [32,67]. In particular, we see applications for tests of quantum mechanics, e.g., in the context of the continuous spontaneous localization model [15,68,69]. Here, the sensitivity scales with the third power of the number of condensed particles and a rapid ensemble preparation together with a minimal final scattering length is required [17]. Moreover, realizing interaction-free BECs in free fall opens up the possibility of another class of noninterferometric tests, probing deviations from the uncertainty principle due to additional heating processes [14,16].

Beyond ${}^{39}\text{K}$, the evaporation methods demonstrated can also be applied to source systems of other atomic species.

For rubidium, suitable magnetic Feshbach resonances exist [70,71], but their narrower width and higher magnetic field strength make them technologically more challenging for improving evaporative cooling. For strontium and ytterbium, magnetic resonances are not available due to the nondegenerate nature of their ground state. In this case, optical Feshbach resonances (OFR), which modulate interatomic interactions by coupling two colliding atoms to a bound molecular state, have recently gained interest, due to their potential applications in molecule formation [72–75]. While broad OFRs are accompanied by high losses caused by the spontaneous decay of the excited molecular state [76], narrow linewidth resonances of the forbidden ${}^1S_0 - {}^3P_1$ intercombination transition suppress this behavior and have been used to efficiently change the atomic scattering length across large intervals [77–79]. Finally, a resonance suitable for thermalization has been identified for ${}^{88}\text{Sr}$ [79,80], offering prospects for direct evaporative cooling and its optimization using our method.

ACKNOWLEDGMENTS

We thank Jan Rudolph for fruitful discussions and helpful comments regarding the general scope of the paper and the performance of evaporative cooling and for thorough proofreading. This work is funded by the Federal Ministry of Education and Research (BMBF) through the funding program Photonics Research Germany under Contract No. 13N14875 and supported by the “ADI 2022” project founded by the IDEX Paris-Saclay, Grant No. ANR-11-IDEX-0003-02. The authors further acknowledge support by the German Space Agency (DLR) with funds provided by the Federal Ministry for Economic Affairs and Climate Action (BMWK) due to an enactment of the German Bundestag under Grants No. DLR 50WM2041 (PRIMUS-IV), and No. 50WM2253A (AI-Quadrat), and by the Deutsche Forschungsgemeinschaft (DFG, German Research Foundation)- Project-ID 274200144—the SFB 1227 DQ-mat within Projects No. A05 and No. B07—and under Germany’s Excellence Strategy—EXC-2123 QuantumFrontiers-Project-ID 390837967.

[1] M. Kasevich and S. Chu, Atomic interferometry using stimulated Raman transitions, *Phys. Rev. Lett.* **67**, 181 (1991).

[2] F. Riehle, Th. Kisters, A. Witte, J. Helmcke, and Ch. J. Bordé, Optical Ramsey spectroscopy in a rotating frame: Sagnac effect in a matter-wave interferometer, *Phys. Rev. Lett.* **67**, 177 (1991).

[3] M. Kasevich and S. Chu, Measurement of the gravitational acceleration of an atom with a light-pulse atom interferometer, *Appl. Phys. B* **54**, 321 (1992).

[4] A. D. Cronin, J. Schmiedmayer, and D. E. Pritchard, Optics and interferometry with atoms and molecules, *Rev. Mod. Phys.* **81**, 1051 (2009).

[5] T. L. Gustavson, P. Bouyer, and M. A. Kasevich, Precision rotation measurements with an atom interferometer gyroscope, *Phys. Rev. Lett.* **78**, 2046 (1997).

[6] B. Canuel, F. Leduc, D. Holleville, A. Gauguet, J. Fils, A. Virdis, A. Clairon, N. Dimarcq, Ch. J. Bordé, A. Landragin, and P. Bouyer, Six-axis inertial sensor using cold-atom interferometry, *Phys. Rev. Lett.* **97**, 010402 (2006).

[7] S. M. Dickerson, J. M. Hogan, A. Sugarbaker, D. M. S. Johnson, and M. A. Kasevich, Multiaxis inertial sensing with long-time point source atom interferometry, *Phys. Rev. Lett.* **111**, 083001 (2013).

[8] I. Dutta, D. Savoie, B. Fang, B. Venon, C. L. Garrido Alzar, R. Geiger, and A. Landragin, Continuous cold-atom inertial sensor with 1 nrad/sec rotation stability, *Phys. Rev. Lett.* **116**, 183003 (2016).

[9] D. Savoie, M. Altorio, B. Fang, L. A. Sidorenkov, R. Geiger, and A. Landragin, Interleaved atom interferometry for high-sensitivity inertial measurements, *Sci. Adv.* **4**, eaau7948 (2018).

[10] D. Schlippert, J. Hartwig, H. Albers, L. L. Richardson, C. Schubert, A. Roura, W. P. Schleich, W. Ertmer, and E. M. Rasel, Quantum test of the universality of free fall, *Phys. Rev. Lett.* **112**, 203002 (2014).

[11] M. G. Tarallo, T. Mazzoni, N. Poli, D. V. Sutyrin, X. Zhang, and G. M. Tino, Test of Einstein equivalence principle for 0-spin and half-integer-spin atoms: Search for spin-gravity coupling effects, *Phys. Rev. Lett.* **113**, 023005 (2014).

[12] H. Albers, A. Herbst, L. L. Richardson, H. Heine, D. Nath, J. Hartwig, C. Schubert, C. Vogt, M. Woltmann, C. Lämmerzahl, S. Herrmann, W. Ertmer, E. M. Rasel, and D. Schlippe, Quantum test of the universality of free fall using rubidium and potassium, *Eur. Phys. J. D* **74**, 145 (2020).

[13] P. Asenbaum, C. Overstreet, M. Kim, J. Curti, and M. A. Kasevich, Atom-interferometric test of the equivalence principle at the 10^{-12} level, *Phys. Rev. Lett.* **125**, 191101 (2020).

[14] A. Bassi, K. Lochan, S. Satin, T. P. Singh, and H. Ulbricht, Models of wave-function collapse, underlying theories, and experimental tests, *Rev. Mod. Phys.* **85**, 471 (2013).

[15] T. Kovachy, P. Asenbaum, C. Overstreet, C. A. Donnelly, S. M. Dickerson, A. Sugarbaker, J. M. Hogan, and M. A. Kasevich, Quantum superposition at the half-metre scale, *Nature (London)* **528**, 530 (2015).

[16] M. Carlesso, S. Donadi, L. Ferialdi, M. Paternostro, H. Ulbricht, and A. Bassi, Present status and future challenges of non-interferometric tests of collapse models, *Nat. Phys.* **18**, 243 (2022).

[17] B. Schrinski, P. Haslinger, J. Schmiedmayer, K. Hornberger, and S. Nimmrichter, Testing collapse models with Bose-Einstein-condensate interferometry, *Phys. Rev. A* **107**, 043320 (2023).

[18] G. Rosi, F. Sorrentino, L. Cacciapuoti, M. Prevedelli, and G. M. Tino, Precision measurement of the Newtonian gravitational constant using cold atoms, *Nature (London)* **510**, 518 (2014).

[19] R. H. Parker, C. Yu, W. Zhong, B. Estey, and H. Müller, Measurement of the fine-structure constant as a test of the standard model, *Science* **360**, 191 (2018).

[20] L. Morel, Z. Yao, P. Cladé, and S. Guellati-Khélifa, Determination of the fine-structure constant with an accuracy of 81 parts per trillion, *Nature (London)* **588**, 61 (2020).

[21] Y. A. El-Neaj, C. Alpigiani, S. Amairi-Pyka, H. Araújo, A. Balaž, A. Bassi, L. Bathe-Peters, B. Battelier, A. Belić, E. Bentine, J. Bernabeu, A. Bertoldi, R. Bingham, D. Blas, V. Bolpasi, K. Bongs, S. Bose, P. Bouyer, T. Bowcock, W. Bowden *et al.*, AEDGE: Atomic experiment for dark matter and gravity exploration in space, *EPJ Quantum Technol.* **7**, 6 (2020).

[22] Y. Du, C. Murgui, K. Pardo, Y. Wang, and K. M. Zurek, Atom interferometer tests of dark matter, *Phys. Rev. D* **106**, 095041 (2022).

[23] L. Badurina, V. Gibson, C. McCabe, and J. Mitchell, Ultralight dark matter searches at the sub-Hz frontier with atom multigradiometry, *Phys. Rev. D* **107**, 055002 (2023).

[24] J. M. Hogan, D. M. S. Johnson, S. Dickerson, T. Kovachy, A. Sugarbaker, S.-wey Chiow, P. W. Graham, M. A. Kasevich, B. Saif, S. Rajendran, P. Bouyer, B. D. Seery, L. Feinberg, and R. Keski-Kuha, An atomic gravitational wave interferometric sensor in low earth orbit (AGIS-LEO), *Gen. Relativ. Gravit.* **43**, 1953 (2011).

[25] B. Canuel, A. Bertoldi, L. Amand, E. P. di Borgo, T. Chantrait, C. Danquigny, M. Dovale Álvarez, B. Fang, A. Freise, R. Geiger, J. Gillot, S. Henry, J. Hinderer, D. Holleville, J. Junca, G. Lefèvre, M. Merzougui, N. Mielec, T. Monfret, S. Pelisson *et al.*, Exploring gravity with the MIGA large scale atom interferometer, *Sci. Rep.* **8**, 14064 (2018).

[26] M.-S. Zhan, J. Wang, W.-T. Ni, D.-F. Gao, G. Wang, L.-X. He, R.-B. Li, L. Zhou, X. Chen, J.-Q. Zhong, B. Tang, Z.-W. Yao, L. Zhu, Z.-Y. Xiong, S.-B. Lu, G.-H. Yu, Q.-F. Cheng, M. Liu, Y.-R. Liang, P. Xu *et al.*, ZAIGA: Zhaoshan long-baseline atom interferometer gravitation antenna, *Int. J. Mod. Phys. D* **29**, 1940005 (2020).

[27] C. Schubert, D. Schlippe, S. Abend, E. Giese, A. Roura, W. P. Schleich, W. Ertmer, and E. M. Rasel, Scalable, symmetric atom interferometer for infrasound gravitational wave detection, [arXiv:1909.01951](https://arxiv.org/abs/1909.01951).

[28] B. Canuel, S. Abend, P. Amaro-Seoane, F. Badaracco, Q. Beaufils, A. Bertoldi, K. Bongs, P. Bouyer, C. Braxmaier, W. Chaibi, N. Christensen, F. Fitzek, G. Flouris, N. Gaaloul, S. Gaffet, C. L. G. Alzar, R. Geiger, S. Guellati-Khélifa, K. Hammerer, J. Harms *et al.*, ELGAR: A European laboratory for gravitation and atom-interferometric research, *Class. Quantum Grav.* **37**, 225017 (2020).

[29] L. Badurina, E. Bentine, D. Blas, K. Bongs, D. Bortoletto, T. Bowcock, K. Bridges, W. Bowden, O. Buchmueller, C. Burrage, J. Coleman, G. Elertas, J. Ellis, C. Foot, V. Gibson, M. G. Haehnelt, T. Harte, S. Hedges, R. Hobson, M. Holynski *et al.*, AION: An atom interferometer observatory and network, *J. Cosmol. Astropart. Phys.* **2020**, 011 (2020).

[30] M. H. Anderson, J. R. Ensher, M. R. Matthews, C. E. Wieman, and E. A. Cornell, Observation of Bose-Einstein condensation in a dilute atomic vapor, *Science* **269**, 198 (1995).

[31] K. B. Davis, M.-O. Mewes, M. A. Joffe, M. R. Andrews, and W. Ketterle, Evaporative cooling of sodium atoms, *Phys. Rev. Lett.* **74**, 5202 (1995).

[32] D. Schlippe, C. Meiners, R. J. Rengelink, C. Schubert, D. Tell, É. Wodey, K. H. Zipfel, W. Ertmer, and E. M. Rasel, Matter-wave interferometry for inertial sensing and tests of fundamental physics, in *CPT and Lorentz Symmetry*, edited by R. Lehnert (World Scientific, Singapore, 2021), pp. 37–40.

[33] T. Hensel, S. Loriani, C. Schubert, F. Fitzek, S. Abend, H. Ahlers, J.-N. Siemß, K. Hammerer, E. M. Rasel, and N. Gaaloul, Inertial sensing with quantum gases: A comparative performance study of condensed versus thermal sources for atom interferometry, *Eur. Phys. J. D* **75**, 108 (2021).

[34] H. Ammann and N. Christensen, Delta kick cooling: A new method for cooling atoms, *Phys. Rev. Lett.* **78**, 2088 (1997).

[35] C. Deppner, W. Herr, M. Cornelius, P. Stromberger, T. Sternke, C. Grzeschik, A. Grote, J. Rudolph, S. Herrmann, M. Krutzik, A. Wenzlawski, R. Corgier, E. Charron, D. Guéry-Odelin, N. Gaaloul, C. Lämmerzahl, A. Peters, P. Windpassinger, and E. M. Rasel, Collective-mode enhanced matter-wave optics, *Phys. Rev. Lett.* **127**, 100401 (2021).

[36] J. Rudolph, W. Herr, C. Grzeschik, T. Sternke, A. Grote, M. Popp, D. Becker, H. Müntinga, H. Ahlers, A. Peters, C. Lämmerzahl, K. Sengstock, N. Gaaloul, W. Ertmer, and E. M. Rasel, A high-flux BEC source for mobile atom interferometers, *New J. Phys.* **17**, 065001 (2015).

[37] D. Becker, M. D. Lachmann, S. T. Seidel, H. Ahlers, A. N. Dinkelaker, J. Grosse, O. Hellmig, H. Müntinga, V. Schkolnik, T. Wendrich, A. Wenzlawski, B. Weps, R. Corgier, T. Franz, N. Gaaloul, W. Herr, D. Lüdtke, M. Popp, S. Amri, H. Duncker

et al., Space-borne Bose–Einstein condensation for precision interferometry, *Nature (London)* **562**, 391 (2018).

[38] K. M. O’Hara, M. E. Gehm, S. R. Granade, and J. E. Thomas, Scaling laws for evaporative cooling in time-dependent optical traps, *Phys. Rev. A* **64**, 051403(R) (2001).

[39] T. Kinoshita, T. Wenger, and D. S. Weiss, All-optical Bose–Einstein condensation using a compressible crossed dipole trap, *Phys. Rev. A* **71**, 011602(R) (2005).

[40] R. Roy, A. Green, R. Bowler, and S. Gupta, Rapid cooling to quantum degeneracy in dynamically shaped atom traps, *Phys. Rev. A* **93**, 043403 (2016).

[41] S. Stellmer, R. Grimm, and F. Schreck, Production of quantum-degenerate strontium gases, *Phys. Rev. A* **87**, 013611 (2013).

[42] A. Urvoy, Z. Vendeiro, J. Ramette, A. Adiyatullin, and V. Vuletić, Direct laser cooling to Bose–Einstein condensation in a dipole trap, *Phys. Rev. Lett.* **122**, 203202 (2019).

[43] Z. Vendeiro, J. Ramette, A. Rudelis, M. Chong, J. Sinclair, L. Stewart, A. Urvoy, and V. Vuletić, Machine-learning-accelerated Bose–Einstein condensation, *Phys. Rev. Res.* **4**, 043216 (2022).

[44] S. Inouye, M. R. Andrews, J. Stenger, H.-J. Miesner, D. M. Stamper-Kurn, and W. Ketterle, Observation of Feshbach resonances in a Bose–Einstein condensate, *Nature (London)* **392**, 151 (1998).

[45] C. D’Errico, M. Zaccanti, M. Fattori, G. Roati, M. Inguscio, G. Modugno, and A. Simoni, Feshbach resonances in ultracold ^{39}K , *New J. Phys.* **9**, 223 (2007).

[46] G. Salomon, L. Fouché, P. Wang, A. Aspect, P. Bouyer, and T. Bourdel, Gray-molasses cooling of ^{39}K to a high phase-space density, *Europhys. Lett.* **104**, 63002 (2013).

[47] A. Herbst, H. Albers, K. Stolzenberg, S. Bode, and D. Schlippert, Rapid generation of all-optical ^{39}K Bose–Einstein condensates using a low-field Feshbach resonance, *Phys. Rev. A* **106**, 043320 (2022).

[48] M. Landini, S. Roy, G. Roati, A. Simoni, M. Inguscio, G. Modugno, and M. Fattori, Direct evaporative cooling of ^{39}K atoms to Bose–Einstein condensation, *Phys. Rev. A* **86**, 033421 (2012).

[49] E. Tiemann, P. Gersema, K. K. Voges, T. Hartmann, A. Zenesini, and S. Ospelkaus, Beyond Born–Oppenheimer approximation in ultracold atomic collisions, *Phys. Rev. Res.* **2**, 013366 (2020).

[50] W. Ketterle and N. J. V. Druten, Evaporative cooling of trapped atoms, in *Advances in Atomic, Molecular, and Optical Physics* (Elsevier, Amsterdam, 1996), pp. 181–236.

[51] C. R. Monroe, E. A. Cornell, C. A. Sackett, C. J. Myatt, and C. E. Wieman, Measurement of Cs–Cs elastic scattering at $T=30\text{ }\mu\text{k}$, *Phys. Rev. Lett.* **70**, 414 (1993).

[52] T. Weber, J. Herbig, M. Mark, H.-C. Nägerl, and R. Grimm, Three-body recombination at large scattering lengths in an ultracold atomic gas, *Phys. Rev. Lett.* **91**, 123201 (2003).

[53] T. Weber, J. Herbig, M. Mark, H.-C. Nägerl, and R. Grimm, Bose–Einstein condensation of cesium, *Science* **299**, 232 (2003).

[54] T. Kraemer, J. Herbig, M. Mark, T. Weber, C. Chin, H.-C. Nägerl, and R. Grimm, Optimized production of a cesium Bose–Einstein condensate, *Appl. Phys. B* **79**, 1013 (2004).

[55] G. Roati, M. Zaccanti, C. D’Errico, J. Catani, M. Modugno, A. Simoni, M. Inguscio, and G. Modugno, ^{39}K Bose–Einstein condensate with tunable interactions, *Phys. Rev. Lett.* **99**, 010403 (2007).

[56] Y. Castin and R. Dum, Bose–einstein condensates in time dependent traps, *Phys. Rev. Lett.* **77**, 5315 (1996).

[57] Yu. Kagan, E. L. Surkov, and G. V. Shlyapnikov, Evolution of a Bose gas in anisotropic time-dependent traps, *Phys. Rev. A* **55**, R18 (1997).

[58] R. Corgier, S. Loriani, H. Ahlers, K. Posso-Trujillo, C. Schubert, E. M. Rasel, E. Charron, and N. Gaaloul, Interacting quantum mixtures for precision atom interferometry, *New J. Phys.* **22**, 123008 (2020).

[59] V. M. Pérez-García, H. Michinel, J. I. Cirac, M. Lewenstein, and P. Zoller, Low energy excitations of a Bose–Einstein condensate: A time-dependent variational analysis, *Phys. Rev. Lett.* **77**, 5320 (1996).

[60] V. M. Pérez-García, H. Michinel, J. I. Cirac, M. Lewenstein, and P. Zoller, Dynamics of Bose–Einstein condensates: Variational solutions of the Gross–Pitaevskii equations, *Phys. Rev. A* **56**, 1424 (1997).

[61] H. Albers, R. Corgier, A. Herbst, A. Rajagopalan, C. Schubert, C. Vogt, M. Woltmann, C. Lämmerzahl, S. Herrmann, E. Charron, W. Ertmer, E. M. Rasel, N. Gaaloul, and D. Schlippert, All-optical matter-wave lens using time-averaged potentials, *Commun. Phys.* **5**, 60 (2022).

[62] S. Loriani, D. Schlippert, C. Schubert, S. Abend, H. Ahlers, W. Ertmer, J. Rudolph, J. M. Hogan, M. A. Kasevich, E. M. Rasel, and N. Gaaloul, Atomic source selection in space-borne gravitational wave detection, *New J. Phys.* **21**, 063030 (2019).

[63] J. Catani, P. Maioli, L. De Sarlo, F. Minardi, and M. Inguscio, Intense slow beams of bosonic potassium isotopes, *Phys. Rev. A* **73**, 033415 (2006).

[64] S. Chaudhuri, S. Roy, and C. S. Unnikrishnan, Realization of an intense cold Rb atomic beam based on a two-dimensional magneto-optical trap: Experiments and comparison with simulations, *Phys. Rev. A* **74**, 023406 (2006).

[65] Z. Lasner, D. Mitra, M. Hiradfar, B. Augenbraun, L. Cheuk, E. Lee, S. Prabhu, and J. Doyle, Fast and high-yield loading of a D_2 magneto-optical trap of potassium from a cryogenic buffer-gas beam, *Phys. Rev. A* **104**, 063305 (2021).

[66] T. Kovachy, J. M. Hogan, A. Sugarbaker, S. M. Dickerson, C. A. Donnelly, C. Overstreet, and M. A. Kasevich, Matter wave lensing to picokelvin temperatures, *Phys. Rev. Lett.* **114**, 143004 (2015).

[67] J. Hartwig, S. Abend, C. Schubert, D. Schlippert, H. Ahlers, K. Posso-Trujillo, N. Gaaloul, W. Ertmer, and E. M. Rasel, Testing the universality of free fall with rubidium and ytterbium in a very large baseline atom interferometer, *New J. Phys.* **17**, 035011 (2015).

[68] P. Pearle, Combining stochastic dynamical state-vector reduction with spontaneous localization, *Phys. Rev. A* **39**, 2277 (1989).

[69] G. C. Ghirardi, P. Pearle, and A. Rimini, Markov processes in Hilbert space and continuous spontaneous localization of systems of identical particles, *Phys. Rev. A* **42**, 78 (1990).

[70] J. L. Roberts, N. R. Claussen, J. P. Burke, C. H. Greene, E. A. Cornell, and C. E. Wieman, Resonant magnetic field control of elastic scattering in cold ^{85}Rb , *Phys. Rev. Lett.* **81**, 5109 (1998).

[71] A. Marte, T. Volz, J. Schuster, S. Dürr, G. Rempe, E. G. M. van Kempen, and B. J. Verhaar, Feshbach resonances in rubidium 87: Precision measurement and analysis, *Phys. Rev. Lett.* **89**, 283202 (2002).

[72] C. P. Koch, F. Masnou-Seeuws, and R. Kosloff, Creating ground state molecules with optical Feshbach resonances in tight traps, *Phys. Rev. Lett.* **94**, 193001 (2005).

[73] C. P. Koch, Perspectives for coherent optical formation of strontium molecules in their electronic ground state, *Phys. Rev. A* **78**, 063411 (2008).

[74] M. Yan, B. J. DeSalvo, Y. Huang, P. Naidon, and T. C. Killian, Rabi oscillations between atomic and molecular condensates driven with coherent one-color photoassociation, *Phys. Rev. Lett.* **111**, 150402 (2013).

[75] S. Taie, S. Watanabe, T. Ichinose, and Y. Takahashi, Feshbach-resonance-enhanced coherent atom-molecule conversion with ultranarrow photoassociation resonance, *Phys. Rev. Lett.* **116**, 043202 (2016).

[76] M. Theis, G. Thalhammer, K. Winkler, M. Hellwig, G. Ruff, R. Grimm, and J. H. Denschlag, Tuning the scattering length with an optically induced Feshbach resonance, *Phys. Rev. Lett.* **93**, 123001 (2004).

[77] R. Ciurył, E. Tiesinga, and P. S. Julienne, Optical tuning of the scattering length of cold alkaline-earth-metal atoms, *Phys. Rev. A* **71**, 030701(R) (2005).

[78] K. Enomoto, K. Kasa, M. Kitagawa, and Y. Takahashi, Optical Feshbach resonance using the intercombination transition, *Phys. Rev. Lett.* **101**, 203201 (2008).

[79] S. Blatt, T. L. Nicholson, B. J. Bloom, J. R. Williams, J. W. Thomsen, P. S. Julienne, and J. Ye, Measurement of optical Feshbach resonances in an ideal gas, *Phys. Rev. Lett.* **107**, 073202 (2011).

[80] T. Zelevinsky, M. M. Boyd, A. D. Ludlow, T. Ido, J. Ye, R. Ciurył, P. Naidon, and P. S. Julienne, Narrow line photoassociation in an optical lattice, *Phys. Rev. Lett.* **96**, 203201 (2006).

2.4 ALL-OPTICAL MATTER-WAVE LENS USING TIME-AVERAGED POTENTIALS

Authors: Henning Albers, Robin Corgier, **Alexander Herbst**, Ashwin Rajagopalan, Christian Schubert, Christian Vogt, Marian Woltmann, Claus Lämmerzahl, Sven Herrmann, Eric Charron, Wolfgang Ertmer, Ernst M. Rasel, Naceur Gaaloul, and Dennis Schlippert

Journal: Communications Physics

Article Number: 5 60 (2022)

DOI: [10.1038/s42005-022-00825-2](https://doi.org/10.1038/s42005-022-00825-2)

Author contribution: W.E., E.M.R., and D.S. designed the experimental setup and the dipole trapping laser system. H.A., A.H., A.R., and D.S. contributed to the design, operation, and maintenance of the laser system and the overall setup. R.C., E.C. and N.G. set the theoretical framework of this work. H.A., R.C., C.S., and D.S. drafted the initial manuscript. H.A., and R.C. performed the analysis of the data presented in this manuscript. H.A., and R.C. under lead of N.G. and C.S. performed the instability study. C.V., M.W., C.L., S.H. together with the other authors discussed and evaluated the results and contributed to, reviewed, and approved of the manuscript.

This article is licenced under a Creative Commons Attribution 4.0 International License [CC BY 4.0](https://creativecommons.org/licenses/by/4.0/) which permits reproduction. No changes to the original content were made.

communications physics

ARTICLE



<https://doi.org/10.1038/s42005-022-00825-2>

OPEN

All-optical matter-wave lens using time-averaged potentials

Henning Albers ¹, Robin Corgier ^{1,2,3}, Alexander Herbst ¹, Ashwin Rajagopalan ¹, Christian Schubert ^{1,4}, Christian Vogt ⁵, Marian Woltmann ⁵, Claus Lämmerzahl ⁵, Sven Herrmann ⁵, Eric Charron ², Wolfgang Ertmer ^{1,4}, Ernst M. Rasel ¹, Naceur Gaaloul ¹ & Dennis Schlippert ¹✉

The precision of matter-wave sensors benefits from interrogating large-particle-number atomic ensembles at high cycle rates. Quantum-degenerate gases with their low effective temperatures allow for constraining systematic errors towards highest accuracy, but their production by evaporative cooling is costly with regard to both atom number and cycle rate. In this work, we report on the creation of cold matter-waves using a crossed optical dipole trap and shaping them by means of an all-optical matter-wave lens. We demonstrate the trade off between lowering the residual kinetic energy and increasing the atom number by reducing the duration of evaporative cooling and estimate the corresponding performance gain in matter-wave sensors. Our method is implemented using time-averaged optical potentials and hence easily applicable in optical dipole trapping setups.

¹Leibniz Universität Hannover, Institut für Quantenoptik, Welfengarten 1, 30167 Hannover, Germany. ²Université Paris-Saclay, CNRS, Institut des Sciences Moléculaires d'Orsay, 91405 Orsay, France. ³LNE-SYRTE, Observatoire de Paris, Université PSL, CNRS, Sorbonne Université 61 avenue de l'Observatoire, 75014 Paris, France. ⁴Deutsches Zentrum für Luft- und Raumfahrt e.V. (DLR), Institut für Satellitengeodäsie und Inertialsensorik, c/o Leibniz Universität Hannover, DLR-SI, Callinstraße 36, 30167 Hannover, Germany. ⁵ZARM Zentrum für angewandte Raumfahrttechnologie und Mikrogravitation, Universität Bremen, Am Fallturm 2, 28359 Bremen, Germany. ✉email: schlippert@iqo.uni-hannover.de

Ever since their first realization, atom interferometers^{1–4} have become indispensable tools in fundamental physics^{5–17} and inertial sensing^{18–30}. The sensitivity of such matter-wave sensors scales with the enclosed space-time area which depends on the momentum transferred by the beam splitters as well as the time the atoms spend in the interferometer.

The expansion of the atomic clouds, used in interferometers, needs to be minimized and well controlled to reach long pulse separation times, control systematic shifts, and create ensembles dense enough to detect them after long time-of-flights. Nevertheless, colder ensembles with lower expansion rates typically need longer preparation times. Therefore, matter-wave sensors require sources with a high flux of large cold atomic ensembles to obtain fast repetition rates.

Bose-Einstein condensates (BECs) are well suited to perform interferometric measurements. They are investigated to control systematic effects related to residual motion at a level lower than a few parts in 10^9 of Earth's gravitational acceleration^{20,31–34}. In addition, due to their narrower velocity distribution³⁵, BECs offer higher beam splitting efficiencies and thus enhanced contrast^{23,36,37}, especially for large momentum transfer^{36,38–43}. Finally, the inherent atomic collisions present in BECs can enhance matter-wave interferometry by enabling (i) ultra-low expansion rates through collective mode dynamics with a recent demonstration of a 3D expansion energy of $k_B \cdot 38^{+6}_{-7}$ pK⁴⁴, and (ii) ultimately the generation of mode entanglement through spin-squeezing dynamics to significantly surpass the standard quantum limit^{45–48}.

Today's fastest BEC sources rely on atom-chip technology, where near-surface magnetic traps allow for rapid evaporation using radio frequency or microwave transitions. This approach benefits from constant high trapping frequencies during the evaporative cooling process, thus leading to repetition rates on the order of 1 Hz with BECs comprising 10^5 atoms⁴⁹.

Anyway, since magnetic traps are not suitable in certain situations optical dipole traps become the tool of choice⁵⁰. Examples are trapping of atomic species with low magnetic susceptibility^{51,52}, or molecules^{53,54} and composite particles^{55,56}. In optical dipole traps external magnetic field allow tuning parameters, e.g., when using Feshbach resonances⁵⁷.

Here, the intrinsic link between trap depth and trap frequencies in dipole traps⁵⁸ inhibits runaway evaporation. Cold ensembles can be only produced in shallow traps, leading to drastically increased preparation time t_p . This long standing problem has been recently overcome through the use of time-averaged potentials, where trap depth and trap frequencies can be controlled independently, thus allowing for more efficient and faster evaporation while maintaining high atom numbers^{52,59}.

In this work, we use dynamic time-averaged potentials for efficient BEC generation and demonstrate an all-optical matter-wave lens capable of further reducing the ensemble's residual kinetic energy. Contrary to pulsed schemes of matter-wave lensing^{44,60–65}, we keep the atoms trapped over the entire duration of the matter-wave lens³⁷, which eases implementation in ground-based sensors. Moreover, we show that with this technique one can short-cut the evaporation sequence prior to the matter-wave lens, which increases the atomic flux by enhancing atom number and reducing cycle time while simultaneously reducing the effective temperature. Our method can largely improve the matter-wave sensor's stability in various application scenarios.

Results

Evaporative cooling. We operate a crossed optical dipole trap at a wavelength of 1960 nm loaded from a ⁸⁷Rb magneto-optical

trap (details in the “Methods” section). The time-averaged potentials are generated by simultaneous center-position modulation of the crossed laser beams in the horizontal plane. Controlling the amplitude of this modulation and the intensity of the trapping beams enables the dynamic control and decoupling of the trapping frequencies and depth. We chose the waveform of the center-position modulation to generate a parabolic potential⁵².

Up to 2×10^7 rubidium atoms are loaded into the trap with trapping frequencies $\omega/2\pi \approx \{140; 200; 780\}$ Hz in $\{x'; y'; z\}$ direction (definition of coordinate systems in the “Methods” section) with a trap depth of $170 \mu\text{K}$. For this we operate the trap at the maximum achievable laser intensity of 12 W and the center-position modulation at an amplitude of $h_0 = 140 \mu\text{m}$.

We perform evaporative cooling by reducing the trap depth exponentially in time while keeping the trapping frequencies at a high level by reducing the amplitude of the center-position modulation. This method allows us to generate BECs with up to 4×10^5 atoms within 5 s of evaporative cooling. By shortening the time constant of the exponential reduction we generate BECs with 5×10^4 (2×10^5) particles within 2 s (3 s) of evaporative cooling. At the end of the evaporation sequence the trap has frequencies of $\omega/2\pi \approx \{105; 140; 160\}$ Hz and a depth of about 200 nK. The expansion velocity of the condensate released from the final evaporation trap is 2 mm s^{-1} , which corresponds to an effective temperature of 40 nK.

All-optical matter-wave lens. Our matter-wave lens can be applied in any temperature regime explorable in our optical trap. We investigate the creation of collimated atomic ensembles for different initial temperatures of the matter-waves. To this aim, the evaporation sequence is stopped prematurely at different times to generate input atomic ensembles at rest with initial trap frequency ω_0 and initial temperature T_0 . We then initiate the matter-wave lens by a rapid decompression⁶⁶ of the trap frequency in the horizontal directions from ω_0 to ω_l . Here we denote by ω_l the lensing potential in analogy with the Delta-kick collimation technique. The reduction of the trapping frequencies from the initial ω_0 to ω_l depends on experimental feasibility, such as the maximum achievable amplitude of the center-position modulation and the modulation amplitude right before the rapid decompression. With ongoing evaporative cooling this amplitude is reduced and thus the trap can be relaxed much further for more continued sequences. However, we need to maintain the confinement in the vertical direction by adjusting the dipole trap's intensity to suppress heating or loss of atoms.

Subsequent oscillations in the trap result in a manipulation in phase space (Fig. 1a, b) for focusing, diffusion, and, importantly collimation of the matter-wave (Fig. 1c). Figure 1c depicts the expansion of a thermal ensemble in 1D for three different holding times (t_{hold}) to highlight the importance of a well chosen timing for the lens. Figure 2 shows exemplary expansion velocities (colored circles) depending on the holding time t_{hold} . The colored curves in this graph display the simulated behavior following the scaling ansatz (details in the “Methods” section) with an error estimation displayed by shaded areas. Only for the final measurement (also shown in the inset in Fig. 2) we create a BEC with a condensed fraction of 92.5% of the total atom number and apply the matter-wave lens to it.

With the presented method we observe oscillations of the expansion rate, which are in good agreement with the simulations for different ensemble temperatures. For all investigated temperatures an optimal holding time exists for which the final expansion rate is minimized (Fig. 3a). The ratios of $\sigma_{v,l}/\sigma_{v,0}$ and ω/ω_0 for each measurement is shown in Fig. 3b.

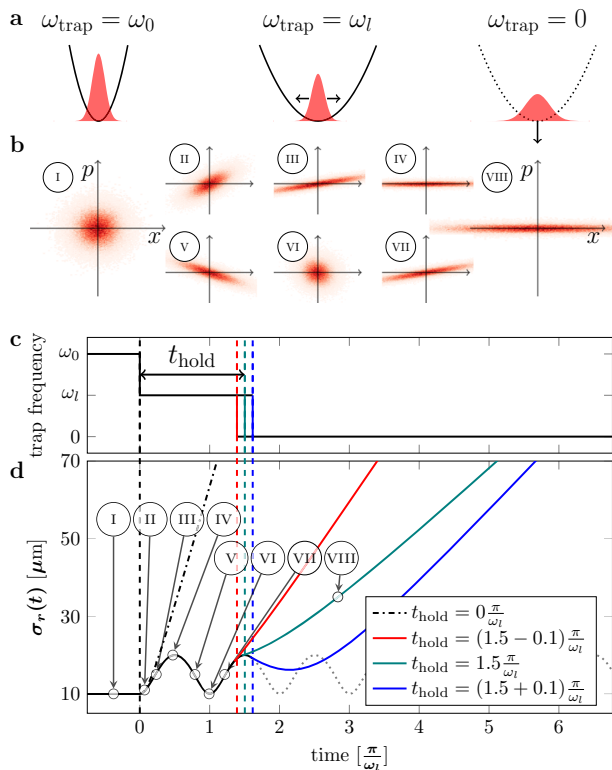


Fig. 1 Scheme of the matter-wave lens. The drawing in **a** shows the three trap configurations and the distribution of the atomic ensemble during the matter-wave lens. At the beginning the trap frequency (ω_{trap}) corresponds to the initial trap frequency (ω_0), which is then decompressed to the lens trap frequency (ω_l). After the holding time (t_{hold}) the trap is switched off ($\omega_{\text{trap}} = 0$). The phase-space (p - x) diagrams in **b** show the atomic distributions at different timings during the matter-wave lens. Panel **c** shows the behavior of the time dependency of the trapping frequency. After the holding time in the initial trap the trapping frequency is rapidly decreased at time $t = 0$. Panel **d** shows the time evolution of the atomic ensemble's size (σ_r), which starts to oscillate (solid and dotted black line) after the trap is relaxed. At time $t_{\text{hold}} = (n + 0.5) \times \pi/\omega_l$, with $n \in \mathbb{N}$, this oscillation reaches an upper turning point (teal curve). The atomic ensemble is released at its maximum size to minimize its later expansion rate. The labeled points (I-VIII) correspond to the phase-space diagrams in **b**. If the release time (t_{hold}) does not match this condition the expansion rate is not minimized (red and blue curve). The dashed-dotted black curve displays the size of a free falling ensemble without lensing, released at time $t = 0$.

The change in atom number from the initial to the lensing trap (Fig. 3a) lies within the error bars and arises mainly due to pointing instabilities of the crossed optical dipole trap beams. The lowest expansion rate is achieved with $553(49) \mu\text{m s}^{-1}$ with a related effective temperature of $3.2(0.6) \text{ nK}$ and an atom number of $4.24(0.02) \times 10^5$. With this method we achieve a more than one order of magnitude lower effective temperature while maintaining a comparable atom number compared to evaporative cooling.

Discussion

In this paper, we demonstrate a technique to reduce the expansion velocity of an atomic ensemble by rapid decompression and subsequent release from a dipole trap at a well-controlled time. The efficiency of the matter-wave lens for higher temperatures is mainly limited experimentally by the limited ratio between the

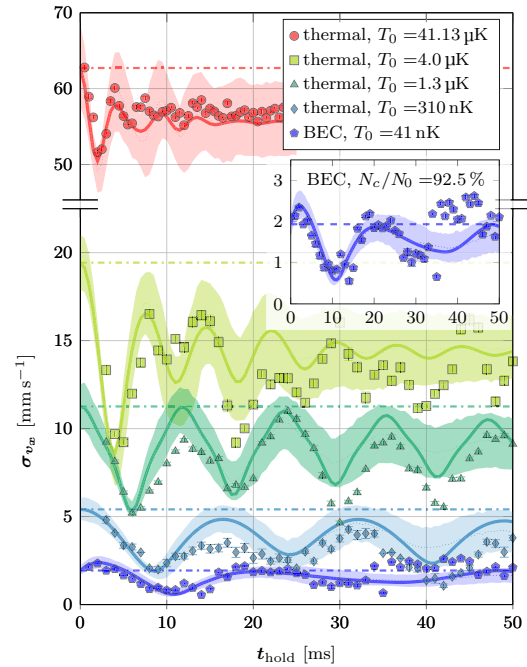


Fig. 2 Oscillations of expansion velocity. Expansion velocity (σ_{v_w}) after 30 ms of time of flight in dependence of the holding time. The graph shows the expansion velocity for thermal ensembles with different initial temperatures T_0 and the Bose-Einstein condensate (BEC) with an initial expansion temperature of $T_0 = 41 \text{ nK}$ and a condensed fraction of $N_c/N_0 = 92.5\%$. The markers show the measurements, the dashed-dotted lines the expansion rate from the initial traps (cf. black dashed-dotted line in Fig. 1). The simulations use the scaling ansatz and are depicted as lines with a shaded 1-sigma error estimation for the used trap parameters. The inset displays the size oscillation of the Bose-Einstein condensate on an enlarged scale for better readability.

initial and the lensing trap frequency ω_l/ω_0 (Fig. 3b) which is constrained by the maximum possible spatial modulation amplitude of the trapping beams. In general, according to the Liouville theorem, the expansion speed reduction of the matter-wave is proportional to $(\omega_0/\omega_l)^2$ where a large aspect ratio enables a better collimated ensemble. The atoms are loaded into the time-average potential with an optimized center-position modulation amplitude of 140 μm, while the maximum is 200 μm. During the evaporation sequence this amplitude is decreased. Consequently, the relaxation of the trap is less efficient at the beginning of the evaporative sequence or directly after the loading of the trap.

Another constraint is that the trap's confinement in the unpainted vertical direction is required to remain constant. If the vertical trap frequency is increased we observe heating effects and suffer from atom loss when it is decreased. To compensate for the trap depth reduction during the switch from the initial to the lensing trap we increase the dipole trap laser's intensity accordingly.

An additional modulation in the vertical direction, e.g., by means of a two-dimensional acousto-optical deflector, as well as an intersection angle of 90° would enable the generation of isotropic traps. In such a configuration, the determination of the optimal holding time will benefit from the in-phase oscillations of the atomic ensemble's size⁶⁷. When applying our matter-wave lens in a dual-species experiment, isotropy of the trap will also improve the miscibility of the two ensembles⁶⁸.

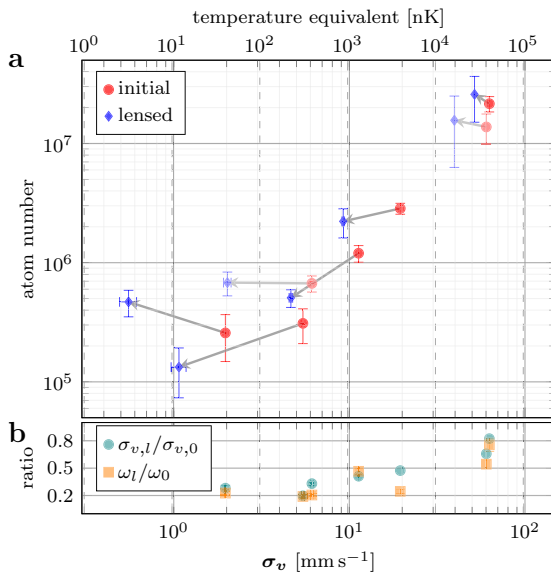


Fig. 3 Expansion velocity dependent performance. Panel a shows the atom number depending on the expansion velocity (σ_v) for the resulting expansion velocity (blue circles) after the matter-wave lens and starting points (red circles). The lines connect the corresponding data points. The error bars arise from the time of flight measurements used to determine the expansion velocity. We use the 1-sigma fitting error of the ballistic expansion for σ_v and the statistical error of measured atom numbers. The two grayed out data points associated with the starting expansion velocities 60 mm s⁻¹ and 6 mm s⁻¹ are not displayed in Fig. 2 while all the others are included. Panel b shows the ratio of the lensed and the initial ensembles expansion velocity ($\sigma_{v,l}/\sigma_{v,0}$) as well as the trapping frequencies (ω_l/ω_0) depending on the starting expansion velocity.

To illustrate the relevance for atom interferometers, we discuss the impact of our source in different regimes (details in the “Methods” section) operated at the standard quantum limit for an acceleration measurement. In a Mach-Zehnder-like atom interferometer^{1,18}, the instability reads

$$\sigma_a(\tau) = \frac{1}{C\sqrt{N} n k_{\text{eff}} T_1^2} \cdot \sqrt{\frac{t_{\text{cycle}}}{\tau}} \quad (1)$$

after an averaging time τ , neglecting the impact of finite pulse durations on the scale factor^{69–71}. Eq. (1) scales with the interferometer contrast C , the atom number per cycle N , the effective wave number $n k_{\text{eff}}$ indicating a momentum transfer during the atom-light interaction corresponding to $2n$ photons, and the separation time between the interferometer light pulses T_1 . The cycle time of the experiment $t_{\text{cycle}} = t_p + 2T_1 + t_d$ includes the time for preparing the ensemble t_p , the interferometer $2T_1$, and the detection t_d . In Eq. (1), the contrast depends on the beam splitting efficiency. This, in turn, is affected by the velocity acceptance and intensity profile of the beam splitting light, both implying inhomogeneous Rabi frequencies, and consequently a reduced mean excitation efficiency^{35,72,73}. Due to expansion of the atomic ensemble and inhomogeneous excitation, a constrained beam diameter implicitly leads to a dependency of the contrast C on the pulse separation time T_1 , which we chose as a boundary for our discussion. We keep the effective wave-number fixed and evaluate $\sigma_a(1\text{ s})$ for different source parameters when varying T_1 .

Figure 4 shows the result for collimated (solid lines) and uncollimated (dotted lines) ensembles in our model (details in the “Methods” section) and compares them to the instability under

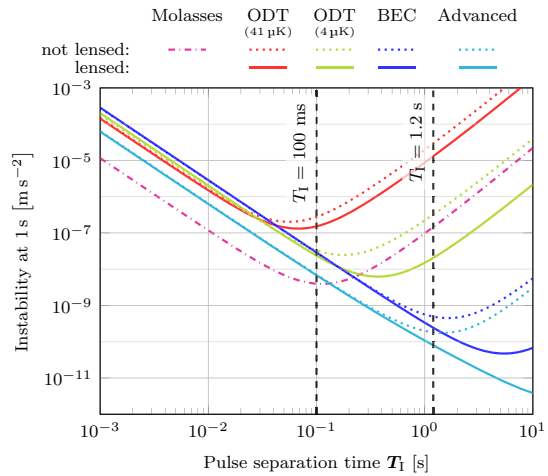


Fig. 4 Instability comparison. Behavior of the instability for shot-noise limited atom interferometers after an integration time of $\tau = 1\text{ s}$ for different sources (Tab. 1) over the pulse separation time T_1 . The instability is estimated for molasses cooled ensembles, thermal ensembles released from the optical dipole trap (ODT), and Bose-Einstein condensates (BEC and Advanced) also released from the optical dipole trap. The colors of the curves, except for the molasses and advanced case, agree with the measurements displayed in Fig. 2. The different source parameters are described in more detail in the “Methods” section.

use of a molasses-cooled ensemble (dash-dotted line). Up to $T_1 = 100\text{ ms}$ and $\sigma_a(1\text{ s}) = 10^{-8}\text{ m s}^{-2}$, the molasses outperforms evaporatively cooled atoms or BECs due to the duration of the evaporation adding to the cycle time and associated losses. In this time regime, the latter can still be beneficial for implementing large momentum transfer beam splitters^{36,38–40,42,43} reducing $\sigma_a(\tau)$ or suppressing systematic errors^{20,31–34,74} which is not represented in our model and beyond the scope of this paper. According to the curves, exploiting higher T_1 for increased performance requires evaporatively cooled atoms or BECs. This shows the relevance for experiments on large baselines^{23,37,74–77} or in microgravity^{78,79}. We highlight the extrapolation for the Very Long Baseline Atom Interferometer (VLBAI)^{76,80}, targeting a pulse separation time of $T_1 = 1.2\text{ s}$ ⁸¹. Here, the model describing our source gives the perspective of reaching picokelvin expansion temperatures of matter-wave lensed large atomic ensembles.

Methods

Experimental realization. The experimental apparatus is designed to operate simultaneous atom interferometers using rubidium and potassium and is described in detail in references^{9,10,82}.

For the experiments presented in this article only rubidium atoms were loaded from a two dimensional to a three dimensional magneto-optical trap (2D/3D-MOT) situated in our main chamber. After 2 s we turn off the 2D-MOT and compress the atomic ensemble by ramping up the magnetic field gradient as well as the detuning of the cooling laser in the 3D-MOT. Subsequent to compression, the atoms are loaded into the crossed dipole trap by switching off the magnetic fields and increasing the detuning of the cooling laser to about -30Γ , with Γ being the natural linewidth of the D_2 transition.

Figure 5 depicts the setup of our crossed optical dipole trap. The center-position modulation of the trapping beams is achieved by modulating the frequency driving the acousto-optical modulator (AOM) (Polytec, ATM-1002FA53.24). A voltage-controlled oscillator (Mini-Circuits, ZOS-150+) generates the signal for this, which is driven by a programmable arbitrary-waveform generator (Rigol, DG1022Z). We chose the waveform to generate a large-volume parabolic potential based on the derivation shown by Roy et al.⁵². The amplitude of the displacement of the center-position of the dipole trap beam, h_0 , is controlled by regulating the amplitude of the AOM’s frequency modulation. This yields a maximum beam displacement of $h_0 = 200\text{ }\mu\text{m}$ (300 μm) at the position of the atoms for the initial (recycled) beam.

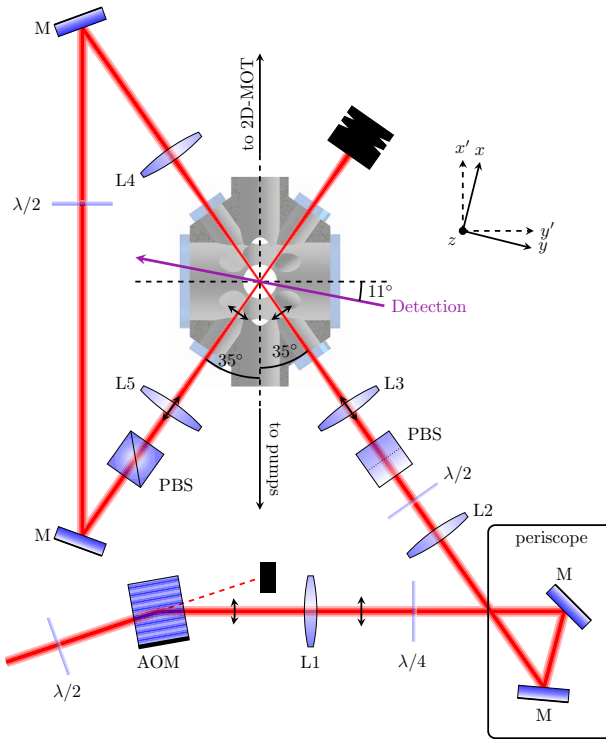


Fig. 5 Experimental setup. Optical setup of the dipole trap and alignment through the vacuum chamber. Vertical arrows point towards the 2D magneto-optical trap (2D-MOT) and the vacuum pumps. The acousto-optical modulator (AOM) is used for modulating the center-position of the laser beams and intensity control. A $\lambda/2$ wave plate rotates the polarization of the beam for best diffraction efficiency of the AOM. Lenses L1 ($f_1 = 100$ mm) and L2 ($f_2 = 300$ mm) magnify the beam radius to about 3 mm, 4 mm (vertical, horizontal). Downstream lenses L3, L4, and L5 ($f_{3,4,5} = 150$ mm) focus, re-collimate and re-focus the beam into the center of the chamber. The $\lambda/2$ and the $\lambda/4$ wave plates set the polarization for maximum transmission at the orthogonal oriented polarization beam splitters (PBS). The mirrors (M) are used to guide the beam through the chamber. The purple arrow indicates the direction of absorption detection along the y-direction.

Data acquisition and analysis. We apply our matter-wave lens subsequent to loading the dipole trap and evaporative cooling. The duration of the complete evaporative sequence is 5 s for the measurements presented here we interrupt this sequence after 0 s, 0.2 s, 1 s, 2 s, 3.5 s, 4.3 s and 5 s. Before the step-wise change of the trap frequency ($\omega_0 \rightarrow \omega_l$) we hold the ensemble in the trap given by the respective evaporation step configuration for 50 ms.

During the matter-wave lens, the rapid decompression of the trap causes oscillations of the ensemble's radius in the lensing trap. Depending on the release time we observe oscillations by performing absorption imaging with iterating t_{hold} for different times after the release from the trap. For each holding time the expansion velocity is extracted by fitting a ballistic expansion. This expansion can be transformed into an effective temperature using:

$$\sigma_{v_i}^2 = \frac{k_B T_i}{m}, \quad (2)$$

along each direction. The measurement is performed for different starting temperatures in the thermal regime as well as the BEC.

The simulations shown in Fig. 2 use the scaling ansatz as described in the “Scaling Ansatz” section. Here, the trapping frequencies of the lens potential in x- and y-direction have been extracted by fitting two damped oscillations to the measured data. The starting expansion velocity was set by choosing a reasonable initial radius of the ensemble (Table 1). The other parameters arise from the measurements or simulations of the trapping potentials. The shaded areas in fig. 2 depict an error estimation of the expansion velocity oscillations obtained from performing the simulation by randomly choosing input parameters from within the error bars for 1000 simulation runs and calculating the mean value as well as the standard deviation for each t_{hold} .

Table 1 Source parameters for the instability estimation.

	σ_r (h/v) [μm]	σ_v (h/v) [mm s^{-1}]	N	t_p [s]
Molasses	750/750	30.9/30.9	4×10^8	2
ODT (41 μK)	65/6.2	62.7/44.5	2.3×10^7	2.7
ODT (41 μK) lensed	86/7.6	51.5/40.8	2.2×10^7	2.7
ODT (4 μK)	15.2/12.2	19.6/12	2.7×10^6	4.7
ODT (4 μK) lensed	49/12.2	9.2/12.9	2.6×10^6	4.7
BEC	3.8/3.3	2/2	4.3×10^5	8.2
BEC lensed	16.9/3.3	0.55/2.2	4.2×10^5	8.2
Advanced	5/5	2/2	1×10^6	1
Advanced lensed	46.1/46.1	0.14/0.14	1×10^6	1

Source parameters for the instability estimation for molasses cooled, released from the optical dipole trap (ODT) with and without evaporation, and Bose-Einstein condensates (BEC and Advanced). The values for the ensemble radius (σ_r) and expansion velocity (σ_v) are given for the horizontal (h) and vertical (v) direction, which corresponds to the transverse and longitudinal direction of the beam splitter respectively. N is the number of atoms and t_p the preparation time to calculate the cycle time t_{cycle} .

Scaling Ansatz. In the case of a thermal ensemble in the collision-less regime, the dynamics of a classical gas can be described using the scaling ansatz^{83,84}, which we briefly recall here for sake of simplicity. Here, the size of the ensemble scales with the time dependent dimensionless factor $b_i(t)$.

$$\ddot{b}_i(t) + \omega_i^2(t)b_i(t) - \omega_{0,i}^2 \frac{\theta_i(t)}{b_i(t)} + \omega_{0,i}^2 \xi \left(\frac{\theta_i(t)}{b_i(t)} - \frac{1}{b_i(t) \prod_j b_j(t)} \right) = 0 \quad (3)$$

$$\dot{\theta}_i(t) + 2 \frac{\dot{b}_i(t)}{b_i(t)} \theta_i(t) + \frac{1}{\tau} \left(\theta_i(t) - \frac{1}{3} \sum_j \theta_j(t) \right) = 0, \quad (4)$$

where θ_i acts as an effective temperature in the directions $i \in x, y, z$. Here $\omega_{0,i}$ denotes the initial angular trap frequency and $\omega_i(t)$ denotes the time-dependent angular trap frequency defined such as: $\omega_i(t) = \omega_{l,i}$ for $0 < t < t_{\text{hold}}$, with $\omega_{l,i}$ being the lensing potential, and $\omega_i(t) = 0$ after the release (see Fig. 1). This system of coupled differential equations contains the mean field interaction given by the factor:

$$\xi = \frac{E_{\text{mf}}}{E_{\text{mf}} + k_B T}, \quad (5)$$

with

$$E_{\text{mf}} = \frac{4\pi\hbar^2 a_s n_0}{m}, \quad (6)$$

where a_s is the s-wave scattering length, n_0 the peak density and m the mass of a single particle. Collision effects are also taken into account through

$$\tau = \tau_0 \times \left(\prod_j b_j \right) \times \left(\frac{1}{3} \sum_k \theta_k \right) \quad (7)$$

with the relaxation time

$$\tau_0 = \frac{5}{4\gamma} \quad (8)$$

and⁸⁴

$$\gamma = \frac{2}{\sqrt{2\pi}} n_0 \sigma_{\text{coll}} \sqrt{\frac{k_B T}{m}}. \quad (9)$$

In the special case of a BEC, the mean field energy is large compared to the thermal ensemble's energy ($\xi \approx 1$) and the time scale on which collisions appear goes to zero ($\tau \approx 0$). In this case the time dependent evolution of the matter-wave can be described following Castin & Dum⁸⁵. Here, the evolution of the BEC's Thomas-Fermi radius, $R_i(t) = b_i(t)R_i(0)$, is described by the time-dependent evolution of the scaling parameter:

$$\ddot{b}_i(t) + \omega_i^2(t)b_i(t) = \frac{\omega_i(0)}{b_i(t)b_x(t)b_y(t)b_z(t)} \quad (10)$$

and $R_i(0)$ is the initial Thomas-Fermi radius of the BEC along the i-th direction. It is worth to notice that recent studies^{86,87} extend the analysis of Guéry-Odelin⁸³ and Pedri et al.⁸⁴ to the BEC regime described by Castin & Dum⁸⁵.

With this set of equations the time evolution of the ensemble's size (σ_{r_i}) and velocity distribution (σ_{v_i}) is determined during the entire sequence of our matter-wave lensing sequence by

$$\sigma_{r_i}(t) = \sigma_{r_i}(0) \times b_i(t) \quad (11)$$

and

$$\sigma_{v_i}(t) = \frac{d\sigma_{r_i}(t)}{dt}. \quad (12)$$

The scaling parameter b_i can be applied either on the radius of a gaussian distributed thermal ensemble or the Thomas-Fermi radius of a BEC.

Estimation of instability in matter-wave sensors. The instability of a matter-wave sensor operating at the standard quantum limit can be estimated using Eq. (1). Here we assume Raman beam splitters ($n = 1$) with a $1/e^2$ -radius of 1.2 cm and a pulse duration of $t_n = 15 \mu\text{s}$. The contrast (C) is taken into account as the product of the excitation probabilities of the atom-light interactions during the Mach-Zehnder type interferometer following Loriani et al.⁷². Table 1 shows the source parameters used for the estimation of the instability. We chose three parameter sets from the here presented measurements of two thermal ensembles released from the optical dipole trap with starting temperatures of $T_0 = 41 \mu\text{K}$ and $4 \mu\text{K}$ and the BEC. Besides that we simulated the performance of the interferometer operated with a molasses cooled ensemble combined with a velocity selective Raman pulse of $30 \mu\text{s}$ ⁷³, based on typical parameters in our experiment, and an advanced scenario. For this we assume a BEC with 1×10^6 atoms after a preparation time $t_p = 1 \text{ s}$ with a starting expansion velocity of 2 mm s^{-1} , as anticipated for the VLBAI setup^{76,80}. We extrapolate the performance of our matter-wave lens for this experiment, resulting in expansion velocities of 0.135 mm s^{-1} corresponding to an equivalent 3D temperature of 200 pK .

Data availability

The data used in this manuscript are available from the corresponding author upon reasonable request.

Received: 20 September 2021; Accepted: 9 February 2022;

Published online: 16 March 2022

References

1. Kasevich, M. & Chu, S. Atomic interferometry using stimulated raman transitions. *Phys. Rev. Lett.* **67**, 181–184 (1991).
2. Kasevich, M. & Chu, S. Measurement of the gravitational acceleration of an atom with a light-pulse atom interferometer. *Appl. Phys. B* **54**, 321–332 (1992).
3. Riehle, F., Kisters, T., Witte, A., Helmcke, J. & Bordé, C. J. Optical ramsey spectroscopy in a rotating frame: Sagnac effect in a matter-wave interferometer. *Phys. Rev. Lett.* **67**, 177–180 (1991).
4. Cronin, A. D., Schmiedmayer, J. & Pritchard, D. E. Optics and interferometry with atoms and molecules. *Rev. Mod. Phys.* **81**, 1051–1129 (2009).
5. Biedermann, G. W. et al. Testing gravity with cold-atom interferometers. *Phys. Rev. A* **91**, 033629 (2015).
6. Bouchendira, R., Cladé, P., Guellati-Khélifa, S., Nez, F. & Biraben, F. New determination of the fine structure constant and test of the quantum electrodynamics. *Phys. Rev. Lett.* **106**, 080801 (2011).
7. Parker, R. H., Yu, C., Zhong, W., Estey, B. & Müller, H. Measurement of the fine-structure constant as a test of the standard model. *Science* **360**, 191–195 (2018).
8. Damour, T. Testing the equivalence principle: why and how? *Classical Quantum Gravity* **13**, A33–A41 (1996).
9. Schlippert, D. et al. Quantum test of the universality of free fall. *Phys. Rev. Lett.* **112**, 203002 (2014).
10. Albers, H. et al. Quantum test of the universality of free fall using rubidium and potassium. *The European Physical Journal D* **74** (2020).
11. Fray, S., Diez, C. A., Haensch, T. & Weitz, M. Atomic interferometer with amplitude gratings of light and its applications to atom based tests of the equivalence principle. *Phys. Rev. Lett.* **93**, 240404 (2004).
12. Bonnin, A., Zahzam, N., Bidel, Y. & Bresson, A. Simultaneous dual-species matter-wave accelerometer. *Phys. Rev. A* **88**, 043615 (2013).
13. Kuhn, C. et al. A bose-condensed, simultaneous dual-species mach-zehnder atom interferometer. *N. J. Phys.* **16**, 073035 (2014).
14. Tarallo, M. et al. Test of einstein equivalence principle for 0-spin and half-integer-spin atoms: Search for spin-gravity coupling effects. *Phys. Rev. Lett.* **113**, 023005– (2014).
15. Zhou, L. et al. Test of equivalence principle at 10^{-8} level by a dual-species double-diffraction raman atom interferometer. *Phys. Rev. Lett.* **115**, 013004 (2015).
16. Asenbaum, P., Overstreet, C., Kim, M., Curti, J. & Kasevich, M. A. Atom-interferometric test of the equivalence principle at the 10-12 level. *Phys. Rev. Lett.* **125**, 191101 (2020).
17. Tino, G. M. Testing gravity with cold atom interferometry: results and prospects. *Quantum Sci. Technol.* **6**, 024014 (2021).
18. Peters, A., Chung, K. Y. & Chu, S. Measurement of gravitational acceleration by dropping atoms. *Nature* **400**, 849–852 (1999).
19. Peters, A., Chung, K.-Y. & Chu, S. High-precision gravity measurements using atom interferometry. *Metrologia* **38**, 25– (2001).
20. Louchet-Chauvet, A. et al. The influence of transverse motion within an atomic gravimeter. *N. J. Phys.* **13**, 065025 (2011).
21. Freier, C. et al. Mobile quantum gravity sensor with unprecedented stability. *J. Phys.: Conf. Ser.* **723**, 012050 (2016).
22. Barrett, B. et al. Dual matter-wave inertial sensors in weightlessness. *Nature Communications* **7** (2016).
23. Hardman, K. et al. Simultaneous precision gravimetry and magnetic gradiometry with a bose-einstein condensate: A high precision, quantum sensor. *Phys. Rev. Lett.* **117**, 138501 (2016).
24. Gersemann, M., Gebbe, M., Abend, S., Schubert, C. & Rasel, E. M. Differential interferometry using a Bose-Einstein condensate. *Eur. Phys. J. D.* **74**, 203 (2020).
25. Savioi, D. et al. Interleaved atom interferometry for high-sensitivity inertial measurements. *Science Advances* **4** (2018).
26. Berg, P. et al. Composite-light-pulse technique for high-precision atom interferometry. *Phys. Rev. Lett.* **114**, 063002 (2015).
27. Stockton, J., Takase, K. & Kasevich, M. Absolute geodetic rotation measurement using atom interferometry. *Phys. Rev. Lett.* **107**, 133001 (2011).
28. Gauguet, A., Canuel, B., Lévéque, T., Chaibi, W. & Landragin, A. Characterization and limits of a cold-atom sagnac interferometer. *Phys. Rev. A* **80**, 063604 (2009).
29. Canuel, B. et al. Six-axis inertial sensor using cold-atom interferometry. *Phys. Rev. Lett.* **97**, 010402 (2006).
30. Geiger, R., Landragin, A., Merlet, S. & Santos, F. P. D. High-accuracy inertial measurements with cold-atom sensors. *AVS Quantum Sci.* **2**, 024702 (2020).
31. Hensel, T. et al. Inertial sensing with quantum gases: a comparative performance study of condensed versus thermal sources for atom interferometry. *Eur. Phys. J. D.* **75**, 108 (2021).
32. Heine, N. et al. A transportable quantum gravimeter employing delta-kick collimated bose-einstein condensates. *Eur. Phys. J. D.* **74**, 174 (2020).
33. Karcher, R., Imanaliev, A., Merlet, S. & Pereira Dos Santos, F. Improving the accuracy of atom interferometers with ultracold sources. *N. J. Phys.* **20**, 113041 (2018).
34. Schkolnik, V., Leykauf, B., Hauth, M., Freier, C. & Peters, A. The effect of wavefront aberrations in atom interferometry. *Appl. Phys. B* **120**, 311–316 (2015).
35. Szigeti, S. S., Debs, J. E., Hope, J. J., Robins, N. P. & Close, J. D. Why momentum width matters for atom interferometry with bragg pulses. *N. J. Phys.* **14**, 023009 (2012).
36. Abend, S. et al. Atom-chip fountain gravimeter. *Phys. Rev. Lett.* **117**, 203003 (2016).
37. Dickerson, S. M., Hogan, J. M., Sugabaker, A., Johnson, D. M. S. & Kasevich, M. A. Multiaxis inertial sensing with long-time point source atom interferometry. *Phys. Rev. Lett.* **111**, 083001 (2013).
38. Gebbe, M. et al. Twin-lattice atom interferometry. *Nat. Commun.* **12**, 2544 (2021).
39. McDonald, G. D. et al. $80/\hbar k$ momentum separation with bloch oscillations in an optically guided atom interferometer. *Phys. Rev. A* **88**, 053620 (2013).
40. Chiow, S.-w., Kovachy, T., Chien, H.-C. & Kasevich, M. $102/\hbar k$ Large Area Atom Interferometers. *Phys. Rev. Lett.* **107**, 130403 (2011).
41. Debs, J. E. et al. Cold-atom gravimetry with a bose-einstein condensate. *Phys. Rev. A* **84**, 033610 (2011).
42. Chiow, S.-w., Herrmann, S., Chu, S. & Müller, H. Noise-immune conjugate large-area atom interferometers. *Phys. Rev. Lett.* **103**, 050402 (2009).
43. Cladé, P., Guellati-Khélifa, S., Nez, F. & Biraben, F. Large momentum beam splitter using bloch oscillations. *Phys. Rev. Lett.* **102**, 240402– (2009).
44. Deppner, C. et al. Collective-mode enhanced matter-wave optics. *Phys. Rev. Lett.* **127**, 100401 (2021).
45. Kruse, I. et al. Improvement of an atomic clock using squeezed vacuum. *Phys. Rev. Lett.* **117**, 143004 (2016).
46. Szigeti, S. S., Nolan, S. P., Close, J. D. & Haine, S. A. High-precision quantum-enhanced gravimetry with a bose-einstein condensate. *Phys. Rev. Lett.* **125**, 100402 (2020).
47. Anders, F. et al. Momentum entanglement for atom interferometry. *Phys. Rev. Lett.* **127**, 140402 (2021).
48. Corgier, R., Gaaloul, N., Smerzi, A. & Pezzè, L. Delta-kick squeezing. *Phys. Rev. Lett.* **127**, 183401 (2021).
49. Rudolph, J. et al. A high-flux bec source for mobile atom interferometers. *N. J. Phys.* **17**, 065001 (2015).
50. Chu, S., Bjorkholm, J. E., Ashkin, A. & Cable, A. Experimental observation of optically trapped atoms. *Phys. Rev. Lett.* **57**, 314–317 (1986).
51. Stellmer, S., Grimm, R. & Schreck, F. Production of quantum-degenerate strontium gases. *Phys. Rev. A* **87**, 013611 (2013).

52. Roy, R., Green, A., Bowler, R. & Gupta, S. Rapid cooling to quantum degeneracy in dynamically shaped atom traps. *Phys. Rev. A* **93**, 043403 (2016).

53. Anderegg, L. et al. Laser cooling of optically trapped molecules. *Nat. Phys.* **14**, 890–893 (2018).

54. Carr, L. D., DeMille, D., Krems, R. V. & Ye, J. Cold and ultracold molecules: science, technology and applications. *N. J. Phys.* **11**, 055049 (2009).

55. Grimm, R., Weidemüller, M. & Ovchinnikov, Y. B. Optical dipole traps for neutral atoms. In *Advances In Atomic, Molecular, and Optical Physics*, vol. 42, 95–170 (Elsevier, 2000).

56. Martínez, I. A., Petrosyan, A., Guéry-Odelin, D., Trizac, E. & Ciliberto, S. Engineered swift equilibration of a brownian particle. *Nat. Phys.* **12**, 843–846 (2016).

57. Salomon, G., Fouché, L., Lepoutre, S., Aspect, A. & Bourdel, T. All-optical cooling of 39K to Bose-Einstein condensation. *Phys. Rev. A* **90**, 033405 (2014).

58. O'Hara, K. M., Gehm, M. E., Granade, S. R. & Thomas, J. E. Scaling laws for evaporative cooling in time-dependent optical traps. *Phys. Rev. A* **64**, 051403 (2001).

59. Condon, G. et al. All-optical bose-einstein condensates in microgravity. *Phys. Rev. Lett.* **123**, 240402 (2019).

60. Ammann, H. & Christensen, N. Delta kick cooling: A new method for cooling atoms. *Phys. Rev. Lett.* **78**, 2088–2091 (1997).

61. Morinaga, M., Bouchoule, I., Karam, J.-C. & Salomon, C. Manipulation of motional quantum states of neutral atoms. *Phys. Rev. Lett.* **83**, 4037–4040 (1999).

62. Myrskog, S. H., Fox, J. K., Moon, H. S., Kim, J. B. & Steinberg, A. M. Modified “δ-kick cooling” using magnetic field gradients. *Phys. Rev. A* **61**, 053412 (2000).

63. Luan, T., Li, Y., Zhang, X. & Chen, X. Realization of two-stage crossed beam cooling and the comparison with delta-kick cooling in experiment. *Rev. Sci. Instrum.* **89**, 123110 (2018).

64. Kanthak, S. et al. Time-domain optics for atomic quantum matter. *N. J. Phys.* **23**, 093002 (2021).

65. Gochnauer, D., Rahman, T., Wirth-Singh, A. & Gupta, S. Interferometry in an atomic fountain with ytterbium bose-einstein condensates. *Atoms* **9**, 58 (2021).

66. Chu, S., Bjorkholm, J. E., Ashkin, A., Gordon, J. P. & Hollberg, L. W. Proposal for optically cooling atoms to temperatures of the order of 10^{-6} K. *Opt. Lett.* **11**, 73 (1986).

67. Li, R.-Z. et al. Expansion dynamics of a spherical bose-einstein condensate. *Chin. Phys. B* **28**, 106701 (2019).

68. Corgier, R. et al. Interacting quantum mixtures for precision atom interferometry. *N. J. Phys.* **22**, 123008 (2020).

69. Bertoldi, A., Minardi, F. & Prevedelli, M. Phase shift in atom interferometers: Corrections for nonquadratic potentials and finite-duration laser pulses. *Phys. Rev. A* **99**, 033619 (2019).

70. Antoine, C. Rotating matter-wave beam splitters and consequences for atom gyroscopes. *Phys. Rev. A* **76**, 033609 (2007).

71. Cheinet, P. et al. Measurement of the sensitivity function in a time-domain atomic interferometer. *IEEE Trans. Instrum. Meas.* **57**, 1141–1148 (2008).

72. Loriani, S. et al. Atomic source selection in space-borne gravitational wave detection. *N. J. Phys.* **21**, 063030 (2019).

73. Kasevich, M. et al. Atomic velocity selection using stimulated raman transitions. *Phys. Rev. Lett.* **66**, 2297–2300 (1991).

74. Abe, M. et al. Matter-wave Atomic Gradiometer Interferometric Sensor (MAGIS-100). *Quantum Sci. Technol.* **6**, 044003 (2021).

75. Badurina, L. et al. AION: an atom interferometer observatory and network. *J. Cosmol. Astropart. Phys.* **2020**, 011–011 (2020).

76. Hartwig, J. et al. Testing the universality of free fall with rubidium and ytterbium in a very large baseline atom interferometer. *N. J. Phys.* **17**, 035011 (2015).

77. Zhou, L. et al. Development of an atom gravimeter and status of the 10-meter atom interferometer for precision gravity measurement. *Gen. Rel. Gravit.* **43**, 1931–1942 (2011).

78. Kulas, S. et al. Miniaturized lab system for future cold atom experiments in microgravity. *Microgravity Sci. Technol.* **29**, 37–48 (2016).

79. Vogt, C. et al. Evaporative cooling from an optical dipole trap in microgravity. *Phys. Rev. A* **101**, 013634 (2020).

80. Schlippert, D. et al. Matter-wave interferometry for inertial sensing and tests of fundamental physics. In *CPT and Lorentz Symmetry* (WORLD SCIENTIFIC, 2020).

81. Schilling, M. et al. Gravity field modelling for the hannover 10 m atom interferometer. *J. Geodesy* **94**, 122 (2020).

82. Zaiser, M. et al. Simple method for generating bose-einstein condensates in a weak hybrid trap. *Phys. Rev. A* **83**, 035601 (2011).

83. Guéry-Odelin, D. Mean-field effects in a trapped gas. *Phys. Rev. A* **66**, 033613 (2002).

84. Pedri, P., Guéry-Odelin, D. & Stringari, S. Dynamics of a classical gas including dissipative and mean-field effects. *Phys. Rev. A* **68**, 043608 (2003).

85. Castin, Y. & Dum, R. Bose-einstein condensates in time dependent traps. *Phys. Rev. Lett.* **77**, 5315–5319 (1996).

86. Modugno, M., Pagnini, G. & Valle-Basagoiti, M. A. Effective self-similar expansion for the gross-pitaevskii equation. *Phys. Rev. A* **97**, 043604 (2018).

87. Viedma, D. & Modugno, M. Effective self-similar expansion of a bose-einstein condensate: Free space versus confined geometries. *Phys. Rev. Res.* **2**, 033478 (2020).

Acknowledgements

This work is funded by the German Space Agency (DLR) with funds provided by the Federal Ministry of Economic Affairs and Energy (BMWi) due to an enactment of the German Bundestag under Grant Nos. DLR 50WM1641 (PRIMUS-III), DLR 50WM2041 (PRIMUS-IV), DLR 50WM2245A (CAL-II), DLR 50WM2060 (CARIOQA), and DLR 50RK1957 (QGYRO). We acknowledge financial support from the Deutsche Forschungsgemeinschaft (DFG, German Research Foundation)-Project-ID 274200144-SFB 1227 DQ-mat within the projects A05, B07, and B09, and -Project-ID 434617780-SFB 1464 TerraQ within the projects A02 and A03 and Germany's Excellence Strategy—EXC-2123 QuantumFrontiers—Project-ID 390837967 and from “Niedersächsisches Vorab” through the “Quantum- and Nano-Metrology (QUANOMET)” initiative within the Project QT3. A.H. and D.S. acknowledge support by the Federal Ministry of Education and Research (BMBF) through the funding program Photonics Research Germany under contract number 13N14875.

Author contributions

W.E., E.M.R., and D.S. designed the experimental setup and the dipole trapping laser system. H.A., A.H., A.R., and D.S. contributed to the design, operation, and maintenance of the laser system and the overall setup. R.C., E.C. and N.G. set the theoretical framework of this work. H.A., R.C., C.S., and D.S. drafted the initial manuscript. H.A., and R.C. performed the analysis of the data presented in this manuscript. H.A., and R.C. under lead of N.G. and C.S. performed the instability study. C.V., M.W., C.L., S.H. together with the other authors discussed and evaluated the results and contributed to, reviewed, and approved of the manuscript.

Funding

Open Access funding enabled and organized by Projekt DEAL.

Competing interests

The authors declare no competing interests.

Additional information

Correspondence and requests for materials should be addressed to Dennis Schlippert.

Peer review information *Communications Physics* thanks the anonymous reviewers for their contribution to the peer review of this work.

Reprints and permission information is available at <http://www.nature.com/reprints>

Publisher's note Springer Nature remains neutral with regard to jurisdictional claims in published maps and institutional affiliations.



Open Access This article is licensed under a Creative Commons Attribution 4.0 International License, which permits use, sharing, adaptation, distribution and reproduction in any medium or format, as long as you give appropriate credit to the original author(s) and the source, provide a link to the Creative Commons license, and indicate if changes were made. The images or other third party material in this article are included in the article's Creative Commons license, unless indicated otherwise in a credit line to the material. If material is not included in the article's Creative Commons license and your intended use is not permitted by statutory regulation or exceeds the permitted use, you will need to obtain permission directly from the copyright holder. To view a copy of this license, visit <http://creativecommons.org/licenses/by/4.0/>.

2.5 MATTER-WAVE COLLIMATION TO PICOKELVIN ENERGIES WITH SCATTERING LENGTH AND POTENTIAL SHAPE CONTROL

Authors: Alexander Herbst, Timothé Estrampes, Henning Albers, Robin Corgier, Knut Stolzenberg, Sebastian Bode, Eric Charron, Ernst M. Rasel, Naceur Gaaloul, and Dennis Schlippert

Journal: Communications Physics

Article Number: 7 132 (2024)

DOI: [10.1038/s42005-024-01621-w](https://doi.org/10.1038/s42005-024-01621-w)

Author contribution: A.H., H.A., S.B., E.M.R. and D.S. designed the experimental setup and the dipole trapping laser system. A.H., H.A., S.B., K.S., E.M.R. and D.S. contributed to the design, operation, and maintenance of the overall setup. T.E., R.C., E.C. and N.G. set the theoretical framework of this work. A.H., T.E. and H.A. with support of R.C., E.C. and N.G. performed the analysis of the data presented in this manuscript. A.H., T.E. and R.C. with support of D.S., E.C., E.M.R. and N.G. drafted the initial manuscript. All authors discussed and evaluated the results and contributed to, reviewed, and approved of the manuscript.

<https://doi.org/10.1038/s42005-024-01621-w>

Matter-wave collimation to picokelvin energies with scattering length and potential shape control

Check for updates

Alexander Herbst¹, Timothé Estrampes^{1,2}, Henning Albers¹, Robin Corgier^{1,3}, Knut Stolzenberg¹, Sebastian Bode¹, Eric Charron^{1,2}, Ernst M. Rasel¹, Naceur Gaaloul¹ & Dennis Schlippert¹

The sensitivity of atom interferometers depends on their ability to realize long pulse separation times and prevent loss of contrast by limiting the expansion of the atomic ensemble within the interferometer beam through matter-wave collimation. Here we investigate the impact of atomic interactions on collimation by applying a lensing protocol to a ³⁹K Bose-Einstein condensate at different scattering lengths. Tailoring interactions, we measure energies corresponding to (340 ± 12) pK in one direction. Our results are supported by an accurate simulation, which allows us to extrapolate a 2D ballistic expansion energy of (438 ± 77) pK. Based on our findings we propose an advanced scenario, which enables 3D expansion energies below 16 pK by implementing an additional pulsed delta-kick. Our results pave the way to realize ensembles with more than 1×10^5 atoms and 3D energies in the two-digit pK range in typical dipole trap setups without the need for micro-gravity or long baseline environments.

Cooling quantum gases to sub-nanokelvin temperatures has enabled breakthroughs in the fields of quantum sensing¹, quantum information², and quantum simulation³. Especially in precision sensing and metrology, atom interferometers^{4–7} have become a state-of-the-art solution and are used for probing general relativity^{8–11}, quantum mechanics^{12–15}, determining fundamental constants^{16–18}, and measuring inertial effects^{19–23}. Interferometers utilizing molasses-cooled atoms, characterized by expansion energies in the range of several microkelvin, offer short experimental cycle times and a high sensor bandwidth^{24–26}. Despite these advantages, their velocity spread limits the accessible free-fall distance and their systematic uncertainty is typically restrained at a few 10^{-8} ms⁻² due to wave-front distortions, when the ensemble is expanding within the interferometer beam^{27,28}. In contrast, Bose-Einstein condensates (BECs)^{29,30} offer significant advantages with respect to controlling systematic errors and their dynamic behavior^{31,32}. In optical dipole traps (ODTs), BECs of various atomic species readily achieve expansion energies in the range of a few tens of nanokelvin^{33–35}, enhancing coherence time and signal-to-noise ratio. However, to meet the demands of future precision experiments, further collimation into the picokelvin regime is required to achieve the long pulse separation times necessary and to avoid loss of contrast^{36–40}. Expansion energies of a few hundred picokelvin have been achieved by direct evaporative cooling⁴¹ and spin gradient cooling⁴². Additionally,

advancements using different types of matter-wave lenses have further reduced expansion energies by an order of magnitude^{43–45}. In this regime, extended free-fall times prior to applying the lens are crucial to minimize atomic interactions, which would otherwise drive the expansion post-lensing^{46,47}. Hence, recent records of a few tens of picokelvin have been realized in unique experimental settings utilizing micro-gravity^{48,49} or long-baseline devices⁴⁷ which both allow for an initial prolonged expansion of the ensemble. In this paper we demonstrate an alternative approach to resolve this issue by use of a Feshbach resonance^{50,51} to tailor interactions during the lens and upon release from the trapping potential. Using a ³⁹K BEC in the weak interaction regime, we observe expansion energies below 400 pK in one dimension. Through dedicated theory simulations, we extrapolate this result to two dimensions, yielding a 2D energy below 500 pK. We hence demonstrate a substantial improvement over previous results achieved with the same method and setup using ⁸⁷Rb⁵². Furthermore, our systematic analysis reveals that the careful adjustment of trapping frequencies and interactions will allow to reach 3D expansion energies below 16 pK, when implementing an additional delta-kick collimation (DKC) pulse⁴³ after a few milliseconds of free fall. Hence, our method allows for state-of-the-art collimation in typical or even compact quantum optics experiments, without excessive hardware or environmental requirements.

¹Leibniz Universität Hannover, Institut für Quantenoptik, Welfengarten 1, 30167 Hannover, Germany. ²Université Paris-Saclay, CNRS, Institut des Sciences Moléculaires d'Orsay, 91405 Orsay, France. ³LNE-SYRTE, Observatoire de Paris, Université PSL, CNRS, Sorbonne Université 61 avenue de l'Observatoire, 75014 Paris, France. e-mail: schlippert@iqo.uni-hannover.de

Results and discussion

Lensing protocol

We apply the matter-wave lensing protocol as described by Albers et al.⁵². A detailed overview of the setup is provided in the experimental apparatus section. The atoms are held in a crossed ODT with recycled beam configuration crossing under an angle of 70°. In the following, the $\{x, y, z\}$ -coordinate system refers to the trap frame as defined by the principal axes of the confining potential and is used to specify all trap frequencies. We image the $\{x', z\}$ -plane, obtaining the camera frame $\{x', y', z\}$ by rotating around the vertical z -axis by approximately 30°. To implement time-averaged optical potentials⁵³ we perform a center-position modulation (CPM) along the horizontal axis of the trapping beams, using an acousto-optical modulator (AOM). This approach allows to create harmonic traps with variable width and depth in the horizontal $\{x, y\}$ -plane, but does not feature independent control of the trap frequencies in x - and y -direction or changing the potential shape in z -direction. By rapidly relaxing the trap within 50 μ s we cause a sudden reduction in trap frequencies from initial frequencies ω_i^I to final frequencies $\omega_i^F < \omega_i^I$ for $i \in \{x, y\}$, inducing collective mode excitations^{54,55}. Subsequently, the ensemble is collimated by turning off the trapping potential at the turning point of the resulting oscillations of the ensemble size.

We apply this method at two different scattering lengths 158 a_0 and 10 a_0 at which the interaction and kinetic energy terms, respectively, dominate (c.f. theoretical model section). In the following we differentiate between expansion energies along a singular axis in i -direction (E_i^{1D}), 2D energies in the horizontal plane in which the matter-wave lens is applied (E^{2D}), and the full three-dimensional expansion energy (E^{3D}). For both measurements at the two different scattering lengths, we use the same initial and final trap configurations, with small variations of the parameters resulting only from pointing instabilities of the ODT beams which we relate to the time passed between the two measurement campaigns. In both cases, the initial trap is realized without any CPM. We find initial trapping frequencies of $2\pi \times \{72, 144, 115\}$ Hz for 158 a_0 and $2\pi \times \{62, 149, 96\}$ Hz for 10 a_0 . After relaxation our final trap frequencies are $2\pi \times \{23, 36, 126\}$ Hz for 158 a_0 and $2\pi \times \{24, 38, 129\}$ Hz for 10 a_0 . In parallel the trap depth is maintained by increasing the laser intensity, suppressing atom number loss.

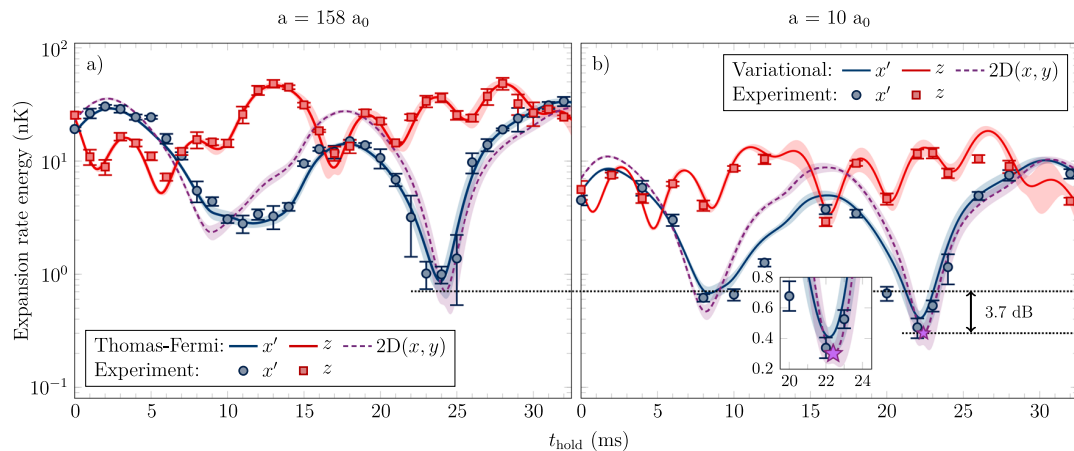


Fig. 1 | Measured and simulated expansion rate energies in one and two dimensions. All measurements (blue circles and red squares) are performed within the camera frame and based on time-of-flight (TOF) series with a total length of 25 ms. The error bars arise from the fit uncertainty of the expansion in the individual TOF series (c.f. data acquisition and analysis section). The dynamics of the ensemble are simulated (lines) simultaneously for all directions within the trap frame for 25 ms TOF and are subsequently transformed into the camera frame. Uncertainty bands are obtained by a Monte-Carlo method based on the detection angle and trap frequency errors matching the oscillations of the ensemble size. Panel a shows the results obtained in the strong interaction regime for a scattering length of 158 a_0 , using the Thomas-Fermi approximation in the theoretical description. Panel

Based on time-of-flight (TOF) measurements of the ensemble's expansion, we determine the expansion energies along the horizontal (collimated) x' - and vertical (not collimated) z -direction within the camera frame for different holding times t_{hold} , after relaxing the trap.

Obtained energies

At a scattering length of 158 a_0 (Fig. 1a) the minimal value in the collimated direction yields $E_x^{1D} = (1.00 \pm 0.17)$ nK and is achieved after a holding time of 24 ms. For 10 a_0 (Fig. 1b) we find the minimum for a holding time of 22 ms after decompression, resulting in a minimal value of $E_x^{1D} = (340 \pm 12)$ pK after up to 25 ms TOF. While the behavior derived from simulations (c.f. data acquisition and analysis section) agrees with these findings, for the points below 1 nK a portion of interaction energy remains and the ensemble has not yet reached the linear expansion regime at that point. When correcting for this effect, by simulating for a TOF of 250 ms the asymptotic behavior yields a minimum of $E_x^{1D} = (429 \pm 56)$ pK after a holding time of 22.1 ms. The excellent agreement between experiment and simulation allows to understand the ensemble's dynamics in the entire horizontal plane, as both theoretical approaches feature coupling of ensemble oscillations in all directions. Including the axis which cannot be directly observed, we extrapolate the resulting 2D expansion energies as depicted by the dashed purple lines in Fig. 1. At 10 a_0 we find a minimal value of $E^{2D} = (301 \pm 65)$ pK for a TOF of 25 ms, which corresponds to an improvement by 3.7 dB over the 158 a_0 case. Extending the simulation to the ballistic regime as before, yields a final value of $E^{2D} = (438 \pm 77)$ pK for 250 ms TOF (Fig. 2a).

Comparison to previous results

In this work we applied our matter-wave collimation protocol previously developed for ^{87}Rb to a ^{39}K BEC and proved the ease of application to another atomic species, demonstrating a reduction of the expansion energy by 13 dB compared to the non-collimated case, as given for vanishing holding time. Considering the mass ratio of both elements, the obtained energy of (1.00 ± 0.17) nK for ^{39}K at 158 a_0 , corresponding to an expansion velocity of (0.46 ± 0.04) mm s $^{-1}$, is comparable to the previously achieved result of (3.2 ± 0.6) nK $\equiv (0.55 \pm 0.05)$ mm s $^{-1}$ with ^{87}Rb ⁵² at its natural

b shows the results obtained in the weak interaction regime at 10 a_0 scattering length. Here we simulate the dynamics based on a variational approach (c.f. theoretical model section). For the data we choose a lower sampling rate, allowing us to increase the number of points per TOF measurement to resolve the lower expansion energies, effectively. In both interaction regimes the measurements agree well with the simulation and the coupling of the dynamics in all dimensions allows for extrapolation of the behavior in the entire horizontal plane as shown by the purple dashed lines. We find an overall improvement of 3.7 dB in the extrapolated 2D expansion rate energy when reducing the scattering length. The purple star highlights the minimum 2D energy at 10 a_0 , as prominently featured in the inset.

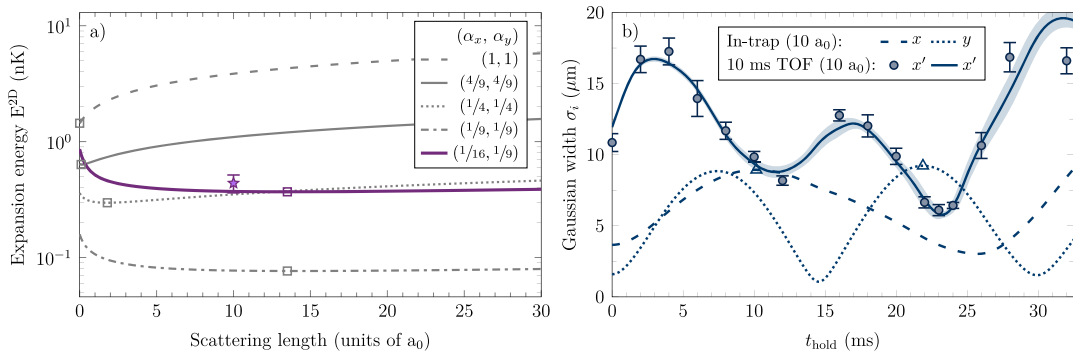


Fig. 2 | Ensemble dynamics in the collimated plane. Panel **a** shows the simulated 2D expansion energy E^{2D} in the collimated plane for different scaling factors α_i and for the configuration used in the experiment (see lensing protocol section) for 250 ms time-of-flight (TOF). For a common frequency reduction along both lensed directions with $\alpha_x = \alpha_y$ taking the values $\{1, 4/9, 1/4, 1/9\}$, the minimal energies are obtained for a scattering length a being respectively $\{0, 0.1, 1.8, 13.5\} a_0$ and identified by the squares for each case. The sequence becomes more robust against changes in the scattering length with larger frequency reduction, as the minima become more shallow. The purple star resembles the lowest 2D experimental expansion energy presented in Fig. 1b (obtained here for 250 ms TOF). While the curves are simulated for a fixed set of parameters, this point is obtained within a Monte-Carlo simulation including all experimental uncertainties. The error bar

denotes 2σ deviation while the central point stands for the mean value (see data acquisition and analysis section). Qualitatively, the experimental configuration closely resembles the case of $\alpha_x = \alpha_y = 1/9$. The resulting expansion energies are globally shifted towards higher values, since $\alpha_x \approx 1/16$ and $\alpha_y \approx 1/9$. This causes the optimal release points to differ for each axis as marked by the triangle symbols in panel **b**, highlighting the importance of a symmetric choice of α -values. Here, the measured ensemble width in x' -direction is shown as blue circles for 10 ms TOF at $10 a_0$ and the error bars represent the standard deviation of at least four measurements. The simulated size after 10 ms TOF is shown as a solid blue line, while the corresponding oscillations of the ensemble widths in x - and y -direction within the trapping potential are shown with blue dashed and dotted lines, respectively.

background scattering length of $\sim 100 a_0$ ⁵⁶. The remaining difference can be attributed to variations in the trap frequency ratios between the two experiments, rather than to the difference in scattering length, since changing the latter by less than a few multiples does not significantly affect the expansion rate when staying within the strong interaction regime^{57,58}. Hence, the observed outcome aligns with expectations as the technique only depends on the ensemble's dynamics governed by interactions and trap frequencies and is accurately described through the Gross-Pitaevskii equation. More importantly, we show that the final expansion energy after the lens can be further reduced by transitioning into the weak interaction regime, as done here by minimizing the scattering length by means of a magnetic Feshbach resonance. By reducing the repulsive forces driving the expansion after release from the trap, we achieve expansion energies well below 1 nK, which is necessary to match the requirements of proposed experiments, e.g. for, but not limited to, gravitational wave detection^{59–64}, a test of the Weak Equivalence Principle^{8,11,65} or the search for dark matter^{66–68}. While the energies realized here are still an order of magnitude larger than in previous demonstrations in two⁴⁷ and three dimensions⁴⁸, our method can be applied directly in the ODT. Hence it is suitable for setups and applications that do not allow for an extended pre-expansion time before applying the lens due to constraints regarding experimental cycle time or spatial dimensions. Lower expansion energies are currently limited by the achievable maximum CPM amplitude of 200 μm which in turn restricts the range of accessible trapping frequencies to the values given in the lensing protocol section.

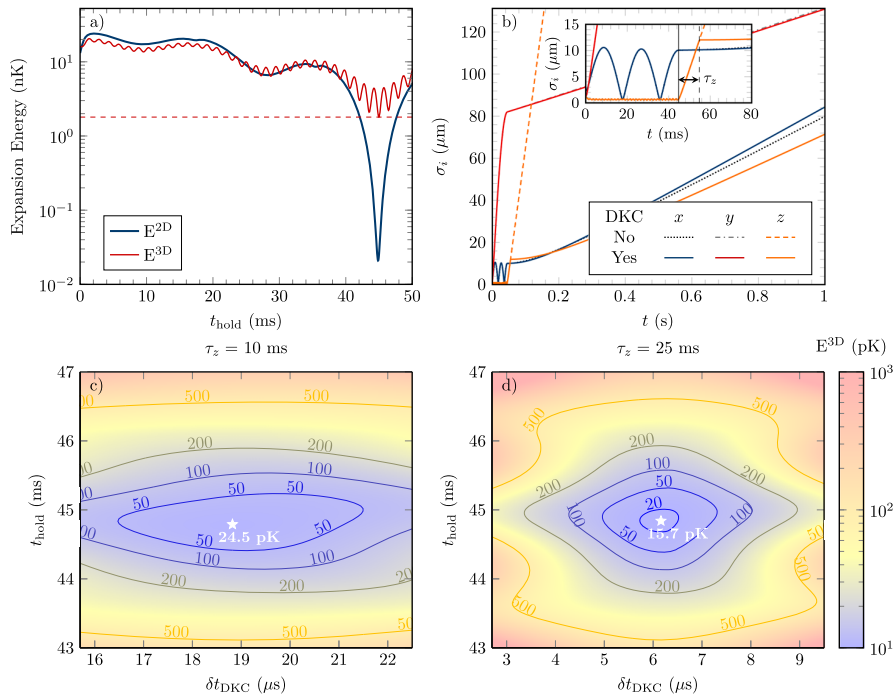
Scattering length and trap frequency dependencies

To gain insight into the impact of the scattering length on the collimation, we analyze the ensemble's behavior in the weak interaction regime by simulating the dynamics with an adapted theoretical model for two different scenarios (Fig. 2a). Starting from trap frequencies of $2\pi \times 60$ Hz in all directions, we apply a common reduction in the horizontal plane while maintaining the frequency along the z -axis, as shown by the theoretical gray lines. For all scenarios, we evaluate the optimal holding time after relaxing the trap for minimizing E^{2D} and study the behavior for different squared trap frequency ratios $\alpha_i = (\omega_i^F/\omega_i^L)^2$, which would provide the energy scaling in the ideal gas regime⁶⁹. As previously discussed by Kovachy et al.⁴⁷ and also observed here, the energy reduction for a BEC is significantly higher due to

an interplay of interactions and coupling of the oscillations of the ensemble widths along each axis. From the theory simulations, we find a reduction of the expansion energy towards a smaller scattering length for $\alpha_x = \alpha_y > 4/9$ as shown by the dashed gray line. This result matches the expected dynamics of an ensemble during free-fall expansion without any additional collimation and is explained by repulsive interactions after removing the trapping potential^{33,57,58}. We identify minimal expansion energy at non-zero interactions for $\alpha_x = \alpha_y \lesssim 4/9$, as depicted by the continuous, dotted, and dash-dotted gray lines. These curves clearly show that for smaller values of α_i , reaching optimal energies requires moving towards higher scattering length values. While in these cases minimizing the interaction energy still reduces the corresponding forces upon release, it also reduces the final ensemble width within the trap. Hence, the kinetic energy from the resulting fundamental momentum spread as given by the uncertainty principle increases and the optimal scattering length must be found considering both contributions. To achieve a minimum momentum spread in free-fall one hence wants to increase the interactions during the lens to maximize the cloud size and cancel them at the release time. However, given that the interactions are controlled via magnetic fields such an optimization is technically not feasible, as it typically takes tens of milliseconds to change the magnetic field⁵¹. Therefore the optimal scattering length has to be found as a trade-off between the maximum size achievable within the trap and minimal repulsive interactions in free fall along the horizontal direction. Such optimized configurations are highlighted by the empty squares in Fig. 2a. Regarding the experimental setup, as shown by the purple line, where the change in aspect ratio is not the same for both directions, $\alpha_x \approx 1/16$ and $\alpha_y \approx 1/9$, we recover the same behavior as described above for the case $\alpha_x = \alpha_y \lesssim 4/9$, but with globally higher energies. The similarity can be explained by the fact that $\sqrt{\alpha_x \alpha_y} = 1/12$. Note here that the purple star is identical to the one already shown in Fig. 1b.

To get further insight into the complex behavior of the matter-wave for different aspect ratios we now compare in Fig. 2b the simulated in-trap oscillations in x - and y -direction, respectively presented with dashed and dotted lines, with the observed ensemble width after 10 ms TOF at $a = 10 a_0$. From the experimental measurements (blue points) we find two distinct minima, each of which can be assigned to the maxima of the underlying ensemble widths within the trap along a different axis (empty blue triangles). In this specific case, the lowest expansion energy E^{2D} is found near the

Fig. 3 | Generating a delta-kick collimated Bose-Einstein condensate in the regime of tens of pK. We take advantage of the holding process after trap relaxation to minimize the energy in the $\{x, y\}$ -plane (a) (red line). Subsequently, a short free-fall time (pre-TOF) τ_z allows the ensemble to expand, followed by a delta-kick collimation (DKC) to collimate the third direction (b). We show the width evolution in all three directions after the optimal holding period without (non-solid lines) and with a DKC (solid lines). The inset shows the dynamics in the trapping potential, highlighting release (solid black line) and DKC (black dashed line) timings. This process leads to a reduced 3D expansion energy expressed as a function of the lensing time and the DKC duration after a pre-TOF of 10 ms (c) and 25 ms (d), leading to respectively 24.5 pK and 15.7 pK.



optimal collimation of the y -direction, closely resembling the case $\alpha_x = \alpha_y = 1/9$ in Fig. 2a. Compared to the symmetric case the globally higher energies are hence explained by the energy contribution of the other direction, which always exhibits a non-vanishing expansion at release, as long as the aspect ratios are not integer multiples of each other. When performing additional simulations at $a = 30 a_0$, we further note that the optimal release timing is extremely robust with respect to changes in the scattering length, giving only 0.3 ms offset in this particular case. While in practice such changes might arise from technical limitations, e.g., due to imperfect control of the Feshbach field, the offset is fundamentally expected, since changing the repulsive interactions within the trap alters the frequency of the excited oscillations.

Overall, our analysis yields the choice of trapping frequencies to be more important due to their enhanced scaling and the effects of asymmetric expansion compared to the exact scattering length knowledge which is more difficult to pinpoint in practice. Besides allowing to extraction of the 2D expansion energy from the measurements, the adequacy between the experiment and theory model in Figs. 1 and 2 allow us in the following to identify advanced collimation scenarios. Consecutively, we discuss two 3D collimation sequences based on the combination of a 2D in-trapped collimation combined with a pulse delta-kick method collimating the third axis to reach the pK regime^{48,70}.

Advanced scenario

Since neither the demonstrated method nor the experimental apparatus is designed to collimate the remaining vertical axis, the achievable 3D expansion energies are limited to the nanokelvin regime, regardless of the performance in the horizontal plane, as shown by the horizontal dashed line in Fig. 3a. To overcome this limitation we consider a short free-fall time (pre-TOF) τ_z at the end of the holding process followed by a pulsed DKC protocol^{13,47–49}. We study the theoretically achievable expansion energies for this sequence in an advanced scenario which is specifically tailored towards the capabilities of an improved apparatus⁷¹ and highlight the crucial requirements for the implementation. Instead of a recycled ODT, the setup features two individually controllable beams, each with up to 16 W of optical power at a wavelength of 1064 nm. This configuration allows us to realize a variety of possible trap geometries and especially to design common turning points for the

oscillations of the ensemble widths along both principal axes. Furthermore, 2D acousto-optical deflectors (AODs) [AA Opto-Electronic DTSXY-400-1064] are used to create time-averaged optical potentials instead of the previously used AOM. In combination with the implemented lens system, their superior bandwidth allows for CPM amplitudes of at least 1.5 mm and consequently to access lower final trap frequencies and expansion energies. Finally, for the DKC, the second AOD axis is needed to shift the ODT beams vertically and match the position of the atomic cloud for a maximum pre-TOF of $\tau_z = 25$ ms, corresponding to a free-fall distance of 3 mm.

For E^{2D} we numerically find minimal values below 20 pK for a holding time of 42.5 ms switching the trap frequencies from $2\pi \times \{152.7, 310.7, 342.6\}$ Hz to $2\pi \times \{28.1, 5.6, 340.0\}$ Hz at $10 a_0$ scattering length (Fig. 3a). For the final trap configuration 150 mW of optical power at a CPM amplitude of 175 μm for one and 450 mW with 800 μm modulation stroke for the other beam is required. Since the frequency along the vertical axis is much higher than the two others, the DKC (black dashed line in the inset of Fig. 3b) will not significantly affect the other direction as shown by the black dotted and dash-dotted curves in Fig. 3b. For an easy configuration with only $\tau_z = 10$ ms pre-TOF, corresponding to a free-fall distance of 490 μm , experimentally accessible in practice, we obtain a minimal 3D expansion energy of $E^{3D} = 24.5$ pK with a $\delta t_{DKC} = 18.8$ μs long delta-kick pulse and 44.8 ms of lensing as shown in Fig. 3c and optimized using a simulated annealing algorithm⁷². Moreover, the implementation is expected to be robust against variations of the experimental parameters as it allows to achieve energies below 50 pK for a wide range of holding and delta-kick durations. Even better performance can be obtained by increasing the pre-TOF duration at the expense of the overall robustness with respect to the delta-kick timing⁴³. For $\tau_z = 25$ ms of pre-TOF, we find final energies as low as $E^{3D} = 15.7$ pK, but requiring a DKC of only $\delta t_{DKC} = 6.2$ μs (Fig. 3d). The simulation explicitly takes the AOD's response time of 3 μs into account, as it is on the same order of magnitude as δt_{DKC} . While other experimental limitations, e.g., due to the bandwidth of the different control loops may apply, the AOD is the slowest component involved and therefore poses the relevant limitation for the advanced scenario, contrary to the measurements in Fig. 1. Nevertheless, such timings can be experimentally challenging when being limited to the center-position modulation frequency below 100 kHz as relevant time scale or using rf-switches with switching times of several μs .

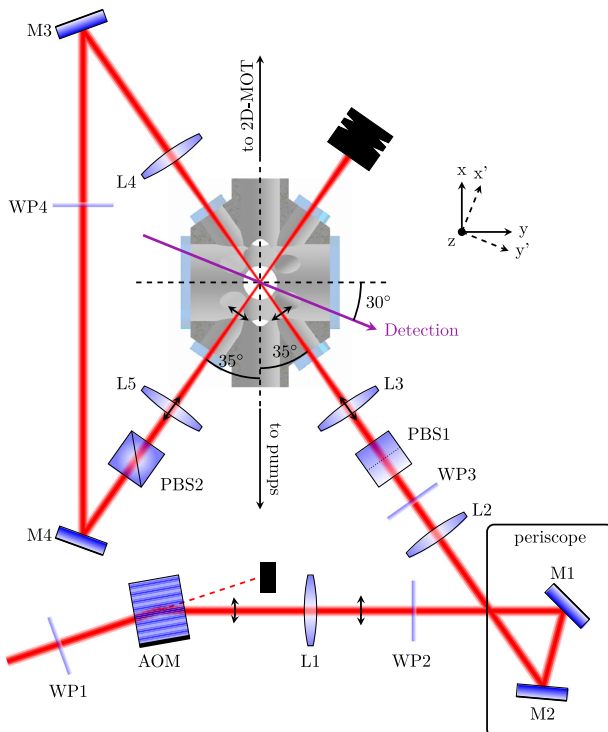


Fig. 4 | Optical dipole trap setup. Time-averaged potentials are implemented with an acousto-optical modulator (AOM). A three-lens system (L_1 , L_2 , L_3) with focal lengths $f_1 = 100$ mm, $f_2 = 300$ mm and $f_3 = 150$ mm, translates the change in AOM deflection angle into a parallel displacement, while simultaneously focusing the beam to a waist of 30 (45) μm in horizontal (vertical) direction. The lenses L_4 and L_5 ($f_{4,5} = 150$ mm) are used to re-collimate the beam after passing the experimental chamber and to re-focus it on the atoms. At each point, optimal polarization is ensured by wave plates (WP1–WP4) with additional orthogonal-oriented polarizing beam splitters (PBS1 and PBS2) in front of the chamber for polarization cleaning. Dielectric mirrors (M1 – M4) are used to guide the beam through the setup. For perfect alignment and equal beam power the trap frame $\{x, y, z\}$, as given by the principal axes of the optical potential, resembles the symmetry axes of the vacuum chamber. The camera frame $\{x', y', z\}$ is obtained by a rotation around the z -axis, with the exact detection angle depending on the beam configuration and alignment. The figure is taken from Albers et al.⁵² and openly licensed via CC BY 4.0. Here the orientation of the detection arrow and the naming of the coordinate systems was altered to account for changes of the apparatus compared to the source material.

For such short signals, arbitrary waveform generators based on direct digital synthesizers (DDS) with a high sampling rate offer a convincing solution. In this case, we use a software-defined radio [Ettus USRP X310], whose DDS allows to interrupt the waveform at any given sample and match the pulse length with a resolution of 50 ns for a typical sampling rate of 20 MHz. As before using a low scattering length assists in the overall collimation. However, simulating the same sequence for a scattering length of $158 a_0$ in particular, still leads to expansion energies of $E^{\text{3D}} = 97.5$ pK for $\tau_z = 10$ ms of pre-TOF and $E^{\text{3D}} = 81.9$ pK for 25 ms pre-TOF with 17.6 μs and 7.1 μs long delta-kick pulses, respectively.

Hence, the analyzed two-step process opens up the path to approach ($a = 158 a_0$) and even exceed ($a = 10 a_0$) the results that were obtained in a drop-tower⁴⁸, on the International Space Station⁴⁹, and within a long-baseline device⁴⁷. Combining these results with a strategy for rapid evaporation⁷¹ and a bright source for fast magneto-optical trap (MOT) loading⁷³, compact or even field-deployable devices can reach experimental repetition rates higher than 0.5 Hz with BECs consisting of 3×10^5 atoms and state-of-the-art collimation.

Methods

Experimental apparatus

We use the same setup as for the previous matter-wave lens study with ^{87}Rb ⁵², featuring a crossed ODT in recycled beam configuration (Fig. 4). A detailed description of the vacuum, laser, and coil systems used can be found in previous publications^{8,10,74}. The ODT is based on a 1960 nm fiber laser [IPG TLR-50-1960-LP] which is intensity stabilized by a feedback loop, controlling a linearized Pockels cell. The crossed trap is realized by recycling the same beam, passing the atoms again under an angle of 70°. We ensure orthogonal beam polarization to avoid running lattice formation. Due to the elliptical beam shape of the fiber laser output, we obtain different beam waists of 30 μm in horizontal and 45 μm in vertical direction. Taking losses at all optical elements into account, the maximal power that can be delivered to the atoms is limited to 8 W for the initial and 6 W for the recycled beam. A custom-made AOM [Polytec ATM-1002FA53.24] is used to deflect the beam, thereby creating time-averaged optical potentials of harmonic shape along one beam axis^{53,75}. It is further utilized to control the beam power at the lower end of the intensity stabilization. By focusing the beam onto the atomic cloud, the change in deflection angle of the AOM is translated into a parallel displacement of the beam. For the initial beam, the bandwidth of the AOM allows for a maximum CPM amplitude of 200 μm . For the recycled beam, the same configuration corresponds to a CPM amplitude of 300 μm due to the additional re-collimation and re-focusing, and the increased path length in-between. Due to the experimental configuration, the recycled beam is fully determined by the state of the initial beam and hence the setup does not allow to choose the trap frequencies in x - and y -direction independently. The required frequency modulation of the rf-signal driving the AOM is generated with a combination of a voltage-controlled oscillator [Mini-Circuits ZOS-150+] to provide the actual signal and an arbitrary waveform generator [Rigol DG1022Z], which provides the waveform. For the whole experimental sequence, a constant modulation frequency of 20 kHz is used, which is sufficiently large compared to any occurring trap frequency. We define the trap frame $\{x, y, z\}$ as the principal axes of the trapping potential, given by the eigenvectors of the curvature in the critical point. In the case of equal ODT beams in terms of power and waist, it resembles the symmetry axis of the experimental setup as shown in Fig. 4, while any deviations from the ideal beam configuration result in rotations of the coordinate system around the z -axis. Finally, detection is performed by absorption imaging with unity magnification. The camera is situated in the $\{x, y\}$ -plane and the related camera frame $\{x', y', z\}$ can be obtained from the trap frame $\{x, y, z\}$ by rotating clockwise around the z -axis by an angle of $\sim 30^\circ$. Note, that the exact angle depends on the beam configuration prior to detection due to the resulting rotation of the trap frame.

Ensemble preparation

We apply a trap loading and state preparation sequence optimized for ^{39}K as described earlier⁷⁴. We load a 3D-magneto-optical trap on the D_2 -line from a 2D-MOT, trapping 1×10^9 atoms within 4 s. Subsequently, we apply a hybrid D_1 - D_2 compression MOT to increase the ensemble's density and gray molasses cooling on the D_1 -line for cooling the ensemble to sub-Doppler temperatures⁷⁶. In this manner, we prepare 4×10^8 atoms at a temperature of 12 μK within 56 ms after turning off the 2D-MOT. For loading the ODT we use a center-position modulation amplitude of 160 μm to improve the mode matching of the crossing region with the cloud, transferring 12×10^6 atoms into the 54 μK deep ODT, with a temperature of 8.5 μK . Afterward, we prepare the ensemble in $|F = 1, m_F = -1\rangle$ with a multi-loop state preparation scheme based on microwave adiabatic rapid passages. This allows to use the broad Feshbach resonance at 32.6 G⁷⁷ to adjust the scattering length to positive values, necessary for direct evaporative cooling⁷⁸. We use the evaporation sequence optimized for the largest number of condensed particles, rather than the shortest experimental cycle time with the highest atomic flux, realizing a quasi-pure BEC of up to 2×10^5 atoms after 3.9 s of evaporative cooling at a scattering length of $158 a_0$. For the measurement at $158 a_0$ we perform the matter-wave lens 100 ms after creating the BEC by increasing the center-position modulation

amplitude to the achievable maximum, as stated before. For the measurement at $10 a_0$, we additionally adiabatically sweep the magnetic field towards the broad minimum between the resonance at 32.6 G and the next higher one at 162.8 G after creating the BEC and before performing the matter-wave lens.

Data acquisition and analysis

We perform TOF measurements for different holding times after relaxing the trap with a total experimental cycle time of 12 s. Subsequently, we describe the obtained density profile either by a Gaussian or a Thomas-Fermi distribution, depending on the scattering length used. For the measurements at $158 a_0$ the Thomas-Fermi radii $R_i(t)$ are transformed into their equivalent standard deviation $\sigma_i(t)$ using $\sigma_i(t) = R_i(t)/\sqrt{7}$ ^{39,70}. Individual data points are taken for a holding time spacing of 1 ms and a TOF spacing of 5 ms. Each measurement is repeated at least four times. At $10 a_0$ we fit a Gaussian to the obtained density distribution. For these measurements, the TOF spacing is reduced to 1 ms at the expense of the holding time spacing which is increased to at least 2 ms, in order to obtain better statistics for the extracted ensemble expansion. For each individual dataset, measurements are performed over the course of 12 h of continuous operation. With this approach, we ensure comparability within each dataset and avoid trap frequency drifts caused by thermal effects from power cycling the 1960 nm laser in between measurement days. To obtain the linear expansion rate for a given holding time, we only consider the data taken for more than 10 ms TOF, avoiding the resolution limitation of our detection system. Finally, the fitted expansion rates v_i are transformed into 1D expansion energy using $E_i^{1D} = k_B T_i/2 = mv_i^2/2$.

To simulate the behavior of the ensemble, we determine the trapping frequencies by fitting the oscillations of the ensemble width with respect to the holding time for a constant TOF in the trap frame and by projecting them into the rotated camera frame, afterward. Since the detection angle relative to the trap frame changes with respect to small deviations of the ODT beam alignment, the exact angle is evaluated for each measurement separately and fitted to the data, as well. We optimize the fit parameters on five different TOFs in between 10 and 25 ms simultaneously with equal weighting, obtaining a single set of values, which provide the overall smallest error. Based on the frequencies found, we perform simulations of the ensemble's behavior using the two approaches provided in the theoretical model section. The error bands stem from 1000 Monte-Carlo simulations within the obtained errors of trap frequencies, detection angle and scattering length (at $10 a_0$) as determined by fitting the ensemble width and the magnetic field characterization of the apparatus.

For the advanced scenario, we take experimental parameters and technical limitations of the setup, e.g., the rise time of the AOD, into account. We search for optimal 3D collimation by simulating a grid with a step size of 36 μ s for the lensing and 62 ns for the DKC, using a simulated annealing algorithm⁷² for the absolute minimum in each case.

Theoretical model

For a scattering length of $158 a_0$, the interaction energy exceeds the kinetic energy of the ensemble, so the BEC dynamics is well described by the scaling equations as derived by Castin et al.⁷⁰ and Kagan et al.⁸⁰:

$$\ddot{\lambda}_i(t) + \omega_i^2(t)\lambda_i(t) = \frac{\omega_i^2(0)}{\lambda_i\lambda_x\lambda_y\lambda_z}, \quad (1)$$

where the dimensionless variable $\lambda_i(t) = R_i(t)/R_i(0)$ characterizes the evolution of the size of the condensate in the direction $i \in \{x, y, z\}$. In this expression, $R_i(t)$ is the Thomas-Fermi radius in the direction i , and the initial radius is given by⁸¹

$$R_i(0) = a_{\text{osc}} \frac{\bar{\omega}(0)}{\omega_i(0)} \left(\frac{15Na}{a_{\text{osc}}} \right)^{1/5}, \quad (2)$$

with the average length of the quantum harmonic oscillator $a_{\text{osc}} = [\hbar/m\bar{\omega}(0)]^{1/2}$ and the geometric mean of the initial trapping frequencies $\bar{\omega}(0) = [\omega_x(0)\omega_y(0)\omega_z(0)]^{1/3}$. From the solution of Eq. (1) we extract the standard deviations $\sigma_i(t) = R_i(t)/\sqrt{7}$ associated with the atomic density, which we compare with the experimental measurements obtained as described in the data acquisition and analysis section.

In the case of a scattering length of $10 a_0$, the Thomas-Fermi approximation is no longer suitable to accurately describe the dynamics of the BEC. Instead, we follow a variational approach and describe the BEC with a Gaussian ansatz^{82,83}. This leads to a harmonic trap to the following set of coupled differential equations

$$\ddot{\sigma}_i(t) + \omega_i^2(t)\sigma_i(t) = \frac{\hbar^2}{4m^2\sigma_i^3(t)} + \frac{\hbar^2aN}{4\sqrt{\pi}m^2\sigma_i\sigma_x\sigma_y\sigma_z}, \quad (3)$$

for the standard deviations $\sigma_i(t)$ of the atomic density. The time-independent version of Eq. (3) is used to determine the initial size $\sigma_i(0)$ of the ensemble, which converges to the oscillator length for vanishing scattering length.

Data availability

The data used in this manuscript is available from the corresponding author upon reasonable request.

Received: 2 November 2023; Accepted: 5 April 2024;

Published online: 25 April 2024

References

1. Degen, C. L., Reinhard, F. & Cappellaro, P. Quantum sensing. *Rev. Mod. Phys.* **89**, 035002 (2017).
2. Mandel, O. et al. Controlled collisions for multi-particle entanglement of optically trapped atoms. *Nature* **425**, 937–940 (2003).
3. Georgescu, I. M., Ashhab, S. & Nori, F. Quantum simulation. *Rev. Mod. Phys.* **86**, 153–185 (2014).
4. Kasevich, M. & Chu, S. Atomic interferometry using stimulated Raman transitions. *Phys. Rev. Lett.* **67**, 181–184 (1991).
5. Kasevich, M. & Chu, S. Measurement of the gravitational acceleration of an atom with a light-pulse atom interferometer. *Appl. Phys. B* **54**, 321–332 (1992).
6. Riehle, F., Kisters, T., Witte, A., Helmcke, J. & Bordé, C. J. Optical Ramsey spectroscopy in a rotating frame: Sagnac effect in a matter-wave interferometer. *Phys. Rev. Lett.* **67**, 177–180 (1991).
7. Cronin, A. D., Schmiedmayer, J. & Pritchard, D. E. Optics and interferometry with atoms and molecules. *Rev. Mod. Phys.* **81**, 1051–1129 (2009).
8. Schlippert, D. et al. Quantum test of the universality of free fall. *Phys. Rev. Lett.* **112**, 203002 (2014).
9. Tarallo, M. G. et al. Test of Einstein equivalence principle for 0-spin and half-integer-spin atoms: Search for spin-gravity coupling effects. *Phys. Rev. Lett.* **113**, 023005 (2014).
10. Albers, H. et al. Quantum test of the universality of free fall using rubidium and potassium. *Eur. Phys. J. D* **74**, 145 (2020).
11. Asenbaum, P., Overstreet, C., Kim, M., Curti, J. & Kasevich, M. A. Atom-interferometric test of the equivalence principle at the 10^{-12} level. *Phys. Rev. Lett.* **125**, 191101 (2020).
12. Carlesso, M. et al. Present status and future challenges of non-interferometric tests of collapse models. *Nat. Phys.* **18**, 243–250 (2022).
13. Kovachy, T. et al. Quantum superposition at the half-metre scale. *Nature* **528**, 530–533 (2015).
14. Bassi, A., Lochan, K., Satin, S., Singh, T. P. & Ulbricht, H. Models of wave-function collapse, underlying theories, and experimental tests. *Rev. Mod. Phys.* **85**, 471–527 (2013).

15. Schrinski, B., Haslinger, P., Schmiedmayer, J., Hornberger, K. & Nimmrichter, S. Testing collapse models with bose-einstein-condensate interferometry. *Phys. Rev. A* **107**, 043320 (2023).
16. Rosi, G., Sorrentino, F., Cacciapuoti, L., Prevedelli, M. & Tino, G. M. Precision measurement of the Newtonian gravitational constant using cold atoms. *Nature* **510**, 518–521 (2014).
17. Parker, R. H., Yu, C., Zhong, W., Estey, B. & Müller, H. Measurement of the fine-structure constant as a test of the standard model. *Science* **360**, 191–195 (2018).
18. Morel, L., Yao, Z., Cladé, P. & Guellati-Khélifa, S. Determination of the fine-structure constant with an accuracy of 81 parts per trillion. *Nature* **588**, 61–65 (2020).
19. Gustavson, T. L., Bouyer, P. & Kasevich, M. A. Precision rotation measurements with an atom interferometer gyroscope. *Physical Review Letters* **78**, 2046–2049 (1997).
20. Canuel, B. et al. Six-axis inertial sensor using cold-atom interferometry. *Phys. Rev. Lett.* **97**, 010402 (2006).
21. Dickerson, S. M., Hogan, J. M., Sugabaker, A., Johnson, D. M. S. & Kasevich, M. A. Multiaxis inertial sensing with long-time point source atom interferometry. *Phys. Rev. Lett.* **111**, 083001 (2013).
22. Dutta, I. et al. Continuous cold-atom inertial sensor with 1 nrad/sec rotation stability. *Phys. Rev. Lett.* **116**, 183003 (2016).
23. Savoie, D. et al. Interleaved atom interferometry for high-sensitivity inertial measurements. *Sci. Adv.* **4**, eaau7948 (2018).
24. Le Gouët, J. et al. Limits to the sensitivity of a low noise compact atomic gravimeter. *Appl. Phys. B* **92**, 133–144 (2008).
25. Hu, Z.-K. et al. Demonstration of an ultrahigh-sensitivity atom-interferometry absolute gravimeter. *Phys. Rev. A* **88**, 043610 (2013).
26. Ménoret, V. et al. Gravity measurements below 10-9 g with a transportable absolute quantum gravimeter. *Sci. Rep.* **8**, 12300 (2018).
27. Louchet-Chauvet, A. et al. The influence of transverse motion within an atomic gravimeter. *N. J. Phys.* **13**, 065025 (2011).
28. Schkolnik, V., Leykauf, B., Hauth, M., Freier, C. & Peters, A. The effect of wavefront aberrations in atom interferometry. *Appl. Phys. B* **120**, 311–316 (2015).
29. Anderson, M., Ensher, J., Matthews, M., Wieman, C. & Cornell, E. Observation of Bose-Einstein condensation in a dilute atomic vapor. *Science* **269**, 198–201 (1995).
30. Davis, K. B., Mewes, M.-O., Joffe, M. A., Andrews, M. R. & Ketterle, W. Evaporative cooling of sodium atoms. *Phys. Rev. Lett.* **74**, 5202–5205 (1995).
31. Schlippert, D. et al. Matter-wave interferometry for inertial sensing and tests of fundamental physics. In: *CPT and Lorentz Symmetry* (WORLD SCIENTIFIC, 2021).
32. Hensel, T. et al. Inertial sensing with quantum gases: a comparative performance study of condensed versus thermal sources for atom interferometry. *Eur. Phys. J. D* **75**, 108 (2021).
33. Weber, T., Herbig, J., Mark, M., Nägele, H.-C. & Grimm, R. Bose-Einstein condensation of cesium. *Science (New York, N.Y.)* **299**, 232–235 (2003).
34. Hardman, K. S. et al. Simultaneous precision gravimetry and magnetic gradiometry with a bose-einstein condensate: a high precision, quantum sensor. *Phys. Rev. Lett.* **117**, 138501 (2016).
35. Gochauer, D., Rahman, T., Wirth-Singh, A. & Gupta, S. Interferometry in an atomic fountain with ytterbium bose-einstein condensates. *Atoms* **9**, 58 (2021).
36. Aguilera, D. N. et al. Ste-quest—test of the universality of free fall using cold atom interferometry. *Classical Quant. Grav.* **31**, 115010 (2014).
37. Trimeche, A. et al. Concept study and preliminary design of a cold atom interferometer for space gravity gradiometry. *Classical Quant. Grav.* **36**, 215004 (2019).
38. Loriani, S. et al. Atomic source selection in space-borne gravitational wave detection. *N. J. Phys.* **21**, 063030 (2019).
39. Corgier, R. et al. Interacting quantum mixtures for precision atom interferometry. *N. J. Phys.* **22**, 123008 (2020).
40. Struckmann, C. et al. Platform and environment requirements of a satellite quantum test of the weak equivalence principle at the 10^{-17} level. *Phys. Rev. D* **109**, 064010 (2024).
41. Leanhardt, A. E. et al. Cooling Bose-Einstein condensates below 500 picokelvin. *Science (New York, N.Y.)* **301**, 1513–1515 (2003).
42. Medley, P., Weld, D. M., Miyake, H., Pritchard, D. E. & Ketterle, W. Spin gradient demagnetization cooling of ultracold atoms. *Phys. Rev. Lett.* **106**, 195301 (2011).
43. Ammann, H. & Christensen, N. Delta kick cooling: a new method for cooling atoms. *Phys. Rev. Lett.* **78**, 2088–2091 (1997).
44. Kalnins, J. G., Amini, J. M. & Gould, H. Focusing a fountain of neutral cesium atoms with an electrostatic lens triplet. *Phys. Rev. A* **72**, 043406 (2005).
45. Müntinga, H. et al. Interferometry with bose-einstein condensates in microgravity. *Phys. Rev. Lett.* **110**, 093602 (2013).
46. Ketterle, W. & Druten, N. V. In *Advances In Atomic, Molecular, and Optical Physics*. 181–236 (Elsevier, 1996).
47. Kovachy, T. et al. Matter wave lensing to picokelvin temperatures. *Phys. Rev. Lett.* **114**, 143004 (2015).
48. Deppner, C. et al. Collective-mode enhanced matter-wave optics. *Phys. Rev. Lett.* **127**, 100401 (2021).
49. Gaaloul, N. et al. A space-based quantum gas laboratory at picokelvin energy scales. *Nat. Commun* **13**, 7889 (2022).
50. Inouye, S. et al. Observation of feshbach resonances in a bose-einstein condensate. *Nature* **392**, 151–154 (1998).
51. Masi, L. et al. Multimode trapped interferometer with noninteracting bose-einstein condensates. *Phys. Rev. Res.* **3**, 043188 (2021).
52. Albers, H. et al. All-optical matter-wave lens using time-averaged potentials. *Commun. Phys.* **5**, 60 (2022).
53. Roy, R., Green, A., Bowler, R. & Gupta, S. Rapid cooling to quantum degeneracy in dynamically shaped atom traps. *Phys. Rev. A* **93**, 043403 (2016).
54. Jin, D. S., Ensher, J. R., Matthews, M. R., Wieman, C. E. & Cornell, E. A. Collective excitations of a Bose-Einstein condensate in a dilute gas. *Phys. Rev. Lett.* **77**, 420–423 (1996).
55. Mewes, M.-O. et al. Collective excitations of a Bose-Einstein condensate in a magnetic trap. *Phys. Rev. Lett.* **77**, 988–991 (1996).
56. Egorov, M. et al. Measurement of s-wave scattering lengths in a two-component bose-einstein condensate. *Phys. Rev. A* **87**, 053614 (2013).
57. Kraemer, T. et al. Optimized production of a cesium Bose-Einstein condensate. *Appl. Phys. B* **79**, 1013–1019 (2004).
58. Roati, G. et al. ³⁹K Bose-Einstein condensate with tunable interactions. *Phys. Rev. Lett.* **99**, 010403 (2007).
59. Hogan, J. M. et al. An atomic gravitational wave interferometric sensor in low earth orbit (agis-leo). *Gen. Relativ. Gravit.* **43**, 1953–2009 (2011).
60. Canuel, B. et al. Exploring gravity with the miga large scale atom interferometer. *Sci. Rep.* **8**, 14064 (2018).
61. Zhan, M.-S. et al. ZAIGA: Zhaoshan long-baseline atom interferometer gravitation antenna. *Int. J. Mod. Phys. D* **29**, 1940005 (2019).
62. Schubert, C. et al. Scalable, symmetric atom interferometer for infrasound gravitational wave detection <http://arxiv.org/abs/1909.01951> (2019).
63. Canuel, B. et al. Elgar—a European laboratory for gravitation and atom-interferometric research. *Classical Quant Grav* **37**, 225017 (2020).
64. Badurina, L. et al. Aion: an atom interferometer observatory and network. *J. Cosmol. Astroparticle Phys.* **2020**, 011 (2020).
65. Ahlers, H. et al. Ste-quest: Space time explorer and quantum equivalence principle space test <https://arxiv.org/abs/2211.15412> (2022).

66. El-Neaj, Y. A. et al. Aedge: Atomic experiment for dark matter and gravity exploration in space. *EPJ Quant. Technol.* **7**, 6 (2020).
67. Du, Y., Murgui, C., Pardo, K., Wang, Y. & Zurek, K. M. Atom interferometer tests of dark matter. *Phys. Rev. D* **106**, 095041 (2022).
68. Badurina, L., Gibson, V., McCabe, C. & Mitchell, J. Ultralight dark matter searches at the sub-hz frontier with atom multigradiometry. *Phys. Rev. D* **107**, 055002 (2023).
69. Chu, S., Bjorkholm, J. E., Ashkin, A., Gordon, J. P. & Hollberg, L. W. Proposal for optically cooling atoms to temperatures of the order of 10^{-6} K. *Opt. Lett.* **11**, 73 (1986).
70. Corgier, R. et al. Fast manipulation of bose-einstein condensates with an atom chip. *N. J. Phys.* **20**, 055002 (2018).
71. Herbst, A. et al. High-flux source system for matter-wave interferometry exploiting tunable interactions. *Phys. Rev. Res.* **6**, 013139 (2024).
72. Kirkpatrick, S., Gelatt, C. D. & Vecchi, M. P. Optimization by simulated annealing. *Science* **220**, 671–680 (1983).
73. Catani, J., Maioli, P., De Sarlo, L., Minardi, F. & Inguscio, M. Intense slow beams of bosonic potassium isotopes. *Phys. Rev. A* **73**, 033415 (2006).
74. Herbst, A., Albers, H., Stolzenberg, K., Bode, S. & Schlippe, D. Rapid generation of all-optical ^{39}K bose-einstein condensates using a low-field feshbach resonance. *Phys. Rev. A* **106**, 043320 (2022).
75. Albers, H. *Time-averaged Optical Potentials for Creating and Shaping Bose-einstein Condensates*. Ph.D. thesis (Leibniz Universität Hannover, 2020).
76. Salomon, G. et al. Gray-molasses cooling of ^{39}K to a high phase-space density. *EPL (Europhysics Letters)* **104**, 63002 (2013).
77. D'Errico, C. et al. Feshbach resonances in ultracold ^{39}K . *N. J. Phys.* **9**, 223 (2007).
78. Landini, M. et al. Direct evaporative cooling of ^{39}K atoms to bose-einstein condensation. *Phys. Rev. A* **86**, 033421 (2012).
79. Castin, Y. & Dum, R. Bose-einstein condensates in time dependent traps. *Phys. Rev. Lett.* **77**, 5315–5319 (1996).
80. Kagan, Y., Surkov, E. L. & Shlyapnikov, G. V. Evolution of a bose gas in anisotropic time-dependent traps. *Phys. Rev. A* **55**, R18 (1997).
81. Pethick, C. J. & Smith, H. Theory of the condensed state. In: *Bose-Einstein Condensation in Dilute Gases*. 159–181 (Cambridge University Press, 2008).
82. Pérez-García, V. M., Michinel, H., Cirac, J. I., Lewenstein, M. & Zoller, P. Low energy excitations of a Bose-Einstein condensate: a time-dependent variational analysis. *Phys. Rev. Lett.* **77**, 5320–5323 (1996).
83. Pérez-García, V. M., Michinel, H., Cirac, J. I., Lewenstein, M. & Zoller, P. Dynamics of Bose-einstein condensates: variational solutions of the Gross-Pitaevskii equations. *Phys. Rev. A* **56**, 1424–1432 (1997).

Acknowledgements

We thank Dorothee Tell for thorough proofreading. This work is funded by the German Space Agency (DLR) with funds provided by the Federal Ministry for Economic Affairs and Climate Action due to an enactment of the German Bundestag under Grant No. DLR 50WM2041 (PRIMUS-IV), 50WM2253A (AI-Quadrat) and supported by the “ADI 2022” project founded by the IDEX Paris-Saclay, ANR-11-IDEX-0003-02. The authors further acknowledge

support by the Federal Ministry of Education and Research (BMBF) through the funding program Photonics Research Germany under contract number 13N14875 and by the Deutsche Forschungsgemeinschaft (DFG, German Research Foundation)-Project-ID 274200144-the SFB 1227 DQ-mat within Project No. A05 and B07 and under Germany's Excellence Strategy—EXC-2123 QuantumFrontiers—Project-ID 390837967.

Author contributions

A.H., H.A., S.B., E.M.R., and D.S. designed the experimental setup and the dipole trapping laser system. A.H., H.A., S.B., K.S., E.M.R., and D.S. contributed to the design, operation, and maintenance of the overall setup. T.E., R.C., E.C., and N.G. set the theoretical framework of this work. A.H., T.E., and H.A. with the support of R.C., E.C., and N.G. performed the analysis of the data presented in this manuscript. A.H., T.E., and R.C. with the support of D.S., E.C., E.M.R., and N.G. drafted the initial manuscript. All authors discussed and evaluated the results and contributed to, reviewed, and approved the manuscript.

Funding

Open Access funding enabled and organized by Projekt DEAL.

Competing interests

The authors declare no competing interests.

Additional information

Correspondence and requests for materials should be addressed to Dennis Schlippe.

Peer review information *Communications Physics* thanks Donatella Casettari, Tiffany Harte and the other, anonymous, reviewer(s) for their contribution to the peer review of this work.

Reprints and permissions information is available at <http://www.nature.com/reprints>

Publisher's note Springer Nature remains neutral with regard to jurisdictional claims in published maps and institutional affiliations.

Open Access This article is licensed under a Creative Commons Attribution 4.0 International License, which permits use, sharing, adaptation, distribution and reproduction in any medium or format, as long as you give appropriate credit to the original author(s) and the source, provide a link to the Creative Commons licence, and indicate if changes were made. The images or other third party material in this article are included in the article's Creative Commons licence, unless indicated otherwise in a credit line to the material. If material is not included in the article's Creative Commons licence and your intended use is not permitted by statutory regulation or exceeds the permitted use, you will need to obtain permission directly from the copyright holder. To view a copy of this licence, visit <http://creativecommons.org/licenses/by/4.0/>.

© The Author(s) 2024

CONCLUSION AND OUTLOOK

3.1 SUMMARY

In this thesis a high flux source system for collimated ^{39}K BECs was realized based on tunable interactions and potential shape control through TAPs. The dynamic tuning of trap frequencies and interactions along the evaporation ramps allowed to create BECs with $(6.14 \pm 0.35) \times 10^4$ condensed particles after only 170 ms of evaporative cooling. It was further shown how this evaporative flux of more than 3×10^5 particles/s can be maintained when transitioning to a longer evaporation duration. In this manner BECs of $(5.73 \pm 0.24) \times 10^5$ condensed particles were created with less than 2 s of evaporative cooling. These results exceed the performance of most other devices by a large margin and even reach the evaporative flux of atom chip traps with strong magnetic confinement [102].

Furthermore, tunable interactions were used to enhance a novel all-optical matter-wave lens based on TAPs. By transitioning into the weak interaction regime ensembles with a 2D expansion energy of (438 ± 77) pK were realized. Dedicated theory simulations allowed to arrive at a thorough and accurate understanding of the related matter-wave dynamics. Ultimately, these findings resulted in a proposed experimental sequence, which has the potential to significantly improve the obtained results by combining a continuous and pulsed DKC. This sequence can only be realized due to the many different upgrades the experiment has undergone in the course of this thesis and explicitly takes into account all remaining technical limitations. With expected 3D expansion energies below 20 pK, this work paves the way to achieve state-of-the-art collimation in common laboratory setups, otherwise only realizable in long-baseline devices [137] or in micro-gravity environments [104].

3.2 FURTHER ENHANCEMENT OF ATOMIC FLUX

As highlighted by the purple stars in Figure 3.1a, the evaporation duration realized in this thesis are only matched by a machine-learning optimized device which, however, features an order of magnitude fewer atoms in the condensate [115]. To the best of my knowledge, the realized evaporation sequence is thus the world's fastest for atom numbers at the order of 10^4 and above, as required for interferometry applications. However, when comparing the total atomic flux, as done in Figure 3.1b, the overall performance of the setup falls short compared to other realizations.

While the all-optical approach avoids a magnetic trap as an intermediate step and enables loading the ODT and preparing the m_F -state within 200 ms, loading the MOT requires 5 s and therefore poses the relevant limitation for the cycle time. More rapid loading schemes have been demonstrated successfully based on bright sources. Utilizing a 2D⁺-MOT configuration [149, 150] already allows to load the subsequent 3D-MOT within few 100 ms.

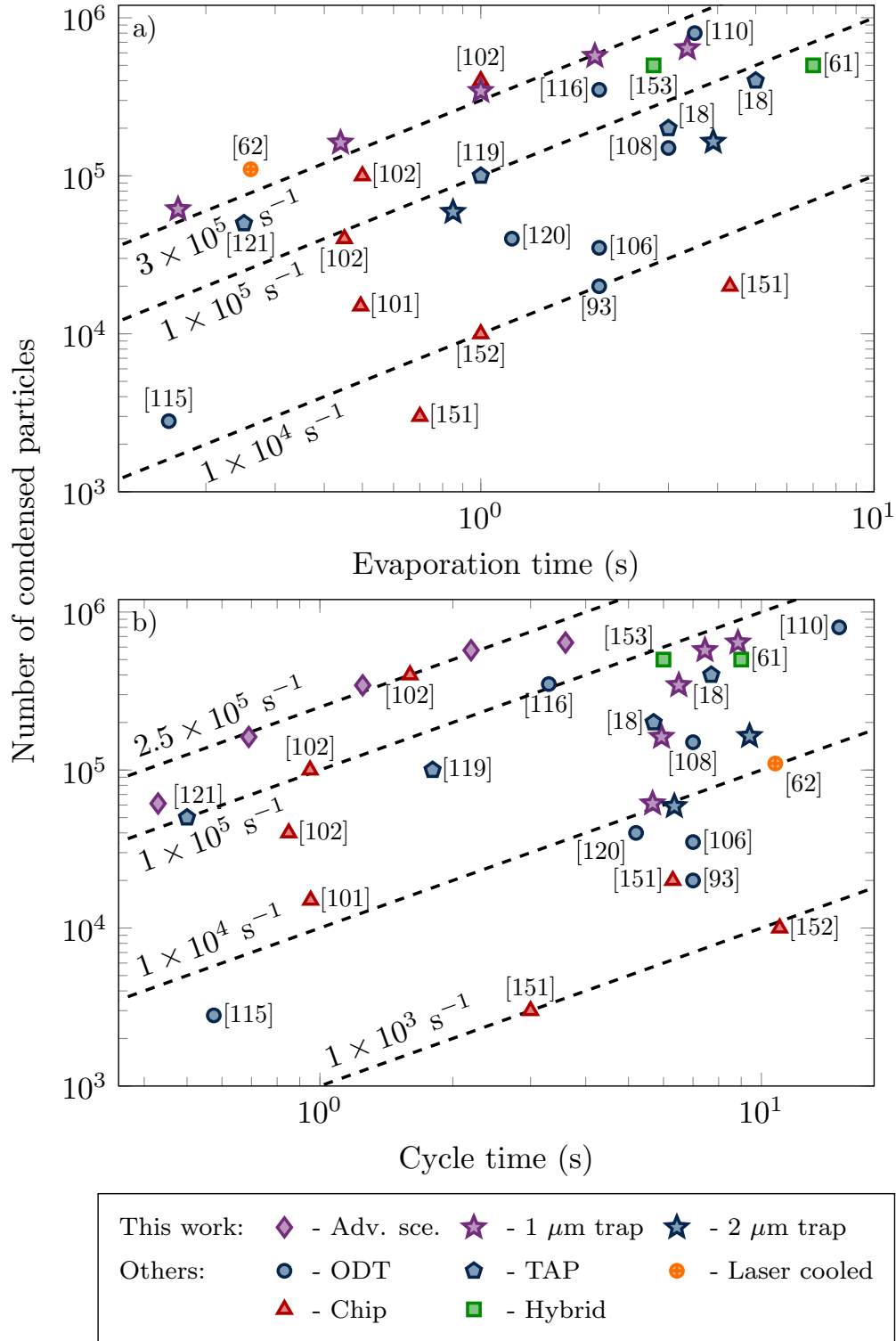


Figure 3.1: Comparison of different atomic source systems for Bose-Einstein condensates.

(a) When only considering the evaporation time, the implemented approach allows to reach the same flux values as other state-of-the-art solutions, while significantly reducing the evaporation time. **(b)** When considering the whole experimental cycle time, the current setup is limited by its MOT loading duration of 5 s. Implementing already demonstrated 2D^+ -MOT systems would allow to improve the performance and reach the values depicted as advanced scenario in a dedicated sensor setup.

Furthermore, the use of cryogenic buffer-gas sources enables shortening the loading time by another order of magnitude with the lowest values yielding around 10 ms [154]. However, such cryogenic solutions might be inadvisable, at least in the scope of compact and mobile devices due to their technical complexity. Combining the methods demonstrated here with a 2D⁺-MOT source as currently implemented in the Hannover VLBAI rubidium source would already allow to significantly reduce the experimental cycle time to below 500 ms. The expected atomic flux for such a configuration is highlighted by the purple diamonds in Figure 3.1b. All in all, the methods developed here demonstrate the viability of an all-optical approach for high-flux source systems, surpassing the capabilities of already existing techniques in terms of speed or atom number while also enabling one to cool non-magnetic atomic species.

3.3 IMPROVED MATTER-WAVE COLLIMATION FOR MULTIPLE ATOMIC SPECIES

3.3.1 Limitations and improvements

As analyzed in publication 5 [148], the realized matter-wave collimation sequence is mainly limited by the achievable trap frequencies and lack of collimation in the vertical direction. With the change from a single AOM in recycled beam configuration to independently controllable beams with 2D steering capability based on AODs this limitation could already be lifted. Improving the achievable CPM stroke from 200 μm to 1.5 mm reduced the minimal trap frequencies in horizontal direction into the 5 - 30 Hz range, while maintaining a sufficient trap depth during the matter-wave lens. In this regime the gravitational sag already becomes relevant and prohibits the use of lower laser beam intensities, which would lead to even shallower traps. Further improvements could hence be achieved by transitioning into a micro-gravity environment or creating a linear potential using TAPs to compensate gravity [155].

3.3.2 Application to other atomic species

Besides improving the matter-wave lens itself, its application to other atomic species is of major interest. While the experiments and related analysis have been performed for ³⁹K and ⁸⁷Rb, the proposed and realized DKC schemes can easily be extended to any other species, as they only rely on the trap geometry. For two atomic species *A* and *B*, their trap frequency ratio is given by

$$\frac{m_A}{\alpha_A} \omega_A^2 = \frac{m_B}{\alpha_B} \omega_B^2, \quad (3.1)$$

where α_i denotes the polarizability of their respective trapped states [18]. Furthermore, when applying the matter-wave lens, the reduction in energy relates to the trap frequency ratio and can be estimated via the Liouville theorem: $E_1/E_0 = (\omega_1/\omega_0)^2$. Although this approach neglects the coupling of the different degrees of freedom and is only valid for the collision-free regime, it allows determining an upper bound for the achievable energy reduction [156]. Consequently, equation 3.1 allows estimating the minimum energy reduction for all other species based on the values found for ³⁹K in publication 5 [148]. Here only the continuous matter-

wave lens of the advanced scenario is considered. By reducing the trap frequencies from $2\pi \times \{152.7, 310.7\}$ Hz to $2\pi \times \{28.1, 5.6\}$ Hz in the horizontal directions, an energy reduction of at least a factor of $\sim \{3 \times 10^1, 3 \times 10^3\}$ seems feasible.

Prime candidates for the application of this collimation scheme are atoms such as ytterbium and strontium which are highly relevant for tests of the gravitational redshift [157] and for gravitational wave detection and the search for dark matter [53], respectively. However, to accurately predict the final expansion energies a scaling [144, 145] or variational approach [146, 147], including the interaction dynamics is required. As before such an approach can then also be used to optimize the interactions with respect to the applied lens. Although both species do not possess magnetic FESHBACH resonances to tune the scattering length to an optimal value, they do feature optical FESHBACH resonances. However, these are generally accompanied by high losses and only allow minor tuning of the scattering length [86]. An important exception are resonances associated with the forbidden inter-combination transition, which circumvent both issues due to the enhanced lifetime of the associated states. By using these resonances changing the scattering length by few multiples of its natural background value has been successfully demonstrated for both species [87, 89]. Even though optical resonances are still limited in terms of tunability compared to their magnetic counterparts, and their exact implementation comes with various challenges, especially with respect to controlling laser intensity and frequency noise, they pose an interesting option to achieve the same scattering length values as ^{39}K and ultimately similar energies. Finally, implementing the present matter-wave collimation schemes in the Hannover VLBAI facility will be instrumental to perform tests of the UFF using ^{170}Yb and ^{87}Rb and investigate possible violations at the 10^{-13} -level and beyond [52].

3.4 TOWARDS BEC INTERFEROMETRY IN ATLAS

Operating the ATLAS apparatus requires its permanent adaptation to the constantly changing experimental needs. This section provides an overview of the immediate next steps needed to realize different interferometer geometries based on the techniques explored in this thesis.

3.4.1 State preparation of $|F = 1, m_F = 0\rangle$

The methods implemented in the scope of this thesis allow the rapid generation of ^{39}K BECs with high particle numbers. As explained in publication 2 [142] and publication 3 [143] operating in the vicinity of the broad FESHBACH resonance at 33.6 G is crucial for the achieved results as it allows dynamic tuning of the scattering length along the evaporation ramp with great accuracy and especially without the need for additional coil setups. However, for atom interferometry, using magnetic insensitive $m_F = 0$ -states is desirable to cancel the ZEEMAN effect to the first order and minimize the associated systematic error. To realize $|F = 1, m_F = 0\rangle$ as interferometry input state, different methods seem feasible. An schematic overview of the most intuitive ones is provided in Figure 3.2 and their implementation will be the immediate next step on the device.

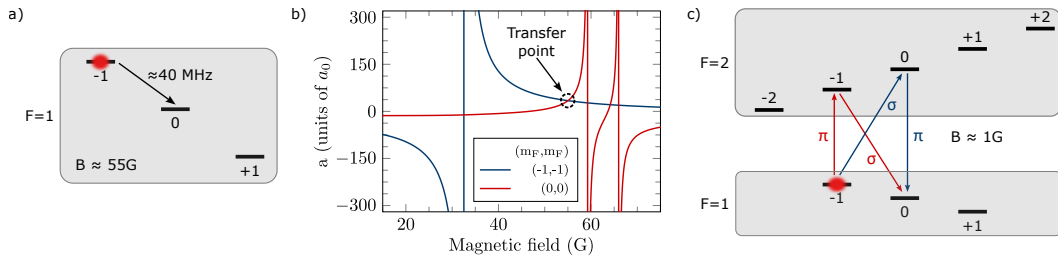


Figure 3.2: **Potential state preparation schemes for $|F = 1, m_F = 0\rangle$.** (a) By using an **RF-ARP**, atoms initially prepared in $|F = 1, m_F = -1\rangle$ can be transferred to $|F = 1, m_F = 0\rangle$. (b) Scattering length of $|F = 1, m_F = -1\rangle$ and $|F = 1, m_F = 0\rangle$ in the relevant region. A suitable magnetic field range for the transfer shown in (a) can be found at around 55 G, where both states share the same scattering length. (c) Alternative preparation schemes in the absence of strong magnetic fields, only making use of already implemented microwave-**ARPs**. Since two consecutive **ARPs** are needed, the atoms can either be transferred by a σ - π -sequence (blue) or by a π - σ -sequence (red).

Ideally, the **BEC** is transferred from $m_F = -1$ to $m_F = 0$ in the $|F = 1\rangle$ -manifold by an **RF-ARP** after its creation (Fig. 3.2a). Such a sequence has the advantage that only a single and relative simple manipulation is needed and similar preparation sequences have already been demonstrated for the creation of quantum droplets [158, 159]. However, special care must be taken to ensure that no quench is induced during the transfer by a non-adiabatic change in the scattering length. A suitable magnetic field value of around 55 G is highlighted in Figure 3.2b, where both m_F -states share the same scattering length. While this field strength is easily accessible after preparing the condensate, the associated **ZEEMAN** shift of $|F = 1, m_F = -1\rangle$ requires an **RF** sweep around 40 MHz. The successful coupling of these frequencies to the atoms is unlikely due to the design of the experiment's vacuum system. Since the **ATLAS** apparatus features a metallic science chamber and its waveguide only has a diameter of 7 cm, it cannot accommodate the corresponding fundamental magnetic modes [160]. This can be remedied by implementing a glass cell design, which also makes it possible to reduce the distance between the antenna and atoms and thus work in the near field regime, thereby significantly simplifying the antenna design.

Alternatively, the atoms can be transferred to $m_F = 0$ prior to evaporative cooling, utilizing one of the transfer sequences depicted in Figure 3.2c. These sequences have the advantage that they only use microwave **ARPs** as already implemented for the currently used state preparation sequence explained in publication 2 [142]. Starting from a pure ensemble in $|F = 1, m_F = -1\rangle$ the atoms can be transferred to $|F = 1, m_F = 0\rangle$ by either a π - σ -sequence:

$$|F = 1, m_F = -1\rangle \xrightarrow{\pi} |F = 2, m_F = -1\rangle \xrightarrow{\sigma} |F = 1, m_F = 0\rangle,$$

or by a σ - π -sequence:

$$|F = 1, m_F = -1\rangle \xrightarrow{\sigma} |F = 2, m_F = 0\rangle \xrightarrow{\pi} |F = 1, m_F = 0\rangle.$$

During the implementation of the new magnetic field stabilization, the depicted transfers have been tested on an individual basis, however the full sequences have not been realized yet. Using a σ -**ARP** from $|F = 1, m_F = -1\rangle$ to $|F = 2, m_F = 0\rangle$

have been found to features a higher transfer efficiency compared to the π -ARP, used on the transition from $|F = 1, m_F = -1\rangle$ to $|F = 2, m_F = -1\rangle$. Likewise, the transition from $|F = 2, m_F = 0\rangle$ to $|F = 1, m_F = 0\rangle$ is more robust than the transfer from $|F = 2, m_F = -1\rangle$ to $|F = 1, m_F = 0\rangle$ since it is insensitive to magnetic field noise to the first order. On the other hand, the lifetime of $|F = 2, m_F = -1\rangle$ was measured to be (1.23 ± 0.05) s, while for $|F = 2, m_F = 0\rangle$ the lifetime was limited to (114 ± 7) ms due to the states rapid depletion from spin changing collision. This can potentially affect the overall transfer efficiency since dead-times between the consecutive ARPs are needed to avoid shifting the magnetic field when coupling the microwave radiation into the magnetic field sensors. Consequently, choosing the right sequence to be used in the future experiments is subject to experimental optimization.

Moreover, the three-body loss coefficient of the first $m_F = 0$ FESHBACH resonance was experimentally determined to be an order of magnitude larger than for the resonance previously used with $m_F = -1$ [158, 159]. Therefore, a reduced evaporation efficiency can be expected with overall smaller BECs and a longer evaporation duration. If evaporation turns out to be too inefficient in future experiments, a possible alternative would be a mixed sequence where $|F = 1, m_F = -1\rangle$ is initially used to benefit from its favorable properties and $|F = 1, m_F = 0\rangle$ is only employed for the final step to cross the phase transition. Such an approach would only minimally extend the experimental sequence to switch off the magnetic field, change the m_F -state and then switch it back on again, while combining the benefits of a fast and efficient evaporation with the optimal input state for the atom interferometer.

3.4.2 Interferometry laser system

For the previous interferometry experiments with sub-DOPPLER cooled atoms, the ATLAS apparatus features a dual-species laser system, capable of driving RAMAN transitions [27]. However, especially in the context of guided and squeezing-enhanced interferometers, both explored in the next sections of this chapter, the implementation of a dedicated BRAGG laser system becomes imperative. To reduce maintenance efforts to a minimum, the laser system to be built should provide capacities for both single BRAGG and also double BRAGG diffraction. At the same time, it should completely replace the existing RAMAN setup.

The proposed design is shown in Figure 3.3a and differs for potassium and rubidium only in the choice of laser wavelength. To enable BRAGG diffraction (Fig. 3.3b), a single laser source is split along two paths. The two AOM1 and AOM2 realize frequency differences in the range of a few kilohertz up to several megahertz by tuning their driving RF-signals, accordingly. Subsequently, the beams are recombeded and the following AOM3 can be used in combination with a programmable direct digital synthesizer for pulse shaping. A special feature of this setup is the use of double-pass configurations, which allows to change the frequencies differences during the interferometry sequence, without loss of intensity. While not relevant in the context of trapped interferometer schemes (c.f. section 3.5), this feature is needed for the free-falling AI in order to compensate the occurring DOPPLER-shift. To realize an interferometer based on RAMAN transitions (Fig. 3.3c), only one of the two initial light paths will be used since the typical frequency differences are

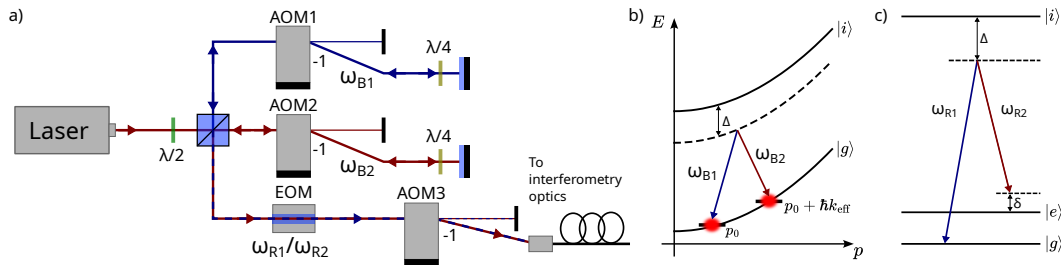


Figure 3.3: **Combined Bragg and Raman laser system.** (a) Proposed setup to combine capabilities for single BRAGG diffraction, double BRAGG diffraction and RAMAN transitions. **AOM1** and **AOM2** create the frequency difference necessary for the BRAGG schemes, while **AOM3** is used for pulse shaping. When switching to RAMAN transitions, only one of the two initial **AOMs** is used and instead the frequency difference is created by the depicted electro-optic modulator (**EOM**). (b) Two-photon BRAGG transition with a global detuning of Δ from the intermediate state $|i\rangle$, transferring $\hbar k_{\text{eff}}$ momentum. (c) Two-photon RAMAN transition between ground state $|g\rangle$ and excited state $|e\rangle$ with global detuning Δ and shift from the resonance by δ .

too large to be realized with **AOMs**. Here, the additionally implemented **EOM** will generate the required frequencies as sidebands and is expected to improve the robustness compared to the previously used phase-locked external-cavity diode lasers.

Based on the specific parameters of the **ATLAS** apparatus, the requirements for the BRAGG component of such a laser system were determined for ^{39}K as part of a bachelor's thesis [161]. Assuming a global detuning of the laser source of $\Delta = 3.5\text{ GHz}$ relative to the $^{39}\text{K D}_2$ -line, an upper limit of the required laser power of 50 mW per BRAGG frequency could be determined. Furthermore, for a maximum free-fall time of 200 ms the DOPPLER detuning was calculated to not exceed 5 MHz . Currently, a modern frequency-doubled fiber laser with total output power of 1 W at 766.701 nm and superior linewidth below 100 kHz is integrated as a laser source to realize the setup. Once the system is complete, first results with single BRAGG diffraction in the free-falling **AI** are expected.

3.4.3 Dual-species considerations for testing the UFF

As demonstrated in publication 1 [139], tests of the **UFF** performed in the **ATLAS** apparatus are currently limited by wavefront aberrations to the 10^{-7} -level. This systematic error is primarily caused by the atomic ensembles expanding in the interferometry beam in conjunction with wavefront errors. As analyzed in Ref. [18], matter-wave lenses can contribute to a significant improvement by reducing and matching the expansion speed of both ensembles. The methods for this were demonstrated in publication 4 [123]. Since the collimation scheme can easily be applied to thermal ensembles, an improved **UFF** test becomes feasible, in which ^{39}K and ^{87}Rb have temperatures in the nanokelvin range, in contrast to the previously used ensembles with a few microkelvins.

When transitioning to **BECs**, a combination of ^{39}K and ^{87}Rb is not straightforward, since the magnetic degree of freedom is already needed to control the

interatomic interactions in ^{39}K and is therefore not available to control interspecies interactions. However, an important exception exists when both species occupy the $|F = 1, m_F = -1\rangle$ -state, which features an interspecies resonance at 117.56 G [162]. Situated between the two broad $m_F = -1$ -resonances of ^{39}K at 32.6 G and 162.8 G, it allows controlling interatomic and interspecies interactions at the same time and tunable dual-species condensates have already been demonstrated [163]. While in this case both species are susceptible to systematic errors caused by the linear ZEEMAN shift, a microwave state transfer to $m_F = 0$, as discussed before, can circumvent this issue once the ensembles have expanded sufficiently and entered the ballistic regime prior to performing the interferometer sequence. This scheme only requires methods that have already been implemented in **ATLAS** within the scope of this thesis and thus constitutes a direct route to a two-species test of the **UFF** with ultracold atoms at the 10^{-9} -level [160] and below.

Alternatively, using mixtures of ^{87}Rb with ^{41}K instead of ^{39}K resolves this issue as well, since ^{41}K features a positive background scattering length and the ^{41}K - ^{87}Rb values have been determined in a favorable range to ensure the stability of a mixed condensate [164]. Detailed studies of its mixing behavior have already been carried out [165–168] and combining these two species with a high performing matter-wave lens is fundamental to proposed high precision experiments [126, 169]. Although the energy level structure of ^{41}K would the use of the current ^{39}K laser system of **ATLAS** with marginal adjustments, the low abundance of ^{41}K represents a major limitation for high-flux source systems. A ^{41}K **MOT** has already been demonstrated, but the individual experimental steps towards a **BEC** would require a complete restructuring of the experimental sequence, including the introduction of sympathetic cooling techniques. Accordingly, the approach with a mixture of ^{39}K - ^{87}Rb under the aid of **FESHBACH** resonances seems to be more promising for the near future.

3.5 GUIDED ATOM INTERFEROMETRY

As analyzed thoroughly in the scope of publication 3 [143] and publication 4 [123], the presented methods allow enhancing free-fall interferometry by enabling dead-time free measurements and extended pulse separation times without loss of contrast. Beyond free-falling geometries, **TAPs** combined with tunable interactions fully unleash their potential when transitioning to guided interferometers in which the atomic ensemble remains trapped during the whole sequence. While free-falling geometries will remain state-of-the-art for precision measurements in fundamental physics [52, 53, 126, 127, 170], guided interferometers are of particular interest for inertial sensing in the scope of navigation applications [171]: The phase resolution of terrestrial free-fall **Al**s scales with the length of the apparatus. Therefore, excellent control of external perturbations over large length scales is needed, which is unfavorable for applications in dynamic environments or when the available space is limited in general. Likewise, measuring accelerations and rotations along more than one axis requires significant effort and developing suitable interferometer geometries and readout schemes remains an active area of research [23, 111, 112, 173]. In contrast, guided geometries allow for long pulse separation times in a compact device. Furthermore, they enable measurements with spatial resolutions in

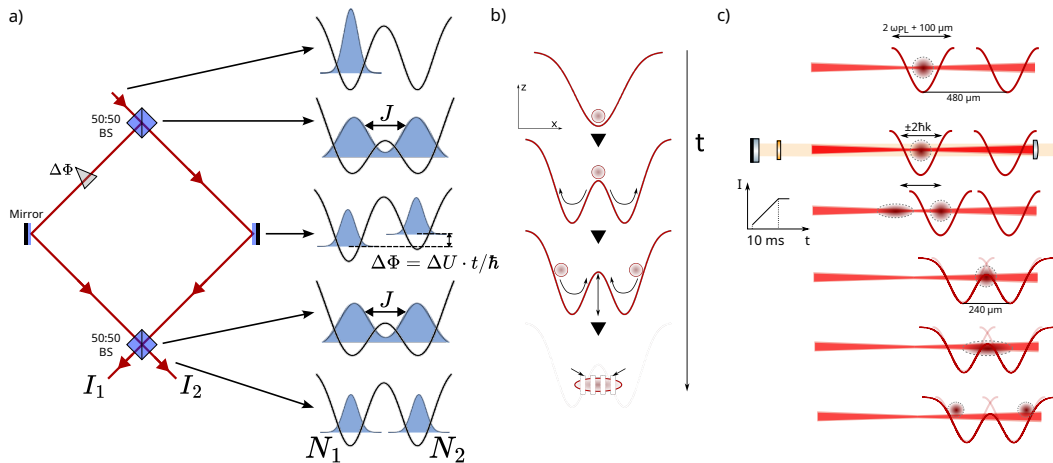


Figure 3.4: **Different realizations of beam splitters in a guided geometry.** (a) Working principle of a guided atom interferometer based on a double-well potential compared to a MACH-ZEHNDER interferometer. Here, beam splitter and recombining are realized through a tunneling process J , which can be controlled by altering the potential barrier height and width. The leading order phase shift $\Delta\phi$ between the wells is induced by the relative potential difference ΔU between them and the time T the atoms are exposed to it. (b) Alternative splitting process, based on raising a potential barrier underneath the BEC. Coherence can be shown by observing spatial fringes when removing the trap at the right time during COM oscillations in the separate wells. (c) Momentum induced tunneling process. A BRAGG-pulse increases the kinetic energy of the BEC, while co-moving the trapping potential. This method also allows the tunneling of wide potential barriers. Figure (b) and (c) are taken from Ref. [172].

the micrometer range, as demonstrated in the scope of a trapped MACH-ZEHNDER interferometer on an atom chip [174].

To realize smooth guiding potentials, most demonstrations are utilizing either magnetic waveguides [175, 176] or ring traps [177–179]. As before, to couple to these traps the atoms must be sufficiently susceptible to magnetic force, which also leads to strong coupling to stray magnetic fields via the linear ZEEMAN effect. In free-falling interferometers this issue is mitigated by preparing the $m_F = 0$ -state after release from the magnetic trap. However, since guided geometries requires the permanent presence of the confining potentials this issue can not be avoided when choosing magnetic guides. Moreover, all of these realizations have in common that they use a comparably low atom number at the order of few 10^3 particles, since interaction induced de-phasing [180] poses a significant problem for the high densities associated with trapped ensembles [181, 182]. On the other hand, using an optical guide allows utilizing magnetically insensitive states. Additionally, they enable using magnetic FESHBACH resonances to tune the interactions close to zero, which has already been shown to be a viable solution to avoid density limitations in an optical lattice interferometer [183, 184]. Compared to these other realizations, an implementation based on TAPs would allow for several unique advantages: As a first step a hybrid approach with BRAGG pulses can easily be implemented. In this scenario one of the trapping beams serves as the waveguide. By superimposing the necessary BRAGG light-fields, acceleration measurements along the waveguide-axis are enabled. Furthermore, the TAP can be used to move the waveguide, thereby

enclosing an area and allowing to measure rotation rates. In both configurations, tunable interactions would be used to enhance atom number and interrogation time. Similar experiments have already been carried out in the group of MALCOLM BOSCHIER and a phase sensitivity to rotations was demonstrated [185, 186].

Extending beyond previous works the second trapping beam can additionally be re-shaped to form a double-well potential as shown in Figure 3.4a. With such a configuration, various beam splitting processes can be realized and are expected to enable light-pulse free ensemble splitting and recombination. In particular, the Quantum TransPORT (QPORT) experiment already investigated a saddle point beam splitter and tunneling processes with and without additional momentum transfer, using ^{87}Rb in an experimental configuration similar to what has been implemented in the ATLAS apparatus [172]: For the saddle point beam splitter (Fig. 3.4b) a potential barrier is raised directly underneath the BEC occupying a single well. This method was able to demonstrate coherent splitting for distances up to $40\text{ }\mu\text{m}$, but is not suitable for recombination processes due to its irreversibility. Alternatively, controlled tunneling has already been shown to be suitable for both splitting and recombination in a magnetic trap [187] and has also been demonstrated in optical guides [188]. For this method the BEC is initially confined in a single well. By moving a second well close to the first one, tunneling processes can be initiated by appropriately shaping the height and width of the remaining potential barrier between the two minima. To date, however, no coherent tunneling has been observed in the QPORT apparatus as its comparably large beam waists of $80\text{ }\mu\text{m}$ restrict the minimum achievable barrier width. This limitation has been overcome by introducing an additional BRAGG-pulse, which accelerates the BEC towards the potential barrier (Fig. 3.4c). Although the resulting kinetic energy does not exceed the potential height, it is sufficient to allow tunneling processes through wider barriers and coherence for this process was demonstrated for up to four center-of-mass (COM) oscillations in the wells. As before, however, this sequence is also not suitable for a recombiner in the context of an interferometry sequence. To successfully implement direct tunneling in the JOSEPHSON-regime, recent proposals require beam waists at the order of $20\text{ }\mu\text{m}$ [189]. While realizing such beam waists is challenging when using large metallic chambers which increase the distance between focusing lens and atomic ensemble, transitioning into the interaction free RABI-regime offers an alternative route to prevent de-phasing and enhance the transmission coefficients [190]. Consequently, with beam waists at the order of $30\text{ }\mu\text{m}$ and the capabilities to tune the scattering length, the ATLAS apparatus is in a promising position to demonstrate coherent splitters and recombiners based on direct tunneling.

When additionally moving the individual wells apart and optionally also the waveguide, suitable space-time areas for interferometry can be enclosed. While different aspects of this proposed sequence have been investigated theoretically in optical tweezers [189, 191] or to extend the separation of two interferometer arms using accelerated optical traps [192], such a sequence has not yet been realized in an experiment. The interferometer schemes for measuring accelerations along the waveguide and rotations perpendicular to it with a light-pulse free sequence are shown in Figure 3.5 and Figure 3.6, respectively.

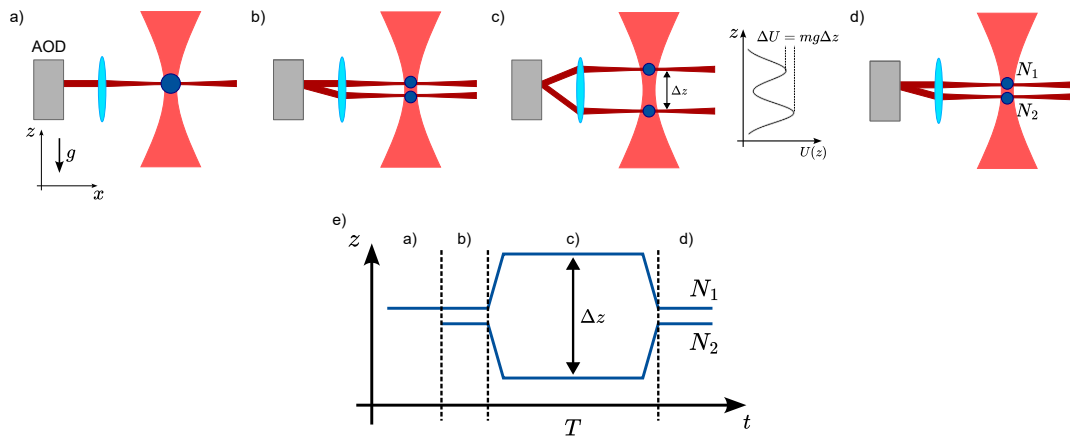


Figure 3.5: Simplified sequence to perform an acceleration measurement along the z -direction with a fully guided interferometer. (a) Atoms are trapped with the waveguide pointing along the measurement direction. Confinement is provided by a second perpendicular beam, which allows to create TAPs with an AOD. (b) Creation of a double-well potential via the AOD and 50:50 beam splitting through controlled tunneling. (c) By moving the wells apart, the ensembles are separated by Δz , and the potential energy due to gravitation is altered. (d) Recombination with another beam splitter through tunneling after moving the wells back together and read-out of the occupation number of the individual wells. (e) Space-time diagram of the interferometer sequence.

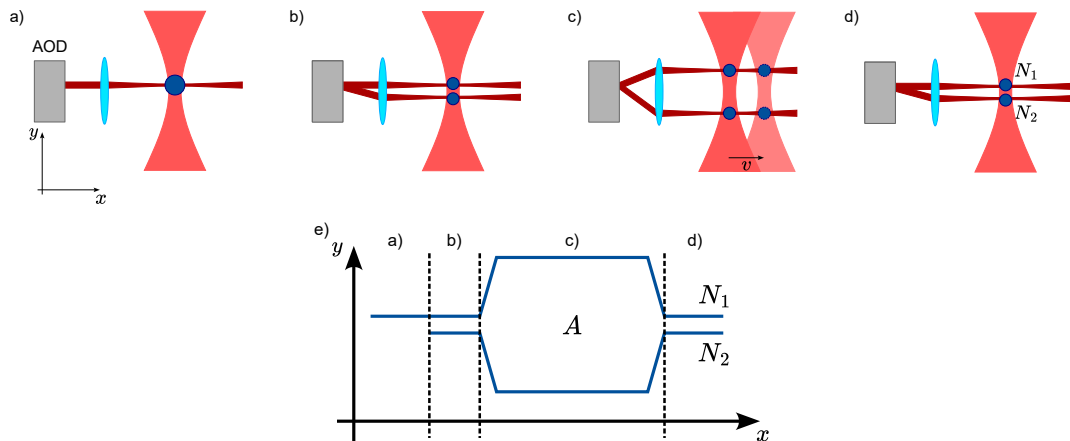


Figure 3.6: Simplified measurement sequence for rotations around the z -direction with a fully guided configuration. (a) Similar to the sequence shown in Figure 3.5 atoms are confined in a waveguide, with the perpendicular beam providing the TAP capabilities. Here the measurement axis of interest is perpendicular to the direction of both beams. (b) Atoms are split through the same tunneling processes as before, realizing a 50:50 beam splitter by controlling the barrier width and height of the double-well potential. (c) Spatial separation of both ensembles in y -direction by moving the wells apart and subsequent translation in x -direction, moving the waveguide with velocity v , thereby enclosing an area A (d) Closing the interferometer by moving the wells back together, realizing another tunneling beam splitter and read-out of the occupation numbers of both wells. (e) Spatial diagram of the interferometer sequence.

For the proposed geometries, one can show that the leading order phase term for measuring an acceleration \vec{a} is given by

$$\Delta\phi = \frac{m}{\hbar} T \Delta \vec{z} \cdot \vec{a}. \quad (3.2)$$

Likewise, for a gyroscope configuration the leading order phase shift for rotations with rotation-rate $\vec{\Omega}$ perpendicular to the enclosed area with surface vector \vec{A} becomes:

$$\Delta\phi = \frac{m}{\hbar} \vec{A} \cdot \vec{\Omega}. \quad (3.3)$$

When considering the exact implementation, shifts of the waveguide and a separation of the double wells by several millimeters are possible in the [ATLAS](#) apparatus. For an interferometer time of $T = 10$ ms with a total atom number of $N = 1 \times 10^5$, a conservative spatial separation of $\Delta z = 1$ mm would already allow for a quantum projection noise limited single shot sensitivity of $\sigma_{\text{acc}} = 5 \times 10^{-7}$ m/s². For the same parameters, the quantum projection noise limited single shot sensitivity for rotations becomes $\sigma_{\text{rot}} = 5 \times 10^{-6}$ rad/s when translating the waveguide by the same distance, enclosing an area of $A = 1$ mm.

In Ref. [7] the requirements for using atom interferometers in conjunction with classical inertial measurement units ([IMUs](#)) for the most demanding navigation applications are outlined. Already the simple measurement schemes depicted here are sufficient to comply with the required accuracy for acceleration measurements of below 1×10^{-6} m/s² / $\sqrt{\text{Hz}}$ with a cycle time of 1 s. Consequently, such an [AI](#) could serve as a stable long time reference for classical [IMUs](#), thereby limiting the navigation error to less than 5 m after 1 h. For a gyroscope application, the same error requires an accuracy below 1×10^{-7} rad/s / $\sqrt{\text{Hz}}$, an order of magnitude below of what can be achieved with the sequence presented in Figure 3.6.

Besides extending the enclosed area A , interaction induced non-classical input states pose another viable option to further increase the sensitivity to meet the requirements [174]. The next and final section explores potential geometries and methods to implement such states in an [AI](#).

3.6 SQUEEZING-ENHANCED INTERFEROMETRY

Ultimately, [TAPs](#) and tunable interactions will enable squeezing-enhanced interferometry in the waveguide and in free-fall. As discussed in the introduction, the theoretical sensitivity of [AIs](#) is bound by numerous factors and can be improved by increasing atom number, momentum transfer or pulse separation time, among others. While in laboratory realizations various noise sources, e.g. detection noise, have to be additionally considered, state-of-the-art devices allow to strongly suppress these contributions leaving quantum noise as the main limiting factor. Different experimental realizations have been shown to reach the fundamental [SQL](#) in phase uncertainty, resulting in a sensitivity scaling proportional to $1/\sqrt{N}$ for a measurement of N uncorrelated atoms [34, 194, 195]. In theory engineering squeezed input states allow to lift this limitations and to approach the Heisenberg limit, scaling as $1/N$ for correlated states [196]. Especially, when the atomic flux cannot be further improved such schemes will become relevant.

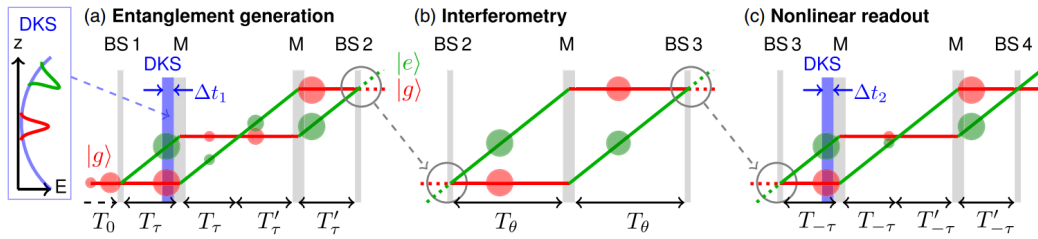


Figure 3.7: A Delta-Kick squeezing-enhanced atom interferometry scheme. (a) Entanglement is created by a focusing Delta-Kick and the subsequent overlapping of the two ensembles at high density. (b) Before the interferometer sequence, the clouds are allowed to expand to realize interaction free ensembles, again. (c) After closing the interferometer, a nonlinear readout scheme can be optionally employed, to further increase the sensitivity by a sequence similar to the initial entanglement generation. Reprinted figure with permission from [Corgier et al., Phys. Rev. Lett. 127, 183401, 2021] [193]. Copyright 2021 by the American Physical Society.

However, their exact implementation and the overall compatibility with the strict requirements that [AIs](#) impose on potential measurement schemes remains an open research question [197]. So far, experimental realizations are mainly limited to proof-of-principle experiments [54]. Most prominently, squeezing internal degrees of freedom has enhanced magnetometers [198] and atomic clocks [199]. In contrast, [AIs](#) require the entanglement of external momentum or spatial modes, addressable with RAMAN or BRAGG transitions. Recently, a first experiment successfully transferred squeezing of the spin degree of freedom of a [BEC](#) to external momentum modes by individually addressing the different spin states via RAMAN and microwave-transitions [94]. This particular scheme has now been implemented into a free-fall [AI](#) and allowed to obtain results with sub-[SQL](#) sensitivity [200]. Alternatively, entanglement can be created through cavity-mediated spin-interactions and an enhanced interferometer has already been demonstrated [201]. Current proposals now make explicit use of the unique features of trapped geometries [202] or matter-wave lenses in free fall [193]. In both proposals interactions are not suppressed during state preparation, but rather used to create entanglement through one-axis twisting dynamics [203] at high densities.

The sequence of the free-fall interferometer is depicted in Figure 3.7. Here, squeezing is introduced in a MACH-ZEHNDER like geometry. After creating a superposition of excited and ground state through a beam splitter, a Delta-Kick pulse allows focusing the ensemble. By choosing the appropriate timing in conjunction with a mirror pulse, both trajectories overlap at highest density, creating interaction induced entanglement. Additional mirror and beam splitter pulses allow to prepare the starting point of the MACH-ZEHNDER interferometer, such that both clouds have expanded sufficiently to guarantee non-interacting ensembles. Optionally, the read-out can be optimized with a sequence similar to the entanglement generation stage to enhance the sensitivity. While this experimental sequence does not require any tunable interactions, the integrated 2D-[AODs](#) enable a straight forward implementation of the entangled linear MACH-ZEHNDER interferometer (Fig. 3.7a/b) in [ATLAS](#). In particular, co-moving the [ODT](#) beams over macroscopic distances of a few

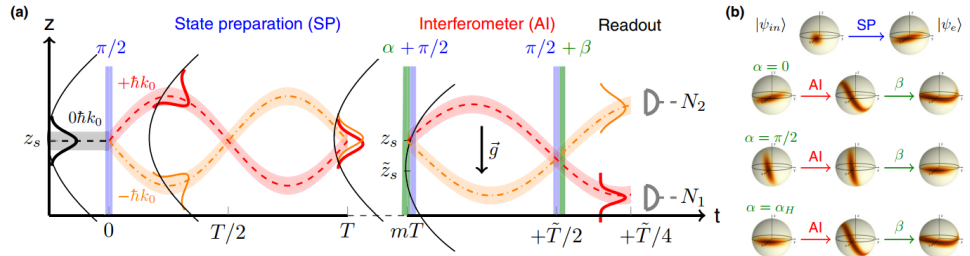


Figure 3.8: **A squeezing-enhance trapped interferometer scheme.** (a) A trapped BEC is split into symmetric momentum modes along gravity via a $\pi/2$ -BRAGG pulses, inducing COM oscillations in the confining potential. Within a free evolution time, both wave-packets are passing each other multiple times, introducing entanglement via interatomic interactions. The actual interferometer sequence consists of two more $\pi/2$ -pulses. In between trap frequency along gravity are lowered, causing the wavepackets to experience an additional acceleration. (b) Both interferometer pulses are prolonged by the additional pulses α and β to maximize the sensitivity. Readout is performed by counting the atom number in both ports when the ensembles are maximally separated. Reprinted figure with permission from [Corgier et al., Phys. Rev. A 103, L061301, 2021] [202]. Copyright 2021 by the American Physical Society.

millimeters allow for an easy implementation of the initial Delta-Kick pulse, while the new interferometry laser system will be used to realize splitting, mirroring and recombination pulses.

However, to use all implemented capabilities of the ATLAS apparatus, the fully trapped sequence is of larger interest [202]. While conceptually similar to the free falling case, state preparation and interferometer sequence rely on COM oscillations in the trap. Due to the permanent confinement of both wavepackets special care has to be taken of interactions, which cannot be avoided due to the high densities. The proposed sequence is shown in Figure 3.8. Initially, a trapped BEC is split into symmetric momentum modes along gravity via a $\pi/2$ -BRAGG pulse. Due to the restoring force of the trap, COM oscillations are induced, causing the wavepackets to cross each other multiple times during an initial evolution time, thereby introducing entanglement via interatomic interactions. The actual interferometer sequence then consists of two more $\pi/2$ -pulses, while reducing trap frequency along gravity in between causing the wavepackets to experience an additional acceleration. To maximize the sensitivity both interferometer pulses are prolonged by the additional pulses α and β to rotate the state on the BLOCH sphere. Readout is performed by counting the atom number in both ports when the ensembles are maximally separated, another half oscillation period after closing the interferometer.

For this scheme, TAPs are perfectly suited to realize the required change in trap frequencies in the direction of gravity, applying the same sequences that have already been used for the matter-wave collimation in publication 4 [123] and publication 5 [148]. Importantly, the rotation pulses α and β are needed to account for phase fluctuations, created by interactions during the interferometer. Here, tunable interactions could serve as an additional method to enhance squeezing during state preparation and subsequently realize a more robust sequence.

3.7 CONCLUSION

The methods developed in this thesis lead towards exciting future work in the field of atom interferometry and tests of fundamental physics. In the realm of light-pulse interferometry with free-falling ensembles, they make a decisive contribution to new and improved tests of the [UFF](#). An immediate implementation for both species in the [ATLAS](#) apparatus will lead to tests at the 10^{-9} -level and below, which will set a new record for the use of two different atomic species. The experience gained during this measurement campaign will subsequently be invaluable to perform experiments in the Hannover [VLBAI](#) facility. There, testing the 10^{-13} -level and beyond will push the boundaries of our understanding of gravity and pave the way for possible revisions of our current theories about the universe. Furthermore, the implemented methods mark a pioneering step towards the development of compact quantum sensors that have the potential for far-reaching applications. With the proposed guided interferometry schemes it will be possible to complement classical inertial measurement units in the near future. In particular, such sensors hold the promise of revolutionizing navigation applications, offering unprecedented accuracy and reliability in a compact and portable form factor. Ultimately, the study of squeezed atom interferometers will challenges the limits of technological feasibility while connecting to the most fundamental questions of quantum mechanics, thereby opening the door to enhanced precision measurements and novel quantum technologies.

BIBLIOGRAPHY

- [1] A. A. Michelson and E. W. Morley. "On the relative motion of the Earth and the luminiferous ether." In: *American Journal of Science* s3-34.203 (1887), pp. 333–345. ISSN: 0002-9599. DOI: [10.2475/ajs.s3-34.203.333](https://doi.org/10.2475/ajs.s3-34.203.333) (cit. on p. 1).
- [2] Tadashi Morokuma, Karl F. Nefflen, T. R. Lawrence, and Thomas M. Klucher. "Interference Fringes with Long Path Difference Using He–Ne Laser*." In: *Journal of the Optical Society of America* 53.3 (1963), p. 394. ISSN: 0030-3941. DOI: [10.1364/JOSA.53.000394](https://doi.org/10.1364/JOSA.53.000394) (cit. on p. 1).
- [3] W. M. Macek and D. T. M. Davis. "ROTATION RATE SENSING WITH TRAVELING-WAVE RING LASERS." In: *Applied Physics Letters* 2.3 (1963), pp. 67–68. ISSN: 0003-6951. DOI: [10.1063/1.1753778](https://doi.org/10.1063/1.1753778) (cit. on p. 1).
- [4] B. P. Abbott et al. "Observation of Gravitational Waves from a Binary Black Hole Merger." In: *Phys. Rev. Lett.* 116 (6 2016), p. 061102. DOI: [10.1103/PhysRevLett.116.061102](https://doi.org/10.1103/PhysRevLett.116.061102). URL: <https://link.aps.org/doi/10.1103/PhysRevLett.116.061102> (cit. on p. 1).
- [5] T. M. Niebauer, G. S. Sasagawa, J. E. Faller, R. Hilt, and F. Klopping. "A new generation of absolute gravimeters." In: *Metrologia* 32.3 (1995), pp. 159–180. ISSN: 0026-1394. DOI: [10.1088/0026-1394/32/3/004](https://doi.org/10.1088/0026-1394/32/3/004) (cit. on p. 1).
- [6] P. Gillot, O. Francis, A. Landragin, F. Pereira Dos Santos, and S. Merlet. "Stability comparison of two absolute gravimeters: optical versus atomic interferometers." In: *Metrologia* 51.5 (2014), pp. L15–L17. ISSN: 0026-1394. DOI: [10.1088/0026-1394/51/5/L15](https://doi.org/10.1088/0026-1394/51/5/L15) (cit. on p. 1).
- [7] Christopher Jekeli. "Navigation Error Analysis of Atom Interferometer Inertial Sensor." In: *Navigation* 52.1 (2005), pp. 1–14. ISSN: 00281522. DOI: [10.1002/j.2161-4296.2005.tb01726.x](https://doi.org/10.1002/j.2161-4296.2005.tb01726.x) (cit. on pp. 1, 76).
- [8] L. de Broglie. "Recherches sur la théorie des Quantas." PhD thesis. Sorbonne Paris, 1924 (cit. on pp. 1, 4).
- [9] Alexander D. Cronin, Jörg Schmiedmayer, and David E. Pritchard. "Optics and interferometry with atoms and molecules." In: *Rev. Mod. Phys.* 81 (3 2009), pp. 1051–1129. DOI: [10.1103/RevModPhys.81.1051](https://doi.org/10.1103/RevModPhys.81.1051). URL: <https://link.aps.org/doi/10.1103/RevModPhys.81.1051> (cit. on pp. 1, 2).
- [10] C. Davisson and L. H. Germer. "The Scattering of Electrons by a Single Crystal of Nickel." In: *Nature* 119.2998 (1927), pp. 558–560. DOI: [10.1038/119558a0](https://doi.org/10.1038/119558a0) (cit. on p. 1).
- [11] L. Marton. "Electron Interferometer." In: *Phys. Rev.* 85 (6 1952), pp. 1057–1058. DOI: [10.1103/PhysRev.85.1057](https://doi.org/10.1103/PhysRev.85.1057). URL: <https://link.aps.org/doi/10.1103/PhysRev.85.1057> (cit. on p. 1).
- [12] L. Marton, J. Arol Simpson, and J. A. Suddeth. "Electron Beam Interferometer." In: *Phys. Rev.* 90 (3 1953), pp. 490–491. DOI: [10.1103/PhysRev.90.490](https://doi.org/10.1103/PhysRev.90.490). URL: <https://link.aps.org/doi/10.1103/PhysRev.90.490> (cit. on p. 1).

- [13] R. Colella, A. W. Overhauser, and S. A. Werner. “Observation of Gravitationally Induced Quantum Interference.” In: *Phys. Rev. Lett.* 34 (23 1975), pp. 1472–1474. DOI: [10.1103/PhysRevLett.34.1472](https://doi.org/10.1103/PhysRevLett.34.1472). URL: <https://link.aps.org/doi/10.1103/PhysRevLett.34.1472> (cit. on p. 1).
- [14] David W. Keith, Christopher R. Ekstrom, Quentin A. Turchette, and David E. Pritchard. “An interferometer for atoms.” In: *Phys. Rev. Lett.* 66 (21 1991), pp. 2693–2696. DOI: [10.1103/PhysRevLett.66.2693](https://doi.org/10.1103/PhysRevLett.66.2693). URL: <https://link.aps.org/doi/10.1103/PhysRevLett.66.2693> (cit. on p. 1).
- [15] O. Carnal and J. Mlynek. “Young’s double-slit experiment with atoms: A simple atom interferometer.” In: *Phys. Rev. Lett.* 66 (21 1991), pp. 2689–2692. DOI: [10.1103/PhysRevLett.66.2689](https://doi.org/10.1103/PhysRevLett.66.2689). URL: <https://link.aps.org/doi/10.1103/PhysRevLett.66.2689> (cit. on p. 1).
- [16] M. R. Andrews, C. G. Townsend, H. Miesner, D. S. Durfee, D. M. Kurn, and W. Ketterle. “Observation of Interference Between Two Bose Condensates.” In: *Science (New York, N.Y.)* 275.5300 (1997), pp. 637–641. ISSN: 0036-8075. DOI: [10.1126/science.275.5300.637](https://doi.org/10.1126/science.275.5300.637) (cit. on p. 1).
- [17] C. Kohstall, S. Riedl, E. R. Sánchez Guajardo, L. A. Sidorenkov, J. Hecker Denschlag, and R. Grimm. “Observation of interference between two molecular Bose–Einstein condensates.” In: *New Journal of Physics* 13.6 (2011), p. 065027. DOI: [10.1088/1367-2630/13/6/065027](https://doi.org/10.1088/1367-2630/13/6/065027) (cit. on p. 1).
- [18] Henning Albers. “Time-averaged optical potentials for creating and shaping Bose–Einstein condensates.” PhD thesis. Leibniz University Hannover, 2020. DOI: [10.15488/10073](https://doi.org/10.15488/10073) (cit. on pp. 2, 9–12, 67, 71).
- [19] Mark Kasevich and Steven Chu. “Atomic interferometry using stimulated Raman transitions.” In: *Phys. Rev. Lett.* 67 (2 July 1991), pp. 181–184. DOI: [10.1103/PhysRevLett.67.181](https://doi.org/10.1103/PhysRevLett.67.181). URL: <https://link.aps.org/doi/10.1103/PhysRevLett.67.181> (cit. on pp. 1–4).
- [20] F. Riehle, Th. Kisters, A. Witte, J. Helmcke, and Ch. J. Bordé. “Optical Ramsey spectroscopy in a rotating frame: Sagnac effect in a matter-wave interferometer.” In: *Phys. Rev. Lett.* 67 (2 July 1991), pp. 177–180. DOI: [10.1103/PhysRevLett.67.177](https://doi.org/10.1103/PhysRevLett.67.177). URL: <https://link.aps.org/doi/10.1103/PhysRevLett.67.177> (cit. on p. 1).
- [21] M. Kasevich and S. Chu. “Measurement of the gravitational acceleration of an atom with a light-pulse atom interferometer.” In: *Applied Physics B* 54.5 (1992), pp. 321–332. ISSN: 0946-2171. DOI: [10.1007/BF00325375](https://doi.org/10.1007/BF00325375) (cit. on p. 1).
- [22] T. L. Gustavson, P. Bouyer, and M. A. Kasevich. “Precision Rotation Measurements with an Atom Interferometer Gyroscope.” In: *Physical Review Letters* 78.11 (Mar. 1997), pp. 2046–2049. DOI: [10.1103/physrevlett.78.2046](https://doi.org/10.1103/physrevlett.78.2046). URL: [\url{https://link.aps.org/doi/10.1103/PhysRevLett.78.2046}](https://link.aps.org/doi/10.1103/PhysRevLett.78.2046) (cit. on p. 2).
- [23] B. Canuel et al. “Six-Axis Inertial Sensor Using Cold-Atom Interferometry.” In: *Phys. Rev. Lett.* 97 (1 July 2006), p. 010402. DOI: [10.1103/PhysRevLett.97.010402](https://doi.org/10.1103/PhysRevLett.97.010402). URL: <https://link.aps.org/doi/10.1103/PhysRevLett.97.010402> (cit. on pp. 2, 72).

- [24] Susannah M. Dickerson, Jason M. Hogan, Alex Sugarbaker, David M. S. Johnson, and Mark A. Kasevich. "Multiaxis Inertial Sensing with Long-Time Point Source Atom Interferometry." In: *Phys. Rev. Lett.* 111 (8 Aug. 2013), p. 083001. DOI: [10.1103/PhysRevLett.111.083001](https://doi.org/10.1103/PhysRevLett.111.083001). URL: <https://link.aps.org/doi/10.1103/PhysRevLett.111.083001> (cit. on pp. 2, 3, 11).
- [25] I. Dutta, D. Savoie, B. Fang, B. Venon, C.L. Garrido Alzar, R. Geiger, and A. Landragin. "Continuous Cold-Atom Inertial Sensor with 1 nrad/sec Rotation Stability." In: *Phys. Rev. Lett.* 116 (2016), p. 183003. DOI: [10.1103/PhysRevLett.116.183003](https://doi.org/10.1103/PhysRevLett.116.183003) (cit. on p. 2).
- [26] D. Savoie, M. Altorio, B. Fang, L. A. Sidorenkov, R. Geiger, and A. Landragin. "Interleaved atom interferometry for high-sensitivity inertial measurements." In: *Science advances* 4.12 (2018), eaau7948. DOI: [10.1126/sciadv.aau7948](https://doi.org/10.1126/sciadv.aau7948) (cit. on p. 2).
- [27] D. Schlippert, J. Hartwig, H. Albers, L. L. Richardson, C. Schubert, A. Roura, W. P. Schleich, W. Ertmer, and E. M. Rasel. "Quantum Test of the Universality of Free Fall." In: *Phys. Rev. Lett.* 112 (20 May 2014), p. 203002. DOI: [10.1103/PhysRevLett.112.203002](https://doi.org/10.1103/PhysRevLett.112.203002). URL: <https://link.aps.org/doi/10.1103/PhysRevLett.112.203002> (cit. on pp. 2, 11, 70).
- [28] M. G. Tarallo, T. Mazzoni, N. Poli, D. V. Sutyrin, X. Zhang, and G. M. Tino. "Test of Einstein Equivalence Principle for o-Spin and Half-Integer-Spin Atoms: Search for Spin-Gravity Coupling Effects." In: *Phys. Rev. Lett.* 113 (2 July 2014), p. 023005. DOI: [10.1103/PhysRevLett.113.023005](https://doi.org/10.1103/PhysRevLett.113.023005). URL: <https://link.aps.org/doi/10.1103/PhysRevLett.113.023005> (cit. on p. 2).
- [29] Peter Asenbaum, Chris Overstreet, Minjeong Kim, Joseph Curti, and Mark A. Kasevich. "Atom-Interferometric Test of the Equivalence Principle at the 10^{-12} Level." In: *Phys. Rev. Lett.* 125 (19 Nov. 2020), p. 191101. DOI: [10.1103/PhysRevLett.125.191101](https://doi.org/10.1103/PhysRevLett.125.191101). URL: <https://link.aps.org/doi/10.1103/PhysRevLett.125.191101> (cit. on p. 2).
- [30] B. Barrett et al. "Testing the universality of free fall using correlated 39K-87Rb atom interferometers." In: *AVS Quantum Science* 4.1 (2022). DOI: [10.1116/5.0076502](https://doi.org/10.1116/5.0076502) (cit. on p. 2).
- [31] Angelo Bassi, Kinjalk Lochan, Seema Satin, Tejinder P. Singh, and Hendrik Ulbricht. "Models of wave-function collapse, underlying theories, and experimental tests." In: *Rev. Mod. Phys.* 85 (2 Apr. 2013), pp. 471–527. DOI: [10.1103/RevModPhys.85.471](https://doi.org/10.1103/RevModPhys.85.471). URL: <https://link.aps.org/doi/10.1103/RevModPhys.85.471> (cit. on p. 2).
- [32] T. Kovachy, P. Asenbaum, C. Overstreet, C. A. Donnelly, S. M. Dickerson, A. Sugarbaker, J. M. Hogan, and M. A. Kasevich. "Quantum superposition at the half-metre scale." In: *Nature* 528.7583 (2015), pp. 530–533. DOI: [10.1038/nature16155](https://doi.org/10.1038/nature16155) (cit. on p. 2).

- [33] Björn Schrinski, Philipp Haslinger, Jörg Schmiedmayer, Klaus Hornberger, and Stefan Nimmrichter. "Testing collapse models with Bose-Einstein-condensate interferometry." In: *Phys. Rev. A* 107 (4 Apr. 2023), p. 043320. doi: [10.1103/PhysRevA.107.043320](https://doi.org/10.1103/PhysRevA.107.043320). URL: <https://link.aps.org/doi/10.1103/PhysRevA.107.043320> (cit. on p. 2).
- [34] G. Rosi, F. Sorrentino, L. Cacciapuoti, M. Prevedelli, and G. M. Tino. "Precision measurement of the Newtonian gravitational constant using cold atoms." In: *Nature* 510.7506 (June 2014), pp. 518–521. doi: [10.1038/nature13433](https://doi.org/10.1038/nature13433) (cit. on pp. 2, 76).
- [35] Richard H. Parker, Chenghui Yu, Weicheng Zhong, Brian Estey, and Holger Müller. "Measurement of the fine-structure constant as a test of the Standard Model." In: *Science* 360.6385 (Apr. 2018), pp. 191–195. doi: [10.1126/science.aap7706](https://doi.org/10.1126/science.aap7706) (cit. on p. 2).
- [36] Léo Morel, Zhibin Yao, Pierre Cladé, and Saïda Guellati-Khélifa. "Determination of the fine-structure constant with an accuracy of 81 parts per trillion." In: *Nature* 588.7836 (2020), pp. 61–65. doi: [10.1038/s41586-020-2964-7](https://doi.org/10.1038/s41586-020-2964-7) (cit. on p. 2).
- [37] M. Hauth, C. Freier, V. Schkolnik, A. Senger, M. Schmidt, and A. Peters. "First gravity measurements using the mobile atom interferometer GAIN." In: *Applied Physics B* 113.1 (2013), pp. 49–55. ISSN: 0946-2171. doi: [10.1007/s00340-013-5413-6](https://doi.org/10.1007/s00340-013-5413-6) (cit. on p. 2).
- [38] B. Fang et al. "Metrology with Atom Interferometry: Inertial Sensors from Laboratory to Field Applications." In: *Journal of Physics: Conference Series* 723 (2016), p. 012049. ISSN: 1742-6588. doi: [10.1088/1742-6596/723/1/012049](https://doi.org/10.1088/1742-6596/723/1/012049) (cit. on p. 2).
- [39] C. Freier, M. Hauth, V. Schkolnik, B. Leykauf, M. Schilling, H. Wziontek, H-G Scherneck, J. Müller, and A. Peters. "Mobile quantum gravity sensor with unprecedented stability." In: *Journal of Physics: Conference Series* 723 (2016), p. 012050. ISSN: 1742-6588. doi: [10.1088/1742-6596/723/1/012050](https://doi.org/10.1088/1742-6596/723/1/012050) (cit. on p. 2).
- [40] Y. Bidel, N. Zahzam, C. Blanchard, A. Bonnin, M. Cadoret, A. Bresson, D. Rouxel, and M. F. Lequentrec-Lalancette. "Absolute marine gravimetry with matter-wave interferometry." In: *Nature communications* 9.1 (2018), p. 627. doi: [10.1038/s41467-018-03040-2](https://doi.org/10.1038/s41467-018-03040-2) (cit. on p. 2).
- [41] R. Geiger et al. "Detecting inertial effects with airborne matter-wave interferometry." In: *Nature communications* 2 (2011), p. 474. doi: [10.1038/ncomms1479](https://doi.org/10.1038/ncomms1479) (cit. on p. 2).
- [42] Maike D. Lachmann et al. "Ultracold atom interferometry in space." In: *Nature Communications* 12.1 (2021), p. 1317. ISSN: 2041-1723. doi: [10.1038/s41467-021-21628-z](https://doi.org/10.1038/s41467-021-21628-z). URL: <https://doi.org/10.1038/s41467-021-21628-z> (cit. on pp. 2, 8).
- [43] David C. Aveline et al. "Observation of Bose-Einstein condensates in an Earth-orbiting research lab." In: *Nature* 582.7811 (2020), pp. 193–197. ISSN: 1476-4687. doi: [10.1038/s41586-020-2346-1](https://doi.org/10.1038/s41586-020-2346-1). URL: <https://doi.org/10.1038/s41586-020-2346-1> (cit. on pp. 2, 8).

- [44] Peter J. Martin, Bruce G. Oldaker, Andrew H. Miklich, and David E. Pritchard. "Bragg scattering of atoms from a standing light wave." In: *Phys. Rev. Lett.* 60 (6 1988), pp. 515–518. DOI: [10.1103/PhysRevLett.60.515](https://doi.org/10.1103/PhysRevLett.60.515). URL: <https://link.aps.org/doi/10.1103/PhysRevLett.60.515> (cit. on p. 3).
- [45] Ernst M. Rasel, Markus K. Oberthaler, Herman Batelaan, Jörg Schmiedmayer, and Anton Zeilinger. "Atom Wave Interferometry with Diffraction Gratings of Light." In: *Phys. Rev. Lett.* 75 (14 1995), pp. 2633–2637. DOI: [10.1103/PhysRevLett.75.2633](https://doi.org/10.1103/PhysRevLett.75.2633). URL: <https://link.aps.org/doi/10.1103/PhysRevLett.75.2633> (cit. on p. 3).
- [46] N. Poli, F.-Y. Wang, M. G. Tarallo, A. Alberti, M. Prevedelli, and G. M. Tino. "Precision Measurement of Gravity with Cold Atoms in an Optical Lattice and Comparison with a Classical Gravimeter." In: *Phys. Rev. Lett.* 106 (3 2011), p. 038501. DOI: [10.1103/PhysRevLett.106.038501](https://doi.org/10.1103/PhysRevLett.106.038501). URL: <https://link.aps.org/doi/10.1103/PhysRevLett.106.038501> (cit. on p. 3).
- [47] Liang Hu, Nicola Poli, Leonardo Salvi, and Guglielmo M. Tino. "Atom Interferometry with the Sr Optical Clock Transition." In: *Phys. Rev. Lett.* 119 (26 2017), p. 263601. DOI: [10.1103/PhysRevLett.119.263601](https://doi.org/10.1103/PhysRevLett.119.263601). URL: <https://link.aps.org/doi/10.1103/PhysRevLett.119.263601> (cit. on p. 3).
- [48] Sheng-wei Chiow, Tim Kovachy, Hui-Chun Chien, and Mark A. Kasevich. "102 \hbar k Large Area Atom Interferometers." In: *Phys. Rev. Lett.* 107 (13 2011), p. 130403. DOI: [10.1103/PhysRevLett.107.130403](https://doi.org/10.1103/PhysRevLett.107.130403). URL: <https://link.aps.org/doi/10.1103/PhysRevLett.107.130403> (cit. on p. 3).
- [49] Martina Gebbe et al. "Twin-lattice atom interferometry." In: *Nature communications* 12.1 (2021), p. 2544. DOI: [10.1038/s41467-021-22823-8](https://doi.org/10.1038/s41467-021-22823-8) (cit. on p. 3).
- [50] T. Rodzinka, E. Dionis, L. Calmels, S. Beldjoudi, A. Béguin, D. Guéry-Odelin, B. Allard, D. Sugny, and A. Gauguet. *Optimal Floquet Engineering for Large Scale Atom Interferometers*. 2024. DOI: [10.48550/arXiv.2403.14337](https://doi.org/10.48550/arXiv.2403.14337) (cit. on p. 3).
- [51] L. Zhou, Z. Y. Xiong, W. Yang, B. Tang, W. C. Peng, K. Hao, R. B. Li, M. Liu, J. Wang, and M. S. Zhan. "Development of an atom gravimeter and status of the 10-meter atom interferometer for precision gravity measurement." In: *General Relativity and Gravitation* 43.7 (2011), pp. 1931–1942. ISSN: 0001-7701. DOI: [10.1007/s10714-011-1167-9](https://doi.org/10.1007/s10714-011-1167-9) (cit. on p. 3).
- [52] J. Hartwig, S. Abend, C. Schubert, D. Schlippert, H. Ahlers, K. Posso-Trujillo, N. Gaaloul, W. Ertmer, and E. M. Rasel. "Testing the universality of free fall with rubidium and ytterbium in a very large baseline atom interferometer." In: *New Journal of Physics* 17.3 (2015), p. 035011. DOI: [10.1088/1367-2630/17/3/035011](https://doi.org/10.1088/1367-2630/17/3/035011) (cit. on pp. 3, 8, 11, 68, 72).
- [53] L. Badurina et al. "AION: an atom interferometer observatory and network." In: *Journal of Cosmology and Astroparticle Physics* 2020.05 (2020), p. 011. DOI: [10.1088/1475-7516/2020/05/011](https://doi.org/10.1088/1475-7516/2020/05/011) (cit. on pp. 3, 9, 68, 72).

- [54] Luca Pezzè, Augusto Smerzi, Markus K. Oberthaler, Roman Schmied, and Philipp Treutlein. "Quantum metrology with nonclassical states of atomic ensembles." In: *Rev. Mod. Phys.* 90 (3 2018), p. 035005. DOI: [10.1103/RevModPhys.90.035005](https://doi.org/10.1103/RevModPhys.90.035005). URL: <https://link.aps.org/doi/10.1103/RevModPhys.90.035005> (cit. on pp. 3, 77).
- [55] S. Loriani et al. "Atomic source selection in space-borne gravitational wave detection." In: *New Journal of Physics* 21.6 (2019), p. 063030. DOI: [10.1088/1367-2630/ab22d0](https://doi.org/10.1088/1367-2630/ab22d0) (cit. on pp. 4, 8).
- [56] W. Ketterle, D. S. Durfee, and D. M. Stamper-Kurn. *Making, probing and understanding Bose-Einstein condensates.* 1999. DOI: [10.48550/arXiv.cond-mat/9904034](https://arxiv.org/abs/cond-mat/9904034) (cit. on pp. 4, 10).
- [57] C. J. Pethick and H. Smith. *Bose-Einstein Condensation in Dilute Gases.* Cambridge University Press, 2011. ISBN: 9780521846516. DOI: [10.1017/CBO9780511802850](https://doi.org/10.1017/CBO9780511802850) (cit. on p. 5).
- [58] A. Einstein. "Quantentheorie des einatomigen idealen Gases." In: *Albert Einstein: Akademie-Vorträge.* Ed. by Dieter Simon. Wiley, 2005, pp. 237–244. ISBN: 9783527406098. DOI: [10.1002/3527608958.ch27](https://doi.org/10.1002/3527608958.ch27) (cit. on p. 5).
- [59] Bose. "Plancks Gesetz und Lichtquantenhypothese." In: *Zeitschrift für Physik* 26.1 (1924), pp. 178–181. ISSN: 1434-6001. DOI: [10.1007/BF01327326](https://doi.org/10.1007/BF01327326) (cit. on p. 5).
- [60] M. H. Anderson, J. R. Ensher, M. R. Matthews, C. E. Wieman, and E. A. Cornell. "Observation of bose-einstein condensation in a dilute atomic vapor." In: *Science (New York, N.Y.)* 269.5221 (1995), pp. 198–201. ISSN: 0036-8075. DOI: [10.1126/science.269.5221.198](https://doi.org/10.1126/science.269.5221.198) (cit. on p. 5).
- [61] K. B. Davis, M. O. Mewes, M. R. Andrews, N. J. van Druten, D. S. Durfee, D. M. Kurn, and W. Ketterle. "Bose-Einstein Condensation in a Gas of Sodium Atoms." In: *Phys. Rev. Lett.* 75 (22 1995), pp. 3969–3973. DOI: [10.1103/PhysRevLett.75.3969](https://doi.org/10.1103/PhysRevLett.75.3969). URL: <https://link.aps.org/doi/10.1103/PhysRevLett.75.3969> (cit. on p. 5).
- [62] Simon Stellmer, Benjamin Pasquiou, Rudolf Grimm, and Florian Schreck. "Laser Cooling to Quantum Degeneracy." In: *Phys. Rev. Lett.* 110 (26 2013), p. 263003. DOI: [10.1103/PhysRevLett.110.263003](https://doi.org/10.1103/PhysRevLett.110.263003). URL: <https://link.aps.org/doi/10.1103/PhysRevLett.110.263003> (cit. on pp. 5, 8).
- [63] Alban Urvoy, Zachary Vendeiro, Joshua Ramette, Albert Adiyatullin, and Vladan Vuletić. "Direct Laser Cooling to Bose-Einstein Condensation in a Dipole Trap." In: *Phys. Rev. Lett.* 122 (20 2019), p. 203202. DOI: [10.1103/PhysRevLett.122.203202](https://doi.org/10.1103/PhysRevLett.122.203202). URL: <https://link.aps.org/doi/10.1103/PhysRevLett.122.203202> (cit. on pp. 5, 8).
- [64] Charles S. Adams, Heun Jin Lee, Nir Davidson, Mark Kasevich, and Steven Chu. "Evaporative Cooling in a Crossed Dipole Trap." In: *Phys. Rev. Lett.* 74 (18 1995), pp. 3577–3580. DOI: [10.1103/PhysRevLett.74.3577](https://doi.org/10.1103/PhysRevLett.74.3577). URL: <https://link.aps.org/doi/10.1103/PhysRevLett.74.3577> (cit. on p. 5).

[65] Kendall B. Davis, Marc-Oliver Mewes, Michael A. Joffe, Michael R. Andrews, and Wolfgang Ketterle. "Evaporative Cooling of Sodium Atoms." In: *Phys. Rev. Lett.* 74 (26 1995), pp. 5202–5205. DOI: [10.1103/PhysRevLett.74.5202](https://doi.org/10.1103/PhysRevLett.74.5202). URL: <https://link.aps.org/doi/10.1103/PhysRevLett.74.5202> (cit. on p. 5).

[66] Chiara D'Errico, Matteo Zaccanti, Marco Fattori, Giacomo Roati, Massimo Inguscio, Giovanni Modugno, and Andrea Simoni. "Feshbach resonances in ultracold 39 K." In: *New Journal of Physics* 9.7 (2007), p. 223. DOI: [10.1088/1367-2630/9/7/223](https://doi.org/10.1088/1367-2630/9/7/223) (cit. on p. 6).

[67] Yu. Kagan, A. E. Muryshev, and G. V. Shlyapnikov. "Collapse and Bose-Einstein Condensation in a Trapped Bose Gas with Negative Scattering Length." In: *Phys. Rev. Lett.* 81 (5 1998), pp. 933–937. DOI: [10.1103/PhysRevLett.81.933](https://doi.org/10.1103/PhysRevLett.81.933). URL: <https://link.aps.org/doi/10.1103/PhysRevLett.81.933> (cit. on p. 6).

[68] Tino Weber, Jens Herbig, Michael Mark, Hanns-Christoph Nägerl, and Rudolf Grimm. "Bose-Einstein condensation of cesium." In: *Science (New York, N.Y.)* 299.5604 (2003), pp. 232–235. DOI: [10.1126/science.1079699](https://doi.org/10.1126/science.1079699) (cit. on pp. 6, 8, 9).

[69] S. L. Cornish, N. R. Claussen, J. L. Roberts, E. A. Cornell, and C. E. Wieman. "Stable ^{85}Rb Bose-Einstein Condensates with Widely Tunable Interactions." In: *Phys. Rev. Lett.* 85 (9 2000), pp. 1795–1798. DOI: [10.1103/PhysRevLett.85.1795](https://doi.org/10.1103/PhysRevLett.85.1795). URL: <https://link.aps.org/doi/10.1103/PhysRevLett.85.1795> (cit. on p. 6).

[70] S. Inouye, M. R. Andrews, J. Stenger, H.-J. Miesner, D. M. Stamper-Kurn, and W. Ketterle. "Observation of Feshbach resonances in a Bose-Einstein condensate." In: *Nature* 392.6672 (1998), pp. 151–154. ISSN: 1476-4687. DOI: [10.1038/32354](https://doi.org/10.1038/32354). URL: <https://doi.org/10.1038/32354> (cit. on p. 6).

[71] Cheng Chin, Rudolf Grimm, Paul Julienne, and Eite Tiesinga. "Feshbach resonances in ultracold gases." In: *Rev. Mod. Phys.* 82 (2 2010), pp. 1225–1286. DOI: [10.1103/RevModPhys.82.1225](https://doi.org/10.1103/RevModPhys.82.1225). URL: <https://link.aps.org/doi/10.1103/RevModPhys.82.1225> (cit. on p. 6).

[72] Christoph Eigen, Jake A. P. Glidden, Raphael Lopes, Eric A. Cornell, Robert P. Smith, and Zoran Hadzibabic. "Universal prethermal dynamics of Bose gases quenched to unitarity." In: *Nature* 563.7730 (2018), pp. 221–224. DOI: [10.1038/s41586-018-0674-1](https://doi.org/10.1038/s41586-018-0674-1) (cit. on p. 6).

[73] S. Jochim, M. Bartenstein, A. Altmeyer, G. Hendl, S. Riedl, C. Chin, J. Hecker Denschlag, and R. Grimm. "Bose-Einstein condensation of molecules." In: *Science (New York, N.Y.)* 302.5653 (2003), pp. 2101–2103. ISSN: 0036-8075. DOI: [10.1126/science.1093280](https://doi.org/10.1126/science.1093280) (cit. on p. 6).

[74] M. W. Zwierlein, C. A. Stan, C. H. Schunck, S. M. F. Raupach, S. Gupta, Z. Hadzibabic, and W. Ketterle. "Observation of Bose-Einstein Condensation of Molecules." In: *Phys. Rev. Lett.* 91 (25 2003), p. 250401. DOI: [10.1103/PhysRevLett.91.250401](https://doi.org/10.1103/PhysRevLett.91.250401). URL: <https://link.aps.org/doi/10.1103/PhysRevLett.91.250401> (cit. on p. 6).

- [75] Kai K. Voges, Philipp Gersema, Mara Meyer zum Alten Borgloh, Torben A. Schulze, Torsten Hartmann, Alessandro Zenesini, and Silke Ospelkaus. "Ultracold Gas of Bosonic $^{23}\text{Na}^{39}\text{K}$ Ground-State Molecules." In: *Phys. Rev. Lett.* 125 (8 2020), p. 083401. DOI: [10.1103/PhysRevLett.125.083401](https://doi.org/10.1103/PhysRevLett.125.083401). URL: <https://link.aps.org/doi/10.1103/PhysRevLett.125.083401> (cit. on p. 6).
- [76] Cindy A. Regal, Christopher Ticknor, John L. Bohn, and Deborah S. Jin. "Creation of ultracold molecules from a Fermi gas of atoms." In: *Nature* 424.6944 (2003), pp. 47–50. DOI: [10.1038/nature01738](https://doi.org/10.1038/nature01738) (cit. on p. 6).
- [77] J. Cubizolles, T. Bourdel, S. J. J. M. F. Kokkelmans, G. V. Shlyapnikov, and C. Salomon. "Production of Long-Lived Ultracold Li_2 Molecules from a Fermi Gas." In: *Phys. Rev. Lett.* 91 (24 2003), p. 240401. DOI: [10.1103/PhysRevLett.91.240401](https://doi.org/10.1103/PhysRevLett.91.240401). URL: <https://link.aps.org/doi/10.1103/PhysRevLett.91.240401> (cit. on p. 6).
- [78] G. Roati, M. Zaccanti, C. D'Errico, J. Catani, M. Modugno, A. Simoni, M. Inguscio, and G. Modugno. " ^{39}K Bose-Einstein Condensate with Tunable Interactions." In: *Phys. Rev. Lett.* 99 (1 2007), p. 010403. DOI: [10.1103/PhysRevLett.99.010403](https://doi.org/10.1103/PhysRevLett.99.010403). URL: <https://link.aps.org/doi/10.1103/PhysRevLett.99.010403> (cit. on pp. 6, 7).
- [79] J. L. Roberts, N. R. Claussen, James P. Burke, Chris H. Greene, E. A. Cornell, and C. E. Wieman. "Resonant Magnetic Field Control of Elastic Scattering in Cold ^{85}Rb ." In: *Phys. Rev. Lett.* 81 (23 1998), pp. 5109–5112. DOI: [10.1103/PhysRevLett.81.5109](https://doi.org/10.1103/PhysRevLett.81.5109). URL: <https://link.aps.org/doi/10.1103/PhysRevLett.81.5109> (cit. on p. 6).
- [80] Cheng Chin, Vladan Vuletić, Andrew J. Kerman, and Steven Chu. "High Resolution Feshbach Spectroscopy of Cesium." In: *Phys. Rev. Lett.* 85 (13 2000), pp. 2717–2720. DOI: [10.1103/PhysRevLett.85.2717](https://doi.org/10.1103/PhysRevLett.85.2717). URL: <https://link.aps.org/doi/10.1103/PhysRevLett.85.2717> (cit. on p. 6).
- [81] L. Khaykovich, F. Schreck, G. Ferrari, T. Bourdel, J. Cubizolles, L. D. Carr, Y. Castin, and C. Salomon. "Formation of a matter-wave bright soliton." In: *Science (New York, N.Y.)* 296.5571 (2002), pp. 1290–1293. ISSN: 0036-8075. DOI: [10.1126/science.1071021](https://doi.org/10.1126/science.1071021) (cit. on p. 6).
- [82] A. Marte, T. Volz, J. Schuster, S. Dürr, G. Rempe, E. G. M. van Kempen, and B. J. Verhaar. "Feshbach Resonances in Rubidium 87: Precision Measurement and Analysis." In: *Phys. Rev. Lett.* 89 (28 2002), p. 283202. DOI: [10.1103/PhysRevLett.89.283202](https://doi.org/10.1103/PhysRevLett.89.283202). URL: <https://link.aps.org/doi/10.1103/PhysRevLett.89.283202> (cit. on p. 6).
- [83] S. Knoop, T. Schuster, R. Scelle, A. Trautmann, J. Appmeier, M. K. Oberthaler, E. Tiesinga, and E. Tiemann. "Feshbach spectroscopy and analysis of the interaction potentials of ultracold sodium." In: *Phys. Rev. A* 83 (4 2011), p. 042704. DOI: [10.1103/PhysRevA.83.042704](https://doi.org/10.1103/PhysRevA.83.042704). URL: <https://link.aps.org/doi/10.1103/PhysRevA.83.042704> (cit. on p. 6).

[84] K. Aikawa, A. Frisch, M. Mark, S. Baier, A. Rietzler, R. Grimm, and F. Ferlaino. “Bose-Einstein Condensation of Erbium.” In: *Phys. Rev. Lett.* 108 (21 2012), p. 210401. DOI: [10.1103/PhysRevLett.108.210401](https://doi.org/10.1103/PhysRevLett.108.210401). URL: <https://link.aps.org/doi/10.1103/PhysRevLett.108.210401> (cit. on p. 6).

[85] P. O. Fedichev, Yu. Kagan, G. V. Shlyapnikov, and J. T. M. Walraven. “Influence of Nearly Resonant Light on the Scattering Length in Low-Temperature Atomic Gases.” In: *Phys. Rev. Lett.* 77 (14 1996), pp. 2913–2916. DOI: [10.1103/PhysRevLett.77.2913](https://doi.org/10.1103/PhysRevLett.77.2913). URL: <https://link.aps.org/doi/10.1103/PhysRevLett.77.2913> (cit. on p. 6).

[86] M. Theis, G. Thalhammer, K. Winkler, M. Hellwig, G. Ruff, R. Grimm, and J. Hecker Denschlag. “Tuning the Scattering Length with an Optically Induced Feshbach Resonance.” In: *Phys. Rev. Lett.* 93 (12 2004), p. 123001. DOI: [10.1103/PhysRevLett.93.123001](https://doi.org/10.1103/PhysRevLett.93.123001). URL: <https://link.aps.org/doi/10.1103/PhysRevLett.93.123001> (cit. on pp. 6, 68).

[87] K. Enomoto, K. Kasa, M. Kitagawa, and Y. Takahashi. “Optical Feshbach Resonance Using the Intercombination Transition.” In: *Phys. Rev. Lett.* 101 (20 2008), p. 203201. DOI: [10.1103/PhysRevLett.101.203201](https://doi.org/10.1103/PhysRevLett.101.203201). URL: <https://link.aps.org/doi/10.1103/PhysRevLett.101.203201> (cit. on pp. 6, 68).

[88] S. Blatt, T. L. Nicholson, B. J. Bloom, J. R. Williams, J. W. Thomsen, P. S. Julienne, and J. Ye. “Measurement of Optical Feshbach Resonances in an Ideal Gas.” In: *Phys. Rev. Lett.* 107 (7 2011), p. 073202. DOI: [10.1103/PhysRevLett.107.073202](https://doi.org/10.1103/PhysRevLett.107.073202). URL: <https://link.aps.org/doi/10.1103/PhysRevLett.107.073202> (cit. on p. 6).

[89] Mi Yan, B. J. DeSalvo, B. Ramachandhran, H. Pu, and T. C. Killian. “Controlling Condensate Collapse and Expansion with an Optical Feshbach Resonance.” In: *Phys. Rev. Lett.* 110 (12 2013), p. 123201. DOI: [10.1103/PhysRevLett.110.123201](https://doi.org/10.1103/PhysRevLett.110.123201). URL: <https://link.aps.org/doi/10.1103/PhysRevLett.110.123201> (cit. on pp. 6, 68).

[90] Eberhard Tiemann, Philipp Gersema, Kai K. Voges, Torsten Hartmann, Alessandro Zenesini, and Silke Ospelkaus. “Beyond Born-Oppenheimer approximation in ultracold atomic collisions.” In: *Phys. Rev. Research* 2 (1 Mar. 2020), p. 013366. DOI: [10.1103/PhysRevResearch.2.013366](https://doi.org/10.1103/PhysRevResearch.2.013366). URL: <https://link.aps.org/doi/10.1103/PhysRevResearch.2.013366> (cit. on p. 7).

[91] Robert L. D. Campbell, Robert P. Smith, Naaman Tammuz, Scott Beattie, Stuart Moulder, and Zoran Hadzibabic. “Efficient production of large ^{39}K Bose-Einstein condensates.” In: *Phys. Rev. A* 82 (6 2010), p. 063611. DOI: [10.1103/PhysRevA.82.063611](https://doi.org/10.1103/PhysRevA.82.063611). URL: <https://link.aps.org/doi/10.1103/PhysRevA.82.063611> (cit. on p. 7).

[92] M. Landini, S. Roy, L. Carcagní, D. Trypogeorgos, M. Fattori, M. Inguscio, and G. Modugno. “Sub-Doppler laser cooling of potassium atoms.” In: *Phys. Rev. A* 84 (4 Oct. 2011), p. 043432. DOI: [10.1103/PhysRevA.84.043432](https://doi.org/10.1103/PhysRevA.84.043432). URL: <https://link.aps.org/doi/10.1103/PhysRevA.84.043432> (cit. on p. 7).

- [93] G. Salomon, L. Fouché, S. Lepoutre, A. Aspect, and T. Bourdel. “All-optical cooling of ^{39}K to Bose-Einstein condensation.” In: *Phys. Rev. A* 90 (3 Sept. 2014), p. 033405. DOI: [10.1103/PhysRevA.90.033405](https://doi.org/10.1103/PhysRevA.90.033405). URL: <https://link.aps.org/doi/10.1103/PhysRevA.90.033405> (cit. on p. 7).
- [94] F. Anders et al. “Momentum Entanglement for Atom Interferometry.” In: *Phys. Rev. Lett.* 127 (14 2021), p. 140402. DOI: [10.1103/PhysRevLett.127.140402](https://doi.org/10.1103/PhysRevLett.127.140402). URL: <https://link.aps.org/doi/10.1103/PhysRevLett.127.140402> (cit. on pp. 7, 77).
- [95] S. S. Szigeti, J. E. Debs, J. J. Hope, N. P. Robins, and J. D. Close. “Why momentum width matters for atom interferometry with Bragg pulses.” In: *New Journal of Physics* 14.2 (2012), p. 023009. DOI: [10.1088/1367-2630/14/2/023009](https://doi.org/10.1088/1367-2630/14/2/023009) (cit. on p. 8).
- [96] H. Müntinga et al. “Interferometry with Bose-Einstein Condensates in Microgravity.” In: *Phys. Rev. Lett.* 110.9 (Feb. 2013). DOI: [10.1103/physrevlett.110.093602](https://doi.org/10.1103/physrevlett.110.093602) (cit. on pp. 8, 9).
- [97] T. Hensel, S. Loriani, C. Schubert, F. Fitzek, S. Abend, H. Ahlers, J.-N. Siemß, K. Hammerer, E. M. Rasel, and N. Gaaloul. “Inertial sensing with quantum gases: a comparative performance study of condensed versus thermal sources for atom interferometry.” In: *The European Physical Journal D* 75.3 (2021). ISSN: 1434-6060. DOI: [10.1140/epjd/s10053-021-00069-9](https://doi.org/10.1140/epjd/s10053-021-00069-9) (cit. on p. 8).
- [98] J. Le Gouët, T. E. Mehlstäubler, J. Kim, S. Merlet, A. Clairon, A. Landragin, and F. Pereira dos Santos. “Limits to the sensitivity of a low noise compact atomic gravimeter.” In: *Applied Physics B* 92.2 (2008), pp. 133–144. ISSN: 0946-2171. DOI: [10.1007/s00340-008-3088-1](https://doi.org/10.1007/s00340-008-3088-1) (cit. on p. 8).
- [99] Zhong-Kun Hu, Bu-Liang Sun, Xiao-Chun Duan, Min-Kang Zhou, Le-Le Chen, Su Zhan, Qiao-Zhen Zhang, and Jun Luo. “Demonstration of an ultrahigh-sensitivity atom-interferometry absolute gravimeter.” In: *Phys. Rev. A* 88 (4 2013), p. 043610. DOI: [10.1103/PhysRevA.88.043610](https://doi.org/10.1103/PhysRevA.88.043610). URL: <https://link.aps.org/doi/10.1103/PhysRevA.88.043610> (cit. on p. 8).
- [100] Vincent Ménoret, Pierre Vermeulen, Nicolas Le Moigne, Sylvain Bonvalot, Philippe Bouyer, Arnaud Landragin, and Bruno Desruelle. “Gravity measurements below 10^{-9} g with a transportable absolute quantum gravimeter.” In: *Scientific reports* 8.1 (2018), p. 12300. DOI: [10.1038/s41598-018-30608-1](https://doi.org/10.1038/s41598-018-30608-1) (cit. on p. 8).
- [101] Daniel M. Farkas, Kai M. Hudek, Evan A. Salim, Stephen R. Segal, Matthew B. Squires, and Dana Z. Anderson. “A compact, transportable, microchip-based system for high repetition rate production of Bose-Einstein condensates.” In: *Applied Physics Letters* 96.9 (2010), p. 093102. DOI: [10.1063/1.3327812](https://doi.org/10.1063/1.3327812) (cit. on p. 8).
- [102] Jan Rudolph et al. “A high-flux BEC source for mobile atom interferometers.” In: *New Journal of Physics* 17.6 (2015), p. 065001. DOI: [10.1088/1367-2630/17/6/065001](https://doi.org/10.1088/1367-2630/17/6/065001) (cit. on pp. 8, 65).

- [103] Dennis Becker et al. “Space-borne Bose–Einstein condensation for precision interferometry.” In: *Nature* 562.7727 (Oct. 2018), pp. 391–395. DOI: [10.1038/s41586-018-0605-1](https://doi.org/10.1038/s41586-018-0605-1) (cit. on p. 8).
- [104] Christian Deppner et al. “Collective-Mode Enhanced Matter-Wave Optics.” In: *Phys. Rev. Lett.* 127 (10 Aug. 2021), p. 100401. DOI: [10.1103/PhysRevLett.127.100401](https://doi.org/10.1103/PhysRevLett.127.100401). URL: <https://link.aps.org/doi/10.1103/PhysRevLett.127.100401> (cit. on pp. 8, 11, 65).
- [105] Naceur Gaaloul et al. “A space-based quantum gas laboratory at picokelvin energy scales.” In: *Nature communications* 13.1 (2022), p. 7889. DOI: [10.1038/s41467-022-35274-6](https://doi.org/10.1038/s41467-022-35274-6) (cit. on p. 8).
- [106] M. D. Barrett, J. A. Sauer, and M. S. Chapman. “All-Optical Formation of an Atomic Bose–Einstein Condensate.” In: *Phys. Rev. Lett.* 87 (1 June 2001), p. 010404. DOI: [10.1103/PhysRevLett.87.010404](https://doi.org/10.1103/PhysRevLett.87.010404). URL: <https://link.aps.org/doi/10.1103/PhysRevLett.87.010404> (cit. on p. 8).
- [107] Yosuke Takasu, Kenichi Maki, Kaduki Komori, Tetsushi Takano, Kazuhito Honda, Mitsutaka Kumakura, Tsutomu Yabuzaki, and Yoshiro Takahashi. “Spin-Singlet Bose–Einstein Condensation of Two-Electron Atoms.” In: *Phys. Rev. Lett.* 91 (4 July 2003), p. 040404. DOI: [10.1103/PhysRevLett.91.040404](https://doi.org/10.1103/PhysRevLett.91.040404). URL: <https://link.aps.org/doi/10.1103/PhysRevLett.91.040404> (cit. on p. 8).
- [108] J.-F. Clément, J.-P. Brantut, M. Robert-de Saint-Vincent, R. A. Nyman, A. Aspect, T. Bourdel, and P. Bouyer. “All-optical runaway evaporation to Bose–Einstein condensation.” In: *Phys. Rev. A* 79 (6 June 2009), p. 061406. DOI: [10.1103/PhysRevA.79.061406](https://doi.org/10.1103/PhysRevA.79.061406). URL: <https://link.aps.org/doi/10.1103/PhysRevA.79.061406> (cit. on p. 8).
- [109] Simon Stellmer, Meng Khoon Tey, Bo Huang, Rudolf Grimm, and Florian Schreck. “Bose–Einstein Condensation of Strontium.” In: *Phys. Rev. Lett.* 103 (20 2009), p. 200401. DOI: [10.1103/PhysRevLett.103.200401](https://doi.org/10.1103/PhysRevLett.103.200401). URL: <https://link.aps.org/doi/10.1103/PhysRevLett.103.200401> (cit. on p. 8).
- [110] M. Landini, S. Roy, G. Roati, A. Simoni, M. Inguscio, G. Modugno, and M. Fattori. “Direct evaporative cooling of ^{39}K atoms to Bose–Einstein condensation.” In: *Phys. Rev. A* 86 (3 Sept. 2012), p. 033421. DOI: [10.1103/PhysRevA.86.033421](https://doi.org/10.1103/PhysRevA.86.033421). URL: <https://link.aps.org/doi/10.1103/PhysRevA.86.033421> (cit. on p. 8).
- [111] B. Barrett, P. Cheiney, B. Battelier, F. Napolitano, and P. Bouyer. “Multidimensional Atom Optics and Interferometry.” In: *Phys. Rev. Lett.* 122 (4 2019), p. 043604. DOI: [10.1103/PhysRevLett.122.043604](https://doi.org/10.1103/PhysRevLett.122.043604). URL: <https://link.aps.org/doi/10.1103/PhysRevLett.122.043604> (cit. on pp. 8, 72).
- [112] Quentin d’Armagnac de Castanet, Cyrille Des Cognets, Romain Arguel, Simon Templier, Vincent Jarlaud, Vincent Ménoret, Bruno Desruelle, Philippe Bouyer, and Baptiste Battelier. *Atom interferometry at arbitrary orientations and rotation rates*. 2024. DOI: [10.48550/arXiv.2402.18988](https://doi.org/10.48550/arXiv.2402.18988) (cit. on pp. 8, 72).

- [113] K. M. O’Hara, M. E. Gehm, S. R. Granade, and J. E. Thomas. “Scaling laws for evaporative cooling in time-dependent optical traps.” In: *Physical Review A* 64.5 (Oct. 2001), p. 051403. DOI: [10.1103/physreva.64.051403](https://doi.org/10.1103/physreva.64.051403) (cit. on p. 8).
- [114] D. Jacob, E. Mimoun, L. de Sarlo, M. Weitz, J. Dalibard, and F. Gerbier. “Production of sodium Bose–Einstein condensates in an optical dimple trap.” In: *New Journal of Physics* 13.6 (2011), p. 065022. DOI: [10.1088/1367-2630/13/6/065022](https://doi.org/10.1088/1367-2630/13/6/065022) (cit. on p. 8).
- [115] Zachary Vendeiro, Joshua Ramette, Alyssa Rudelis, Michelle Chong, Josiah Sinclair, Luke Stewart, Alban Urvoy, and Vladan Vuletić. “Machine-learning-accelerated Bose-Einstein condensation.” In: *Phys. Rev. Res.* 4 (4 Dec. 2022), p. 043216. DOI: [10.1103/PhysRevResearch.4.043216](https://doi.org/10.1103/PhysRevResearch.4.043216). URL: <https://link.aps.org/doi/10.1103/PhysRevResearch.4.043216> (cit. on pp. 8, 65).
- [116] T. Kinoshita, T. Wenger, and D.S. Weiss. “All-optical Bose-Einstein condensation using a compressible crossed dipole trap.” In: *Phys. Rev. A* 71.1 (2005), p. 011602. DOI: [10.1103/PhysRevA.71.011602](https://doi.org/10.1103/PhysRevA.71.011602) (cit. on p. 8).
- [117] David McGloin, G. Spalding, H. Melville, W. Sibbett, and K. Dholakia. “Applications of spatial light modulators in atom optics.” In: *Optics express* 11.2 (2003), pp. 158–166. DOI: [10.1364/OE.11.000158](https://doi.org/10.1364/OE.11.000158) (cit. on p. 9).
- [118] K. Henderson, C. Ryu, C. MacCormick, and M. G. Boshier. “Experimental demonstration of painting arbitrary and dynamic potentials for Bose–Einstein condensates.” In: *New Journal of Physics* 11.4 (2009), p. 043030. DOI: [10.1088/1367-2630/11/4/043030](https://doi.org/10.1088/1367-2630/11/4/043030) (cit. on p. 9).
- [119] Richard Roy, Alaina Green, Ryan Bowler, and Subhadeep Gupta. “Rapid cooling to quantum degeneracy in dynamically shaped atom traps.” In: *Phys. Rev. A* 93 (4 Apr. 2016), p. 043403. DOI: [10.1103/PhysRevA.93.043403](https://doi.org/10.1103/PhysRevA.93.043403). URL: <https://link.aps.org/doi/10.1103/PhysRevA.93.043403> (cit. on p. 9).
- [120] Dorothee Tell. “A prototype apparatus for very long baseline atom interferometry.” PhD thesis. 2024. DOI: [10.15488/17346](https://doi.org/10.15488/17346) (cit. on pp. 9, 11).
- [121] G. Condon et al. “All-Optical Bose-Einstein Condensates in Microgravity.” In: *Physical Review Letters* 123.24 (Dec. 2019). DOI: [10.1103/physrevlett.123.240402](https://doi.org/10.1103/physrevlett.123.240402) (cit. on p. 9).
- [122] Mareike Hetzel. “Number-resolved Analysis of Many-body Quantum States.” PhD thesis. 2023. DOI: [10.15488/15588](https://doi.org/10.15488/15588) (cit. on p. 9).
- [123] Henning Albers et al. “All-optical matter-wave lens using time-averaged potentials.” In: *Communications Physics* 5.1 (2022). DOI: [10.1038/s42005-022-00825-2](https://doi.org/10.1038/s42005-022-00825-2) (cit. on pp. 10, 13, 71, 72, 78).
- [124] C. Schubert et al. *Differential atom interferometry with ${}^87\text{Rb}$ and ${}^85\text{Rb}$ for testing the UFF in STE-QUEST*. 2013. DOI: [10.48550/arXiv.1312.5963](https://doi.org/10.48550/arXiv.1312.5963) (cit. on p. 9).
- [125] A. Trimeche et al. “Concept study and preliminary design of a cold atom interferometer for space gravity gradiometry.” In: *Classical and Quantum Gravity* 36.21 (2019), p. 215004. ISSN: 0264-9381. DOI: [10.1088/1361-6382/ab4548](https://doi.org/10.1088/1361-6382/ab4548) (cit. on p. 9).

[126] Christian Struckmann, Robin Corgier, Sina Loriani, Gina Kleinsteenberg, Nina Gox, Enno Giese, Gilles Métris, Naceur Gaaloul, and Peter Wolf. “Platform and environment requirements of a satellite quantum test of the weak equivalence principle at the 10^{-17} level.” In: *Phys. Rev. D* 109 (6 2024), p. 064010. DOI: [10.1103/PhysRevD.109.064010](https://doi.org/10.1103/PhysRevD.109.064010). URL: <https://link.aps.org/doi/10.1103/PhysRevD.109.064010> (cit. on pp. 9, 72).

[127] B Canuel et al. “ELGAR—a European Laboratory for Gravitation and Atom-interferometric Research.” In: *Classical and Quantum Gravity* 37.22 (2020), p. 225017. DOI: [10.1088/1361-6382/aba80e](https://doi.org/10.1088/1361-6382/aba80e). URL: <https://dx.doi.org/10.1088/1361-6382/aba80e> (cit. on pp. 9, 72).

[128] K. S. Hardman, P. J. Everitt, G. D. McDonald, P. Manju, P. B. Wigley, M. A. Sooriyabandara, C. C. N. Kuhn, J. E. Debs, J. D. Close, and N. P. Robins. “Simultaneous Precision Gravimetry and Magnetic Gradiometry with a Bose-Einstein Condensate: A High Precision, Quantum Sensor.” In: *Phys. Rev. Lett.* 117 (13 2016), p. 138501. DOI: [10.1103/PhysRevLett.117.138501](https://doi.org/10.1103/PhysRevLett.117.138501). URL: <https://link.aps.org/doi/10.1103/PhysRevLett.117.138501> (cit. on p. 9).

[129] Daniel Gochnauer, Tahiyat Rahman, Anna Wirth-Singh, and Subhadeep Gupta. “Interferometry in an Atomic Fountain with Ytterbium Bose-Einstein Condensates.” In: *Atoms* 9.3 (2021), p. 58. DOI: [10.3390/atoms9030058](https://doi.org/10.3390/atoms9030058) (cit. on p. 9).

[130] A.E. Leanhardt, T.A. Pasquini, M. Saba, A. Schirotzek, Y. Shin, D. Kielpinski, D.E. Pritchard, and W. Ketterle. “Cooling Bose-Einstein Condensates Below 500 Picokelvin.” In: *Science* 301.5639 (2003), pp. 1513–1515. DOI: [10.1126/science.1088827](https://doi.org/10.1126/science.1088827) (cit. on p. 9).

[131] Patrick Medley, David M. Weld, Hirokazu Miyake, David E. Pritchard, and Wolfgang Ketterle. “Spin Gradient Demagnetization Cooling of Ultracold Atoms.” In: *Phys. Rev. Lett.* 106 (19 May 2011), p. 195301. DOI: [10.1103/PhysRevLett.106.195301](https://doi.org/10.1103/PhysRevLett.106.195301). URL: <https://link.aps.org/doi/10.1103/PhysRevLett.106.195301> (cit. on p. 9).

[132] Hubert Ammann and Nelson Christensen. “Delta Kick Cooling: A New Method for Cooling Atoms.” In: *Phys. Rev. Lett.* 78 (11 Mar. 1997), pp. 2088–2091. DOI: [10.1103/PhysRevLett.78.2088](https://doi.org/10.1103/PhysRevLett.78.2088). URL: <https://link.aps.org/doi/10.1103/PhysRevLett.78.2088> (cit. on p. 9).

[133] C. Monroe, W. Swann, H. Robinson, and C. Wieman. “Very cold trapped atoms in a vapor cell.” In: *Phys. Rev. Lett.* 65 (13 1990), pp. 1571–1574. DOI: [10.1103/PhysRevLett.65.1571](https://doi.org/10.1103/PhysRevLett.65.1571). URL: <https://link.aps.org/doi/10.1103/PhysRevLett.65.1571> (cit. on p. 9).

[134] E. Maréchal, S. Guibal, J.-L. Bossennec, R. Barbé, J.-C. Keller, and O. Gorceix. “Longitudinal focusing of an atomic cloud using pulsed magnetic forces.” In: *Phys. Rev. A* 59 (6 1999), pp. 4636–4640. DOI: [10.1103/PhysRevA.59.4636](https://doi.org/10.1103/PhysRevA.59.4636). URL: <https://link.aps.org/doi/10.1103/PhysRevA.59.4636> (cit. on p. 9).

- [135] I. Shvarchuck, Ch. Buggle, D. S. Petrov, K. Dieckmann, M. Zielonkowski, M. Kemmann, T. G. Tiecke, W. von Klitzing, G. V. Shlyapnikov, and J. T. M. Walraven. “Bose-Einstein Condensation into Nonequilibrium States Studied by Condensate Focusing.” In: *Phys. Rev. Lett.* 89 (27 2002), p. 270404. DOI: [10.1103/PhysRevLett.89.270404](https://doi.org/10.1103/PhysRevLett.89.270404). URL: <https://link.aps.org/doi/10.1103/PhysRevLett.89.270404> (cit. on p. 9).
- [136] Juris G. Kalnins, Jason M. Amini, and Harvey Gould. “Focusing a fountain of neutral cesium atoms with an electrostatic lens triplet.” In: *Phys. Rev. A* 72 (4 2005), p. 043406. DOI: [10.1103/PhysRevA.72.043406](https://doi.org/10.1103/PhysRevA.72.043406). URL: <https://link.aps.org/doi/10.1103/PhysRevA.72.043406> (cit. on p. 9).
- [137] Tim Kovachy, Jason M. Hogan, Alex Sugarbaker, Susannah M. Dickerson, Christine A. Donnelly, Chris Overstreet, and Mark A. Kasevich. “Matter Wave Lensing to Picokelvin Temperatures.” In: *Phys. Rev. Lett.* 114 (14 Apr. 2015), p. 143004. DOI: [10.1103/PhysRevLett.114.143004](https://doi.org/10.1103/PhysRevLett.114.143004). URL: <https://link.aps.org/doi/10.1103/PhysRevLett.114.143004> (cit. on pp. 11, 65).
- [138] Étienne Clément Wodey. “Methods for very long baseline atom interferometry.” PhD thesis. 2021. DOI: [10.15488/11356](https://doi.org/10.15488/11356) (cit. on p. 11).
- [139] Henning Albers et al. “Quantum test of the Universality of Free Fall using rubidium and potassium.” In: *The European Physical Journal D* 74.7 (2020). ISSN: 1434-6060. DOI: [10.1140/epjd/e2020-10132-6](https://doi.org/10.1140/epjd/e2020-10132-6) (cit. on pp. 11, 71).
- [140] G. Salomon, L. Fouché, P. Wang, A. Aspect, P. Bouyer, and T. Bourdel. “Gray-molasses cooling of 39 K to a high phase-space density.” In: *EPL (Europhysics Letters)* 104.6 (2013), p. 63002. ISSN: 0295-5075. DOI: [10.1209/0295-5075/104/63002](https://doi.org/10.1209/0295-5075/104/63002) (cit. on p. 12).
- [141] L. Antoni-Micollier, B. Barrett, L. Chichet, G. Condon, B. Battelier, A. Landragin, and P. Bouyer. “Generation of high-purity low-temperature samples of K39 for applications in metrology.” In: *Physical Review A* 96.2 (Aug. 2017). DOI: [10.1103/physreva.96.023608](https://doi.org/10.1103/physreva.96.023608) (cit. on p. 12).
- [142] A. Herbst, H. Albers, K. Stolzenberg, S. Bode, and D. Schlippert. “Rapid generation of all-optical ³⁹K Bose-Einstein condensates using a low-field Feshbach resonance.” In: *Phys. Rev. A* 106 (4 Oct. 2022), p. 043320. DOI: [10.1103/PhysRevA.106.043320](https://doi.org/10.1103/PhysRevA.106.043320). URL: <https://link.aps.org/doi/10.1103/PhysRevA.106.043320> (cit. on pp. 12, 68, 69).
- [143] A. Herbst, T. Estrampes, H. Albers, V. Vollenkemper, K. Stolzenberg, S. Bode, E. Charron, E. M. Rasel, N. Gaaloul, and D. Schlippert. “High-flux source system for matter-wave interferometry exploiting tunable interactions.” In: *Phys. Rev. Res.* 6 (1 2024), p. 013139. DOI: [10.1103/PhysRevResearch.6.013139](https://doi.org/10.1103/PhysRevResearch.6.013139). URL: <https://link.aps.org/doi/10.1103/PhysRevResearch.6.013139> (cit. on pp. 13, 14, 68, 72).
- [144] Y. Castin and R. Dum. “Bose-Einstein Condensates in Time Dependent Traps.” In: *Physical Review Letters* 77.27 (Dec. 1996), pp. 5315–5319. DOI: [10.1103/physrevlett.77.5315](https://doi.org/10.1103/physrevlett.77.5315) (cit. on pp. 14, 68).

[145] Yu. Kagan, E. L. Surkov, and G. V. Shlyapnikov. "Evolution of a Bose gas in anisotropic time-dependent traps." In: *Phys. Rev. A* 55 (Jan. 1997), R18. DOI: [10.1103/PhysRevA.55.R18](https://doi.org/10.1103/PhysRevA.55.R18). URL: <https://link.aps.org/doi/10.1103/PhysRevA.55.R18> (cit. on pp. 14, 68).

[146] Víctor M. Pérez-García, H. Michinel, J. I. Cirac, M. Lewenstein, and P. Zoller. "Low Energy Excitations of a Bose-Einstein Condensate: A Time-Dependent Variational Analysis." In: *Phys. Rev. Lett.* 77 (27 Dec. 1996), pp. 5320–5323. DOI: [10.1103/PhysRevLett.77.5320](https://doi.org/10.1103/PhysRevLett.77.5320). URL: <https://link.aps.org/doi/10.1103/PhysRevLett.77.5320> (cit. on pp. 14, 68).

[147] Víctor M. Pérez-García, Humberto Michinel, J. I. Cirac, M. Lewenstein, and P. Zoller. "Dynamics of Bose-Einstein condensates: Variational solutions of the Gross-Pitaevskii equations." In: *Phys. Rev. A* 56 (2 Aug. 1997), pp. 1424–1432. DOI: [10.1103/PhysRevA.56.1424](https://doi.org/10.1103/PhysRevA.56.1424). URL: <https://link.aps.org/doi/10.1103/PhysRevA.56.1424> (cit. on pp. 14, 68).

[148] Alexander Herbst, Timothé Estrampes, Henning Albers, Robin Corgier, Knut Stolzenberg, Sebastian Bode, Eric Charron, Ernst M. Rasel, Naceur Gaaloul, and Dennis Schlippert. "Matter-wave collimation to picokelvin energies with scattering length and potential shape control." In: *Communications Physics* 7.1 (2024). DOI: [10.1038/s42005-024-01621-w](https://doi.org/10.1038/s42005-024-01621-w) (cit. on pp. 14, 67, 78).

[149] Saptarishi Chaudhuri, Sanjukta Roy, and C. S. Unnikrishnan. "Realization of an intense cold Rb atomic beam based on a two-dimensional magneto-optical trap: Experiments and comparison with simulations." In: *Phys. Rev. A* 74 (2 2006), p. 023406. DOI: [10.1103/PhysRevA.74.023406](https://doi.org/10.1103/PhysRevA.74.023406). URL: <https://link.aps.org/doi/10.1103/PhysRevA.74.023406> (cit. on p. 65).

[150] J. Catani, P. Maioli, L. De Sarlo, F. Minardi, and M. Inguscio. "Intense slow beams of bosonic potassium isotopes." In: *Phys. Rev. A* 73 (3 2006), p. 033415. DOI: [10.1103/PhysRevA.73.033415](https://doi.org/10.1103/PhysRevA.73.033415). URL: <https://link.aps.org/doi/10.1103/PhysRevA.73.033415> (cit. on p. 65).

[151] M. Horikoshi and K. Nakagawa. "Atom chip based fast production of Bose-Einstein condensate." In: *Applied Physics B* 82.3 (2006), pp. 363–366. ISSN: 0946-2171. DOI: [10.1007/s00340-005-2083-z](https://doi.org/10.1007/s00340-005-2083-z).

[152] T. van Zoest et al. "Bose-Einstein condensation in microgravity." In: *Science (New York, N.Y.)* 328.5985 (2010), pp. 1540–1543. ISSN: 0036-8075. DOI: [10.1126/science.1189164](https://doi.org/10.1126/science.1189164).

[153] Q. Bouton, R. Chang, A. L. Hoendervanger, F. Nogrette, A. Aspect, C. I. Westbrook, and D. Clément. "Fast production of Bose-Einstein condensates of metastable helium." In: *Phys. Rev. A* 91 (6 2015), p. 061402. DOI: [10.1103/PhysRevA.91.061402](https://doi.org/10.1103/PhysRevA.91.061402). URL: <https://link.aps.org/doi/10.1103/PhysRevA.91.061402>.

[154] Zack Lasner, Debayan Mitra, Maryam Hiradfar, Benjamin Augenbraun, Lawrence Cheuk, Eunice Lee, Sridhar Prabhu, and John Doyle. "Fast and high-yield loading of a D_2 magneto-optical trap of potassium from a cryogenic buffer-gas beam." In: *Phys. Rev. A* 104 (6 2021), p. 063305. DOI: [10.1103/PhysRevA.104.063305](https://doi.org/10.1103/PhysRevA.104.063305). URL: <https://link.aps.org/doi/10.1103/PhysRevA.104.063305> (cit. on p. 67).

- [155] Kosuke Shibata, Hidehiko Ikeda, Ryota Suzuki, and Takuya Hirano. "Compensation of gravity on cold atoms by a linear optical potential." In: *Phys. Rev. Res.* 2 (1 2020), p. 013068. DOI: [10.1103/PhysRevResearch.2.013068](https://doi.org/10.1103/PhysRevResearch.2.013068). URL: <https://link.aps.org/doi/10.1103/PhysRevResearch.2.013068> (cit. on p. 67).
- [156] P. Pedri, D. Guéry-Odelin, and S. Stringari. "Dynamics of a classical gas including dissipative and mean-field effects." In: *Phys. Rev. A* 68 (4 2003), p. 043608. DOI: [10.1103/PhysRevA.68.043608](https://doi.org/10.1103/PhysRevA.68.043608). URL: <https://link.aps.org/doi/10.1103/PhysRevA.68.043608> (cit. on p. 67).
- [157] Christian Ufrecht, Fabio Di Pumbo, Alexander Friedrich, Albert Roura, Christian Schubert, Dennis Schlippert, Ernst M. Rasel, Wolfgang P. Schleich, and Enno Giese. "Atom-interferometric test of the universality of gravitational redshift and free fall." In: *Phys. Rev. Res.* 2 (4 2020), p. 043240. DOI: [10.1103/PhysRevResearch.2.043240](https://doi.org/10.1103/PhysRevResearch.2.043240). URL: <https://link.aps.org/doi/10.1103/PhysRevResearch.2.043240> (cit. on p. 68).
- [158] G. Semeghini, G. Ferioli, L. Masi, C. Mazzinghi, L. Wolswijk, F. Minardi, M. Modugno, G. Modugno, M. Inguscio, and M. Fattori. "Self-Bound Quantum Droplets of Atomic Mixtures in Free Space." In: *Phys. Rev. Lett.* 120 (23 2018), p. 235301. DOI: [10.1103/PhysRevLett.120.235301](https://doi.org/10.1103/PhysRevLett.120.235301). URL: <https://link.aps.org/doi/10.1103/PhysRevLett.120.235301> (cit. on pp. 69, 70).
- [159] C. R. Cabrera, L. Tanzi, J. Sanz, B. Naylor, P. Thomas, P. Cheiney, and L. Tarruell. "Quantum liquid droplets in a mixture of Bose-Einstein condensates." In: *Science* 359.6373 (2018), pp. 301–304. DOI: [10.1126/science.aa05686](https://doi.org/10.1126/science.aa05686). URL: <https://www.science.org/doi/abs/10.1126/science.aa05686> (cit. on pp. 69, 70).
- [160] Dennis Schlippert. "Quantum tests of the universality of free fall." PhD thesis. Leibniz University Hannover, 2014. DOI: [10.15488/8361](https://doi.org/10.15488/8361) (cit. on pp. 69, 72).
- [161] Luka Petersen. "Bragg Lasersystem für die Atominterferometrie mit Kalium." Bachelor's Thesis. Leibniz University Hannover, 2022 (cit. on p. 71).
- [162] Andrea Simoni, Matteo Zaccanti, Chiara D'Errico, Marco Fattori, Giacomo Roati, Massimo Inguscio, and Giovanni Modugno. "Near-threshold model for ultracold KRb dimers from interisotope Feshbach spectroscopy." In: *Phys. Rev. A* 77 (5 2008), p. 052705. DOI: [10.1103/PhysRevA.77.052705](https://doi.org/10.1103/PhysRevA.77.052705). URL: <https://link.aps.org/doi/10.1103/PhysRevA.77.052705> (cit. on p. 72).
- [163] L. Wacker, N. B. Jørgensen, D. Birkmose, R. Horchani, W. Ertmer, C. Klempt, N. Winter, J. Sherson, and J. J. Arlt. "Tunable dual-species Bose-Einstein condensates of ^{39}K and ^{87}Rb ." In: *Phys. Rev. A* 92 (5 2015), p. 053602. DOI: [10.1103/PhysRevA.92.053602](https://doi.org/10.1103/PhysRevA.92.053602). URL: <https://link.aps.org/doi/10.1103/PhysRevA.92.053602> (cit. on p. 72).
- [164] G. Ferrari, M. Inguscio, W. Jastrzebski, G. Modugno, G. Roati, and A. Simoni. "Collisional Properties of Ultracold K-Rb Mixtures." In: *Phys. Rev. Lett.* 89 (5 2002), p. 053202. DOI: [10.1103/PhysRevLett.89.053202](https://doi.org/10.1103/PhysRevLett.89.053202). URL: <https://link.aps.org/doi/10.1103/PhysRevLett.89.053202> (cit. on p. 72).

[165] G. Modugno, M. Modugno, F. Riboli, G. Roati, and M. Inguscio. "Two Atomic Species Superfluid." In: *Phys. Rev. Lett.* 89 (19 2002), p. 190404. DOI: [10.1103/PhysRevLett.89.190404](https://doi.org/10.1103/PhysRevLett.89.190404). URL: <https://link.aps.org/doi/10.1103/PhysRevLett.89.190404> (cit. on p. 72).

[166] G. Thalhammer, G. Barontini, L. De Sarlo, J. Catani, F. Minardi, and M. Inguscio. "Double Species Bose-Einstein Condensate with Tunable Inter-species Interactions." In: *Phys. Rev. Lett.* 100 (21 2008), p. 210402. DOI: [10.1103/PhysRevLett.100.210402](https://doi.org/10.1103/PhysRevLett.100.210402). URL: <https://link.aps.org/doi/10.1103/PhysRevLett.100.210402> (cit. on p. 72).

[167] A. Burchianti, C. D'Errico, S. Rosi, A. Simoni, M. Modugno, C. Fort, and F. Minardi. "Dual-species Bose-Einstein condensate of ^{41}K and ^{87}Rb in a hybrid trap." In: *Phys. Rev. A* 98 (6 2018), p. 063616. DOI: [10.1103/PhysRevA.98.063616](https://doi.org/10.1103/PhysRevA.98.063616). URL: <https://link.aps.org/doi/10.1103/PhysRevA.98.063616> (cit. on p. 72).

[168] Baptist Piest. "Bose-Einstein condensation of K-41 and Rb-87 on an atom chip for sounding rocket missions." PhD thesis. 2021. DOI: [10.15488/11014](https://doi.org/10.15488/11014) (cit. on p. 72).

[169] Robin Corgier, Sina Loriani, Holger Ahlers, Katerine Posso-Trujillo, Christian Schubert, Ernst M. Rasel, Eric Charron, and Naceur Gaaloul. "Interacting quantum mixtures for precision atom interferometry." In: *New Journal of Physics* 22.12 (2020), p. 123008. DOI: [10.1088/1367-2630/abcbc8](https://doi.org/10.1088/1367-2630/abcbc8) (cit. on p. 72).

[170] Mahiro Abe et al. "Matter-wave Atomic Gradiometer Interferometric Sensor (MAGIS-100)." In: *Quantum Science and Technology* 6.4 (2021), p. 044003. DOI: [10.1088/2058-9565/abf719](https://doi.org/10.1088/2058-9565/abf719) (cit. on p. 72).

[171] Carlos L. Garrido Alzar. "Compact chip-scale guided cold atom gyroimeters for inertial navigation: Enabling technologies and design study." In: *AVS Quantum Science* 1.1 (2019). DOI: [10.1116/1.5120348](https://doi.org/10.1116/1.5120348) (cit. on p. 72).

[172] D. Schlippert, S. Bode, A. Herbst, and K. Stolzenberg. *QuIS-g - Sachbericht zum Verwendungsnachweis Teil II: Eingehende Darstellung*. Leibniz University Hannover, 2023 (cit. on pp. 73, 74).

[173] Matthias Gersemann, Martina Gebbe, Sven Abend, Christian Schubert, and Ernst M. Rasel. "Differential interferometry using a Bose-Einstein condensate." In: *The European Physical Journal D* 74.10 (2020). ISSN: 1434-6060. DOI: [10.1140/epjd/e2020-10417-8](https://doi.org/10.1140/epjd/e2020-10417-8) (cit. on p. 72).

[174] T. Berrada, S. van Frank, R. Bücker, T. Schumm, J-F Schaff, and J. Schmiedmayer. "Integrated Mach-Zehnder interferometer for Bose-Einstein condensates." In: *Nature communications* 4 (2013), p. 2077. DOI: [10.1038/ncomms3077](https://doi.org/10.1038/ncomms3077) (cit. on pp. 73, 76).

[175] Sajun Wu, Edward Su, and Mara Prentiss. "Demonstration of an Area-Enclosing Guided-Atom Interferometer for Rotation Sensing." In: *Phys. Rev. Lett.* 99 (17 2007), p. 173201. DOI: [10.1103/PhysRevLett.99.173201](https://doi.org/10.1103/PhysRevLett.99.173201). URL: <https://link.aps.org/doi/10.1103/PhysRevLett.99.173201> (cit. on p. 73).

[176] P. Navez, S. Pandey, H. Mas, K. Poulios, T. Fernholz, and W. von Klitzing. “Matter-wave interferometers using TAAP rings.” In: *New Journal of Physics* 18.7 (2016), p. 075014. DOI: [10.1088/1367-2630/18/7/075014](https://doi.org/10.1088/1367-2630/18/7/075014) (cit. on p. 73).

[177] S. J. Kim, H. Yu, S. T. Gang, D. Z. Anderson, and J. B. Kim. “Controllable asymmetric double well and ring potential on an atom chip.” In: *Phys. Rev. A* 93 (3 2016), p. 033612. DOI: [10.1103/PhysRevA.93.033612](https://doi.org/10.1103/PhysRevA.93.033612). URL: <https://link.aps.org/doi/10.1103/PhysRevA.93.033612> (cit. on p. 73).

[178] S. J. Kim, H. Yu, S. T. Gang, and J. B. Kim. “Matter-wave beam splitter on an atom chip for a portable atom interferometer.” In: *Applied Physics B* 123.5 (2017). ISSN: 0946-2171. DOI: [10.1007/s00340-017-6719-6](https://doi.org/10.1007/s00340-017-6719-6) (cit. on p. 73).

[179] Hoon Yu, Seung Jin Kim, and Jung Bog Kim. “Toward atom interferometer gyroscope built on an atom chip.” In: *Journal of the Korean Physical Society* 82.9 (2023), pp. 819–826. ISSN: 0374-4884. DOI: [10.1007/s40042-023-00768-z](https://doi.org/10.1007/s40042-023-00768-z) (cit. on p. 73).

[180] Yvan Castin and Jean Dalibard. “Relative phase of two Bose-Einstein condensates.” In: *Phys. Rev. A* 55 (6 1997), pp. 4330–4337. DOI: [10.1103/PhysRevA.55.4330](https://doi.org/10.1103/PhysRevA.55.4330). URL: <https://link.aps.org/doi/10.1103/PhysRevA.55.4330> (cit. on p. 73).

[181] J. E. Debs, P. A. Altin, T. H. Barter, D. Döring, G. R. Dennis, G. McDonald, R. P. Anderson, J. D. Close, and N. P. Robins. “Cold-atom gravimetry with a Bose-Einstein condensate.” In: *Phys. Rev. A* 84 (3 2011), p. 033610. DOI: [10.1103/PhysRevA.84.033610](https://doi.org/10.1103/PhysRevA.84.033610). URL: <https://link.aps.org/doi/10.1103/PhysRevA.84.033610> (cit. on p. 73).

[182] G. D. McDonald, H. Keal, P. A. Altin, J. E. Debs, S. Bennetts, C. C. N. Kuhn, K. S. Hardman, M. T. Johnsson, J. D. Close, and N. P. Robins. “Optically guided linear Mach-Zehnder atom interferometer.” In: *Phys. Rev. A* 87 (1 2013), p. 013632. DOI: [10.1103/PhysRevA.87.013632](https://doi.org/10.1103/PhysRevA.87.013632). URL: <https://link.aps.org/doi/10.1103/PhysRevA.87.013632> (cit. on p. 73).

[183] M. Fattori, C. D’Errico, G. Roati, M. Zaccanti, M. Jona-Lasinio, M. Modugno, M. Inguscio, and G. Modugno. “Atom Interferometry with a Weakly Interacting Bose-Einstein Condensate.” In: *Phys. Rev. Lett.* 100 (8 2008), p. 080405. DOI: [10.1103/PhysRevLett.100.080405](https://doi.org/10.1103/PhysRevLett.100.080405). URL: <https://link.aps.org/doi/10.1103/PhysRevLett.100.080405> (cit. on p. 73).

[184] Leonardo Masi et al. “Multimode trapped interferometer with noninteracting Bose-Einstein condensates.” In: *Phys. Rev. Res.* 3 (4 2021), p. 043188. DOI: [10.1103/PhysRevResearch.3.043188](https://doi.org/10.1103/PhysRevResearch.3.043188). URL: <https://link.aps.org/doi/10.1103/PhysRevResearch.3.043188> (cit. on p. 73).

[185] Katarzyna Krzyzanowska, Jorge Ferreras, Changhyun Ryu, Edward Carlo Samson, and Malcolm Boshier. *Matter Wave Analog of a Fiber-Optic Gyroscope*. 2022. DOI: [10.48550/arXiv.2201.12461](https://doi.org/10.48550/arXiv.2201.12461) (cit. on p. 74).

[186] Hyosub Kim, Katarzyna Krzyzanowska, K. C. Henderson, C. Ryu, Eddy Timmermans, and Malcolm Boshier. *One second interrogation time in a 200 round-trip waveguide atom interferometer*. 2022. DOI: [10.48550/arXiv.2201.11888](https://doi.org/10.48550/arXiv.2201.11888) (cit. on p. 74).

[187] T. Berrada, S. van Frank, R. Bücker, T. Schumm, J.-F. Schaff, J. Schmiedmayer, B. Julía-Díaz, and A. Polls. “Matter-wave recombiners for trapped Bose-Einstein condensates.” In: *Phys. Rev. A* 93 (6 2016), p. 063620. DOI: [10.1103/PhysRevA.93.063620](https://doi.org/10.1103/PhysRevA.93.063620). URL: <https://link.aps.org/doi/10.1103/PhysRevA.93.063620> (cit. on p. 74).

[188] A. Trenkwalder et al. “Quantum Phase Transitions with Parity-Symmetry Breaking and Hysteresis.” In: *Nature Physics* 12.9 (2016), pp. 826–829. ISSN: 1745-2473. DOI: [10.1038/nphys3743](https://doi.org/10.1038/nphys3743) (cit. on p. 74).

[189] A. Duspayev and G. Raithel. “Tractor atom interferometry.” In: *Phys. Rev. A* 104 (1 2021), p. 013307. DOI: [10.1103/PhysRevA.104.013307](https://doi.org/10.1103/PhysRevA.104.013307). URL: <https://link.aps.org/doi/10.1103/PhysRevA.104.013307> (cit. on p. 74).

[190] Hannah Paltzer. “Modelling of a Trapped BEC Interferometry Experiment.” Master’s Thesis. Leibniz University Hannover, 2022 (cit. on p. 74).

[191] Jonathan Nemirovsky, Rafi Weill, Ilan Meltzer, and Yoav Sagi. “Atomic interferometer based on optical tweezers.” In: *Phys. Rev. Res.* 5 (4 2023), p. 043300. DOI: [10.1103/PhysRevResearch.5.043300](https://doi.org/10.1103/PhysRevResearch.5.043300). URL: <https://link.aps.org/doi/10.1103/PhysRevResearch.5.043300> (cit. on p. 74).

[192] Gayathrini Premawardhana, Jonathan Kunjummen, Sarthak Subhankar, and Jacob M. Taylor. *Feasibility of a trapped atom interferometer with accelerating optical traps*. 2023. DOI: [10.48550/arXiv.2308.12246](https://doi.org/10.48550/arXiv.2308.12246) (cit. on p. 74).

[193] Robin Corgier, Naceur Gaaloul, Augusto Smerzi, and Luca Pezzè. “Delta-Kick Squeezing.” In: *Phys. Rev. Lett.* 127 (18 2021), p. 183401. DOI: [10.1103/PhysRevLett.127.183401](https://doi.org/10.1103/PhysRevLett.127.183401). URL: <https://link.aps.org/doi/10.1103/PhysRevLett.127.183401> (cit. on p. 77).

[194] A. Gauguet, B. Canuel, T. Lévèque, W. Chaibi, and A. Landragin. “Characterization and limits of a cold-atom Sagnac interferometer.” In: *Phys. Rev. A* 80 (6 2009), p. 063604. DOI: [10.1103/PhysRevA.80.063604](https://doi.org/10.1103/PhysRevA.80.063604). URL: <https://link.aps.org/doi/10.1103/PhysRevA.80.063604> (cit. on p. 76).

[195] F. Sorrentino, Q. Bodart, L. Cacciapuoti, Y.-H. Lien, M. Prevedelli, G. Rosi, L. Salvi, and G. M. Tino. “Sensitivity limits of a Raman atom interferometer as a gravity gradiometer.” In: *Phys. Rev. A* 89 (2 2014), p. 023607. DOI: [10.1103/PhysRevA.89.023607](https://doi.org/10.1103/PhysRevA.89.023607). URL: <https://link.aps.org/doi/10.1103/PhysRevA.89.023607> (cit. on p. 76).

[196] Z. Y. Ou. “Fundamental quantum limit in precision phase measurement.” In: *Physical Review A* 55.4 (1997), pp. 2598–2609. ISSN: 1050-2947. DOI: [10.1103/PhysRevA.55.2598](https://doi.org/10.1103/PhysRevA.55.2598) (cit. on p. 76).

[197] Stuart S. Szigeti, Onur Hosten, and Simon A. Haine. “Improving cold-atom sensors with quantum entanglement: Prospects and challenges.” In: *Applied Physics Letters* 118.14 (2021). ISSN: 0003-6951. DOI: [10.1063/5.0050235](https://doi.org/10.1063/5.0050235) (cit. on p. 77).

- [198] R. J. Sewell, M. Koschorreck, M. Napolitano, B. Dubost, N. Behbood, and M. W. Mitchell. “Magnetic Sensitivity Beyond the Projection Noise Limit by Spin Squeezing.” In: *Phys. Rev. Lett.* 109 (25 2012), p. 253605. DOI: [10.1103/PhysRevLett.109.253605](https://doi.org/10.1103/PhysRevLett.109.253605). URL: <https://link.aps.org/doi/10.1103/PhysRevLett.109.253605> (cit. on p. 77).
- [199] Edwin Pedrozo-Peña et al. “Entanglement on an optical atomic-clock transition.” In: *Nature* 588.7838 (2020), pp. 414–418. DOI: [10.1038/s41586-020-3006-1](https://doi.org/10.1038/s41586-020-3006-1) (cit. on p. 77).
- [200] Christophe Cassens, Bernd Meyer-Hoppe, Ernst Rasel, and Carsten Klempert. *An entanglement-enhanced atomic gravimeter*. 2024. DOI: [10.48550/arXiv.2404.18668](https://doi.org/10.48550/arXiv.2404.18668) (cit. on p. 77).
- [201] Graham P. Greve, Chengyi Luo, Baochen Wu, and James K. Thompson. “Entanglement-enhanced matter-wave interferometry in a high-finesse cavity.” In: *Nature* 610.7932 (2022), pp. 472–477. DOI: [10.1038/s41586-022-05197-9](https://doi.org/10.1038/s41586-022-05197-9) (cit. on p. 77).
- [202] Robin Corgier, Luca Pezzè, and Augusto Smerzi. “Nonlinear Bragg interferometer with a trapped Bose-Einstein condensate.” In: *Phys. Rev. A* 103 (6 2021), p. L061301. DOI: [10.1103/PhysRevA.103.L061301](https://doi.org/10.1103/PhysRevA.103.L061301). URL: <https://link.aps.org/doi/10.1103/PhysRevA.103.L061301> (cit. on pp. 77, 78).
- [203] Masahiro Kitagawa and Masahito Ueda. “Squeezed spin states.” In: *Phys. Rev. A* 47 (6 1993), pp. 5138–5143. DOI: [10.1103/PhysRevA.47.5138](https://doi.org/10.1103/PhysRevA.47.5138). URL: <https://link.aps.org/doi/10.1103/PhysRevA.47.5138> (cit. on p. 77).

ACKNOWLEDGMENTS

A doctoral thesis is neither a short nor an easy undertaking and many wonderful people have accompanied me along the way. I would like to take this opportunity to thank all those I have had the pleasure of working alongside over the last few years. Without you, this thesis would not have become what it is today:

First of all, I would like to thank **Dennis Schlippert**. You gave me the opportunity to write my doctoral thesis at the Institute of Quantum Optics. Thank you for the trust you placed in me and for having me on your team. Ever since I started you have been a source of guidance, consistently offering assistance and insightful counsel. Your supportive yet challenging mentorship has fostered my personal and academic growth, enabling me to navigate the challenges and successes encountered along the way.

I am equally indebted to **Ernst Rasel** for his foundational role in establishing our research group and cultivating an environment of collaboration and passion for physics. Whenever things got difficult and it was not clear in which direction to proceed, you were able to help with your immense wealth of experience, especially in steering our publications towards their optimal direction.

I would also like to thank **Éric Charron** for agreeing to act as external referee for this thesis and for his contributions to our joint publications. It was always impressive to see how you went through the manuscripts almost in real time.

None of this would have been achievable without the collective effort of an exceptional team behind me. I am sincerely thankful to all members of the QuIS-g project, which I was lucky enough to join for this thesis. In particular, I want to thank **Henning Albers**. Atlas was your experiment when I started, and you helped me to get to grips with all the little details needed to operate such a complex machine. I learned a lot from you and your calm and collected manner were a tremendous help to get through the first year. In the same way, **Sebastian Bode** always had the right solutions at hand when it came to tearing the apparatus apart and doing something with it that it was never designed for. Your motivating manner made every undertaking, no matter how difficult, fun. Together with **Knut Stolzenberg**, it was the three of you who made this time something truly special, be it at the joint conferences, the countless discussions over coffee or by simply working together.

I would also like to thank the theory team led by **Naceur Gaaloul** for their immense support. Above all, **Timothé Estrampes'** tireless determination to improve the simulations of the experiments was pivotal to our success. I am immensely grateful for the opportunity to have collaborated with you. Likewise, with **Robin Corgier** I had the most amazing five-minute-long discussion about "...that one line in the manuscript..." which turned out to last four hours.

Special thanks go to **Dorothee Tell** from the VLBAI team. Despite working on different projects, we often faced similar questions and challenges. Working on solutions together with you was both enjoyable and productive. Also, I have to thank **Mouine Abidi** for his camaraderie. Sharing an office with you has been an experience I cherish. Furthermore, I would like to thank **Baptist Piest** for accompanying me on my very first steps at the institute during my master's thesis. Similarly, **Torben Schulze** introduced me to the exciting realm of Feshbach resonances and willingly shared his knowledge about how to deal with potassium atoms.

For the enriching discussions, friendships forged, and the enjoyable moments shared, I extend my thanks to: **Phillip Barbey, Jonas Böhm, Kai Frye-Arndt, Matthias Gersemann, Hendrik Heine, Nina Heine, Mareike Hetzel, Maike Lachmann, Ali Lezeik, Ashwin Rajagopalan, Vera Vollenkemper, Étienne Wodey and Klaus Zipfel**. Now a new generation of students is taking over: **Wei Liu, Daida Thomas, Constantin Avvacumov, Patrick Rößler, Vishu Gupta and Kai Grensemann**, I am looking forward to what you gonna achieve in the future.

Behind the scenes many people work to keep the infrastructure of the institute up and running. I would like to thank **Kai-Martin Knaak** for his help with all the problems related to electronics and the team at the mechanics workshop led by **Alexander Vocino, Jonas Peter** and **Mathias Scholz**, who were always ready to respond to my last-minute requests as quickly as possible. For all the help with administrative tasks, formal questions, organizational issues and financial reports I want to thank **Birgit Ohlendorf, Anne-Dore Göldner-Pauer, Stephanie Kaisik** and **Bianca Thiel**.

Lastly, to my friends and family, I am deeply grateful for your unwavering support throughout this journey. Your unconditional encouragement has been my pillar of strength, and I owe much of my success to you.

PUBLICATIONS

PUBLICATIONS IN PEER-REVIEWED JOURNALS:

Henning Albers, **Alexander Herbst**, Logan L. Richardson, Hendrik Heine, Dipankar Nath, Jonas Hartwig, Christian Schubert, Christian Vogt, Marian Woltmann, Claus Lämmerzahl, Sven Herrmann, Wolfgang Ertmer, Ernst M. Rasel, and Dennis Schlippert, "Quantum test of the universality of free fall using rubidium and potassium", *The European Physical Journal D* **74** (2020), doi: [10.1140/epjd/e2020-10132-6](https://doi.org/10.1140/epjd/e2020-10132-6).

Baptist Piest, Vera Vollenkemper, Jonas Böhm, **Alexander Herbst**, and Ernst M. Rasel, "Red- and blue-detuned magneto-optical trapping with liquid crystal variable retarders", *Review of Scientific Instruments* **93**, 023202 (2022), doi: [10.1063/5.0071619](https://doi.org/10.1063/5.0071619).

Henning Albers, Robin Corgier, **Alexander Herbst**, Ashwin Rajagopalan, Christian Schubert, Christian Vogt, Marian Woltmann, Claus Lämmerzahl, Sven Herrmann, Eric Charron, Wolfgang Ertmer, Ernst M. Rasel, Naceur Gaaloul, and Dennis Schlippert "All-optical matter-wave lens using time-averaged potentials", *Communications Physics* **5**, 60 (2022), doi: [10.1038/s42005-022-00825-2](https://doi.org/10.1038/s42005-022-00825-2).

Alexander Herbst, Henning Albers, Knut Stolzenberg, Sebastian Bode, and Dennis Schlippert, "Rapid generation of all-optical ^{39}K Bose-Einstein condensates using a low-field Feshbach resonance", *Physical Review A* **106**, 043320 (2022), doi: [10.1103/PhysRevA.106.043320](https://doi.org/10.1103/PhysRevA.106.043320).

Alexander Herbst, Timothé Estrampes, Henning Albers, Vera Vollenkemper, Knut Stolzenberg, Sebastian Bode, Eric Charron, Ernst M. Rasel, Naceur Gaaloul, and Dennis Schlippert, "High-flux source system for matter-wave interferometry exploiting tunable interactions", *Physical Review Research* **6**, 013139 (2024), doi: [10.1103/PhysRevResearch.6.01313](https://doi.org/10.1103/PhysRevResearch.6.01313).

Alexander Herbst, Timothé Estrampes, Henning Albers, Robin Corgier, Knut Stolzenberg, Sebastian Bode, Eric Charron, Ernst M. Rasel, Naceur Gaaloul, and Dennis Schlippert, "Matter-wave collimation to picokelvin energies with scattering length and potential shape control", *Communications Physics* **7**, 132 (2024), doi: [10.1038/s42005-024-01621-w](https://doi.org/10.1038/s42005-024-01621-w).

OTHER PUBLICATIONS:

Knut Stolzenberg, Christian Struckmann, Sebastian Bode, Rui Li, **Alexander Herbst**, Vera Vollenkemper, Daida Thomas, Ernst M. Rasel, Naceur Gaaloul, and Dennis Schlippert, "Multi-axis inertial sensing with 2D arrays of Bose Einstein Condensates", doi: [10.48550/arXiv.2403.08762](https://arxiv.org/abs/2403.08762).

CURRICULUM VITAE

PERSONAL DETAILS:

Name: Alexander Georg Herbst
Date of birth: June 16, 1992
Place of birth: Hannover
Nationality: german

EDUCATION:

Jan. 2019 - Jun. 2024	Doctoral studies at Institute of Quantum Optics, Leibniz University Hannover, Germany Group: Dr. Schlippert/Prof. Dr. Rasel
Oct. 2017 - Nov. 2018 and Oct. 2014 - Sep. 2016	Master of Science (Physics) Leibniz University Hannover, Germany Thesis with Prof. Dr. Rasel
Oct. 2016 - Sep. 2017	Master Studies University of Würzburg, Germany and Luleå University of Technology, Sweden
Oct. 2011 - Sep. 2014	Bachelor of Science (Physics) Leibniz University Hannover, Germany Thesis with Prof. Dr. Giulini
Jun. 2011	Allgemeine Hochschulreife (Abitur) Bismarckschule Hannover, Germany

WORK

Jan. 2019 - today Research assistant at Institute of Quantum Optics, Leibniz University Hannover, Germany
Group: Dr. Schlippert/Prof. Dr. Rasel

Jun. 2017 - Sep. 2017 Research intern at Max Planck Institute for Plasma Physics, Germany
Group: Prof. Dr. Helander

Apr. 2016 - Sep. 2016 Student assistant at Institute of Theoretical Physics, Leibniz University Hannover, Germany
Group: Prof. Dr. Werner